2015

Atomistic simulation of plasticity mediated by grain boundary and stacking fault tetrahedron in FCC metals

Liang Zhang
University of Wollongong

Atomistic Simulation of Plasticity Mediated by Grain Boundary and Stacking Fault Tetrahedron in FCC Metals

A Thesis Presented

By

Liang Zhang

in Partial Fulfillment of the Requirements for the Degree

Doctor of Philosophy

School of Mechanical, Materials and Mechatronic Engineering
Faculty of Engineering and Information Science
University of Wollongong

2015

TABLE OF CONTENTS

TABLE OF CONTENTS III

ACKNOWLEDGEMENT VII

ABSTRACT VIII

LIST OF PUBLICATIONS X

LIST OF TABLES XII

LIST OF FIGURES XIII

Chapter 1: **Introduction** 1

1.1 Research Background 1

1.1.1 Grain boundary 1

1.1.2 Stacking fault tetrahedron 5

1.2 Research Objective 7

1.3 Thesis Structure 9

Chapter 2: **Literature Review** 11

2.1 Grain Boundary Structure and Energy 11

2.1.1 Structure and energy of symmetric GB 11

2.1.2 Structure and energy of asymmetric GB 14

2.1.3 Faceting and dissociation of GB 19

2.2 Grain Boundary Induced Plasticity 22

2.2.1 Grain boundary sliding 23

2.2.2 Grain boundary migration 26

2.2.3 Interaction of grain boundary and dislocation 31

2.2.4 Dislocation nucleation from grain boundary 35

2.3 Stacking Fault Tetrahedron Induced Plasticity 37

2.3.1 Interaction of SFT with dislocation 37

2.3.2 Interaction of SFT with twin boundary 41

2.4 Summary 43
Chapter 3: **Introduction of Simulation Methodology** 45
3.1 Molecular Dynamics (MD) Simulation 45
3.2 Potentials used in MD simulations 49
3.3 MD code LAMMPS.....51
3.4 Visualization Methods 52
3.5 Dislocation Extraction Algorithm (DXA).....55
3.6 Summary 57
Chapter 4: **Study on the Generalized Stacking Fault Energy of FCC Metals**.....58
4.1 Introduction.....58
4.2 Simulation Methodology 60
4.3 Results and Discussion 63
4.4 Summary 72
Chapter 5: **Dislocation Nucleation in Copper Bicrystal with <1 1 0> Symmetric Tilt Grain Boundary** 73
5.1 Introduction.....73
5.2 Simulation Methodology 74
5.2.1 Simulation model 74
5.2.2 Simulation details.....76
5.2.3 GB Energy calculation 77
5.3 Simulation Results 79
5.3.1 GB structure and energy 79
5.3.2 Tensile response 82
5.3.3 Dislocation nucleation from GB with θ<109.5° 84
5.3.4 Dislocation nucleation from θ=109.5° and θ=114.5° GBs 89
5.3.5 Dislocation nucleation from GB with θ>114.5° 91
5.4 Discussion 95
5.5 Summary 98

Chapter 6: **Tensile Deformation Behaviour of Σ5 Tilt Grain Boundaries in Copper Bicrystal** 100
6.1 Introduction 100
6.2 Simulation Method 102
6.2.1 Model construction 102
6.2.2 GB energy calculation 104
6.2.3 Molecular dynamics simulation 104
6.3 Results 106
6.3.1 GB structure and energy 106
6.3.2 Mechanical response 109
6.3.3 Deformation mechanism 110
6.4 Discussion 114
6.5 Summary 118
Chapter 7: **Shear Response of Copper Bicrystals with Σ11 Grain Boundaries** 121
7.1 Introduction 121
7.2 Simulation Methodology 123
7.3 Results and Discussion 126
7.3.1 Grain boundary structure 126
7.3.2 The shear response of Σ11(1 1 3) Φ=0 °GB 127
7.3.3 The shear response of Σ11(2 2 5)/(4 4 1) Φ=54.74° GB 130
7.3.4 The shear response of Σ11(5 5 7)/(**7 7 1**) Φ=70.53° GB 133
7.3.5 The shear response of Σ11(3 3 2) Φ=90° GB 137
7.3.6 Evolution of the dissociated stacking fault 139
7.4 Summary 142
Chapter 8: **Atomic Mechanisms of Stacking Fault Tetrahedron Induced Plasticity in Copper Single Crystal** 143
8.1 Introduction 143
8.2 Simulation method 146

8.3 Results.....149
8.3.1 Compressive and tensile stress response.....149
8.3.2 Deformation mechanism of SFT for [1 0 0] orientation.....152
8.3.3 Deformation mechanism of SFT for [1 1 0] orientation.....156
8.3.4 Deformation mechanism of SFT for [1 1 1] orientation.....159
8.4 Discussion.....162
8.4.1 Different reduction in yield stress.....162
8.4.2 Compression/tension asymmetry.....166
8.4.3 Unfaulting of the Frank loop.....168
8.5 Summary.....171
Chapter 9: **Conclusions and Recommendations**.....178
9.1 Overview.....178
9.2 Study on the Generalized Stacking Fault Energy of FCC Metals.....179
9.3 Dislocation Nucleation in Cu Bicrystal with <1 1 0> Symmetric Tilt GBs179
9.4 Tension Deformation Behaviour of Σ5 GBs in Cu Bicrystal.....180
9.5 Shear Response of Cu Bicrystals with Σ11 GBs.....181
9.6 Stacking Fault Tetrahedron Induced Plasticity in Cu Single Crystal.....182
9.7 Recommendations for Future Work.....184
REFERENCES.....187

ACKNOWLEDGEMENT

I would like to thank my supervisors Prof. Kiet Tieu and A/Prof. Cheng Lu for their guidance and advice during my PhD study in the past 4 years. They have allowed me the freedom to direct this research project according to my own observations, developing in me the ability to think creatively and independently. I have been always motivated by their attitude toward my research and pleased by their advices on my work. I am truly honoured to have them as my PhD supervisors.

I also want to thank my group mates, Linqing Pei, Xing Zhao and Kuiyu Cheng for making a friendly environment where working was fun and alive. Thanks for their thoughtful and insightful discussions and suggestions in my research. Their patience on answering my questions and their advices that helped me a lot in performing better job on my thesis.

Thanks to China Scholarship Council (CSC) for financial support during my PhD study in the past 4 years, and thanks to the University of Wollongong for providing an International Postgraduate Tuition Award (IPTA) scholarship. Simulations in the thesis were performed using the High Performance Computer cluster supported by the University of Wollongong.

Thanks to my parents and my family members for their strong support during my PhD study. Finally, I would like to give my particular thanks to my lovely girlfriend Dan Wang, thanks for her patient and understanding during my 4 years leaving for studying in Australia.

ABSTRACT

Nanocrystalline material has been the subject of widespread research over the past couple of decades. When the grain sizes of crystals are down to nanoscale, the so-called nanocrystalline material can exhibit distinct physical properties, unlike their conventional counterparts. The strength and plastic deformation of nanocrystalline material were among the most broadly investigated properties from the mechanical and material perspective. But since the rapid increases in computational power, atomistic simulation has been used extensively to study the mechanical properties of nanocrystalline material from which enormous progress has been made in computational simulation to understand the deformation mechanisms at an atomic scale. In this thesis, molecular dynamics (MD) simulations were carried out to study two common types of crystal defect induced plasticity in nanocrystalline metallic materials, i.e. grain boundary (GB) and stacking fault tetrahedron (SFT).

The first part of this thesis focuses on symmetric GBs where MD simulations were carried out to study dislocation nucleation from a number of ⟨1 1 0⟩ tilt GBs that covered a wide range of misorientation angles (θ). The results indicated that the mechanical behaviour of GBs and the energy barrier of dislocation nucleation from GBs were closely related to the lattice crystallographic orientation, GB energy, and the intrinsic GB structures. An atomistic analysis of the nucleation mechanisms provided details of dislocation nucleation and emission from the GBs.

The second part of the thesis focuses on the structure and mechanical property of asymmetric GBs, with the results showing that the structure of Σ5 and Σ11 asymmetric GBs with different inclination angles (Φ) consisted of structural units that are closely related to their corresponding symmetric GBs. Tensile deformation was carried out on the bicrystal models with Σ5 GBs under either 'free' or 'constrained' boundary conditions, and the results indicated that the stress state can play an

important role in the dislocation nucleation mechanisms. Different deformation mechanisms were reported due to the Σ11 GB structures, including GB migration coupled to shear deformation, GB sliding caused by local atomic shuffling, or nucleation of dislocations and stacking faults from the GB.

In the third part, MD simulations were used to investigate the atomic mechanisms of SFT induced plasticity in Cu single crystal. The mechanical response and deformation mechanisms of SFT depended mainly on the crystal orientation and loading direction. The structural transformation of SFT was prevalent under the applied loading; this resulted in a different reduction of yield stress in compression and tension, and also caused a decreased or reversed compression/tension asymmetry. Compressive stress can result in the unfaulting of Frank loop in some crystal, and the process of unfaulting was closely related to the size of the dislocation loop and the stacking fault energy according to the elastic theory of dislocation.

The research in this thesis provides a fundamental understanding of grain boundary and stacking fault tetrahedron induced crystal plasticity at nanometer size, and it can help to enrich the theoretical basis for improving the performance of nanocrystalline materials.

LIST OF PUBLICATIONS

Zhang L., Lu C., Tieu K., Su L., Pei L., Zhao X., Michal G. "Atomic mechanisms of stacking fault tetrahedra induced plasticity in copper single crystals". (to be submit).

Zhang L., Lu C., Tieu K., Zhao X., Pei L. (2015) "Shear Response of Copper Bicrystal with ∑11 Symmetric and Asymmetric Tilt Grain Boundaries by Molecular Dynamics Simulation". *Nanoscale* **7**, 7224-7233. (RSC)

Pei L., Lu C., Zhao X., **Zhang L.**, Cheng K., Michal G., Tieu K. (2015) Brittle versus ductile behaviour of nanotwinned copper: A molecular dynamics study. *Acta Materialia* 89, 1-13. (Elsevier)

Zhang L., Lu C., Tieu K., Pei L., Zhao X., Cheng K. (2015) "Molecular dynamics study on the grain boundary dislocation source in nanocrystalline copper under tensile loading". *Materials Research Express* 2, 035009. (IOP)

Zhang L., Lu C., Tieu K., Zhao X., Pei L., Michal G.(2015) "Molecular Dynamics Simulation on Generalized Stacking Fault Energies of FCC Metals under Preloading Stress". *Chinese Physics B* 24, 088106. (IOP)

Pei L., Lu C., Tieu K., Zhao X., **Zhang L.**, Cheng K., Michal G. (2015) Brittle versus ductile fracture behaviour in nanotwinned FCC crystals. *Materials Letters* 152, 65-67. (Elsevier)

Pei L., Lu C., Tieu K., Zhao X., **Zhang L.**, Cheng K. (2015) Ductile-to-brittle fracture transition in polycrystalline nickel under tensile hydrostatic stress. *Computational Materials Science* **109**, 147-156.

Zhang L., Lu C. & Tieu K. (2014) "Atomistic Simulation of Tensile Deformation Behaviour of ∑5 Tilt Grain Boundaries in Copper Bicrystal". *Scientific Reports* 4, 5919. (Nature)

Zhang L., Lu C., Tieu K., Pei L., Zhao X. (2014) "Effect of Stress State on Deformation and Fracture of Nanocrystalline Copper by Molecular Dynamics Simulation." *Chinese Physics B* 23, 098102. (IOP)

Zhang L., Lu C., Michal G., Tieu K., Cheng K. (2014) "Molecular dynamics study on the atomic mechanisms of coupling motion of [0 0 1] symmetric tilt grain boundaries in copper bicrystal". *Materials Research Express* 1, 015019. (IOP)

Zhang L., Lu C., Tieu K., Zhao X., Pei L., Cheng K. (2014) "Atomistic Simulation on the Structure and Mechanical Response of Σ3, Σ5 Tilt Grain Boundaries under Tension". *TMS Annual Meeting Proceedings* [Oral Presentation at 143rd TMS Annual Meeting, San Diego, USA.]

Zhang L., Lu C. & Tieu K. (2013) "Molecular Dynamics Simulation on Σ5 Grain Boundaries of Copper Bicrystal under Tensile and Shear Deformation". *MRS Symposium Proceedings* [Oral Presentation at 2013 MRS Fall Meeting, Boston, USA.]

LIST OF TABLES

Table 4.1 Elastic modulus of Cu, Ni and Al under tension and compression. 64

Table 5.1 Summary information of different [1 1 0] symmetric tilt GBs in Cu bicrystal.....77

Table 5.2 Schmid factor of resolved shear stress on the {1 1 1}<1 1 2> slip system for the [1 1 0] tilt grain boundaries. 99

Table 6.1 Details of Σ5 grain boundary and dimensions of bicrystal models. ..102

Table 7.1 Details of Σ11 grain boundary and dimensions of bicrystal models. 124

Table 8.1 Yield stress of perfect crystals and crystals with SFT at different temperatures.....152

Table 8.2 Simulation results of perfect crystals and crystals with an SFT under uniaxial compression (C) and tension (T) at 10 K.....177

LIST OF FIGURES

Chapter-1

Figure 1.1 A mechanism map for deformation behaviour showing the nominal changes in the underlying mechanisms of plasticity at different grain sizes. 3

Chapter-2

Figure 2.1 Atomic structure of selected [0 0 1] symmetrical tilt GBs in Cu at 0 K. 12

Figure 2.2 The grain boundary energy of nickel shown as a function of (a) the tilt angle in the <1 1 0> direction. (b) the twist angle in the <1 1 1> direction. (c) the tilt angle in the <0 0 1> direction. 13

Figure 2.3 Six Σ3 grain boundary structures in Cu for various inclination angles. 15

Figure 2.4 Grain boundary energy as a function of inclination angle for Cu and Al.....16

Figure 2.5 Grain boundary energy of (a) Σ5 and (b) Σ13 asymmetric tilt grain boundaries with the <1 0 0> tilt axis as a function of inclination angle. 18

Figure 2.6 Grain boundary energy of (a) Σ9 and (b) Σ11 asymmetric tilt grain boundaries with the <1 1 0> tilt axis as a function of inclination angle. 18

Figure 2.7 Atomic structure of selected Σ11[110] asymmetrical grain boundaries with inclination angles (a) Φ=46.7 °and (b) Φ=74.2 °.....19

Figure 2.8 HRTEM image of the GB heat-treated at different temperature. 20

Figure 2.9 The relative boundary energy γ_B/γ_I as a function of the inclination angle of (a) ∑11[1 1 0] and (b) ∑9[1 1 0] asymmetric tilt GBs of Cu at 1273K.....21

Figure 2.10 (a) Schematic drawing for faceting. (b) Schematic drawing for dissociation of the $\sum 9\{447\}_A\{001\}_B$ boundary.....22

Figure 2.11 The relative sliding displacements of two grains with a misorientation angle of 25.2 °under different applied forces. 24

Figure 2.12 The effect of misorientation angle on GB sliding distance as a function of time.....24

Figure 2.13 (a) GB displacement versus time during MD simulations at 800 K under a shear parallel to the GB plane and normal to the tilt axis. The shear rate is 1 m/s. (b) The coupling factor b obtained by MD simulations at 800 K as a function of the tilt angle.....27

Figure 2.14 Diagram of mechanical responses to shear of [0 0 1] symmetrical tilt GBs in Cu.....28

Figure 2.15 GB displacement and shear stress at (a) 100 K, (b) 500 K and (c) 900 K and the imposed grain translation velocity 1 m/s for the $\sum 21$ GB in Al. 29

Figure 2.16 Schematic of dislocation propagation along a GB by a chain of dislocation reactions.....30

Figure 2.17 Schematic illustration of the dislocation avoidance mechanism for an asymmetrical GB moving upward. 30

Figure 2.18 Schematic of intersection of slip planes and grain boundary. 32

Figure 2.19 Different steps of the interaction between a “positive” dislocation and a symmetrical $\sum 57$ tilt grain boundary.....34

Figure 2.20 The nucleation of partial dislocation loops under uniaxial tensile deformation of the asymmetric tilt grain boundary with different angles in Cu at 10K.....37

Figure 2.21 Structure of a perfect stacking-fault tetrahedra following the shear by four screw dislocations. 39

Figure 2.22 MD simulation of reaction details between a screw dislocation and a

6 nm SFT (276 vacancies) at 300 K and under 100 MPa. 40

Figure 2.23 High-resolution TEM of SFTs and their interaction mechanism with twin boundaries. 43

Chapter-3

Figure 3.1 Four different methods of visualization of grain boundary and dislocation segment within a nanocrystalline environment.. 54

Chapter-4

Figure 4.1 Simulation model for calculating the generalized stacking fault (GSF) energy curve. 61

Figure 4.2 Schematic view of the atom positions when calculating the GSF curve. 61

Figure 4.3 Stress-strain curves for uniaxial tension and compression of Cu, Al and Ni along (a) [1 1 1] direction, (b) [1 1 -2] direction, and (c) [1 -1 0] direction. 64

Figure 4.4 Influences of the stress state on the generalized stacking fault energy curve in Cu. 66

Figure 4.5 Influence of the stress state on the generalized stacking fault energy curve in Ni. 66

Figure 4.6 Influences of the stress state on the generalized stacking fault energy curve in Al. 68

Figure 4.7 Variations of ratio of stable stacking fault energy to unstable stacking fault energy (γsf/γusf) with preloading stress along (a) [1 1 1] direction, (b) [1 1 -2] direction, and (c) [1 -1 0] direction. 70

Figure 4.8 Variations of ratio of unstable twin fault energy to unstable stacking fault energy (γutf/γusf) with preloading stress along (a) [1 1 1] direction, (b) [1 1 -2] direction, and (c) [1 -1 0] direction. 72

Chapter-5

Figure 5.1 (a) Schematic of the bicrystal model and the tension deformation applied onto the model. 75

Figure 5.2 The energy barrier of dislocation nucleation from (a) Σ9(1 1 4) GB and (b) Σ19(3 3 1) GB calculated by Equation (5-2). 79

Figure 5.3 The equilibrium structures of the Cu <1 1 0> tilt GB structures with misorientation angles θ<109.5 ° obtained by the energy minimization procedure and subsequent MD relaxation at 10 K. 80

Figure 5.4 The equilibrium structures of the Cu <1 1 0> tilt GB structures with misorientation angles θ>109.5 ° obtained by the energy minimization procedure and subsequent MD relaxation at 10 K. 81

Figure 5.5 The energy of Cu <1 1 0> tilt GBs shown as a function of the misorientation angle at 0 K after energy minimization procedure..... 82

Figure 5.6 Stress-strain curves of Cu <1 1 0> tilt GBs with misorientation angles (a) θ<109.5 ° and (b) θ>109.5 ° at 10 K. (c) Maximum tensile stress as a function of misorientation angle. 83

Figure 5.7 Dislocation nucleation from Cu bicrystal with (a) Σ9(1 1 4) θ=38.9 ° GB (b) Σ139(3 3 11) θ=42.2 °GB (c) Σ3(1 1 2) θ=70.5 °GB and (d) Σ17(2 2 3) θ=86.6 °GB under uniaxial tension at 10 K..... 86

Figure 5.8 Dislocation nucleation from Cu bicrystal with Σ11(1 1 3) θ=50.5 °GB under uniaxial tension at 10 K. 88

Figure 5.9 (a)-(b) Dislocation nucleation from Cu bicrystal with Σ3(1 1 1) θ=109.5 °GB under uniaxial tension at 10 K. 90

Figure 5.10 Dislocation nucleation and propagation from (a) Σ11(3 3 2) GB, (b) Σ9(2 2 1) GB, (c) Σ19(3 3 1) GB and (d) Σ73(6 6 1) GB under a uniaxial tension at 10 K. 92

Figure 5.11 Enlarged view of dislocation nucleation from (a) Σ11(3 3 2) GB, (b) Σ9(2 2 1) GB, (c) Σ19(3 3 1) GB and (d) Σ73(6 6 1) GB. 95

Figure 5.12 Maximum tensile stress of GBs plotted as a function of GB energy 97

Figure 5.13 Energy barrier of dislocation nucleation from GB plotted as a function of maximum tensile stress. 97

Chapter-6

Figure 6.1 Schematic of Cu bicrystal with a Σ5 [0 0 1] asymmetric tilt grain boundary.....103

Figure 6.2 (a) Schematic of tension simulation model under (b) free tension boundary condition and (c) constrained tension boundary condition. 106

Figure 6.3 Σ5 GB structures of Cu for various inclination angles Φ at 0K. 108

Figure 6.4 Grain boundary energy as a function of inclination angle of six Σ5 GBs. 109

Figure 6.5 Mechanical response of Σ5 GBs with different inclination angles Φ at 10 K under (a) free tension boundary condition and (b) constrained tension boundary condition.....110

Figure 6.6 Snapshots of Cu bicrystal with Σ5 (Φ=0°) GB at different deformation stage under free tension boundary condition.....112

Figure 6.7 Snapshots of Cu bicrystal with Σ5 (Φ=11.31°) GB at different deformation stage under free tension boundary condition.....112

Figure 6.8 Snapshots of Cu bicrystal with Σ5 (Φ=18.43°) GB at different deformation stage under constrained tension boundary condition. 114

Figure 6.9 The maximum Schmid factor as a function of GB inclination angle for grain A and grain B of the bicrystal models. 116

Figure 6.10 Snapshots of Cu bicrystal with Σ5 (Φ=0°) GB at different deformation stage under constrained tension boundary condition. 118

Figure 6.11 Dislocation nucleation and propagation in Cu bicrystal under free tension boundary condition at 10 K with (a) Σ5 (Φ = 0°) GB, (b) Σ5 (Φ = 11.31 ৎ) GB, (c) Σ5 (Φ = 18.43°) GB, (d) Σ5 (Φ = 26.57°) GB, (e) Σ5 (Φ =

30.96 ͦ) GB and (f) Σ5 (Φ = 45°) GB. 119

Figure 6.12 Dislocation nucleation and propagation in Cu bicrystal under constrained tension boundary condition at 10 K with (a) Σ5 (Φ = 0°) GB, (b) Σ5 (Φ = 11.31°) GB, (c) Σ5 (Φ = 18.43°) GB, (d) Σ5 (Φ = 26.57°) GB, (e) Σ5 (Φ = 30.96°) GB and (f) Σ5 (Φ = 45°) GB. 120

Chapter-7

Figure 7.1 Schematic of shear deformation applied onto the bicrystal model 125

Figure 7.2 The equilibrium structures of the Σ11 symmetric and asymmetric GBs obtained by the energy minimization procedure and subsequent MD relaxation at 10 K. 127

Figure 7.3 Shear response of Σ11(1 1 3) Φ=0° GB. 129

Figure 7.4 Shear response of Σ11(2 2 5)/(4 4 1) Φ=54.74° GB. 131

Figure 7.5 Shear response of Σ11(5 5 7)/(7 7 1) Φ=70.53 ͦ-A GB. 134

Figure 7.6 Shear response of Σ11(5 5 7)/(7 7 1) Φ=70.53°-B GB. 137

Figure 7.7 Shear response of Σ11(3 3 2) Φ=90° GB. 139

Figure 7.8 The length of stacking fault as a function of simulation time for different Σ11 asymmetric GBs. 141

Chapter-8

Figure 8.1 Snapshots to illustrate the process of an SFT generated from a vacancy triangular platelet based on the Silcox-Hirsch mechanism. 147

Figure 8.2 Stress-strain curves of perfect crystals and crystals with SFT under uniaxial compression and tension for [1 0 0], [1 1 0] and [1 1 1] directions. 151

Figure 8.3 Snapshots of SFT configuration in crystal with [1 0 0] orientation at different stages of deformation during uniaxial compression. 154

Figure 8.4 Snapshots of SFT configuration in crystal with [1 0 0] orientation at

different stages of deformation during uniaxial tension. 156
Figure 8.5 Snapshots of SFT configuration in crystal with [1 1 0] orientation at different stages of deformation during uniaxial compression.....157
Figure 8.6 Snapshots of SFT configuration in crystal with [1 1 0] orientation at different stages of deformation during uniaxial tension. 158
Figure 8.7 Snapshots of SFT configuration in crystal with [1 1 1] orientation at different stages of deformation during uniaxial compression.....161
Figure 8.8 Snapshots of SFT configuration in crystal with [1 1 1] orientation at different stages of deformation during uniaxial tension. 162
Figure 8.9 Yield stresses of perfect single crystals and crystals with SFT as a function of elastic modulus for various of crystal orientations under (a) uniaxial compression and (b) uniaxial tension.....164
Figure 8.10 The reduction in yield stresses under uniaxial compression and tension as a function of elastic modulus for various of crystal orientations. 164
Figure 8.11 The reduction in yield stresses under uniaxial compression and tension for [1 0 0], [1 1 0] and [1 1 1] orientations at different simulation temperatures. 166
Figure 8.12 C/T asymmetry ratio of perfect crystal and crystal with SFT as a function of elastic modulus for different crystal orientations. 168
Figure 8.13 C/T asymmetry ratio for [1 0 0], [1 1 0] and [1 1 1] orientations at different simulation temperatures. 168
Figure 8.14 Stress-strain curves of perfect crystals and crystals with SFT under uniaxial compression and tension along different crystal orientations. 173
Figure 8.15 Stereographic triangle showing the crystallographic orientations investigated in this chapter. 176

CHAPTER 1

Introduction

1.1 Research Background

Plastic deformation has been an interesting area of research in recent years as modelling methods are constantly being developed to find the related governing deformation mechanisms. When materials deform, a nucleation of dislocations is commonly observed at the summit of the load-displacement (stress-strain) curves that is ascribed to the onset of plasticity. Dislocation can generally nucleate homogeneously from a perfect lattice or heterogeneously from structural defects, although the latter plays the predominant role in the deformation mechanisms for nanocrystalline materials. Grain boundary (GB) and stacking fault tetrahedra (SFT) are common types of defects in metallic materials, so their effects on the nucleation of dislocations and consequently on the onset of plasticity, will be studied in this work.

1.1.1 Grain boundary

Compared to conventional coarse grained materials, nanostructured or nanocrystalline materials reveal many advanced characteristics[1-4] such as ultrahigh strength, superior wear resistance, and possible superplastic formability at low temperatures and high strain rates. These superior characteristics have stimulated widespread interest in the mechanical properties and novel deformation mechanisms of nano-sized materials over the past three decades. Many experimental and simulation results have revealed that the deformation mechanisms of materials with small grain sizes are predicted to be radically different from coarse grained materials because plasticity at the nanoscale (with an average or entire range of grain size finer than 100 nm) are mediated mostly by grain boundary deformation processes[5,6].

By considering the strengthening of grain size refinement in metals and alloys, Fig.1.1 illustrates the mechanism map for deformation by showing the nominal changes in the underlying mechanisms of plasticity at different grain sizes. For conventional metallic materials with an average grain size larger than 100 nm, dislocation nucleation from intra-grains or grain boundaries, and their propagation, is the primary deformation mechanisms that induce the onset of plasticity. The strengthening behaviour in this grain size region is characterised very well by the Hall-Petch relationship (see Region-1 in Fig.1.1), by indicating that the yield strength increases as the grain size decreases. A physical basis for this behaviour is associated with the difficulty of dislocation movement across grain boundaries and stress concentration due to dislocation pile-up. In this region, dislocation pile-up against the grain boundaries and other intragranular dislocation mechanisms are the dominant strength-controlling processes. However, as the grain size decreases to less than 100 nm, the grain boundary volume fraction increases significantly, the dislocation operation becomes increasingly more difficult, and the grain boundary mediated process becomes increasingly more important. In Region-2, the homogeneous intra-granular nucleation of dislocation is restricted, the Hall-Petch relationship weakens due to the heterogeneous nucleation and emission of dislocations from the grain boundary. In particular, when the grain size is reduced to the order of 10 nm, there is a critical grain size below which the strength of materials decreases with any further reduction in grain size, i.e. “inverse” Hall-Petch behaviour (see Region-3 in Fig.1.1). In this region, dislocation nucleation becomes limited and grain boundary mediated processes such as GB sliding and GB rotation become the dominant deformation mechanisms.

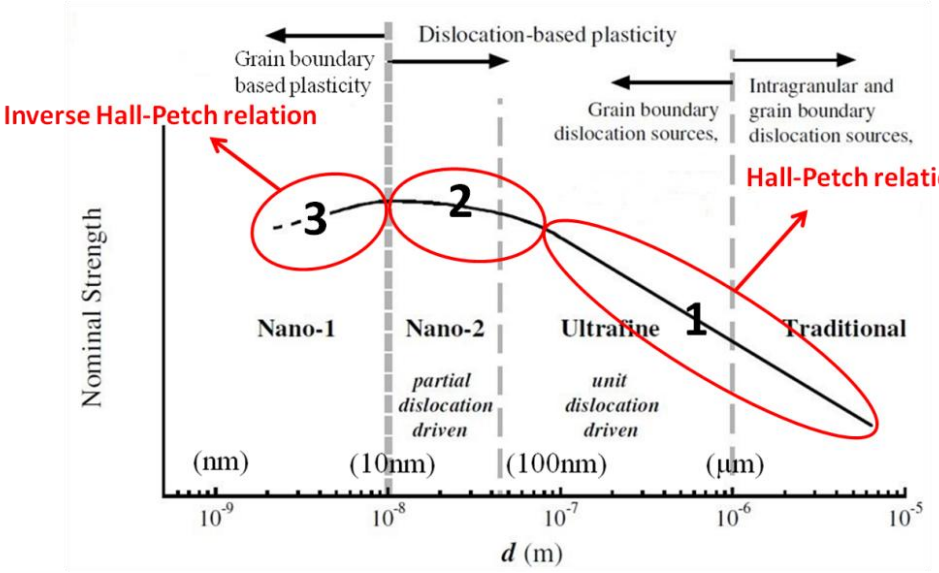

Figure 1.1 A mechanism map for deformation behaviour showing the nominal changes in the underlying mechanisms of plasticity at different grain sizes. [1]

There is considerable experimental evidence to support the phenomenon observed in Fig.1.1 where the nanocrystalline metals should exhibit higher strength; indeed, extreme strength and hardness have been observed experimentally in nanocrystalline metals. For example, Khan[7] et al. tested the mechanical strength of aluminium with a wide range of grain sizes (from 40 nm to 45,000 nm) obtained by ball milling. A large increase in the yield strength of the nanocrystalline aluminium occurred as the grain size decreased. By using high quality samples, Chen et al.[8] reported that the hardness of nanocrystalline copper with an average grain size of 10 nm can be as high as 3 GPa, which corresponds to a yield strength of about 1 GPa, which is more than one order of magnitude higher than coarse-grained copper (about 50 MPa). Moreover, the classic Hall-Petch relationship was not applicable when the grain sizes were typically between 10-20 nm[9,10], where the nanocrystalline metal had a lower yield strength and a decreasing grain size in this regime. Some in situ transmission electron microscopy (TEM) experiments have revealed the underlying deformation mechanisms of these length scale effects. For example, partial dislocations were observed from grain boundaries with the production of stacking faults and deformation twins in nanocrystalline aluminum and copper[11,12], and grain

boundary sliding and rotation processes were reported during the deformation in nanocrystalline nickel[13]. While some insight into the deformation mechanisms of nanocrystalline materials was obtained by TEM experiments, these experiments at a nanoscale were very difficult to perform because TEM requires samples with a thickness comparable to the grain size, and this may induce the structure to relax and thus change the grain boundary structure, so they are not reliable for studying the mechanisms of grain boundaries induced heterogeneous dislocation nucleation. Moreover, to explore the possible mechanisms of materials with extremely small grain size, fully dense nanocrystalline bulk samples with uniform grain sizes of about 10 nm are required, and they too are very difficult to produce.

Facilitated by rapid increases in computational power, atomistic simulation has been used extensively to study the mechanical properties of nanocrystalline materials and great progress has been made in simulating and understanding deformation mechanisms at an atomic scale. Molecular dynamics (MD) simulation is an effective tool to study the behaviour of plastic deformation because the deformation conditions can be controlled and a detailed investigation of the underlying atomic scale processes can be made. One of the successful cases of using MD simulation is to investigate the critical grain size at which the Hall-patch relationship breaks down. Earlier experimental observations[6] of the inverse Hall-patch relationship in Cu were debated because the experiments had been attributed to samples with defects such as flaws, porosity, or contamination. However, these interference factors can be completely ruled out by MD simulations where samples free of defects can be constructed. By using MD simulation, Van Swygenhoven et al.[14] identified a critical grain size for Cu of about 8 nm, but for grains smaller than 8 nm, plastic deformation was dominated by GB sliding. Another MD simulation study by Schiøtz and Jacobsen[15] indicated that a maximum flow strength occurred in Cu at a grain size of 10-15 nm, which corresponds to a shift in the microscopic deformation mechanism from dislocation-mediated plasticity to GB

sliding. While the mechanical properties predicted by MD simulations quantitatively agree with the limited experimental results, the simulations provided extremely detailed atomistic information, and this enabled us to explore certain GB structures and their effect on the plasticity of nanocrystalline materials.

1.1.2 Stacking fault tetrahedron

Point defects such as interstitials, vacancies, and their clusters, are very common in metallic crystals. They were found to play a significant role in the initiation of plastic deformation in crystalline metals[16,17,18] because vacancies are required thermodynamically in crystals. The equilibrium concentration of vacancies is typically very low at low temperatures, but it grows exponentially with temperature. In some circumstances the actual concentration of vacancies can be much higher than the corresponding equilibrium value. For example, higher vacancy concentrations can be formed during rapid quenching when the vacancies do not have enough time to diffuse to sinks such as surfaces or grain boundaries. Severe plastic deformation can also increase the concentration of vacancies through dislocation interactions. Moreover, increased concentrations of vacancies are often observed in crystalline metals that are subjected to radiation damage, where high-energy particles knock atoms off their equilibrium lattice sites.

Stacking fault tetrahedra (SFTs) are ubiquitous vacancy clustered defects in face-centred cubic (FCC) metals, due to their favourable structure that contains close packed planes (which do not exist in body-centred cubic (BCC) materials) and also due to the lower stacking fault energies in FCC materials. A high density of nanometre-sized SFTs has been commonly found in metals subjected to plastic deformation, quenching from high temperatures, or irradiation[19,20]. The size of an SFT can be as small as several atoms, typically generated by collision cascades, to the largest size observed of up to several hundred nanometres that were introduced by quenching. Until now, three SFT formation mechanisms have been proposed; the first is a Frank loop dissociation mechanism (or namely the Silcox-Hirsch

mechanism) proposed by Silcox and Hirsch in 1959[21], where the first observation of SFTs using TEM was explained on the basis of the dissociation of a vacancy-type Frank dislocation loop. Later on, MD simulations studies[22] also supported this explanation. Another formation mechanism of SFTs was proposed by Czjzek et al.[23], who stated that an SFT is formed by the absorption of single vacancies from a small triangular-shaped nucleus of vacancies, with an edge length of less than five atoms. Uberuaga and co-workers[24] recently disclosed the third mechanism by accelerated MD, namely the void collapse mechanism where an SFT can be formed directly from a void collapsing.

SFTs can act as dislocation sources or interact with dislocations inside a material. For large size grains, the SFTs act like obstacles to dislocation motion, leading to increased yield strength and decreased ductility[25,26]. At small scale sizes where dislocations are less likely to be present, nucleation of dislocations from SFTs may dominate the deformation mechanism at the incipience of plasticity in the materials[27,28]. Previous in situ straining experiments[29] revealed that dislocation interactions with SFTs resulted in many different phenomena, including the complete absorption of SFT, partial absorption of SFT, that results in a smaller SFT, destruction of SFT leaving a super jogged dislocation, and the SFT collapsing into a triangular Frank loop via the inverse Silcox-Hirsch mechanism. These experimental observations provided useful insights into the formation of defect free channels in irradiated materials, but the irradiation induced and quenching induced SFTs were so small it was difficult to identify the deformation mechanisms clearly. Alternatively, MD simulations can reproduce in situ interaction processes so they have been widely used to explore the mechanisms of interaction between dislocations and SFTs, as well as the dislocation nucleation that originated from SFT in small volume crystals.

1.2 Research Objective

The research objective of this thesis is to use atomistic simulations to examine the grain boundary and stacking fault tetrahedron induced plasticity in nanocrystalline FCC metals. This thesis is focused on the mechanical response of the simulation models and the underlying deformation mechanisms, particularly the heterogeneous dislocation nucleation from the two types of defects.

The structure and energy of the grain boundary are known to play an important role in the mechanical behaviour and underlying deformation mechanisms of nanocrystalline materials. In particular, as the grain size decreases, one of the mechanisms that can play a vital role in the mechanical behaviour of nanocrystalline materials is the heterogeneous nucleation and emission of dislocations from the GBs. The dislocation nucleation event can be viewed as the activation of a dislocation source that lies within or close to the boundary. Previous research has used atomistic simulations to investigate the nucleation and propagation of dislocations from the grain boundary in both polycrystal and bicrystal configurations. However, there is a lack of comprehensive understanding of the relationship between the GB structure, GB energy, and their influence on the onset of small scale plasticity.

Dislocation nucleation in the MD simulations of three-dimensional (3D) nanocrystalline samples is very complex. The combined tilt and twist character of grain boundaries and the inclined boundary plane with respect to the tensile axis, complicated an analysis of the role of specific GB structures in the simulations. Moreover, different boundaries may nucleate and emit dislocations at different stresses, so separating out the individual effects of GB structural units on dislocation nucleation becomes very difficult. An alternative method is to use bicrystal simulations to study the dislocation nucleation mechanism for specific GBs. A bicrystal model was used in this study because the geometry and structure of the GB can be precisely specified, thus promoting correlations between the grain boundary structure and material properties.

The computer modelling of GBs in previous studies focused mostly on the symmetrical boundaries, i.e. boundaries which possess mirror symmetry of crystallographic planes and directions across the boundary plane. Asymmetrical boundaries have also been studied but not as extensively as symmetrical ones. However, most GBs in real polycrystalline materials are asymmetrical but unfortunately, our current understanding of atomic structure, energies, and the mechanical properties of asymmetrical GBs remains rather limited. Asymmetric tilt grain boundaries present an interesting case for studying dislocation nucleation because of the faceted structure and dissimilar adjoining crystal orientations.

While a number of studies have investigated the formation of SFT or their interaction with other structural defects (mainly dislocations), little knowledge is available on the effects of SFT on dislocation nucleation, even though SFT has been determined as having a strong effect on the mechanical response of materials in the case of incipient plasticity. For example, recent atomistic simulations of nanoindentation[30] showed that SFTs were the most critical to the onset of plastic deformation of a variety of point defects, and moreover, they can lower the yield stress by up to 50% compared to a perfect crystal. Therefore, it is necessary to explore the mechanical behaviour of materials in the presence of this defect, and the underlying deformation mechanism induced by SFT must be understood in small volume crystals.

Overall, there are several fundamental questions regarding the onset of small scale plasticity that will be addressed in this thesis.

1. How does the GB structure and GB energy change as a function of the GB plane orientation? What is the relationship between the GB structure/energy and the mechanical response of the simulation samples?
2. What is the predominant deformation mechanism at the onset of plastic deformation of nano sized bicrystals? How does the GB structure affect the specific dislocation nucleation mechanism? What is the influence of the GB

energy on the nucleation process?

3. Do asymmetric GBs have a well-defined boundary structure? Is there any relationship between asymmetric GBs and their corresponding symmetric GBs? What is the difference in the dislocation nucleation process between symmetric GB and asymmetric GB?
4. What is the atomic mechanism of SFT induced plasticity in small volume crystal where dislocation is unlikely to be present? How does crystal orientation influence the mechanical response of the simulation samples in the presence of SFT, and what is the underlying dislocation nucleation mechanism?
5. What is the effect of the stress state on the generalised stacking fault energy of FCC metals and its possible influence on the deformation mechanism?

1.3 Thesis Structure

Most researches of this thesis have been peer-reviewed and published in journals (listed in page IX). The research results of this thesis are broken down into two categories: grain boundary induced plasticity and stacking fault tetrahedra induced plasticity. The thesis is organised as follows:

Chapter-2 gives an overview of the most recent developments in the area of atomistic modelling with an emphasis on the grain boundary structures and their impact on the properties and deformation mechanisms of nanocrystalline materials. The interaction of stacking fault tetrahedra with dislocation and twin boundary are also reviewed in this chapter, and the mechanisms are summarised.

Chapter-3 gives a brief introduction to the simulation methodology used in this thesis, including the MD simulation methodology, potentials used in MD simulation, MD code LAMMPS, and the recent developed visualisation and post-process technologies.

Chapter-4 studies the generalised stacking fault energy of several FCC metals that can reflect the accuracy of the potential used in our simulations. The effect of preloading stress on the generalised stacking fault energy is also investigated.

Chapter-5 studies the mechanical property and dislocation nucleation mechanisms of a series of <1 1 0> symmetric tilt grain boundaries of copper. Specifically, this chapter examines the GB structure and GB energy as a function of the GB plane orientation, the nucleation mechanisms are presented and classified for different orientation range, and the nucleation barriers are correlated with the GB energy.

Chapter-6 and Chapter-7 study the structure and mechanical property of a number of asymmetric tilt grain boundaries. Chapter-6 examines copper bicrystals with Σ5 asymmetric tilt GBs under tension, and considers two different tensile boundary conditions. Chapter-7 examines copper bicrystals with Σ11 asymmetric tilt GBs under shear, and also reports on different grain boundary mediated deformation mechanisms.

Chapter-8 studies the stacking fault tetrahedron induced plasticity in a small volume crystal without initial dislocations. A uniaxial tensile or compressive loading was applied on the copper single crystal in the presence of an SFT. The effects of the crystal orientation and loading direction on the deformation mechanism are discussed.

Chapter-9 concludes the overall work of this thesis and proposes future research directions.

CHAPTER 2

Literature Review

This chapter gives an overall review of the molecular dynamic simulation studies on crystal plasticity induced by grain boundary (GB) and stacking fault tetrahedron (SFT) in nanocrystalline metals.

2.1 Grain Boundary Structure and Energy

2.1.1 Structure and energy of symmetric GB

The influence of grain boundary structure on the mechanical behaviour of bicrystals and poly-crystals was investigated because the grain boundary can have profound effects on the deformation mechanisms. The deformation mechanisms of nanocrystalline metals differ markedly from those found in their coarse-grained counterparts, and result in unique, superior mechanical characteristics. Without a structural model for nanocrystalline materials, their mechanical behaviour is difficult to rationalise so this chapter begins the literature review with a particular emphasis on the structure of GB and its relationship to GB energy.

A lot of atomistic studies focused on symmetric GB structures where high angle boundaries can be described using a simple structural unit and low angle boundaries with GB dislocation networks. The previous work[31-33] revealed that a GB structure in nanocrystalline metals does not differ very much from that found in coarse grained metals. In the these studies it was found that the GBs of nanocrystalline metals have a large degree of order, and are made of structural units that are usually observed in conventional high-angle GBs. For low-angle boundaries, GB dislocation networks have also been observed in nanocrystalline metals, regardless of the grain size. These results preclude nanocrystalline interfaces as being highly disordered, amorphous-like boundaries.

Cahn et al.[34] researched a series of [0 0 1] symmetrical tilt GBs in copper and found that all the GBs were coincident site lattice (CSL) boundaries characterised by Σ values (reciprocal density of CSL sites). The structure of each GB was determined by minimising the total energy of the simulation system. The GBs studied covered tilt angles from 11.42° to 79.61° and Σ value from 5 to 101, and revealed that they all contained topologically identical kite-shaped structural units (see Fig.2.1); they only differed in the distance separating the structural units and their positions relative to the GB plane. The relatively low angle Σ37(61 0) (θ= 18.9°) GB shown in Fig.2.1(a) contained an array of dislocations whose cores were formed by the structural units, and the Burgers vectors were **b**=[1 0 0]. Likewise, the relatively low angle Σ41(540) (θ= 77.3°) GB shown in Fig. 2.1(d) were composed of **b**=-1/2[1 1 0] dislocations formed by the units.

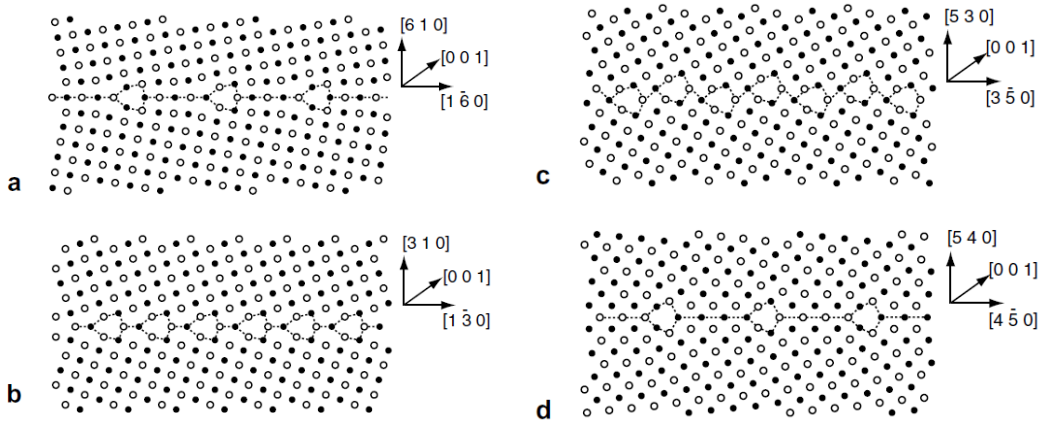

Figure 2.1 Atomic structure of selected [0 0 1] symmetrical tilt GBs in Cu at 0 K. (a) Σ37(610) (θ= 18.9°); (b) Σ5(310) (θ=36.9°); (c) Σ17(530) (θ= 61.9°); (d) Σ41(540) (θ= 77.3°). The filled and open circles represent rows of atoms with positions in alternating (002) planes.[34]

There is a strong correlation between the structure and energy in GBs. The boundary energy in Cu was determined experimentally using transmission electron microscopy (TEM) as a function of the misorientation angle for [1 0 0] and [1 1 0] symmetrical twist boundaries[35], and symmetrical tilt boundaries of [1 0 0] and [1 1 0][36]. Sangid et al.[37] carried out a series of simulation work of Ni for various symmetrical twist and tilt grain boundary angles about various axis. The results are shown in Fig.2.2. In Fig. 2.2(a), a tilt GB was constructed about a rotation along the

<1 1 0> axis of the crystal. It can be seen that this curve contains local minimums and cusps that correspond to the preferred energy configurations as a result of the special Σ GBs in the CSL. At a rotation of 0◦, the atoms are in a perfect lattice configuration but at a rotation of 50.48◦, the defect structure at the interface is simple and therefore corresponds to a local minimum in the energy and the Σ11 GB. A 109.47◦ tilt rotation about the <1 1 0> axis has the lowest energy of any GB, which corresponds to a very simple defect structure known as a coherent twin or a Σ3 GB. Since these low energy boundaries are more likely to exist in materials, these boundaries are more abundant in this material because annealing twins form during processing. Other types of GBs, specifically <1 1 1> twist and <0 0 1> tilt, are analysed as shown in Figs. 2.2(b) and (c), respectively.

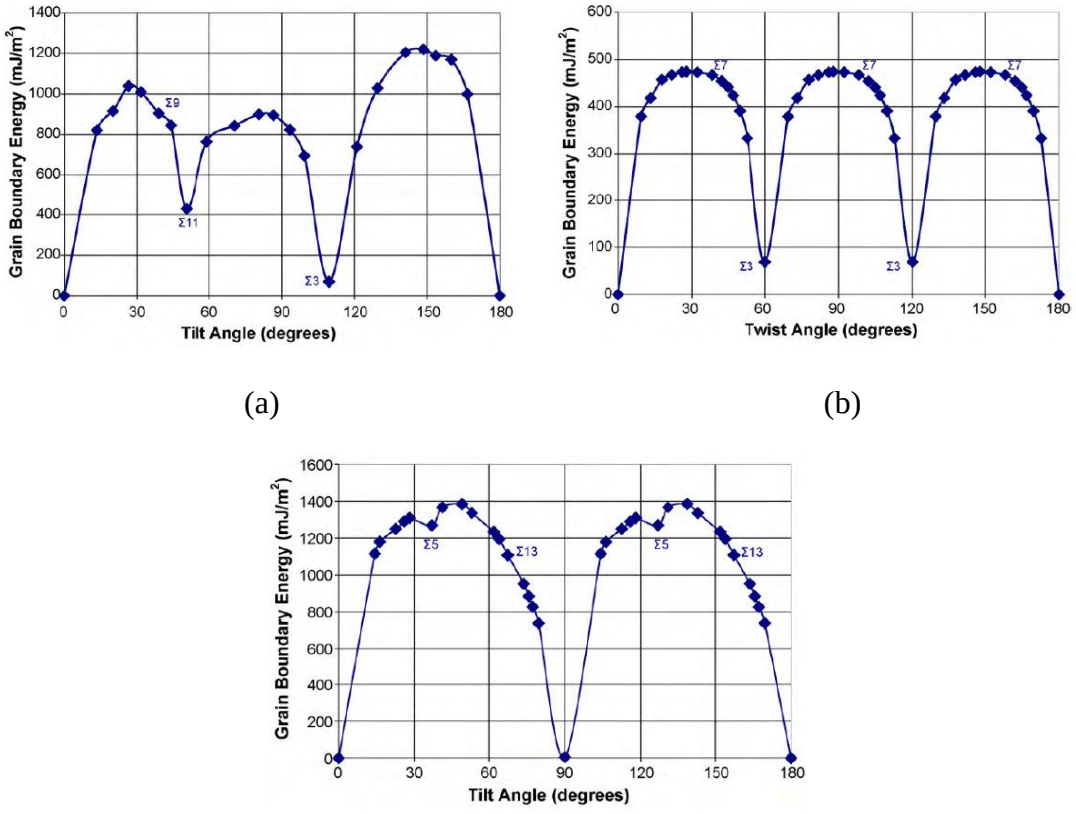

Figure 2.2 The grain boundary energy of nickel shown as a function of (a) the tilt angle in the 1 0> direction. (b) the twist angle in the <1 1 1> direction. (c) the tilt angle in the <0 0 1> direction.[37]

2.1.2 Structure and energy of asymmetric GB

While lots of atomistic simulations have focused on the effect that the symmetric GB plane has on the energy, structure and other GB properties, very few atomistic simulations have explored the role of the grain boundary plane orientation on the structure and energy of asymmetric GB. Atomistic simulations of an asymmetric GB plane can be categorised into several areas. First, some of the initial atomistic simulations that explored the energy and structure of asymmetric GBs[38] were limited by the accuracy of potentials despite the advances in embedded atom method (EAM) potentials and methodology that can increase our understanding of the energies and structures of asymmetric GBs. A second category of atomistic simulations of asymmetric GBs focused on the structure of specific GB planes (e.g. the 9R phase) to explain the observed GB structure from HRTEM images[39-42], or calculate certain GB properties (e.g. the shear deformation response of a few specific asymmetric GBs)[43]. Another category of asymmetric GB atomistic simulations investigated the effect of the grain boundary plane orientation on the GB properties or deformation mechanisms. For example, Zhang and Srolovitz[44] studied the GB mobility and self-diffusivity properties, as well as the atomic migration mechanisms for Σ5 GBs in Ni.

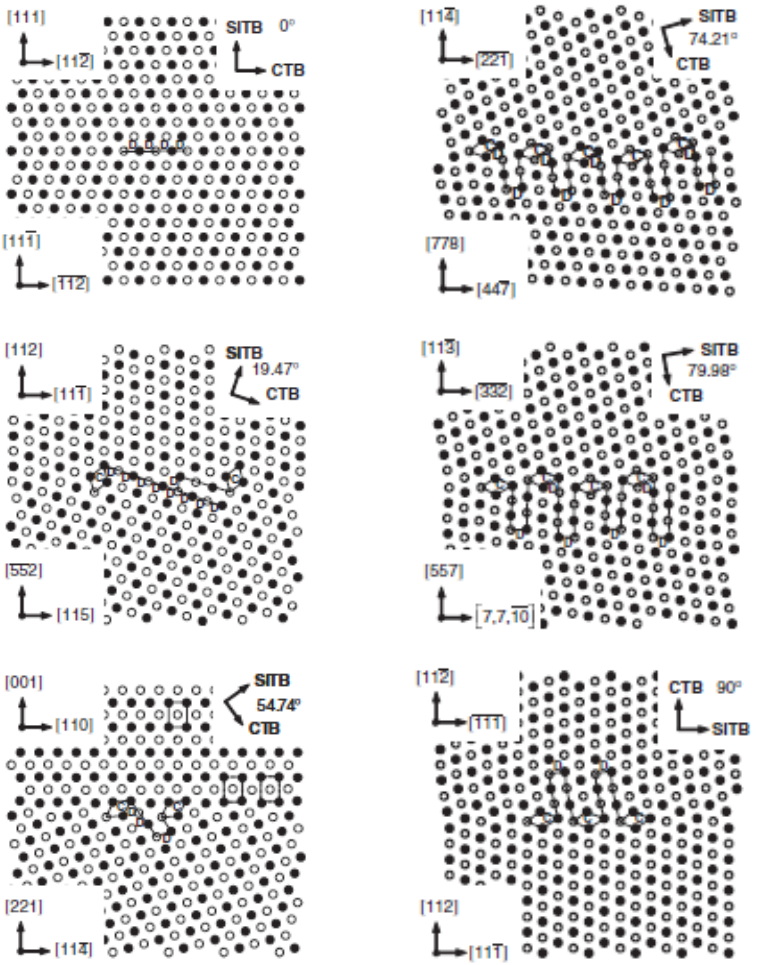

Figure 2.3 Six Σ3 grain boundary structures in Cu for various inclination angles. 0 °is the CTB, 90°is the SITB , while the other four GBs are Σ3 ATGBs.[45]

Tschopp and Mcdowell[45] explored Σ3<1 1 0> GB structures to identify the various equilibrium and metastable structures. For all Σ3 tilt GBs with a <1 1 0> misorientation axis, the GB plane determines whether the Σ3 boundary is a coherent twin boundary (CTB) or a symmetric incoherent twin boundary (SITB). In addition to these two symmetric tilt GBs (STGBs), all the grain boundary planes between the CTB and SITB are asymmetric tilt grain boundaries (ATGBs). The results of this simulation showed that the Σ3 asymmetric tilt grain boundaries in the <1 1 0> system were composed of only structural units of the two symmetric tilt GBs (see Fig.2.3). Furthermore, based on the structure of ATGBs, they assumed that the self-energies of the individual facets corresponding to the CTB and SITB contributed additively, and derived the equation for the GB energy for Σ3 ATGBs as:

$$\gamma_\phi = \gamma_{CTB}\cos\phi + \gamma_{SITB}\sin\phi \quad (2\text{-}1)$$

This equation was plotted against the calculated GB energies of Σ3 GBs in Fig. 2.4. The deviation of the fitted GB energy and calculated value of Cu when ϕ>70.53° occurred because the 9R phase became dissociated from the GB region.

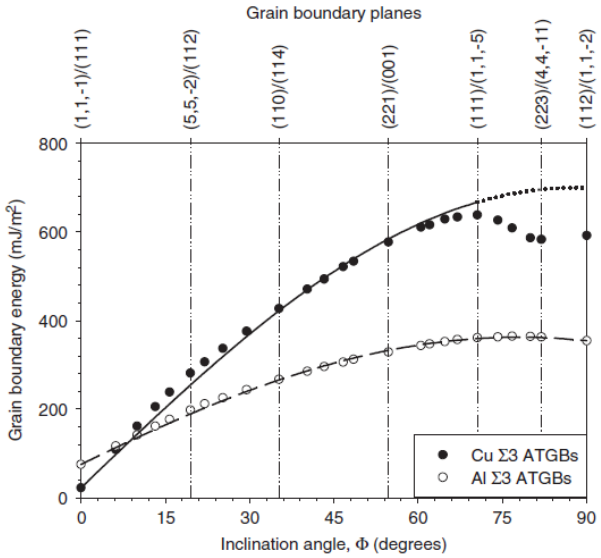

Figure 2.4 Grain boundary energy as a function of inclination angle for Cu and Al. The fits for these values follow Equation.(2-1).[45]

Tschopp and Mcdowell[46] further researched the ATGBs of Σ5 and Σ13 systems with a boundary plane rotated about the [1 0 0] misorientation axis, and the Σ9 and Σ11 systems rotated about the [1 1 0] misorientation axis. The simulation confirmed that these asymmetric boundaries were faceted into the symmetric tilt boundaries. Asymmetric tilt GB energies were calculated as a function of the inclination angle and compared to an energy relationship based on faceting into the two symmetric tilt grain boundaries in each system. They concluded that a more general equation to calculate the energy of ATGBs was:

$$\gamma_A = \gamma_{S1} \cdot \left[\cos\Phi - \sin\Phi\left(\frac{\cos\alpha}{\sin\alpha}\right)\right] + \gamma_{S2} \cdot \left[\frac{\sin\Phi}{\sin\alpha}\right] \quad (2\text{-}2)$$

where γ_A is the predicted ATGB energy, γ_{S1} and γ_{S2} are the calculated STGB energies, and α is the inclination angle separating two STGBs of the same CSL system (α=30° for the <1 1 1> system, α=45° for the <1 0 0> system and α=90° for

the <1 1 0> system). Fig.2.5 and Fig.2.6 give the predicted GB energy results of the four CSL systems. The Σ5 and Σ13 GBs in the <1 0 0> system agree with the above energy relationship, but the Σ9 and Σ11 GBs in the <1 1 0> system deviated from the idealised energy relationship. They gave two factors to explain this deviation: (1) Given equal energies of the two STGBs, as α decreases, the degree of anisotropy in the ATGB energies decreases and the more likely it is that the ATGB will ideally facet into two STGBs. (2) The anisotropy in the two STGB energies ($\gamma_S=\gamma_{S1}-\gamma_{S2}$) may also impact on whether the ATGB will follow the trend in this relationship. Thus, the low anisotropy of the Σ9 STGB energies combined with α=90° resulted in a high predicted ATGB energy due to faceting into the two Σ9 STGBs; this was much higher than the calculated energies of the Σ9 STGBs.

Brown and Mishin[47] investigated the energies and equilibrium atomic structures of asymmetrical Σ11[1 1 0] tilt GBs in Cu over the entire range of inclination angles Φ and found that these boundaries dissociated into a low angle GB formed by Shockley partial dislocations and a high-angle non-Σ11 boundary. The two product boundaries were separated by a layer of an FCC-based long period structure containing an array of intrinsic stacking faults. The simulations also revealed that asymmetrical GBs tended to break into nanometre-scale facets, and the facet planes often, but not always, corresponded to a nearby symmetrical boundary with a low energy (Fig.2.7(a)). For example, the Σ11[1 1 0] tilt GBs formed facets that were not Σ11 and did not even belong to any particular CSL (Fig.2.7(b)). The latter finding was important because it exposes a significant limitation of the CSL model for GBs.

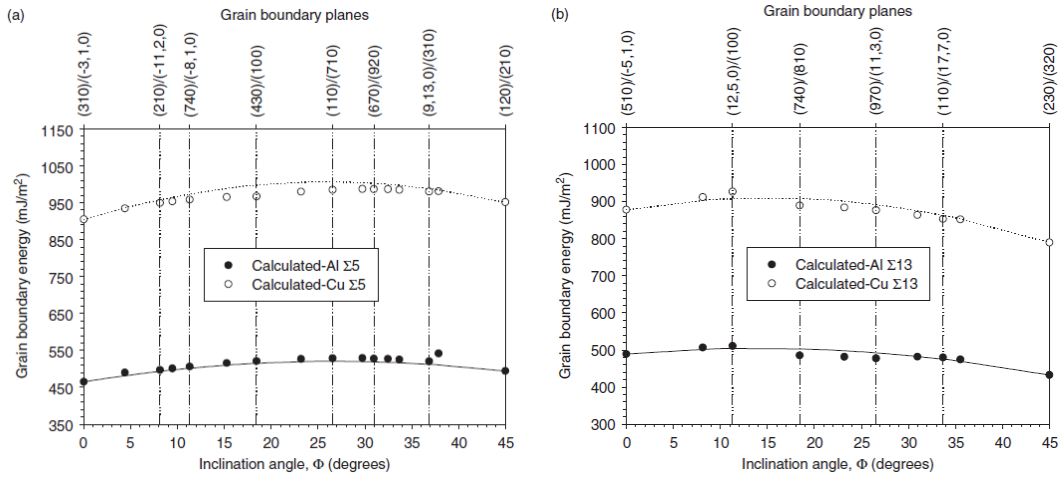

Figure 2.5 Grain boundary energy of (a) Σ5 and (b) Σ13 asymmetric tilt grain boundaries with the <1 0 0> tilt axis as a function of inclination angle.[46]

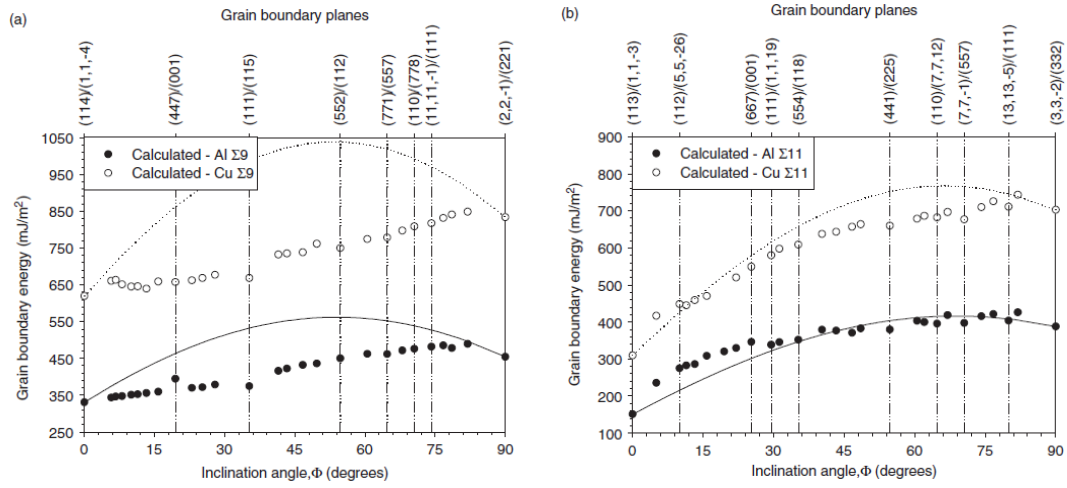

Figure 2.6 Grain boundary energy of (a) Σ9 and (b) Σ11 asymmetric tilt grain boundaries with the <1 1 0> tilt axis as a function of inclination angle.[46]

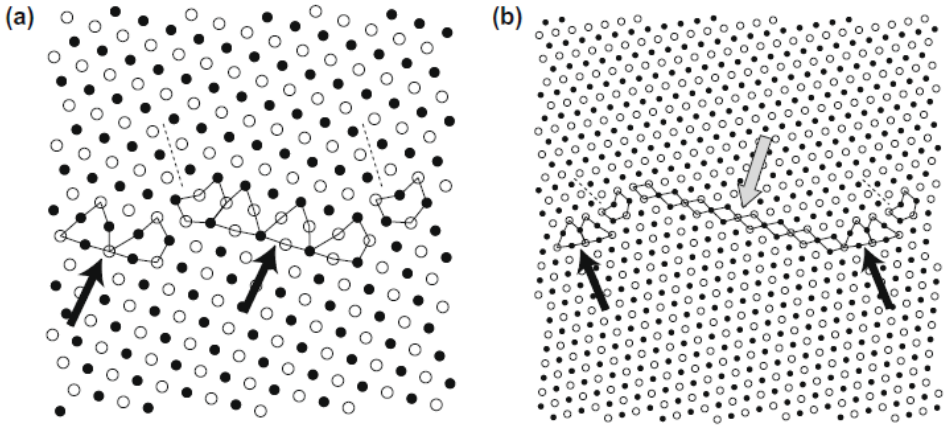

Figure 2.7 Atomic structure of selected Σ11[110] asymmetrical grain boundaries with inclination angles (a) Φ=46.7 ° and (b) Φ=74.2 °. The gray arrow shows a facet with the structure of the Σ11[110] (113) symmetrical tilt boundary. The black arrows show facets with the structure of an incommensurate non-Σ11 boundary with a (001)/(111) plane matching. The dashed lines indicate intrinsic stacking faults originating from the junctions of the nano facets. [47]

2.1.3 Faceting and dissociation of GB

The faceting of an interface can be regarded as a phase transition in which a flat (single phase) interface is transformed into a phase structure consisting of two or more facet types (phases) that coexist along lines of intersection; indeed, faceting of the grain boundary occurs in many metals under appropriate conditions. Many investigators have pointed out that the segregation of solute atoms on a boundary is one of the most important conditions for faceting. Also, the existing experimental evidence[48,52,53] showed that the transition of GB faceting and de-faceting can happen when the test samples were heated or cooled in a range of temperature.

Lee et al.[48] found a correlation between GB faceting and de-faceting transition and changes in the temperature dependence. They observed the temperature dependence of faceting on an asymmetric ∑5 GB in SrTiO3 using high resolution transmission electron microscopy (HRTEM). In their experiment, below 1300 ℃, this GB faceted into symmetric (310) and asymmetric (100)/(430) GB planes. At 1300 ℃, in addition to the asymmetric facet, the symmetrical (210) facet appeared; in fact three different facets were observed at this temperature. At 1400 ℃ and 1500 ℃, the asymmetrical facet disappeared and the two kinds of symmetrical facets

remained. At 1600 ℃, faceting disappeared and the GB became de-faceted, as shown in Fig.2.8.

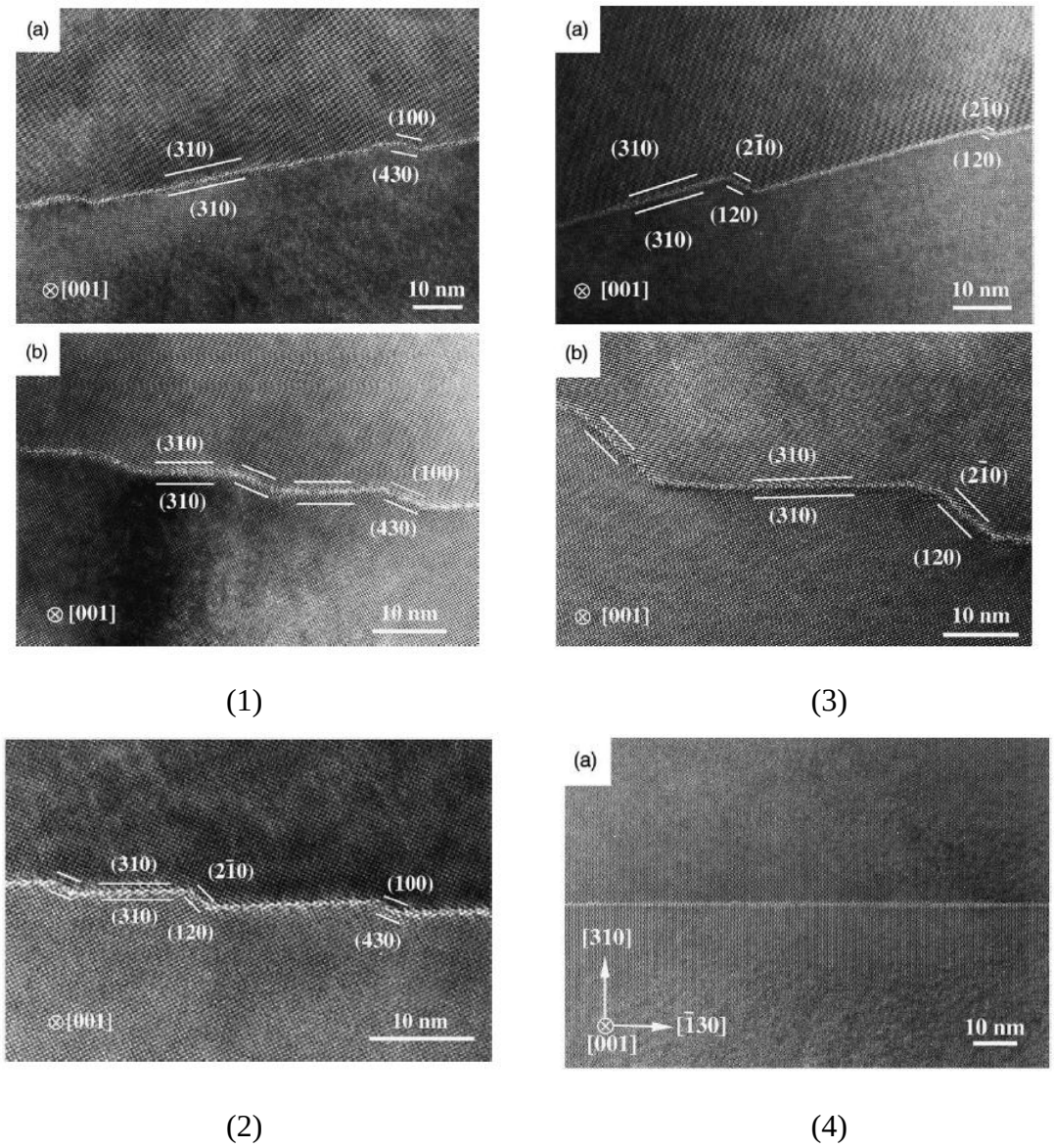

Figure 2.8 HRTEM image of the GB heat-treated at different temperature. Fig.(1a) 1100 ℃ for 7 days and Fig. (1b) 1200 ℃ for 5 days. In both cases the GB does not remain planar, but breaks up into the symmetric (310) and (100)//(430) facets. Fig.(2) 1300 ℃ for 5 days. In addition to the two pre-existing facets, the symmetric (210) facet appears. Fig.(3a) 1400 ℃ and Fig.(3b) 1500 ℃ for 3 days. The GB exhibits symmetric (310) and (210) facets. Fig.(4) 1600 ℃ for 1 day showing a completely defaceted structure. [48]

Goukon et al.[49,50] used a silica particle observation (SPO) method to determine experimentally the boundary energies of ∑11[1 1 0] asymmetric tilt GBs with a misorientation angle of 50.5° and ∑9[1 1 0] asymmetric tilt GBs with a misorientation angle of 38.9 °in Cu for various inclination angles between 0 °and 90 °.

The inclination angle dependence on the boundary energy was utilised to quantitatively evaluate the possibility of faceting and dissociation for the boundary. Fig. 2.9 gives the relative boundary energy γ_B/γ_I as a function of the inclination angle of ∑11[1 1 0] and ∑9[1 1 0] asymmetric tilt grain boundaries in Cu at 1273 K, where γ_B/γ_I is the boundary energy γ_B of Cu relative to the interfacial energy γ_I of Cu/silica.

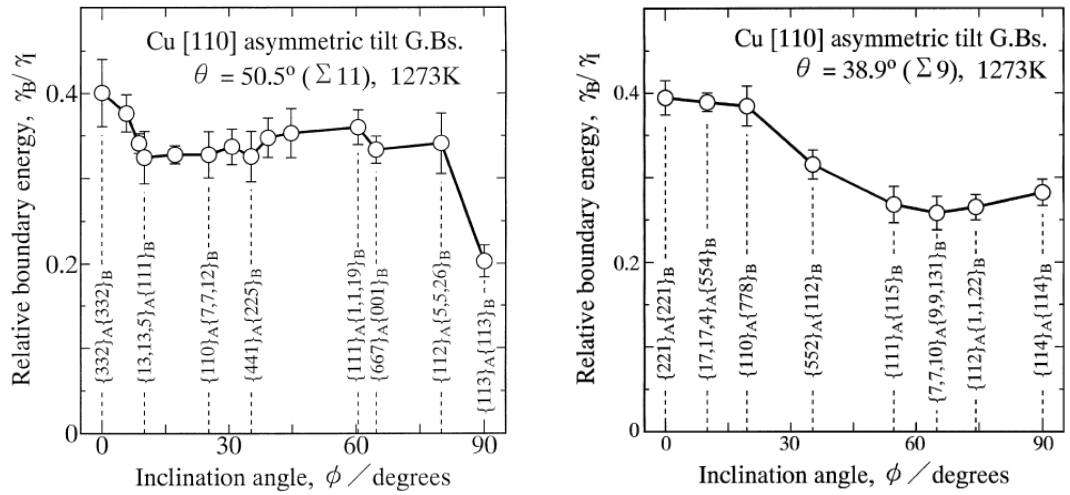

Figure 2.9 The relative boundary energy γ_B/γ_I as a function of the inclination angle of (a) ∑11[1 1 0] and (b) ∑9[1 1 0] asymmetric tilt GBs of Cu at 1273 K. [49] and [50]

In order for a grain boundary to be faceted spontaneously, the decrease in the total boundary energy must overcome the increase in the total boundary area. When the boundary energy is known as a function of the inclination angle, both changes in the total boundary energy and area are easily evaluated. In order to test whether the total boundary energy actually decreases owing to faceting Goukon et al.[49] proposed a parameter *f* which stands for the ratio of the total boundary energy of the faceted boundaries to the initially flat boundary. When the total boundary energy decreases owing to faceting, *f* becomes smaller than unity, and for such a value of *f*, faceting may occur spontaneously.

Sutton and Balluffi[51] proposed that the dissociation of ∑9{1 1 1}{1 1 5} and {4 4 7}{0 0 1} boundaries into ∑3{1 1 1}{1 1 1} and {1 1 2}{1 1 2} twin boundaries was geometrically possible. Goukon et al.[50] used the parameter *g*, which indicates

the ratio of the total boundary energy of the twin boundaries to the initial asymmetrical boundary. If the total boundary energy decreases owing to the dissociation, *g* is smaller than unity, but for such a value of *g*, this dissociation may occur spontaneously. Fig.2.10 is a schematic drawing of faceting and dissociation. According to the evaluation, faceting into the {1 1 2}{5 5 2} boundary is possible for the {7 7 8}{1 1 0}, {5 5 4}{17 17 4} and {2 2 1}{2 2 1} boundaries. Furthermore, dissociation into the ∑3{1 1 1}{1 1 1} and {1 1 2}{1 1 2} twin boundaries is feasible for the {4 4 7}{0 0 1} boundary, as shown in Fig.2.10(b).

$$f = \frac{\gamma_B(\phi_1)S_1 + \gamma_B(\phi_2)S_2}{\gamma_B(\gamma_0)\gamma_0} \tag{2-3}$$

$$g = \frac{1}{\gamma_{B0}\, S_0} \sum_{i=1}^{n} \gamma_{Bi} S_i \tag{2-4}$$

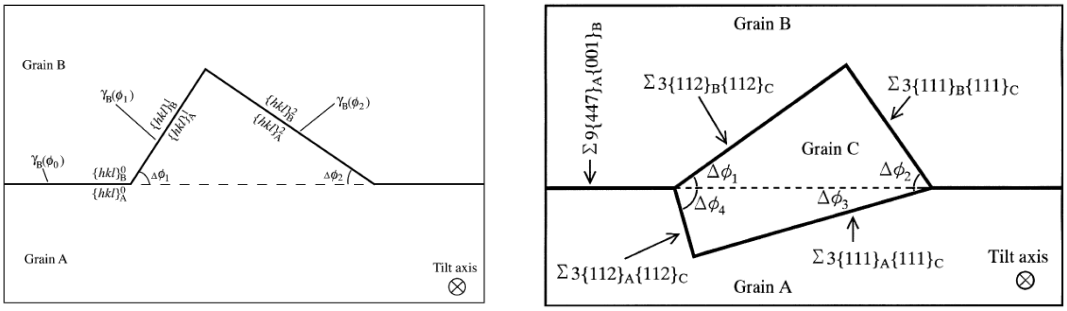

(a) (b)

Figure 2.10 (a) Schematic drawing for faceting. (b) Schematic drawing for dissociation of the ∑9{447}$_A${001}$_B$ boundary into the ∑3 {112}$_B${112}$_C$, {111}$_B${111}$_C$, {111}$_A${111}$_C$ and {112}$_A${112}$_C$ twin boundaries.[50]

2.2 Grain Boundary Induced Plasticity

Grain boundaries are often the sites of plasticity initiation under applied mechanical loads. Much of the recent scientific interest in nanocrystalline materials is associated with the atomic level mechanisms of plastic deformation in the grain boundaries. Fruitful results of GB-based mechanisms have been obtained by atomistic simulations.

2.2.1 Grain boundary sliding

Grain boundary sliding involves the rigid translation of one grain over another parallel to the grain boundary interface, it has been studied both in theory and with experiments, and reviewed extensively[52,53] because it is a key deformation mechanism at the elevated temperatures in superplastic forming[54] and quick plastic forming[55]. GB sliding mediates the plastic flow of polycrystalline materials[54,55], especially when the grain sizes drop to the nanometre scale[56] and when the deformation temperature is relatively high[57,58].

Qi and Krajewski[59] used MD simulations to study the effect of applied force and GB misorientation on GB sliding in bicrystal Al at 750 K. For a given misorientation, increasing the applied force increased the amount of sliding. Three sliding behaviours were observed depending on the force applied (see Fig.2.11): (a) at a low force, no sliding occurred, indicating a threshold stress type behaviour; (b) at intermediate forces, the amount of sliding increased linearly with time; and (c) at high forces, the amount of sliding increased parabolically with time. In addition, the GB misorientation angle had a strong effect on the amount of sliding, and while the amount of sliding increased with GB energy, it did not correlate with the GB misorientation angle, as Fig.2.11 shows. Moreover, the applied stress must be larger than the critical stress to initiate GB sliding, which indicated that a critical threshold stress exists; this critical stress decreased with increasing GB energy.

Du et al.[60] used the MD simulation method at a temperature of 750K to investigate the effect of vacancies in the grain boundary vicinity on the sliding of Al bicrystals. The threshold stress for GB sliding of one symmetrical tilt GB and five asymmetrical tilt GBs was computed and then compared with their different structures and energies. They found that without vacancies, low energy Σ3 GB exhibited much less sliding than other high energy GBs. The addition of vacancies to Σ3 grain boundaries decreased the threshold stress for grain boundary sliding by increasing the GB diffusivity. A higher concentration of vacancies enhanced this

effect. The influence of vacancies on GB diffusivity and GB sliding was negligible for high energy GBs, due to the already high atomic mobility in these boundaries.

It has been shown that the sliding resistance of GBs was closely related to GBs energy. Chandra and Namilae[61,62] also proposed considering a direct correlation between GB energy and GB sliding distance in Al symmetrical tilt boundaries. Their results showed that the lower the GB energy, the smaller the sliding distance. This conclusion was supported by a large number of studies on thermally activated GB sliding that showed that faster GB sliding occurred due to higher GB self-diffusion rates, which correlated with GB energy and GB volume.

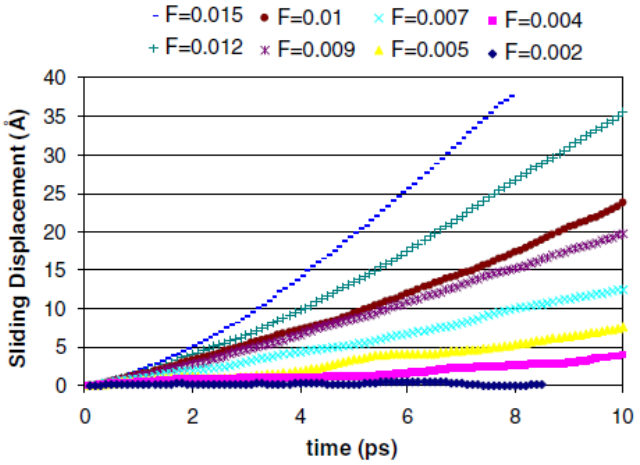

Figure 2.11 The relative sliding displacements of two grains with a misorientation angle of 25.2 ° under different applied forces. Forces are given in eV/A˚. [59]

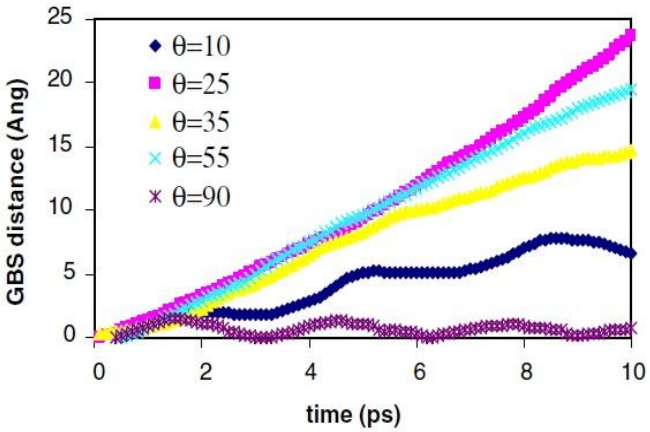

Figure 2.12 The effect of misorientation angle on GB sliding distance as a function of time. [59]

While the influence of the GB structure on thermally activated sliding behaviour has been well documented, researches also focused on the contribution that the

athermal effects had on the GB sliding behaviour of nanocrystalline materials. Schiøtz and co-workers have simulated the deformation of nanocrystalline copper at both zero temperature[63] and finite temperature[64]. By using MD simulations, they have shown that GB sliding remained the main deformation mechanism at all grain sizes up to 13 nm, even at zero temperature. It may generally be assumed that the strength of GB against sliding is the thermally activated effects. However, Schiøtz and co-worker's results showed that interfaces in nanocrystalline metals, where a diffusional explanation is not relevant at zero temperature, may indeed be dominated by the athermal contribution to GB sliding.

Furthermore, Sansoz and Molinari[43,65] performed a molecular simulation using the quasi-continuum method to understand how GB structure influences the GB sliding mechanism in the athermal limit. Their investigation of zero temperature simulations showed that GB energy alone cannot be used as a relevant parameter to predict the sliding of nanoscale high-angle boundaries when no thermally activated mechanisms were involved, a special boundary structure (i.e. the E structural unit) presenting in the period of Σ tilt GBs was found to be responsible for the onset of sliding by atomic shuffling. GB sliding strength (the maximum shear stress reached before GB sliding) in the athermal limit showed slight variations between the different interface configurations, but had no apparent correlation with the GB structure.

Unlike the above conclusion, Cahn et al.[34] found that GBs with some special structural units showed obvious migration when shear deformation was applied while fast or pure GB sliding was found in those asymmetric GBs organised by disorder atoms without special structural units. In a series of papers[66-68], sliding along a high-symmetry ∑11[110] (113) tilt GB in Al was studied by molecular statics. As expected, a perfect GB with a ground-state structure exhibited an extremely high sliding resistance, while extrinsic defects such as small steps and partial dislocations, reduced the critical stress of sliding by orders of magnitude. This contradiction of previous results indicates that the sliding resistance related to

GB structure and energy needs further investigation.

2.2.2 Grain boundary migration

GB migration coupled to shear deformation is now recognised as a very common phenomenon that initiates plastic deformation of the grains. The basic idea of the coupling effect is that a shear stress applied to a GB induces its normal motion, and in turn, the GB motion induced by an applied shear stress, or by any other driving force, produces shear deformation of the volume swept by the motion. Because this deformation is usually a simple shear parallel to the GB plane, the GB motion is coupled to grain translations. Moreover, the coupled motion of a curved GB induces grain rotation[69,70] that in turn creates a driving force for normal GB motion.

The coupled state of a boundary exists independently of the driving forces applied, indeed, it has been shown[71,72] that GB migration caused by shear deformation follows the geometric rules of coupling. The coupling effect is characterised by a factor β that is equal to the ratio of the tangential grain translation to the associated normal GB displacement or the ratio of the tangential and normal velocities V and V_n. This coupling is called perfect if $\beta = V/V_n$ is a geometric constant that only depends on the GB bicrystallography and not on the GB velocity or driving force. Simulations have identified dozens of coupled GBs, and this motion has also been observed in experiments on bicrystals in many metals where the experimental coupling factors matched their perfect geometric values[73-75].

Cahn et al.[71] used [0 0 1] symmetrical tilt GBs in copper as a model to calculate the coupling factor β between the GB motion and grain translations by MD simulations over the entire misorientation range and a wide range of temperatures. In their research, any ordered GB should be able to couple to shear stresses. Cahn et al. simulations showed good agreement with the predicted geometric model of coupling. The coupling factor has an abrupt switch from one branch to another at a tilt angle of about 35 °, as shown in Fig.2.13 Another important finding of their simulations was that many GBs lost their coupling ability at high temperatures and

responded to the applied stress by sliding rigidly, without any normal motion; in fact a transition from coupling to sliding occurred continuously over a temperature range until the coupling completely disappeared. There are two possible mechanisms for this transition: in one the GB structure becomes highly disordered (due to pre-melting), which precludes the deformation and rotation of the structural units, and in other cases the GB structure remains well ordered and can support coupled motion, but the temperature activates the sliding mechanisms with lower critical stresses, making sliding the dominant response to the applied stress. Fig.2.14 shows an example of a temperature–misorientation diagram of the mechanical responses of [0 0 1] symmetrical tilt GBs in copper.

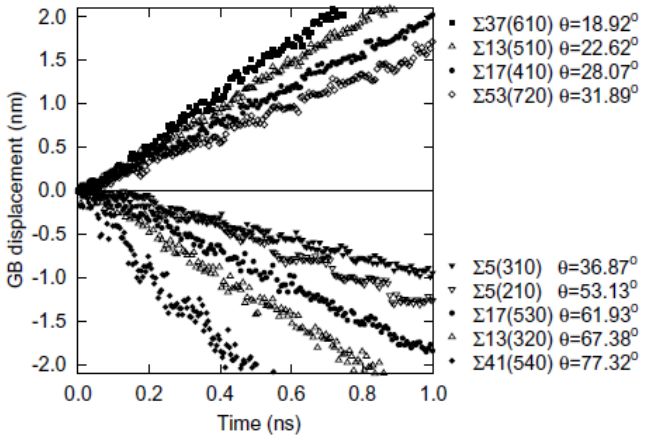

(a)

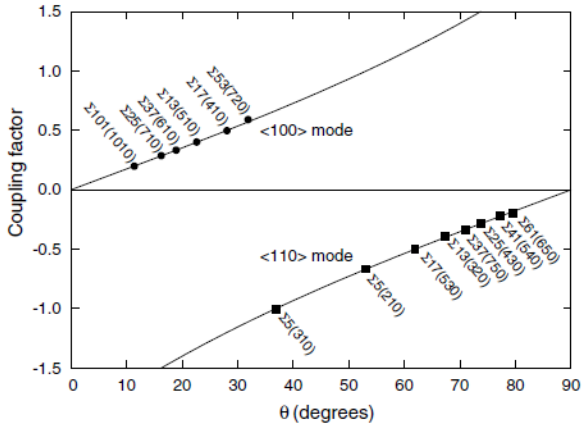

(b)

Figure 2.13 (a) GB displacement versus time during MD simulations at 800 K under a shear parallel to the GB plane and normal to the tilt axis. The shear rate is 1 m/s. (b) The coupling factor b obtained by MD simulations at 800 K as a function of the tilt angle. The lines represent

two branches of b predicted by the geometric model of coupling. [71]

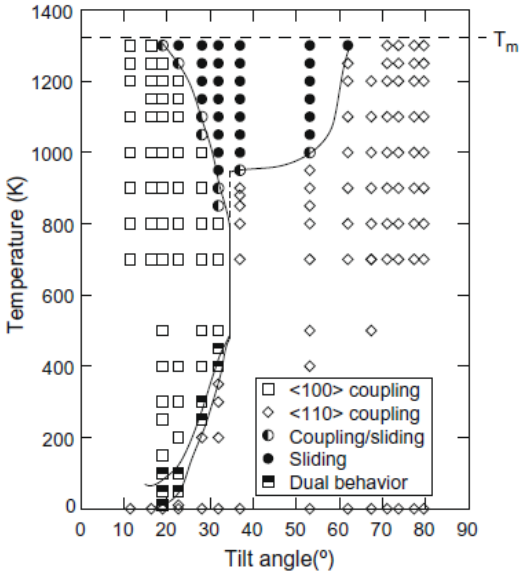

Figure 2.14 Diagram of mechanical responses to shear of [0 0 1] symmetrical tilt GBs in Cu. Note that for high angle GBs coupling is replaced by sliding at about 0.7 of the melting point T_m. [71]

Simulations have also provided important insights into the dynamics of stress-driven GB motion[72]. At low temperatures and relatively high velocities, the motion exhibits a stick–slip behaviour characterised by a saw-tooth time dependence of the stress and a stop-and-go character of the motion (see Fig.2.15). The magnitude of the peak stress increased with the GB velocity V but decreased with temperature T.

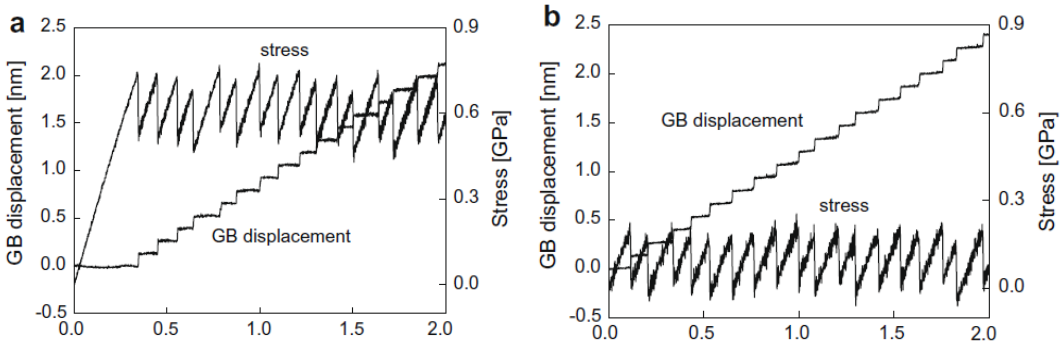

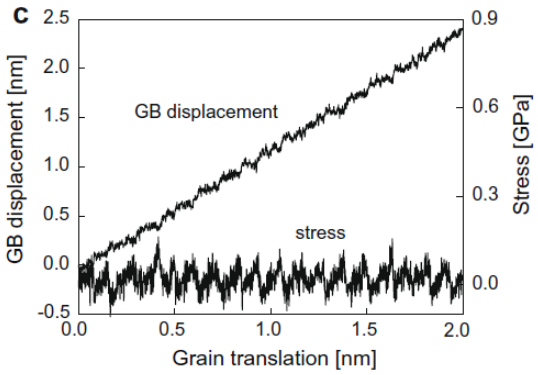

Figure 2.15 GB displacement and shear stress at (a) 100 K, (b) 500 K and (c) 900 K and the imposed grain translation velocity 1 m/s for the ∑21 GB in Al. [72]

While this coupling effect has been well confirmed for symmetrical tilt GBs, little is known about the coupling ability of asymmetrical boundaries. Based on the classic theory by Read and Shockley[76], the non-uniform structure of asymmetric GBs consists of more than two types of dislocations that can block each other when gliding on the intersecting planes and prevent a coupled motion. Therefore, the migration of asymmetric GBs was thought to be impossible, but recent MD simulations[77-79] have suggested this may not be the case. The geometric rules of coupling or migration mechanisms of asymmetric GBs is less known.

Trautt et al.[78] applied a combination of molecular dynamics and phase field crystal simulations to investigate the stress-driven motion of asymmetrical GBs between cubic crystals over the entire range of inclination angles. The MD simulations indicated that the dislocations usually found a way to glide past each other without completely blocking themselves, so they proposed two mechanisms by which the dislocations could avoid blocking each other while preserving the total Burgers vector, i.e. dislocation reactions and dislocation avoidance. The typical dislocation reaction mechanism is shown in Fig.2.16, where a single 1/2<110> dislocation propagated through an array of <100> dislocations; the process of dislocation propagation produces a slight downward displacement of the dislocation array, and multiple dislocation passes can produce significant GB displacements. The remarkable feature of this mechanism is that it does not require a dislocation

climb, despite the fact that the propagating dislocation has a Burgers vector component normal to the GB plane. Another mechanism was dislocation avoidance. When the ratio of the numbers of the two types of dislocations was large, Trautt et al. observed that the minority dislocations tended to lag behind the majority dislocations and then return to the boundary when a suitable gap was available. This process is illustrated schematically in Fig.2.17 for a dislocation ratio of 2:1. The proposed mechanisms must still be verified and more migration mechanisms are expected for asymmetric GBs in future atomistic simulation work.

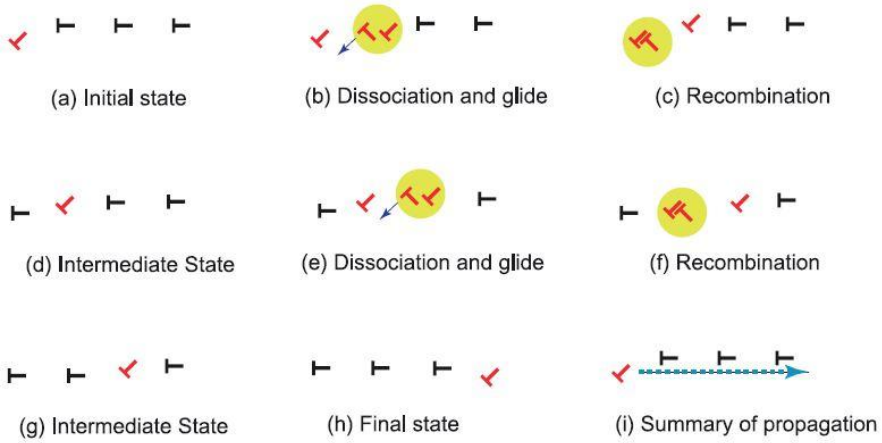

Figure 2.16 Schematic of dislocation propagation along a GB by a chain of dislocation reactions.[78]

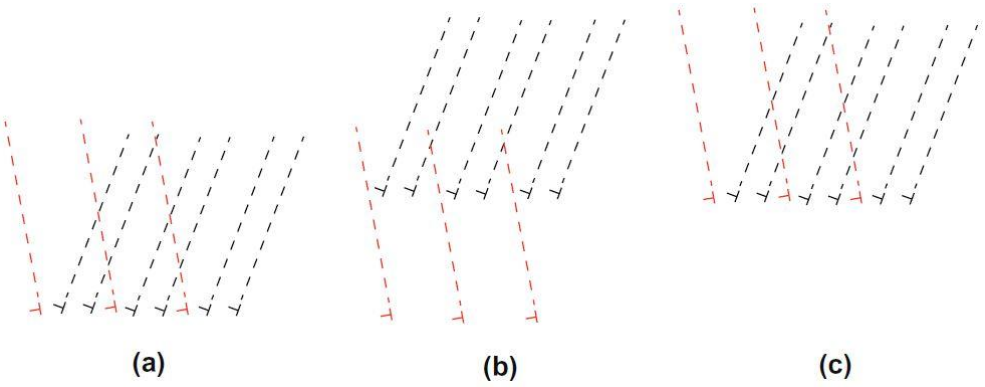

Figure 2.17 Schematic illustration of the dislocation avoidance mechanism for an asymmetrical GB moving upward.[78]

2.2.3 Interaction of grain boundary and dislocation

Interaction between the lattice dislocation and grain boundary plays an important role in the mechanical behaviour of materials, including its strength and plasticity. Dislocation/GB interactions can be in several forms where GBs act as obstacles to dislocation motion that leads to dislocation pile-up and material hardening, or as either sinks, or sources of dislocations contribute to dislocation annihilation and generation in individual grains, or as transmissible interfaces through which a dislocation can move on to a neighbouring grain from the original one. The complex nature of dislocation/GB interactions makes them a difficult problem that is not yet fully resolved. The details remain complicated, for example, an absorbed lattice dislocation may be transformed into a few grain boundary dislocations[80-83], or a dislocation can be reflected back to the original grain with the possibility that the site of reflection is not exactly on the same dislocation/GB reaction site[84-86]. One or more of these phenomena may occur simultaneously, but that depends on various factors such as GB geometry[87-89] and the characteristics of the incoming dislocation. Of all the aforementioned possible reactions, particular attention has been paid to slip transmission across the GB.

At an earlier time, Shen et al.[90,91] studied dislocations through grain boundaries in FCC and BCC polycrystalline metals using dynamic in situ high voltage electron microscopy, static transmission electron microscopy, and anisotropic elastic stress analysis. They found that when dislocations propagated across grain boundaries, the activated slip system can be predicted from the pile-up properties and grain boundary orientation using a combined criterion based on boundary geometric factors and internal stresses. They used these two conditions to demonstrate their ability to predict the active slip systems in 4 static cases and 1 dynamic in-situ case in 304 stainless steel. However, the predicted slip system may not have a favourable geometric condition, an inconsistency that occurred twice in their five examples.

To remove this inconsistency, Lee et al.[92] proposed a modified set of conditions to

determine the active slip system based on dynamic in-situ TEM deformation experiments. These three conditions are as follows:

(1) The Geometric Condition: The angle between the lines of intersection of the incoming and outgoing slip planes with the grain boundary should be minimised;

(2) The Resolved Shear Stress Condition: The resolved shear stress acting on the outgoing slip system from the incoming piled-up dislocations should be maximised.

(3) The Residual Grain-boundary Dislocation Condition: The Burgers vector of the residual dislocation is determined from the difference between the Burgers vectors of the incoming and outgoing dislocations. The magnitude of the Burgers vectors of this residual dislocation should be minimised. This and the resolved shear stress condition determine the active slip direction.

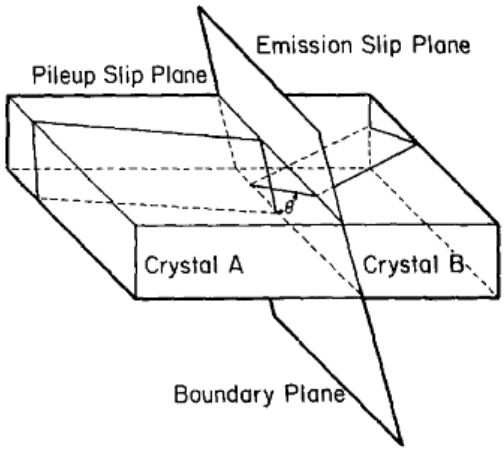

Figure 2.18 Schematic of intersection of slip planes and grain boundary.[92]

Koning et al.[93,94] identified these three conditions by applying a combination of MD simulations and a line tension model. In the MD simulations, slip transmission of dislocation loops nucleated from a crack tip near a series of pure tilt GBs in Ni. It was found that the interaction between the dislocations and GBs differed depending on the nature of the boundary and varied between unimpeded slip transmissions to complete blockage of dislocations at the boundary. They developed a simple line tension (LT) model to describe the effect of a GB on the glide of lattice dislocations

across the boundary, and concluded that the slip transmission resistance due to GB was a function of three variables that are the same as the three conditions mentioned above. Unlike the empirical rules, their model provided a quantitative measure of slip transmission resistance for each pair of incoming and outgoing slip systems, and that is the critical stress of source activation.

Bachurin et al.[87] investigated the interaction between lattice dislocations and symmetrical and asymmetrical tilt GBs in <1 1 1> textured thin nickel films using atomistic simulation methods. Beside the three conditions mentioned above, they found that the misorientation angle of the GB, the sign of the burgers vector of the incoming dislocation and the exact site where the dislocation meets the GB, were all important parameters determining the ability of the dislocation to penetrate the boundary.

For small-angle GB, the transmission depends on the change in misorientation between the grains due to the burgers vector of the incoming dislocations: a "positive" dislocation that increases local misorientation and penetrates more easily through a GB than a "negative" dislocation. Fig.2.19 shows the different steps of the interaction between a "positive" dislocation and a symmetrical $\sum 57(\theta=11.31°)$ tilt GB. The simulation of asymmetric GBs showed that the GB inclination had a minor influence on the observed mechanisms and did not significantly alter the de-pinning stresses of the transmitted dislocations. Unlike the small-angle GB, the results of high-angle tilt GBs showed that the local relaxation and accommodation of the incoming lattice dislocation made direct nucleation and transmission very difficult.

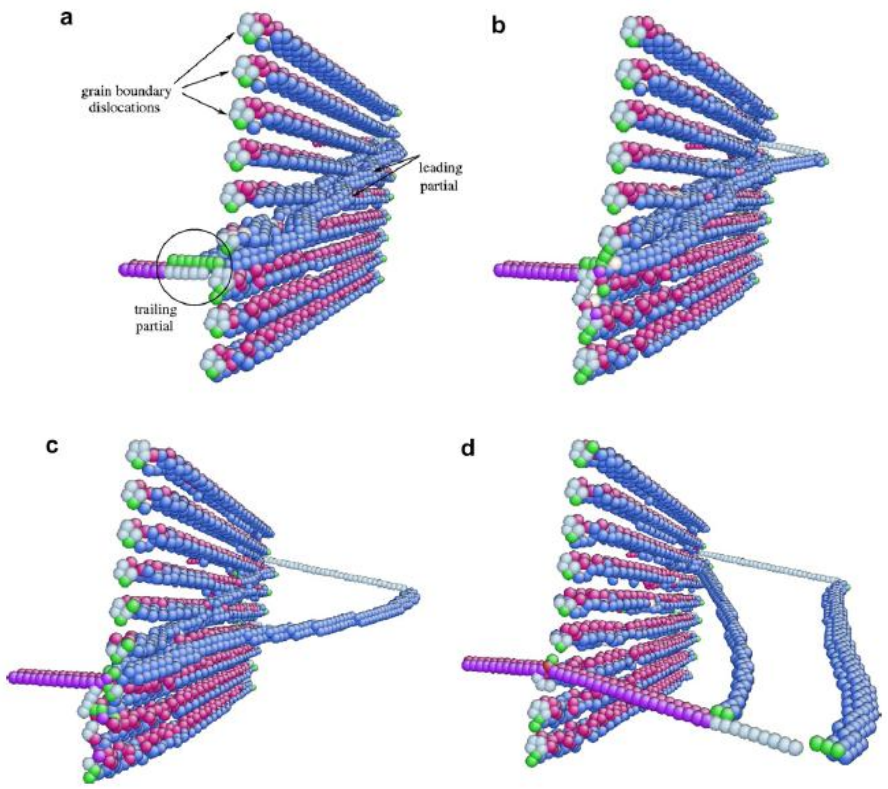

Figure 2.19 Different steps of the interaction between a dislocation and a symmetrical ∑57 tilt grain boundary. (a) At 0.64% strain the leading partial dislocation enters the grain boundary, whereas the trailing partial (indicated by the circle) is blocked before entering the grain boundary; (b) nucleation of the leading partial dislocation at 1.04% strain at the (back) free surface; (c) propagation of the leading partial dislocation into grain 2 at 1.12% strain; (d) propagation of the trailing partial dislocation into grain 2 at approximately 1.20% strain. [87]

Jin et al.[95,96] studied dislocation interaction with coherent twin boundaries in FCC metals and found that under an applied shear stress, a perfect screw dislocation could either transmit though the boundary or dissociate into partials in the boundary plane, depending on the generalised stacking fault energy and other material-dependent parameters. However, with an incident mixed (60°) dislocation, the dissociation reactions at the boundary were more complex and resulted in partials gliding into the neighbouring twin and leaving a locked configuration at the boundary.

It has been known that dislocation piling-up against GB is generally inevitable in plastic deformation and plays an important role in the dislocation/GB interaction; in fact pile-up of dislocations changes the stress fields near the site of dislocation/GB interaction. The interaction between subsequent incoming dislocations and GBs is

affected by residual defects generated by previous dislocation/GB interactions[80,81,83,86,97], a result that has been experimentally verified by the results of Lee et al.[92,98,99]. Computationally, Dewald and Curtin[81] studied the interaction of piling-up edge dislocations with ∑11(1 1 3)[-1 2 -1] STGBs in bicrystal Al using the coupled atomistic/discrete dislocation method. Unlike the results in isolated dislocation studies, their results revealed that for a small number of incoming dislocations, the nucleation of GB dislocations and GB dislocation dipoles dominated the reaction. They also researched into screw dislocations impinging on tilt boundaries in Al[80] and 60° dislocations impinging on Σ3, Σ9 and Σ11 tilt boundaries in Al[100]. Yu and Wang[101] studied the interactions between specified numbers of piled-up lattice dislocations and ∑11(1 1 3) symmetrical tilt grain boundaries in bicrystal copper using the quasi-continuum method. They proposed a unified geometrical criterion to predict "hard" and "easy" dislocation transmission without explicitly defining the "positive" and "negative" dislocation/GB interactions. It has been demonstrated that the pile-up of incoming dislocations had a remarkable influence on the "positive" and "negative" interactions, and can even activate dislocation transmission at smaller external loadings.

2.2.4 Dislocation nucleation from grain boundary

It has been well established from MD simulations[102-108] and experimental observations[11,12] that GBs can serve as sources of dislocations that induced a plastic deformation in nanocrystalline samples where the small grain sizes resulted in a heterogeneous nucleation and emission of dislocations from the grain boundary. This dislocation nucleation event can be viewed as an activation of the dislocation source that lies within or near the boundary. Previous researches used atomistic simulations to investigate the nucleation and propagation of dislocations from the GB in the nanocrystal and bicrystal configurations introduced by Van Swygenhoven et al.[22] and Tschopp et al.[23]. Bicrystal configurations have provided an insight into how the GB degrees of freedom impact on the GB structure and dislocation nucleation event, so the

review in this section will focus on bicrystal models.

Spearot et al.[75,76] used MD simulations to study how applied tensile stresses affected the <1 0 0> and <1 1 0> symmetrical tilt GBs in aluminium and copper. The mechanical failure along the boundaries was initiated by the emission of partial dislocation into the grains, accompanied by atomic rearrangements in the boundary. These rearrangements often resulted in the formation of ledges which gave rise to a stress concentration. The tensile strength of the boundary depended on the orientation of the tensile load relative to the boundary plane and on certain structural features of the boundary. They proposed a simple model to illustrate the impact that interfacial porosity and stresses acting on the slip-plane in non-glide directions had on the tensile interface strength. While the proposed model could model the tensile strength of GBs with a <100> misorientation axis and many GBs with a <110> misorientation axis, it failed to predict the tensile strength of <110> GBs with a misorientation angle where $\theta>109.5°$. The significant drop in the tensile strength of these GBs was assumed to be related to the special GB structures with the E structural units. Later, Tschopp et al.[109] and Tucker et al.[110] used atomistic simulations to investigate the structure and interfacial free volume of <110> symmetric tilt GBs within a misorientation range $109.5°<\theta< 180°$ and containing the E structural unit. They calculated the GB free volume along with the spacing and connectivity of free volume and found that free volume provided a valuable insight into the atomic scale processes associated with stress-induced dislocation nucleation from GBs.

Tschopp and McDowell[108] used a bicrystal model to investigate dislocation nucleation from $\sum 3$ asymmetric tilt GBs under uniaxial tension applied perpendicular to the boundary. It is interesting to see how dislocation nucleation mechanisms can change markedly with the inclination angle for identical misorientations. The mechanisms for dislocation nucleation in Cu asymmetric boundaries were divided into three regimes: low ($\Phi\leq35.26°$), intermediate ($35.26°<\Phi<70.53°$), and high ($\Phi\geq70.53°$) inclination angles. At low inclination angles the dissociation and nucleation processes

occurred on different slip planes, so the stress required for dislocation was relatively high. At intermediate inclination angles the dislocation dissociation and nucleation processes occurred on the same slip plane, so the stress required for nucleation was low. At high inclination angles the extended dissociation of the boundary resulted in an increased volume of the 9R phase. Fig.2.20 shows the uniaxial tensile deformation of the asymmetric tilt GB at different inclination angles in Cu at 10K.

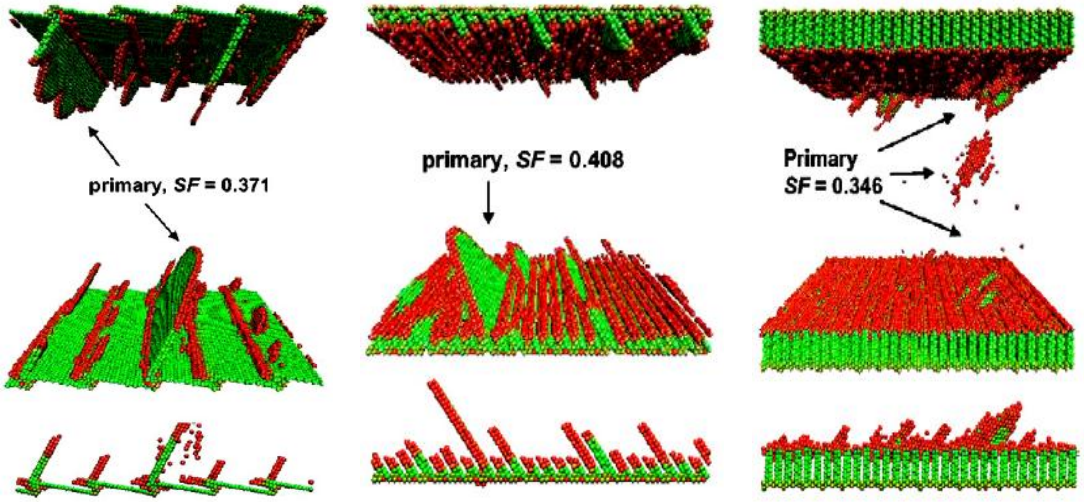

(a) (b) (c)

Figure 2.20 The nucleation of partial dislocation loops under uniaxial tensile deformation of the asymmetric tilt grain boundary with different angles in Cu at 10K. Strain rate (a) ε=7.7% (b) ε=4.8% (c) ε=9.3%. SF-Schmid factor. [108]

2.3 Stacking Fault Tetrahedron Induced Plasticity

2.3.1 Interaction of SFT with dislocation

A high number of nanometre sized stacking fault tetrahedra are commonly found in metals with low stacking fault energy, by irradiation, rapid quenching or sever plastic deformation. In this situation the stacking fault tetrahedra act as obstacles to dislocation motion leading to an increased yield strength, decreased ductility, and plastic instability. Therefore, understanding the interaction between gliding dislocations and stacking fault tetrahedra is critical in order to reliably predict the mechanical properties of nanocrystalline metals.

The atomistic interactions between gliding dislocations and perfect SFTs have

recently been studied using molecular dynamics simulations[29,111-117]. For instance, Wirth et al.[111] carried out MD simulation to study the interaction of a moving edge dislocation with SFT in Cu, and found that a perfect SFT acted as a hard obstacle for dislocation motion and, although the SFT was sheared by the dislocation passage, it remained largely intact. Niewczas and Hoagland[115] studied the interaction of isolated Shockley dislocations with SFT by MD simulation using a copper potential. An analysis of the interaction process revealed that a SFT cut by a single Shockley dislocation remained stable regardless of where the intersection took place. Depending on the position of the cutting plane with respect to the tetrahedron, the Shockley dislocation passed the SFT by: (1) shearing its apex, (2) forming a residual loop around the SFT and/or, (3) interacting with the dislocations at the tetrahedron base. The latter reactions led to the formation of Shockley dislocations that were mobile in two faces of the parent tetrahedron, and eventually making it penetrable to other dislocations moving on adjacent planes during twin thickening.

In situ straining experiments coupled with MD simulations were conducted by Robach et al.[29] to study the interactions that occurred between dislocations and SFT in irradiated or rapidly quenched copper and gold. This interaction can result in the SFT being sheared into two defects, converted to another type of defect, or annihilated. The tetrahedron can be sheared by the interaction at high applied stress. The interaction of an edge dislocation with a dissociated Frank loop revealed that absorption of the loop was a pair of super-jogs on the dislocations, and these super-jogs were then re-emitted as a perfect dislocation loop. Moreover, multiple shear interactions resulted in an SFT being separated into a small perfect SFT and a partially dissociated Frank loop bound by stair-rod and Shockley partial dislocations, as shown in Fig.2.21.

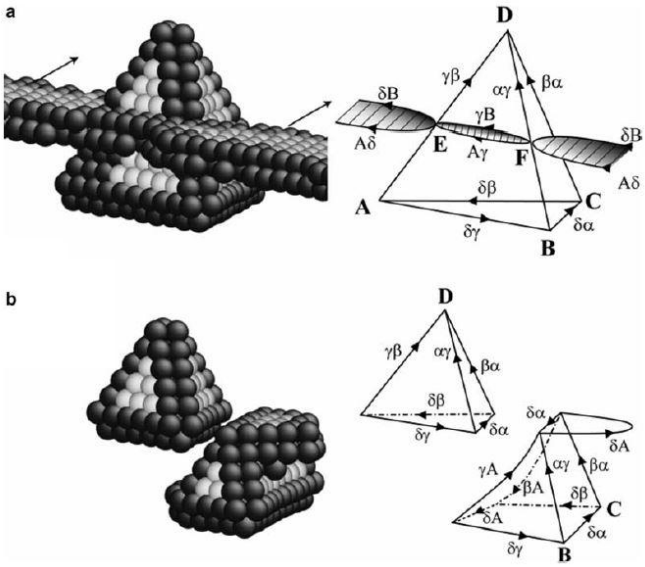

Figure 2.21 Structure of a perfect stacking-fault tetrahedra following the shear by four screw dislocations. [29]

The observed interactions between SFTs and screw dislocations are more complex than edge dislocations because the screw dislocation can cross-slip. Martinez et al.[25] presented a comprehensive dislocation dynamics study of the strength of SFT to screw dislocation glide in Cu. They obtained strength maps of SFT as a function of the dislocation glide plane-SFT intersection height, interaction orientation, and the length of the dislocation line. SFTs generally became weak obstacles if the area between the dislocations and SFTs was small, so based on this result they proposed simple scaling laws with the slipped area as the only variable. These laws could describe all the strength curves so they were used to derive a simple model of dislocation-SFT strength. The stresses required to break through obstacles in the 2.5-4.8 nm size range were computed to be 100-300 MPa, which was in good agreement with some experimental estimations and MD calculations. Fan and Wang[118] used an MD simulation to study the dislocation mechanism of the reaction between SFT and screw dislocation in copper and found that at high temperatures, the SFT was completely absorbed by screw dislocation, with help from the Lomer-Cottrell lock transforming into Lomer dislocation, whereas at low temperatures this transformation rarely occurred rarely and a perfect SFT remained

after the reaction. This complete absorption mechanism helps us understand the defect-free channels in irradiated materials.

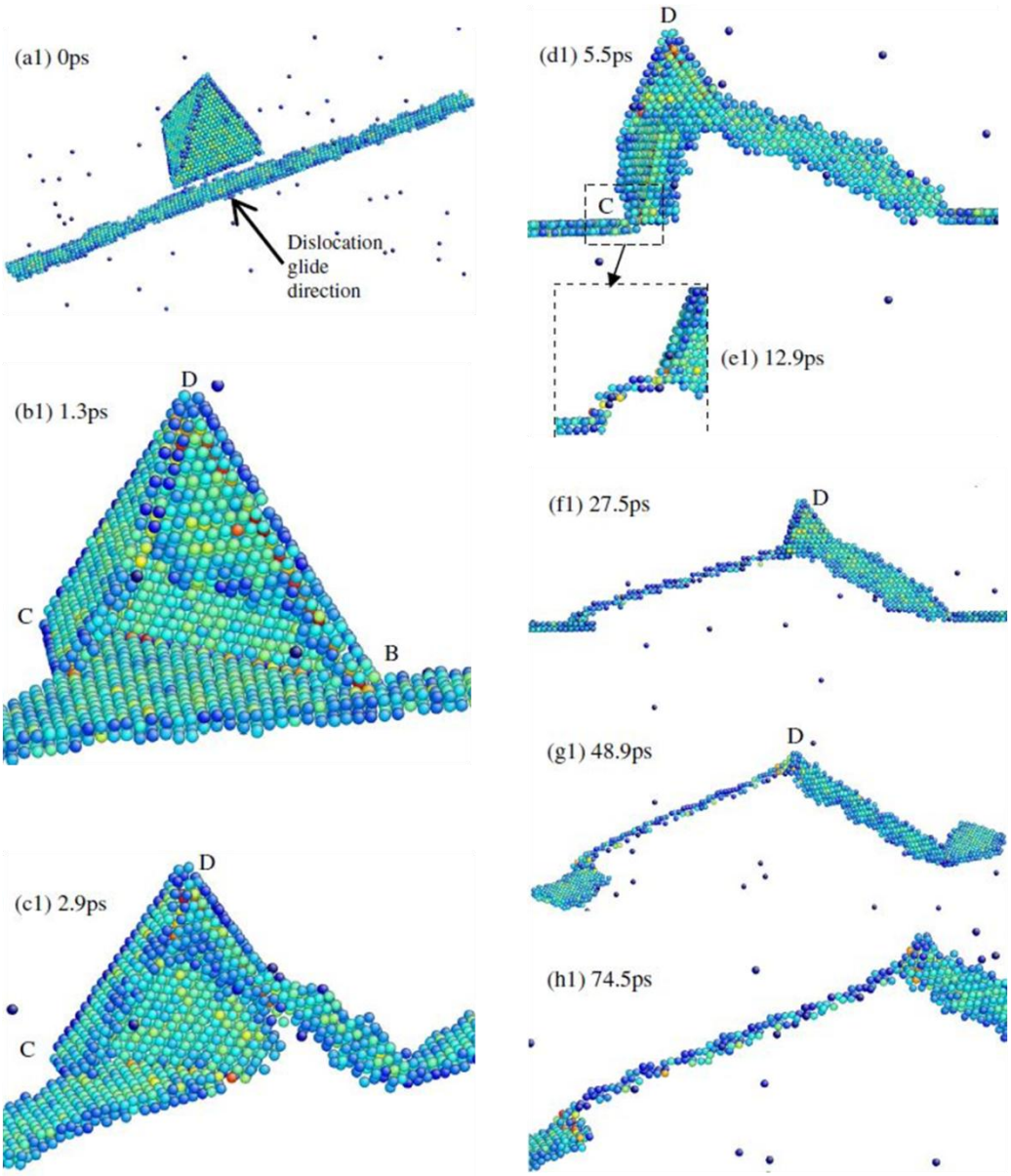

Figure 2.22 MD simulation of reaction details between a screw dislocation and a 6 nm SFT (276 vacancies) at 300 K and under 100 MPa. [118]

A recent transmission electron microscopy investigation of high-energy proton irradiated copper[119] showed that almost 50% of the visible SFT population were not perfect SFTs, they consisted of truncated SFT or overlapping SFT. Saintoyant et al.[113] used MD simulations to study the interaction between gliding dislocations (with either edge or screw character) and truncated SFT or overlapping SFT. This simulation showed that defect shearing was the most common result when an edge

dislocation interacted with a truncated SFT, and this ultimately led to complete separation into two smaller defect clusters. The most common result of interaction with a screw dislocation was a partial absorption of the truncated SFT that resulted in the formation of super-jog segments as the defect was absorbed into the dislocation core. Partial absorption and shear also resulted in the removal of isolated vacancies from the defect that either broke the truncated SFT or overlapping SFT into two or more smaller defect clusters. These results were consistent with MD observations of dislocation interaction with perfect SFT and led to the conclusion that the dislocation reaction with SFT, truncated SFT, and overlapping SFT are largely governed by shear interactions that produce smaller defects, although partial absorption is possible for specific interaction geometries.

2.3.2 Interaction of SFT with twin boundary

Previous experimental observations of the structure of irradiated and plastically deformed austenitic steels revealed the presence of narrow, defect-free twins[120], which indicated that defect-free channels were formed inside the mechanical twins. While the interaction between dislocation and SFT has been studied extensively, as reviewed above, the fundamental mechanism involved in the interaction of twin boundary and SFT has rarely been considered in the literature. Niewczas and Hoagland[121] conducted MD simulations to study the interaction of moving twin boundaries with SFT and found that a twin growing by a ledge mechanism produced substantial damage to the SFT. The products of these reactions depended on the direction of twin growth with respect to the SFT, but they generally led to the production of qualitatively different defect structures in the twin lattice. Typical structures that were produced in the twin included product were SFTs, free vacancies, planar stacking faults bounded by partial dislocations, mutually linked stacking faults on non-coplanar $\{111\}_T$ planes, small $\{111\}_T$ tetrahedra and their partial forms. Moreover, the interaction of lenticular twins with small SFTs formed product SFTs in the twin lattice that were rotated by $60°$ with respect to the parent defect.

However, their prediction from simulation received very little attention because the proposed interactions require frequent migration of Shockley partials and twin boundaries, and this only occurs sporadically in conventional bulk metallic materials with coarse grains. Hence, there was no experimental evidence to verify their predicted SFT removal mechanism to date.

Yu et al.[122] recently observed the radiation induced migration of coherent and incoherent twin boundaries by in situ Kr ion irradiation of epitaxial nanotwinned Ag and found that the migrating twin boundaries played a distinct role during the removal of radiation-induced SFTs. Here the density of SFT in irradiated nanotwinned Ag was much lower than its bulk counterpart, indeed, compared with predictions by the MD simulations, two fundamental interaction mechanisms were identified. When a mobile twin boundary reached an SFT from its apex, as shown in the upper case in Fig.2.23(b), the SFT-twin boundary interaction transformed the {111} apex of SFT in matrix to a smaller $\{100\}_T$ tetrahedron residing temporarily within the twin lattice, which then collapsed rapidly into a partial loop on the {111} plane in the twinned crystal. Stacking faults also formed next to the twin boundary. Continuous migration of the twin boundary towards the SFT led to the further consumption of a truncated SFT. Stacking faults absorbed vacancies supplied by the SFT and continuously expanded along the twin boundary, but when the SFT was approached by a mobile twin boundary from its base, as shown in the lower panel of Fig.2.23(b), a mobile Shockley partial dislocation (a/6[121]) propagating along the twin boundary could interact with stair-rod dislocations at the base of SFT. The interactions with AB and AC led to new mobile Shockley partials (a/6[211] and a/6[112]) whose propagating on ABD and ACD planes of the SFT can result in the defaulting of Frank loops. The two scenarios predicted by MD simulations were consistent with the experimental observations shown in Fig.2.23(a). These experimental results indicated that significant mobility can make twin boundaries an attractive candidate for removing radiation-induced SFTs and other defects.

However, while the MD simulations showed that twin boundaries in nano-twinned Cu can migrate rapidly under stress or annealing through the movement of mobile Shockley partials, the physical mechanisms and details of radiation-induced twin boundary migration are still not clear and therefore require more atomistic simulations.

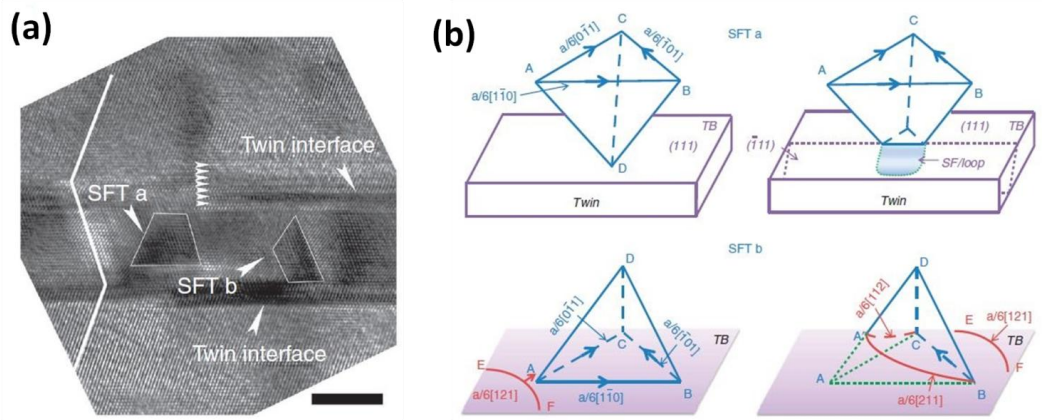

Figure 2.23 High-resolution TEM of SFTs and their interaction mechanism with twin boundaries. (a) HRTEM image of two truncated SFTs during their interactions with CTBs. SFT-a was truncated from its apex, whereas SFT-b was destructed from its base. Scale bar, 4 nm. (b) Schematics of two types of interactions between SFTs and twin boundaries corresponding to the two cases in (a). [122]

2.4 Summary

The literature studying plastic deformation induced by grain boundary and stacking fault tetrahedron were reviewed in this chapter. Previous works have shown that atomistic simulation is an effective way of investigating the deformation mechanisms of nanocrystalline materials and could provide a better understanding of the plastic deformation process at the atomic level. However, there is still no comprehensive understanding of the relationship between the GB structure, GB energy, mechanical response, and the underlying deformation mechanisms. Moreover, the computer modelling of GBs mostly focused on symmetrical grain boundaries, whereas asymmetrical boundaries have been studied but not as extensively as the symmetrical ones. Our current understanding of the atomic structure, energies, and deformation mechanisms of asymmetrical GBs remains

rather limited. While many previous studies have investigated the formation of SFT or their interactions with other structural defects (mainly dislocations), little knowledge is available on the effects of SFT on plastic deformation in a small volume crystal where dislocation is unlikely to be present. The studies in this thesis will provide incremental information as well as some new insights into these questions.

CHAPTER 3

Introduction of Simulation Methodology

With the rapid development of computational technology, extensive progress has been made in the molecular dynamics (MD) simulation of materials at the atomic scale. In this chapter, the MD method will be introduced briefly and its potential for use in simulation, visualisation tools, and other post-processing techniques will be described.

3.1 Molecular Dynamics (MD) Simulation

Given the extremely rapid increases in recent years in processor speed coupled with the development of ever larger massively parallel computing architectures, atomic-level simulations have provided novel insights into the structure and thermo-mechanical behaviour of nanocrystalline materials. Of the various approaches to atomic level simulation developed over previous decades, including lattice statics, lattice dynamics, Monte Carlo and molecular dynamics (MD), the last one has been proven to be very useful when investigating plastic deformation. MD simulations have recently advanced to a level where the complex dislocation and grain boundary processes in heavily deformed materials with a sub-micron grain size can be modelled.

Molecular dynamics algorithm

In the molecular dynamics method the evolution of atomic positions is described using Newton's 2nd Law of motion,

$$\dot{\mathbf{p}}^{\mathrm{i}} = \mathbf{F}^{\mathrm{i}} = m\dot{\mathbf{v}}^{\mathrm{i}} \tag{3-1}$$

where

$$\dot{\mathbf{r}}^{\mathrm{i}} = \frac{d\mathbf{r}^{\mathrm{i}}}{dt} = \frac{\mathbf{p}^{\mathrm{i}}}{m} \tag{3-2}$$

Here m is the mass, $\mathbf{p}^i$ is the momentum, $\mathbf{v}^i$ and $\mathbf{r}^i$ are the velocity and displacement of the i^{th} atom, and the 'dot' denotes the first derivative with respect to time. Equations (3-1) and (3-2) represent the equations of motion for a system of atoms that is isolated from the environment. The most widely used method to solve Equations (3-1) and (3-2) in molecular dynamics is the velocity-Verlet finite-difference algorithm[123]. This algorithm has many desirable properties because its form is exactly time reversible (which allows the equations of motion to be propagated forward in time without iteration) and symplectic (the volume in phase space is conserved), insuring long simulation time stability and convergence[124]. Also, the velocity-Verlet algorithm is efficient because it only requires one force evaluation per time step,

$$\mathbf{v}^i\left(t+\frac{\Delta t}{2}\right)=\mathbf{v}^i(t)+\frac{\Delta t}{2m}\mathbf{F}^i(t) \tag{3-3}$$

$$\mathbf{r}^i(t+\Delta t)=\mathbf{r}^i(t)+\Delta t\mathbf{v}^i\left(t+\frac{\Delta t}{2}\right) \tag{3-4}$$

$$\mathbf{v}^i(t+\Delta t)=\mathbf{v}^i\left(t+\frac{\Delta t}{2}\right)+\frac{\Delta t}{2m}\mathbf{F}^i(t+\Delta t) \tag{3-5}$$

Here Δt is the molecular dynamics time step for the simulation, which is typically in the order of femtoseconds. In the velocity-Verlet algorithm, the velocity of each atom is first calculated at a half time step forward in time using the current value of the atomic forces. The atomic positions are then updated to $t+\Delta t$ using the values of the atomic velocities at the half time step, and then a force calculation is performed using the updated atomic positions. Finally, the atomic velocities are evolved to the full time step using the updated force vector.

Equations (3-1) and (3-2) represent the equations of motion for a system of atoms that is isolated from the environment (micro-canonical ensemble). However, most problems in the mechanics and materials science community require that the system interact with the surrounding environment. One method to accomplish this in the MD framework is to introduce the concept of an extended system[125] where Newton's equations of motion are augmented and coupled to additional differential equations

that characterise the relationship between the system and the environment. For example, to model the atomic trajectories within the constant pressure, constant temperature (NPT) ensemble, the following set of equations is proposed[126],

$$\dot{\mathbf{r}}^{\mathrm{i}} = \frac{\mathbf{p}^{\mathrm{i}}}{m} + \eta(\mathbf{r}^{\mathrm{i}} - \mathbf{R}_0)$$

$$\dot{\mathbf{p}}^{\mathrm{i}} = \mathbf{F}^{\mathrm{i}} - (\eta + \zeta\mathbf{I})\mathbf{p}^{\mathrm{i}}$$

$$\dot{\zeta} = \mathrm{v}_{\mathrm{T}}^2\left(\frac{T}{T_0} - 1\right)$$

$$\dot{\boldsymbol{\eta}} = \frac{\mathrm{v}_{\mathrm{p}}^2}{NkT_0}\mathrm{V}(\sigma - \mathbf{P}_0\mathbf{I})$$

$$\dot{\mathbf{h}} = \eta\mathbf{h} \qquad (3\text{-}6)$$

Here $\mathbf{R}_0$ is the centre of mass of the system, the isobaric coefficient of friction (η) is a function of the desired pressure or stress ($\mathbf{P}_0$), Boltzmann's constant (k) and the constant pressure damping coefficient (V_P). The thermodynamic coefficient of friction (ζ) is a function of the thermal reservoir temperature (T_0), and the thermostatic rate (V_T). The boundaries of the system are defined by a set of vectors (**h**) that are aligned along the edges of the periodic unit cell. Melchionna et al.[126] showed that the equations of motion in equations (3-6) that were derived from earlier versions by Nose and Hoover[127,128], correctly reproduced the NPT distribution function. Furthermore, since the equations (3-6) do not require the atomic positions or velocities to be scaled in order to reproduce the NPT ensemble, they can easily be incorporated into the standard framework of a MD code.

Superiority of MD simulation

Several unique features of MD simulations are particularly relevant to the deformation studies of materials in nanoscale. Based on the solution of Newton's equations for a system of atoms interacting via some prescribed inter-atomic interaction potential function, MD simulations can expose real-time behaviour during deformation. They can elucidate the behaviour of a fully characterised nanocrystal model system in terms of the underlying interfacial structure, driving forces and atomic-level mechanisms, and also deform to rather large plastic strains

that enable deformation to be observed under very high GB and dislocation densities. This enables the intra- and inter-granular dislocation and GB processes in a deformation regime where they compete on an equal footing to be identified, and thus provide insights into the underlying mechanisms at the atomic level, that are not available from experiments. For example, recent successes include the identification of atomic level mechanisms for dislocation nucleation from, and annihilation at the GBs[63,129]; the prediction[130] and recent experimental verification[131] of mechanical twinning in nanocrystal Al; elucidation of the mechanistic causes for the crossover from a dislocation to a GB-based deformation mechanism with decreasing grain size[132]; the observation of shear bands[133] and their relationship to dimpled fracture surface[134].

Limitation of MD simulation

The fundamental limitations inherent to an MD approach are well known; MD simulation is limited to relatively small model systems consisting of typically millions of atoms, and the reliability of the inter-atomic potentials used and the relatively short time period (of typically 10 ns, or about 10^7 MD time steps) over which the dynamics of the system can be probed. The descriptions used to describe the inter-atomic force in most MD simulations are of empirical or semi-empirical origin, so while they extremely efficient computationally, they cannot fully capture the many-bodied nature of electronic bonding, particularly its complex and consistent variation as a function of local structure and chemistry in the vicinity of defects. Moreover, the short time duration to which MD simulations are inherently limited is particularly relevant to the simulation of plastic deformation. As a consequence, such simulations always involve extremely high strain rates (of typically $>10^7$ s^{-1}, corresponding to 1% strain in 1 ns), which is many orders of magnitude higher than in experiments. To render the deformation observable within such a short observation window, stresses that are usually much larger than in experiments must be applied.

Significance of MD simulation

In spite of some limitations inherent to the MD approach, large-scale MD simulations demonstrated that these simulations have now reached a level of fidelity where they can,

(1) Provide meaningful and novel atomic-level insights into dislocation and GB processes in nanocrystalline materials that are not readily obtainable from experiments.

(2) Provide valuable guidance towards sorting through the large and often contradictory body of experimental information.

(3) Expose the underlying concepts governing the complex interplay between dislocation and GB processes.

(4) Revolutionise our understanding of plastic-deformation processes in heavily deformed materials, and elucidate the physical mechanisms controlling technologically important processes, such as superplastic forming.

(5) Completely characterise the highly inhomogeneous state of internal stress that will undoubtedly spur the development of better deformation models based on materials-physics.

3.2 Potentials used in MD simulations

A suitable selection of inter-atomic potential to directly decide the accuracy of MD results leads to great challenges in developing a precise inter-atomic potential. The most used potentials are limited to the pair potential (e.g. Lennard-Jones potential and Morse potential) and multi-body potential (e.g. EAM potential) for pure metal in MD simulations. Unlike other types of potentials, embedded atom method (EAM) has many advantages in representing the atomic interplay, because at the surface of a crystal the atomic bonds may have different properties than in the bulk, while pair potentials cannot capture this effect. The limitation of modelling pair potentials is more obvious in a complex situation, particularly the dependence of the properties of chemical bonds between pairs of atoms. However, this behaviour is very

important for metals because the quantum mechanical effects describe the influence of the electron gas. To accurately represent the change in bond properties at the surface, a description that considers the environment of an atom is needed to determine the bond strength. Therefore, the bond energy between two particles is no longer a function of its distance, it is a function of the positions of all the other particles in the immediate vicinity. This behaviour can be captured in multi-body potentials. The use of EAM has been demonstrated effectively in recent MD simulation.

The embedded-atom method (EAM) was first developed by Daw and Baskes[135,136] to describe atomic bonding in FCC metallic systems. In this method each atom is viewed as an embedded impurity in the bulk of other atoms. To approximate the potential energy of a set of atoms, the EAM includes both pair interactions between nuclei of atoms i and j and the embedding energy as a function of the local background electron density around i^{th} atom,

$$U = \sum_{i,j(j\neq i)} G^{i}\left(\rho_{ave}^{j}\left(r^{ij}\right)\right) + \frac{1}{2}\sum_{i,j(j\neq i)} \varphi\left(r^{ij}\right) \qquad (3\text{-}7)$$

Here G^{i} is the embedding energy function, ρ_{ave}^{j} is the spherically averaged background electron density due to neighbours of the ith atom, φ is the pair interaction, and r^{ij} is the distance between atoms i and j. The embedding energy is assumed to depend solely on the intensity of the local background electrons provided by the surrounding atoms and its lower derivatives. The density of these background electrons is calculated using a linear superposition of the densities from neighbouring atoms,

$$\rho_{ave}^{j}\left(r^{ij}\right) = \sum_{i,j(j\neq i)} \rho_{ave}^{j}\left(r^{i} - r^{j}\right) \qquad (3\text{-}8)$$

This summation is performed over local atoms within a specified cut-off distance that typically includes at least the nearest first and second neighbours. Since the density of the background electrons is a local quantity, the embedded-atom method

can be used to examine systems with crystalline defects, such as dislocations and grain boundaries. The EAM is known as a semi-empirical approximation because the embedding energy, density of the background electrons and pair interaction functions are tailored to match certain material properties from *ab initio* calculations and experimental observations. Typical material properties include the lattice constant, bulk modulus, elastic constants, vacancy formation energy and sublimation energy. Inter-atomic potentials recently developed are fitted to additional structural properties such as the stacking fault energy.

In this study the EAM potentials developed by Mishin et al. for FCC metals were used[137,138]; indeed these potentials are widely used in MD simulations and they can fit a large set of experimental and first-principles data. For example, for Cu, Mishin et al. report an intrinsic stacking fault energy and an unstable stacking fault energy from their simulation result are 44.4mJ/m^2 and 158mJ/m^2, respectively, which are very close to the experimental measurement 45mJ/m^2 and 162mJ/m^2[137]. Similarly for Al, Mishin et al. report an intrinsic stacking fault energy of 146 mJ/m^2 and an unstable stacking fault energy of 168 mJ/m^2, both of which compare favourable to the experimental values[138].

3.3 MD code LAMMPS

The MD code LAMMPS[139] was used to carry out the simulations in this thesis; LAMMPS is a classical molecular dynamics code that models an ensemble of particles in a liquid, solid, or gaseous state, and it can also model atomic, polymeric, biological, metallic, granular, and coarse grained systems using a variety of force fields and boundary conditions. In most instances LAMMPS generally integrates Newton's equations of motion for collections of atoms, molecules, or macroscopic particles that interact via short- or long-range forces with a variety of initial and/or boundary conditions. It can model systems with only a few particles, and up to millions or billions. For computational efficiency LAMMPS uses neighbour lists to keep track of nearby particles. These lists are optimised for systems with particles that

are repulsive at short distances, so that the local density of particles never becomes too large. On parallel machines, LAMMPS uses spatial-decomposition techniques to partition the simulation domain into small 3D sub-domains, one of which is assigned to each processor. Processors communicate and store "ghost" atom information for atoms that border their sub-domain. LAMMPS is most efficient (in a parallel sense) for systems whose particles fill a 3D rectangular box with roughly uniform density. LAMMPS has the following general features (http://lammps.sandia.gov/) that enable it to be flexible and thus powerful;

• runs on a single processor or in parallel

• distributed-memory message-passing parallelism (MPI)

• spatial-decomposition of simulation domain for parallelism

• open-source distribution

• highly portable C++

• optional libraries used: MPI and single-processor FFT

• GPU (CUDA and OpenCL) and OpenMP support for many code features

• easy to extend with new features and functionality

• runs from an input script

• syntax for defining and using variables and formulas

• syntax for looping over runs and breaking out of loops

• run one or multiple simulations simultaneously (in parallel) from one script

• build as library, invoke LAMMPS thru library interface or provided Python wrapper

• couple with other codes: LAMMPS calls other code, other code calls LAMMPS, umbrella code calls both

3.4 Visualisation Methods

As introduced previously, an MD simulation is an effective way to model materials with atomic-scale resolution. Such atomistic simulation models generate three dimensional atomic configurations or trajectories that usually need further analysis

in order to generate new scientific insights. Powerful analysis and visualisation techniques play a key role in this process as simulated systems become larger and more complex. Without the right software tools, key information would remain undiscovered, inaccessible, and unused. The task of visualisation packages such as Atomeye[140] and Ovito[141], are used to translate the raw atomic coordinates into a meaningful graphical representation that can be interpreted by researchers.

As well as capturing the essential properties of a nanocrystalline system, atoms often numbering in the millions must be included in an MD simulation, and obviously, inspection at the atomic scale requires appropriate visualisation methods. Several methods have been developed to characterise the structure of defects that cannot be achieved simply through experiments. These methods facilitate the observation of atomic scale processes related to thermal processes during sample annealing or to the deformation mechanisms during plastic deformation. The major visualisation methods used in the present study, including potential energy, local stress and strain, centre-symmetric parameter and common neighbour analysis (CNA), are summarised in the following text.

Potential energy

The simplest visualisation method is to view atoms according to their local potential energy. In a nanocrystalline system, GB regions can be identified to some extent by only viewing those atoms with energies greater than a certain threshold; for instance, exceeding the cohesive energy by a value that equates to the latent heat of melting. Such a method for identifying the GB region must be used with caution because by definition, only those atoms in a high energy configuration are being considered, which naturally biases the probed GB structure to more disordered configurations. Fig.3.1(a) shows the atomic positions of those atoms with a cohesive energy of approximately 0.1 eV higher than the FCC crystalline energy. Using this criterion the GB and partial dislocation core are visible.

Local stress and strain

Equation (3-9) based on the viral theorem was used to calculate the stress of each atom.

$$\sigma = \frac{1}{V}\left(\frac{1}{2}\sum_j \sum_{i\neq j} \frac{U'}{\mathbf{r}^{ij}} \mathbf{r}_\alpha^{ij} \mathbf{r}_\beta^{ij} - \sum_i m^i \boldsymbol{v}^i \boldsymbol{v}^i\right) \quad (3\text{-}9)$$

where V is the volume of representative partition element, U' is the derivative of the potential energy with respect to position. $\mathbf{r}^{ij}$ is the distance vector between atoms i and j, *i.e.*, $\mathbf{r}^{ij} = \mathbf{r}^i - \mathbf{r}^j$. The subscripts α and β denote components in the α and β directions, respectively. *m* is the mass and *v* is the velocity of each atom. Fig.3.1(b) shows how the atoms are shaded according to local stress.

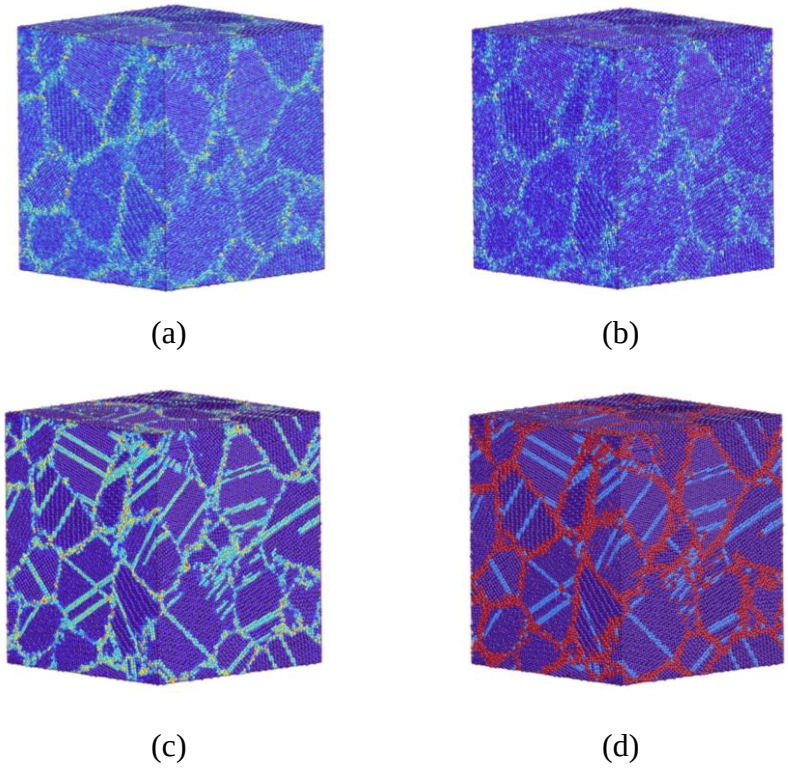

(a) (b)

(c) (d)

Figure 3.1 Four different methods of visualization of grain boundary and dislocation segment within a nanocrystalline environment. Atoms are shaded according to (a) potential energy, (b) local stress, (c) centre-symmetric parameter and (d) common neighbour analysis (CNA).

Centre-symmetric parameter

The centre-symmetry parameter was computed using the following formula

$$P = \sum_{i=1}^{N/2} \left|\vec{R}_i + \vec{R}_{i+N/2}\right| \quad (3\text{-}10)$$

where N is the number of the nearest neighbouring atoms. For FCC or BCC, N was set

to 12 and 8 respectively. $\vec{R}_i$ and $\vec{R}_{i+N/2}$ are vectors from the central atom to a particular pair of nearest neighbours. P was used to identify the atoms within the crystalline lattice, dislocation core, stacking fault and free surface. Fig.3.1(c) shows the atoms are shaded according to centre-symmetric symmetry.

Common neighbour analysis (CNA)

The atomic visualisation of grain and GB structures has been greatly facilitated by a medium range analysis of all atoms within the sample that ascribes a local crystallinity class to each atom. This was carried out by selecting the common neighbours of a pair of atoms separated by no more than a second nearest neighbour distance, and introducing a classification scheme for the nearest-neighbour bond pathways between the two atoms. Since each crystalline symmetry has a unique topological signature, when all the second nearest neighbour bond permutations are enumerated, a local symmetry label can be assigned to each atom. In this classification scheme, there are five kinds of CNA patterns: (1) FCC=1, (2) HCP=2, (3) BCC=3, (4) icosohedral=4, (5) unknown=5.

This local atomic classification scheme allows the GB network and structure to be easily identified. A significant advantage of such a local crystallinity analysis is that the (1 1 1) HCP planes represent twin planes, and two neighbouring parallel (1 1 1) HCP planes represent an intrinsic stacking fault. The visualisation of the twin planes has allowed for an easy identification of GBs containing structural units of a symmetric boundary. In the case of stacking fault defects, this approach has given evidence for partial dislocation activity. Fig.3.1(d) reveals the power of this visualisation technique where the dislocation core, stacking fault, and surrounding GBs are clearly seen.

3.5 Dislocation Extraction Algorithm (DXA)

While standard visualisation techniques in principle provide the option to identify the defect structure, a quantitative analysis and a detailed investigation of dislocation

lines and other crystal defects in atomistic simulation data remain a challenge. A novel method, called dislocation extraction algorithm (DXA) and developed by Alexander Stukowski[142,143], can extract dislocation lines in a fully automated way. This method translates the 'topological network' of disordered atoms into a network of connected dislocation segments, thereby preserving the true connectivity of crystal defects and the dislocation network down to the atomic level. The output provided by this method is a network of one dimensional dislocation lines that conform to the Burgers vector conservation rule. Moreover, this method delivers a geometric description of all other crystal defects that cannot be represented by dislocation lines (e.g. grain boundaries, surfaces, and pores, etc.), that are very useful for visualisation purposes and other applications. The DXA method consists of three principal steps:

(1) The common neighbour analysis (CNA) method is used to identify crystal line atoms. The remaining atoms are called 'disordered atoms'.

(2) A closed and orientable two dimensional manifold is constructed that separates the crystalline atoms from the disordered ones.

(3) For each dislocation segment, an arbitrary Burgers circuit path is found on the manifold enclosing the segment. This closed circuit is moved in both directions to the two opposing ends of the dislocation segment. While the circuit is advanced in each direction, a one-dimensional line representing the dislocation segment is constructed.

The DXA method was designed to divide the wealth of information stored in the snapshot of an atomistic simulation into its relevant and dispensable parts. The complexity of the relevant crystal defects is reduced as far as possible by transforming them into a higher level description that only consists of dislocation lines (and their Burgers vectors), stacking fault planes, and defect surfaces. Stukowski recently developed a new and more robust code that incorporates a generalised and extended version of DXA. This updated version of DXA[144,145], also

known as the *Crystal Analysis Tool*, supports a much wider range of crystal lattice types and can identify partial dislocations as well as grain boundary dislocations. For example, complex structures such as CSL grain boundaries consisting of large structural units can be identified, and fcc stacking faults and fcc coherent twin boundaries can be differentiated between because they cannot be discriminated by a local coordination analysis alone.

3.6 Summary

This chapter briefly introduced molecular dynamics (MD) simulation, and despite its inherent limitations in some aspects, it is an effective way of capturing the main properties of nanocrystalline materials and it can provide insights into dislocation and GB processes at the atomic level that are not readily obtainable from experiments. The potential of EAM has many advantages in representing the atomic interplay in MD simulations. Different methods of visualisation were introduced and the common neighbour analysis (CNA) technique that determined an effective way of identifying defects in the structure and its evolution during these simulations will be used throughout this thesis. The dislocation extraction algorithm (DXA) is a powerful method of characterising the topological structure of dislocations in a crystalline material.

CHAPTER 4

Study on the Generalised Stacking Fault Energy of FCC Metals

The inter-atomic potential used in the MD simulation played a critical role in achieving accurate and reliable simulation results. To validate its potential, the generalised stacking fault (GSF) energies can be calculated by the MD simulation, including unstable stacking fault energy (γ_{usf}), stable stacking fault energy (γ_{sf}) and unstable twin fault energy (γ_{utf}), and then compared with the values determined from the experimental measurements. Furthermore, the study of stacking fault energy can result in a better understanding of the dislocation slip behaviour in nanocrystalline material. The effect of preloading stress (tensile stress or compressive stress) on the GSF curve and its possible influence on the deformation mechanisms in nanocrystalline material will be discussed in this chapter. The work in this chapter has been published previously in *Chinese Physics B* **24**, 088106.

4.1 Introduction

The mechanisms inherent in the plastic deformation of nanocrystalline materials have been studied extensively because of their proven superior functional and mechanical properties[146-149]. The plastic deformation of conventional coarse-grained material is mainly caused by dislocation nucleation and its motion inside the grains. However, nanoscale confinement severely restricts the operation of traditional dislocation generation mechanisms in nanocrystalline materials. Both experiment[150-152] and molecular dynamics (MD) simulations[63,64,153] have reported a deviation from traditional Hall-Petch constitutive behaviour. Many researches[1,154-156] indicated that the dislocation activities inside the grains decrease when the average grain size is less than 100 nm, whereas the mechanisms mediated by the grain boundary (GB) become

dominant. For example, a small grain size can result in heterogeneous nucleation and emission of dislocations from GBs[104,106,108]. Yamakov et al.[157] proposed a deformation mechanism map that describes the transition from dislocation-driven to GB-mediated plastic deformation based on the splitting distance between partial dislocations and the stacking fault energy γ_{sf}. Van Swygenhoven et al.[33] revealed that γ_{sf} alone cannot capture the important physics of the nucleation of partial dislocations from GBs, so a correct explanation of the nature of slip in nanocrystalline metal requires the generalised stacking fault energy (GSF) curve that was first introduced by Vitek[158,159], involving both stable stacking fault energy γ_{sf} and unstable stacking fault energy γ_{usf}. Since only a single point, known as the intrinsic (or stable) stacking fault γ_{sf} can be measured experimentally, many efforts to calculate the GSF curve are based on modelling and simulation methods such as density functional theory (DFT) and molecular dynamics (MD). However, most previous simulation studies in calculating the GSF were conducted in undeformed or stress free crystal structures that are far from the actual situation where the micro or nano-components can be deformed under a multiple stress state. The preloading strain or stress on crystal structures significantly influences the GSF curve. For instance, Zimmerman et al.[160] observed that the unrelaxed γ_{usf} value of 175 mJ/m^2 was reduced to 99 mJ/m^2 after bi-axially stretching the lattice by 4% when calculating the GSF curve of Cu. Tschopp and McDowell[161] used the MD simulations to investigate the influence of normal stress on the GSF curve in Cu and found that the compressive (tensile) normal stress increased (decreases) the unstable stacking fault energy γ_{usf}, while the stable stacking fault energy γ_{sf} changed in an opposite manner. Moreover, the effect of the stress state on the GSF curve was not only limited in the normal direction of the slip plane and lateral stress can also influence the value of the generalised stacking fault energy. Ogata and Yip.[162] used the DFT to calculate the stacking fault energies of Al and Cu to study their ideal shear strengths. Their results indicated that the hydrostatic pressure hada significant effect on the critical resolved shear stress on an atomic scale. Furthermore,

Tschopp et al.[25] and Spearot et al.[106,163] proposed that the stress required for dislocation nucleation depended on the Schmid stress component (resolved shear stress in the slip direction) and non-Schmid stress component (resolved normal stress and resolved shear stress perpendicular to the slip direction) acting on the {1 1 1} slip plane. Our previous work[164,165] also showed that the stress state can play an important role in dislocation nucleation and fracture of nanocrystalline Cu.

All of these studies showed that the GSF curve can be affected by the magnitude and direction of the applied stress. In a previous study, Rice[166] indicated that the unstable stacking fault energy γ_{usf} of the GSF curve was related to the energy barrier for dislocation nucleation. Tadmor and Hai[167,168] developed a criterion for the deformation mechanism of mechanical twinning, and also found that the 'twinning tendency' was closely related to the unstable twin fault energy γ_{utf} of the GSF curve. In this sense the energy barriers of dislocation nucleation and twinning formation in crystals can be influenced by the stress state of crystal lattice. The present work carried out MD simulations to investigate the effects of preloading stress with different directions and magnitudes on the GSF curves of three FCC metals (Cu, Al and Ni). The values of the unstable stacking fault energy (γ_{usf}), stable stacking fault energy (γ_{sf}) and unstable twin fault energy (γ_{utf}) were considered.

4.2 Simulation Methodology

In this study the EAM potentials developed by Mishin et al. for Cu[137], Al[138], and Ni[169] were used; indeed these potentials are widely used in MD simulations and they can fit a large set of experimental and first-principles data.

In order to calculate the GSF, a simulation cell was created with the [1 1 -2], [1 1 1] and [1 -1 0] directions along the X, Y, and Z axis, respectively. The simulation cell was divided into two blocks in the Z direction, as shown in Fig.4.1. A free boundary condition was applied in the Y direction, while periodic boundary conditions were used in the X and Z directions. Similar boundary conditions were adopted in Ref.[170] to study how vacancy defects affect the GSF energy of FCC

metals. The GSF curve was determined by rigidly displacing the upper block on the X-Z plane along the X direction while fixing the lower block and calculating the change in energy in the whole simulation model. When displacing the upper block along the X ([1 1 -2]) direction, the lateral motion of atoms was constrained.

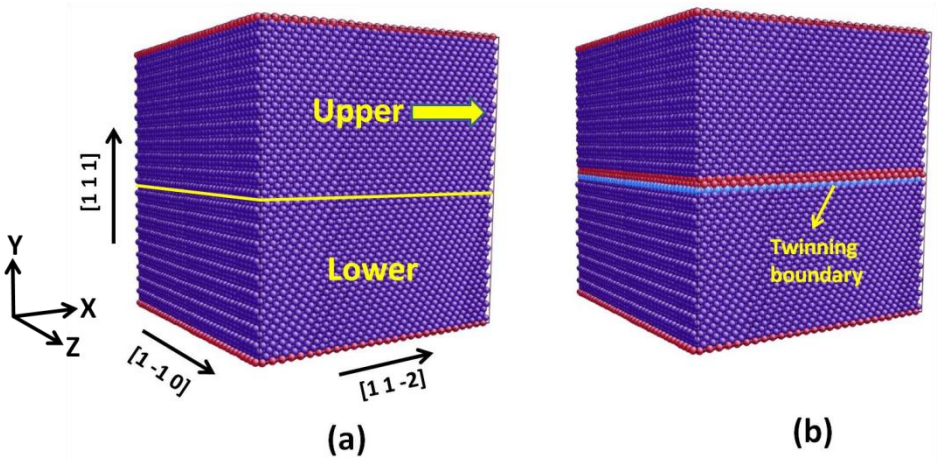

Figure 4.1 Simulation model for calculating the generalized stacking fault (GSF) energy curve. (a) The starting configuration with perfect fcc lattice. (b) A twinning boundary was formed after rigidly displacing the upper block on a (1 1 1) plane along a [1 1 -2] direction. Atoms with perfect fcc structure are coloured with dark blue, the red atoms represent the stacking fault and the free surface, the light blue atoms indicate the twin fault.

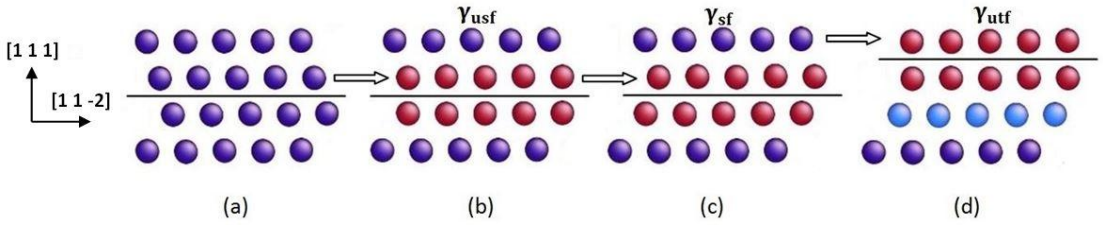

Figure 4.2 Schematic view of the atom positions when calculating the GSF curve. (a) perfect fcc crystal (b) unstable stacking fault (c) stable stacking fault, and (d) unstable twin fault. Configurations is viewed from the [1 -1 0] direction. Atoms with perfect fcc structure are coloured with dark blue, the red atoms represent the stacking fault and the light blue atoms represent the twin fault.

When calculating γ_{usf} and γ_{sf}, the starting configuration consisted of perfect FCC lattices[160,166] (see Fig.4.2(a)). Along the path, the system first passed through an energy barrier referred to as the unstable stacking fault energy γ_{usf}. The position of the displaced atoms is shown in Fig.4.2(b). Zimmerman et al.[160] indicated that the ideal displacement of the fcc lattice when γ_{usf} was reached equals one half of the

partial Burgers vector $a_0/\sqrt{6}$ (a_0 is the equilibrium fcc lattice parameter). The simulation cell stabilised when the displacement was $a_0/\sqrt{6}$, although the cell was not in its optimum equilibrium structure. The configuration in Fig.4.2(c) was known as the intrinsic stacking fault. Slip in the <1 1 2> direction was common because γ_{usf} was lowest in this direction. When calculating γ_{utf}, the starting configuration was a pre-existing stacking fault[138]. Specifically, γ_{utf} was calculated by shifting the block rigidly along the [1 1 -2] direction on the (1 1 1) plane that was one atomic layer above a stacking fault previously formed by shearing, as shown in Fig.4.2(d). Fig.4.1(b) shows the configuration of the simulation cell when a twinning boundary was formed after rigidly displacing the upper block.

To simulate the influence of the stress state on the GSF curve, the simulation cell was uniformly strained along one of the following directions: [111], [11-2] and [1-10] had a constant rate of 10^8/s at 1 K. The high strain rate was inherent in the simulations for computational efficiency and to have a desired amount of deformation within a given simulation time. An isobaric-isothermal (NPT) ensemble was used during the uniaxial tensile or compression. While the strain deformation took place in one direction, pressures in the lateral directions were kept at zero. The system stress was attained by calculating the pressure of the entire system of atoms, and the pressure was computed using the formula:

$$P_{ij} = \frac{1}{V}\left[\sum_k^N m_k v_{k_i} v_{k_j} + \sum_k^N r_{k_i} f_{k_j}\right], (i, j = x, y, z)$$

where the first term uses the components of the kinetic energy tensor and the second term uses the components of the virial tensor, N is the total number of atoms in the simulation model, V is the simulation model volume, and r and f are the distance vector and the force vector respectively. System strain was derived from the positions of the periodic boundaries.

4.3 Results and Discussion

Fig.4.3 shows the stress-strain responses of the three fcc metals (Cu, Al and Ni) investigated under uniaxial tension and compression along the [1 1 1], [1 1 -2], and [1 -1 0] directions. The stresses shown in Fig.4.3 are the magnitudes of the tensile stress and compressive stress. Obviously, due to material anisotropy, the elastic modulus was slightly different for different loading directions, whereas the tension-compression asymmetries in elastic response were evident in all directions. The elastic modulus of compression was generally higher than the tension, and this trend of asymmetry was more obvious for Al than for the other two metals. The elastic modulus calculated from the initial slope of the MD simulations is listed in Table 4.1. The nonlinear stress-strain response shown in Fig.4.3 was due to non-negligible lattice rotation during elastic deformation at high strain[161]. There was also a nonlinear elastic effect for Al in the [1 -1 0] direction.

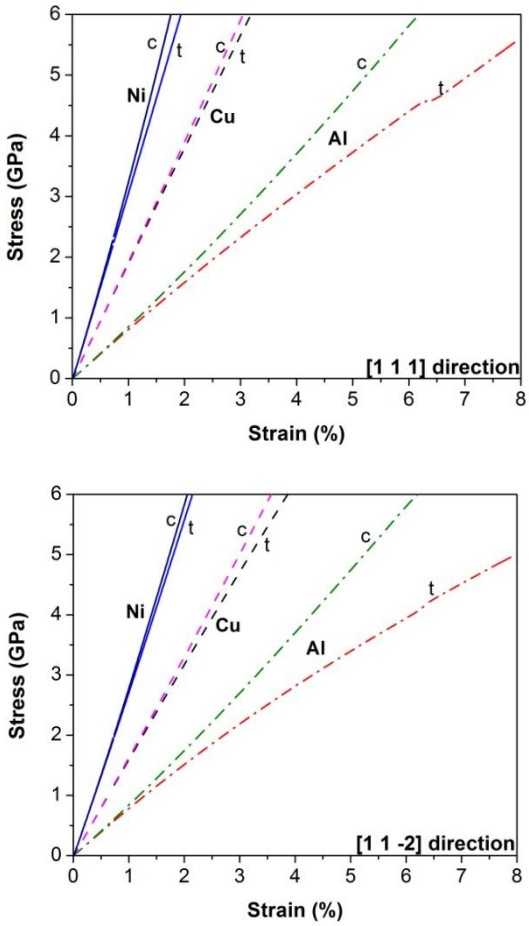

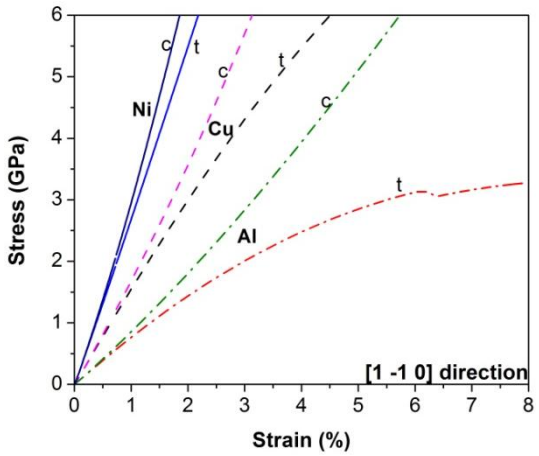

Figure 4.3 Stress-strain curves for uniaxial tension and compression of Cu, Al and Ni along (a) [1 1 1] direction, (b) [1 1 -2] direction, and (c) [1 -1 0] direction. The negative values of compressive stress are plotted. Letter **t** means uniaxial tension while **c** refers to uniaxial compression.

Table 4.1 Elastic modulus of Cu, Ni and Al under tension and compression.

		Elastic Modulus (GPa)		
Element	**Preloading**	$\mathbf{E_{[1\,1\,1]}}$	$\mathbf{E_{[1\,1\,-2]}}$	$\mathbf{E_{[1\,-1\,0]}}$
Cu	Tension	189.8	159.1	154.4
	Compression	192.3	162.0	167.9
Ni	Tension	305.4	270.4	268.2
	Compression	323.4	277.3	294.8
Al	Tension	80.7	78.0	76.1
	Compression	84.9	83.7	85.3

The influence of the preloading stress on the GSF curve of Cu is shown in Fig.4.4. In a normal [1 1 1] direction and lateral [1 -1 0] direction, the tensile (compressive) stress reduces (increases) the unstable stacking fault energy (γ_{usf}) and the unstable twin fault energy (γ_{utf}). The larger the preloading stress, the larger the decreases (increases) in the value, but the stable stacking fault energy (γ_{sf}) changes in an opposite manner in the [1 1 1] direction. The value of γ_{sf} increases under preloading tensile stress and decreases under compressive stress, and this was more noticeable at higher compressive stress. For example, γ_{sf} increased by 4.9% at a tensile stress of 5 GPa and decreased by 17.5% at a compressive stress of 5 GPa. Unlike those cases in

the [1 1 1] and [1 -1 0] directions, the tensile stress increased the values of γ_{usf} and γ_{utf} in the [1 1 -2] direction while the compressive stress reduced the values. Note that under preloading stresses in all directions, the values of γ_{usf}, γ_{sf} and γ_{utf} may reach, before or after their ideal displacement, a value that can be expected from geometric considerations; ideally, in the figures $\delta_{sf}=\frac{1}{2}a_0/\sqrt{6}$, $\delta_{usf}=a_0/\sqrt{6}$, and $\delta_{utf}=\frac{3}{2}a_0/\sqrt{6}$, where a_0 is the equilibrium FCC lattice parameter. This deviation was mainly due to pre-strain changes in the inter-atomic distance of the equilibrium structure.

Fig.4.5 shows the effects of the stress state on the GSF curve of Ni where the influence of tensile and compressive stresses on the GSF curve of Ni in all directions were generally similar to the stress effect of Cu. In the [1 1 1] and [1 -1 0] directions, γ_{usf} and γ_{utf} decreased (increased) as the magnitude of the tensile (compressive) stress increased, while the tensile and compressive stress effects were in an opposite way (in the [1 1 -2] direction). The influence of the preloading stress on the GSF curve of Ni was not as obvious as that of Cu, and the deviation of the ideal displacement when each value was reached was less than Cu. This occurred because Ni had a higher elastic modulus than Cu (see Fig.4.3), i.e., the lattice deformation and change in the inter-atomic distance were less in Ni than in Cu at the same applied stress.

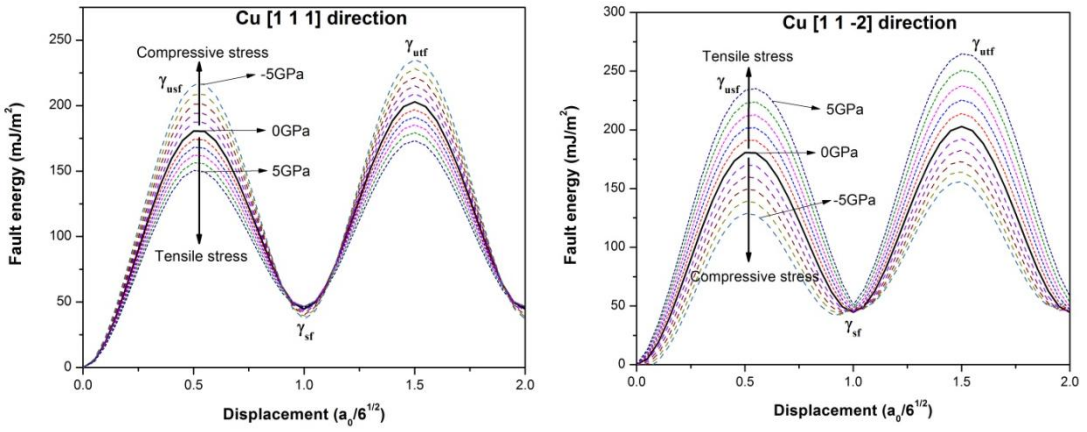

(a) (b)

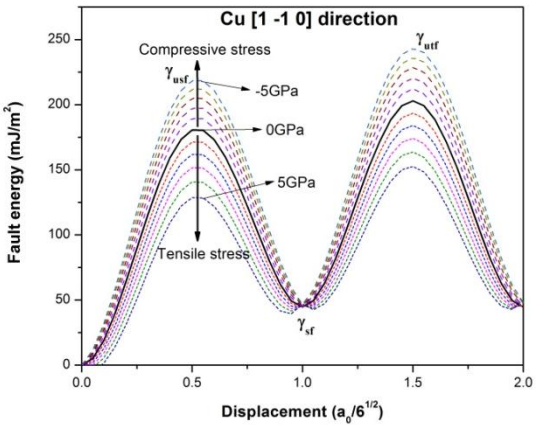

(c)

Figure 4.4 Influences of the stress state on the generalized stacking fault energy curve in Cu. The tensile and compressive stress are applied along (a) [1 1 1] direction, (b) [1 1 -2] direction, and (c) [1 -1 0] direction.

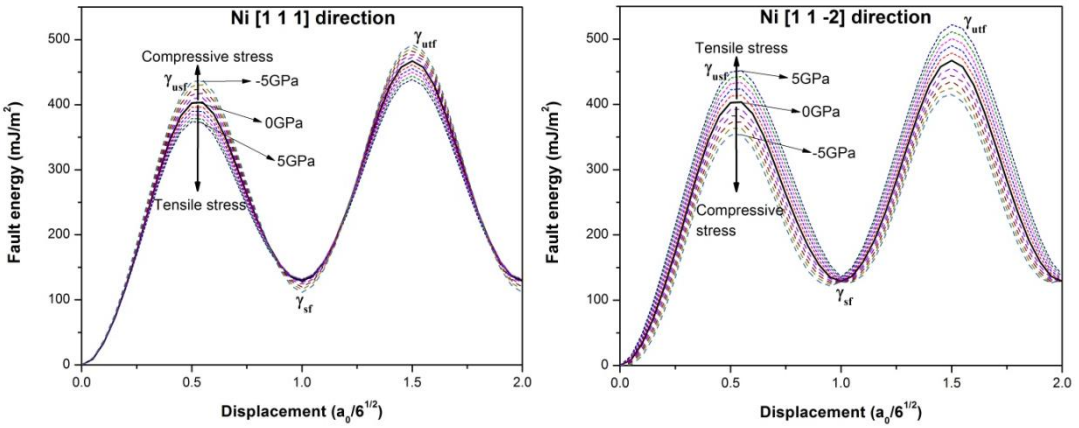

(a) (b)

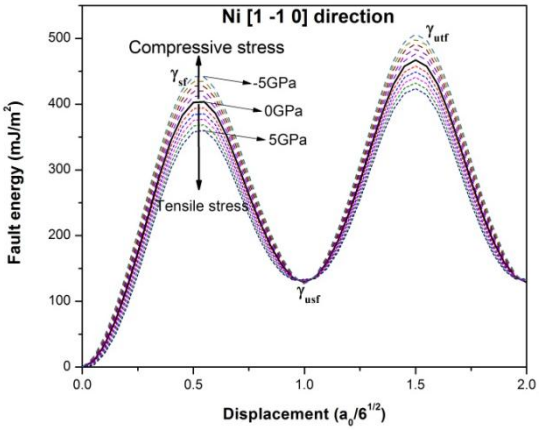

(c)

Figure 4.5 Influence of the stress state on the generalized stacking fault energy curve in Ni. The tensile and compressive stress was applied along (a) [1 1 1] direction, (b) [1 1 -2] direction, and (c) [1 -1 0] direction.

The preloading stress of Cu and Ni had an obvious influence on the values of γ_{usf} and γ_{utf}., while their influence on the value of γ_{sf} was limited. However, this was not the case for Al where the preloading stress can greatly influence the three values in all directions, especially in the normal [1 1 1] direction. Fig.4.6 shows how the tensile and compressive stress influenced the GSF curve of Al. In Fig.4.6(a), the values of γ_{usf}, γ_{sf} and γ_{utf} increased by 41.2%, 59.8% and 43.3% at 5 GPa compressive stress and dropped sharply by 53.5%, 82.7% and 59.4% respectively at 5 GPa tensile stress. Other differences of Al from Cu and Ni in the GSF curve were observed in [1 -1 0] direction. In Fig.4.4(c) and Fig.4.5(c), γ_{usf} and γ_{utf} decreased in tension and increased in compression, whereas in Fig.6(c), this effect acted in an opposite manner. Moreover, the applied tension stress played a small role in the values of γ_{usf} and γ_{utf} in [1 -1 0] direction, which experienced a 1.1% and 2.3% increase respectively at 3 GPa tensile stress. Moreover, the values of different fault energies can change faster at a higher tensile stress in the [1 1 -2] and [1 -1 0] directions due to the nonlinear elastic effect in these directions of Al.

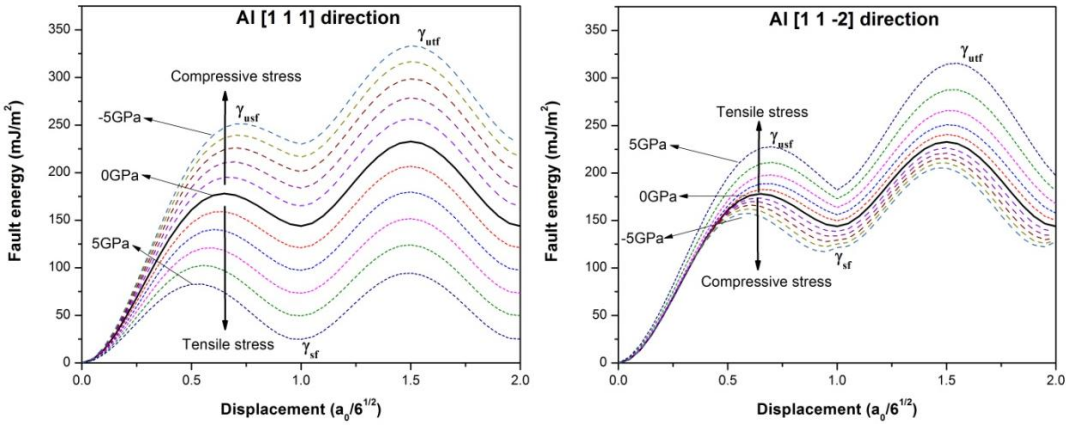

(a) (b)

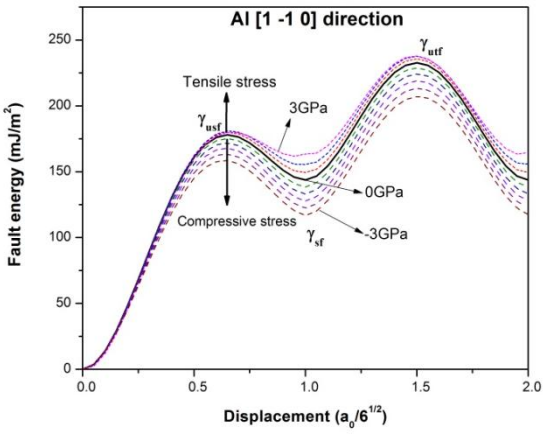

(c)

Figure 4.6 Influences of the stress state on the generalized stacking fault energy curve in Al. The tensile and compressive stress are applied along (a) [1 1 1] direction, (b) [1 1 -2] direction, and (c) [1 -1 0] direction.

In previously published studies, MD simulations have revealed that a small gain size in nanocrystalline material can result in a heterogeneous nucleation and emission of dislocations from the GBs. This deformation mechanism has been confirmed by recent in situ transmission electron microscopic experiments[11,12]. These experiments also showed that stacking faults and deformation twins can be formed through the emission of partial dislocations from the GBs. Van Swygenhoven et al.[33] indicated that every aspect of the GSF curve should be incorporated to understand the slip activities observed in simulations, while the deformation cannot be explained by means of the absolute value of γ_{sf} alone, as suggested by Yamakov et al.[157]. Specifically, whether the movements of extended partial dislocations or full dislocations dominates the deformation mechanism in a simulation, they can be explained in terms of the ratio γ_{sf}/γ_{usf}. A γ_{sf}/γ_{usf} value closer to unity indicates that full dislocations can be nucleated in FCC metals.

Fig.4.7 shows the variations of the γ_{sf}/γ_{usf} ratio as functions of the preloading stress in different directions. For Cu and Ni, the applied tensile stress increased the value of γ_{sf}/γ_{usf} while the compressive stress decreased this value in the [1 1 1] and [1 -1 0] directions. In the [1 1 -2] direction, this effect acts in an opposite manner. Overall, the influences of applied stress on the value of γ_{sf}/γ_{usf} for Cu and Ni were

not obvious because it was at a relatively low level (ranging from 0.17 to 0.33 for Cu and 0.26 to 0.37 for Ni), which means the nucleation of partial dislocation and its propagation in the grain were still the dominant mechanism in nanocrystalline Cu and Ni, even under a high stress concentration.

With Al, the γ_{sf}/γ_{usf} ratio decreased significantly with the preloading tensile stress in the [1 1 1] direction (see Fig.4.7(a)). At a tensile stress of 5 GPa, the γ_{sf}/γ_{usf} ratio dropped to the same level as for Cu and Ni. The sharp decrease of γ_{sf}/γ_{usf} indicated that the nucleation of full dislocation (with the trailing partial dislocation) observed in the simulations of Al[33,104] may be restricted under the tensile stress applied normal to the slip plane, i.e., the extended partial dislocation may dominate the deformation mechanisms, which was the same as Cu and Ni. Moreover, the compressive stress applied in the [1 1 1] direction and tensile stress in the [1 -1 0] direction increased the γ_{sf}/γ_{usf} ratio to a level closer to unity, as shown in Fig.4.7(a) and Fig.7(c). This means that the trailing partial dislocations can nucleate more easily and the separation between the leading and trailing partials was shortened. The effect of the stress in the [1 1 -2] direction on the ratio γ_{sf}/γ_{usf} was not obvious and ranged from 0.74 to 0.83.

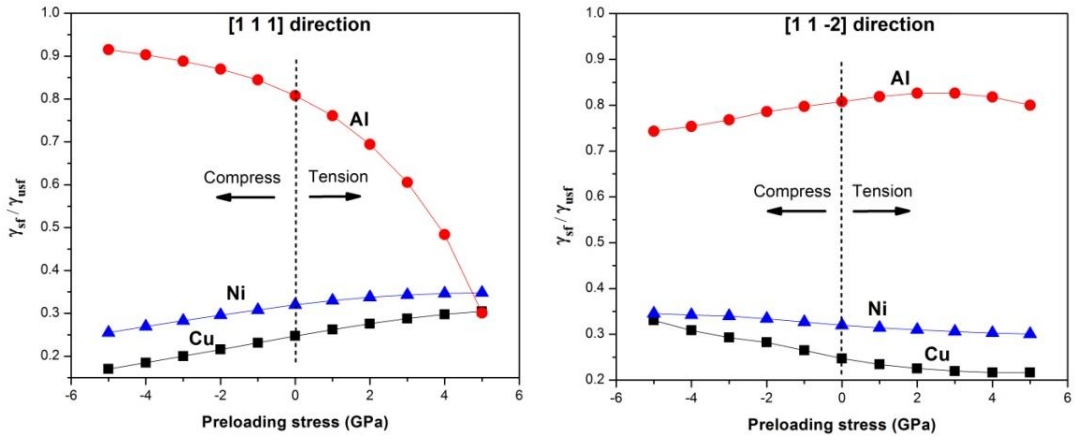

(a) (b)

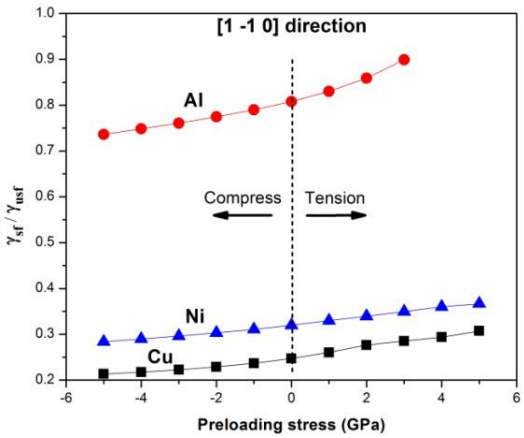

(c)

Figure 4.7 Variations of ratio of stable stacking fault energy to unstable stacking fault energy (γ_{sf}/γ_{usf}) with preloading stress along (a) [1 1 1] direction, (b) [1 1 -2] direction, and (c) [1 -1 0] direction.

As reported previously [163,164], the twinning nucleation in a simulation depended on the $\gamma_{utf}/\gamma_{usf}$ ratio, where γ_{utf} relates to the energy barrier for twinning formation and γ_{usf} was associated with the barrier for a full dislocation nucleation. This ratio controls the competition between the two possible mechanisms. The values of γ_{utf} was larger than γ_{usf} in all of our simulations of the GSF curve, which was consistent with the case discussed by Van Swygenhoven et al.[33]. This can explain why mechanical twinning was not seen as the dominant mechanism in most MD simulations of nanocrystalline samples with defect-free grains because it must overcome the larger energy barrier. The influence of the stress applied onto the $\gamma_{utf}/\gamma_{usf}$ ratio is shown in Fig.4.8. Here the value of $\gamma_{utf}/\gamma_{usf}$ for Cu was generally at its lowest level in all the three tested metals, and this value was closer to unity when the compressive stress was applied normal to the slip plane (see Fig.4.8(a)). This means that the barriers for twinning formation and for dislocation nucleation were comparable and twinning was easier to grow in Cu under certain conditions. For example, Lu et al.[171] found that the nanoscale growth twins in the Cu sample could effectively increase the strength of the material. The tensile stress applied in the [1 1 1] and [1 -1 0] directions and compressive stress in the [1 1-2] direction increase the value of $\gamma_{utf}/\gamma_{usf}$ for Cu and thus increased the difficulty in twinning formation.

With Ni, the stress on the $\gamma_{utf}/\gamma_{usf}$ ratio was insignificant in all directions, with the ratios ranging from 1.13 to 1.18.

The $\gamma_{utf}/\gamma_{usf}$ of Al was much higher than Cu and Ni, which indicated that twinning was more difficult to form in Al. However, the tensile stress in the [1 1 1] direction can sharply reduce the value from 1.31 in stress free condition to 1.14 at 5 GPa preloading stress. This sharp decrease of $\gamma_{utf}/\gamma_{usf}$ means that twinning may be seen as a deformation mechanism in high stress concentrations, especially when the tensile stress has a high component normal to the slip plane. For example, a twinning deformation mechanism was seen in the experiments[12,172] where the twin boundary nucleation became favourable over full dislocation nucleation when a high shear stress was provided (for example, during ball milling and high-pressure torsion). The tensile stresses in the [1 1 -2] and [1 -1 0] direction increased the value of $\gamma_{utf}/\gamma_{usf}$ for Al and thus can increase the difficulty in twinning formation.

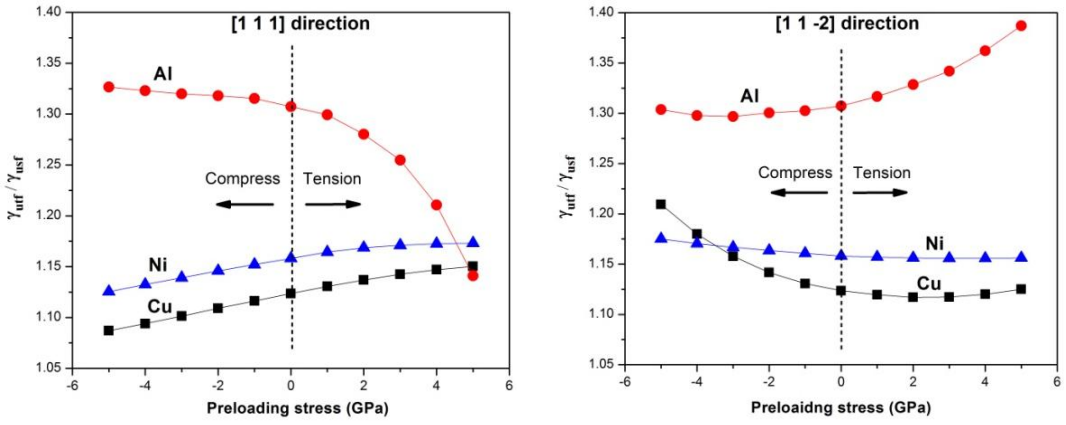

(a) (b)

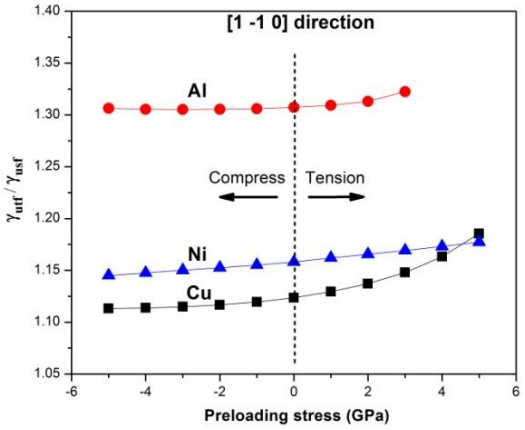

(c)

Figure 4.8 Variations of ratio of unstable twin fault energy to unstable stacking fault energy ($\gamma_{utf}/\gamma_{usf}$) with preloading stress along (a) [1 1 1] direction, (b) [1 1 -2] direction, and (c) [1 -1 0] direction.

4.4 Summary

Molecular dynamics (MD) simulations were carried out to investigate the effects of stress on generalised stacking fault (GSF) energy for three FCC metals (Cu, Al and Ni). The simulation cell was deformed by uniaxial tension or compression in each of the [1 1 1], [1 1 -2] and [1 -1 0] directions before shifting the lattice to calculate the GSF curve. These simulations showed that the unstable stacking fault energy (γ_{usf}), stable stacking fault energy (γ_{sf}), and unstable twin fault energy (γ_{utf}) of the three metals could change with the preloaded tensile or compressive stress in different directions. The γ_{sf}/γ_{usf} ratio, which is related to the energy barrier of the full dislocation nucleation, and the $\gamma_{utf}/\gamma_{usf}$ ratio, which is related to the energy barrier of twinning formation, are dependent on the preloading stress. The present study revealed that the stress state can change the energy barriers of the nucleation of defects in a crystal lattice, and thereby play an important role in the deformation mechanism of nanocrystalline material.

CHAPTER 5

Dislocation Nucleation in Copper Bicrystal with <110> Symmetric Tilt Grain Boundary

For nanocrystalline materials with a small grain size, the conventional plastic deformation mechanisms dominated by dislocation processes become difficult and the GB mediated deformation mechanisms become increasingly important. One of the mechanisms that can play a profound role in the strength and plasticity of metallic polycrystalline materials is the heterogeneous nucleation and emission of dislocations from the GB. In this chapter molecular dynamics simulations were carried out to study the dislocation nucleation in copper bicrystals with various <1 1 0> tilt GBs covering a wide range of misorientation angles. The work of this chapter has been published in *Materials Research Express* **2**, 035009.

5.1 Introduction

Grain boundary (GB) strengthening at low temperatures is a common phenomenon in polycrystalline materials. One of the best known theories, as described by the Hall-Petch equation, predicts an increase of flow stress with decreasing grain size, but as the grain sizes are reduced to nanometer scale and the percentage of GB atoms correspondingly increases, the traditional view of dislocation-driven plasticity in nanocrystalline materials must be reconsidered[156]. Experimental measurements[173,174] have shown various deviations from the Hall-Petch equations as the grain sizes reached nanometer scale. A lot of prior research work conducted by experiments[13,131,152,175] and computational simulations[5,64,130,153,176,177] revealed that below a certain critical grain size, in the order of 10 nm, dislocation nucleation inside the grain becomes limited and the GB-mediated processes (*e.g.*, GB sliding, GB migration and grain rotation) becomes the dominant deformation mechanisms[130,177].

While these deformation mechanisms at larger scales have been studied for decades, an atomic level understanding of the GB accommodation mechanism is limited.

As the grain size decreases, one of the mechanisms playing a vital role in the deformation of nanocrystalline materials is the heterogeneous nucleation and emission of dislocations from the GBs. This deformation mechanism has been observed in many simulation works[102-104,106,108,164], and was also confirmed by in situ transmission electron microscopy (TEM) experiments[11,12]. However, experiments at a nanoscale can be very time consuming and costly, and TEM requires samples with a thickness comparable to the grain size, which may induce the structure to relax and thus change the GB structure[156]. Fortunately, molecular dynamics (MD) simulations with a carefully designed model system can be used to investigate the GB structures and the dislocation nucleation mechanisms of nanocrystalline materials.

Previously published atomistic studies have shown that differences in the mechanical behaviour and the underlying deformation mechanisms commonly result from variations in the grain boundary structure[178]. However, details of the dislocation nucleation mechanisms at the grain boundary at the atomic level, and the correlation of GB structures and GB properties with these mechanisms are still not fully understood. Randle[179] showed that the <1 1 0> tilt GBs are a preferred interface configuration and of importance for FCC materials. Therefore this chapter concentrates on the dislocation nucleation from the <1 1 0> tilt GBs and investigates the underlying atomistic mechanisms.

5.2 Simulation Methodology

5.2.1 Simulation model

The embedded-atom method (EAM) potential developed by Mishin et al. for Cu[137] was used because it can fit a large set of experimental and first principles data. In this study a bicrystal model was created by constructing two separate grains (grain-A and grain-B as shown in Fig.5.1(a)) with different crystallographic orientations, and

joined them together along the Y axis. All the Cu bicrystal models used in this study had a symmetric tilt misorientation about $[1\ \bar{1}\ 0]$ in the Z direction, but periodic boundary conditions were applied in all directions (X, Y and Z axis). It must be noted that the periodic boundary condition in the Y direction introduced a second boundary plane into the model. A schematic of the bicrystal simulation model is shown in Fig.5.1(a), and a typical constructed simulation model is shown in Fig.5.1(b). GBs with different rotation angles (θ) investigated in this study were listed in Table.1.

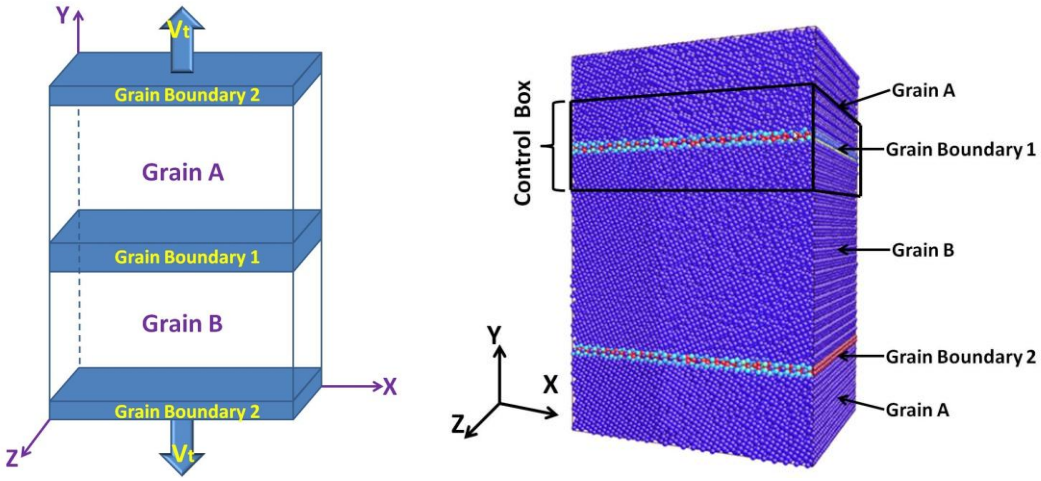

(a) (b)

Figure 5.1 (a) Schematic of the bicrystal model and the tension deformation applied onto the model. The grain boundary was created by a symmetric tilt rotation of grain-A and grain-B around the $[1\ \bar{1}\ 0]$ direction (z axis). (b) A typical simulation model constructed by LAMMPS and visualized in Atomeye. The atoms were coloured according to their potential energy; blue atoms have a perfect fcc structure while the atoms with different colours defined the grain boundary plane.

The possible influence of the bicrystal model scale on the simulation result are fully considered in this work. Specifically, the width of the interface in X direction is long enough to produce a serials of interface periods from which the boundary structures can be generally predicted. The length of the bicrystal model in Y direction is considered to avoid the interaction of the two boundary planes which can affect the nucleation stress and the character of the nucleated partial dislocation. Furthermore, if the thickness of the bicrystal model in Z direction is reduced to a few atomic planes, dislocation will be restricted to occur on certain slip system. In this study, each

bicrystal model was approximately 162Å×290Å×162Å (X×Y×Z), and the total number of atoms in each simulation model was approximately 6.5×10^5. Previous work[106] showed that this cell size is large enough to avoid image effects from the periodic boundaries on the mechanisms associated with three dimensional dislocation nucleation.

5.2.2 Simulation details

The equilibrium GB structures were obtained by molecular statics simulations where a standard conjugate gradient method was used to determine the minimum energy configurations. A number of initial "starting positions" of grain-A and grain-B were tested to find the best GB structures[180-182] with the lowest system energies. It is worth noting that for each initial configuration, the size of the model had to be adjusted to construct identical atomic structures of the two boundary planes. This operation was necessary to ensure they had the same equilibrium structures after their energy was minimised, otherwise different GB structures may exist in a bicrystal model. After attaining its minimum energy configuration the simulation model was equilibrated using MD in the isobaric-isothermal (NPT) ensemble at a pressure of 0 bar and a temperature of 10 K for 20 ps.

During dynamic loading, uniaxial tension at a constant rate of 5×10^8/s was applied perpendicular to the boundary plane (along the Y direction), while pressure in the lateral directions was kept at zero. An isobaric-isothermal (NPT) ensemble was used during the dynamic deformation. The simulation temperature was maintained at 10 K and an integration time step of 1 fs was used throughout the MD simulations. The fluctuating internal energy of the monitored atoms due to entropy was found to be very small (in the order of 0.0011eV) at this temperature[89], and this low temperature environment actually facilitated our visualisation and analysis of the results. Our focus was on the nucleation mechanisms from the diversity of GBs presented in this study, so the influence of the strain rate and temperature on the results will not be discussed. The visualisation tools Atomeye[140] and Ovito[141] were used to illustrate the

bicrystal models. The common neighbour analysis (CNA) technique[63] was used to identify the structural defects and their evolution during the simulations. The dislocation extraction algorithm (DXA)[145,183] was used to compute the Burgers vectors of the nucleated dislocations from the boundary plane.

Table 5.1 Summary information of different [1 $\bar{1}$ 0] symmetric tilt GBs in Cu bicrystal.

GB plane Σ (h k l)	**Misorientation angle θ (°)**	**GB energy γ_{GB} (mJ/m^2)**	**Tensile strength σ (GPa)**	**Nucleation barrier $\gamma_{barrier}$ (mJ/m$^{3)}$**
Σ19{1 1 6}	26.5 °	788	6.45 / 8.8*	2.23
Σ9{1 1 4}	38.9 °	684	8.94 / 9.41	4.13
Σ139{3 3 11}	42.2 °	643	7.83 / 10.14	3.12
Σ11{1 1 3}	50.5 °	319	9.55 / 10.1	4.85
Σ33{2 2 5}	58.9 °	581	7.97 / 11.16	2.8
Σ3{1 1 2}	70.5 °	591	9.47 / 12.41	4.7
Σ17{2 2 3}	86.6 °	660	9.86 / 14.36	3.35
Σ17{3 3 4}	93.4 °	644	11.57 / 14.88	5.05
Σ3{1 1 1}	109.5 °	26	17 / 17	—
Σ171{11 11 10}	114.5 °	296	1.6 / 13.9	0.1
Σ11{3 3 2}	129.5 °	535	2.57 / 13.48	0.45
Σ291{11 11 7}	131.5 °	810	2.86 / 12.77	0.33
Σ9{2 2 1}	141.1 °	833	4.07 / 11.78	0.75
Σ19{3 3 1}	153.5 °	856	3.87 / 8.82	0.79
Σ73{6 6 1}	166.6 °	681	3.32 / 6.59	0.65

* The maximum tensile stress of single crystal are listed for comparison.

5.2.3 GB Energy calculation

To calculate the GB energy and measure the energy barrier for dislocation nucleation from a GB, a control box was placed along the entire grain boundary[89] (see Fig.5.1(b)). The energy associated with the GB (γ_{GB}) was calculated by Equation (5-1),

$$\gamma_{GB} = \frac{E_{box\_m} - N \cdot E_{atom}}{A} \quad (5\text{-}1)$$

where E_{box_m} is the potential energy of the control box within the bicrystal model after an energy minimisation procedure, E_{atom} is the potential energy of a single atom in the perfect Cu lattice (-3.54eV), N is the total number of atoms contained in the model, and A is the area of the GB plane ($A=L_x*L_z$). The energy of dislocation nucleation barrier was calculated by Equation (5-2),

$$\gamma_{\text{barrier}} = \frac{\sum_i^n E_{\text{box\_t}}^i - E_{\text{box\_e}}}{V} \quad (5\text{-}2)$$

where E_{box_e} is the energy of the control box after the system was equilibrated at 10 K. For each atom i within the control box, the real time energy during dynamic tension $E_{box\_t}^i$ was measured at a certain interval timestep. V is the volume of the control box ($V=A*L_{box\_y}$), where L_{box_y} is the height of the control box.

Fig.5.2 gives the calculated results of Σ9(1 1 4) GB and Σ19(3 3 1) GB by using control boxes with three different sizes L_{box_y} (L_{box_y} = 30 Å, 60 Å and 200 Å). The figures show the same trend and the very small deviations of the peak values. This indicates that the size of the control box had a small influence on the simulation results. In this work L_{box_y} was set to 60 Å for all the calculations, and the results are listed in Table-5.1

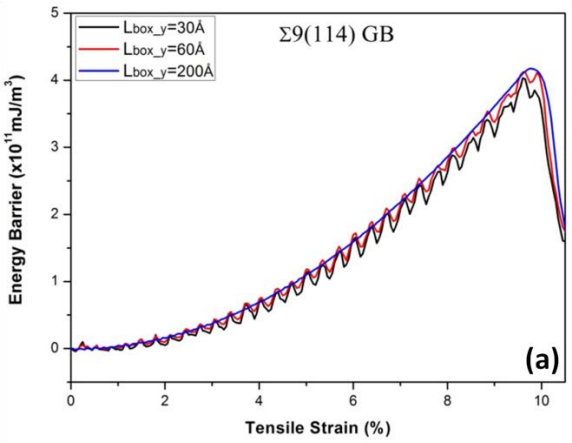

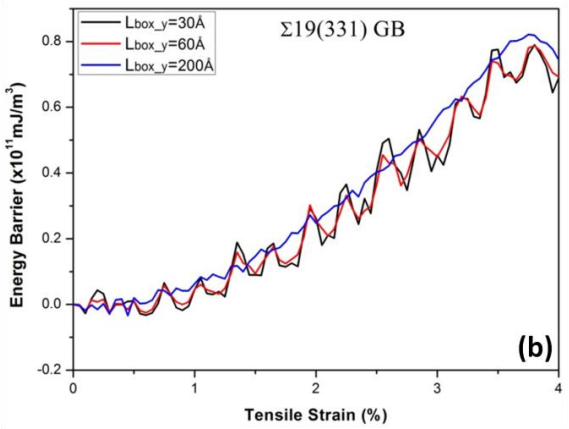

Figure 5.2 The energy barrier of dislocation nucleation from (a) Σ9(1 1 4) GB and (b) Σ19(3 3 1) GB calculated by Equation (5-2). Different size of control box with L_{box_y}= 30 Å, 60 Å and 200 Å were tested.

5.3 Simulation Results

5.3.1 GB structure and energy

The GBs investigated in this study are listed in Table-5.1. A detailed view of the Cu <1 1 0> tilt GB structures with misorientation angles $0° < \theta < 180°$ after energy minimisation at 0K are shown in Fig.5.3 and Fig.5.4. Due to the symmetry of the fcc lattice, the misorientation angles varying from 0° to 180° covers all the distinct boundary structures of the <1 1 0> tilt GBs. The viewing direction is along the [1 $\bar{1}$ 0] crystallographic direction (Z axis) and the positions of the atoms were projected onto the X-Y plane for clarity. The structural units proposed by Rittner and Seidman[180] are used to illustrate the boundary structures. The white circles and black circles in the figures represent atoms on two consecutive (0 0 2) atomic plane along the Z direction, respectively.

Most boundary structures can generally be characterised by the structure unit model, as outlined by the solid lines in Fig.5.3 and Fig.5.4. Here, some GB structures are not symmetrical about the boundary plane. Of all the <1 1 0> tilt GBs, three boundary structures were found to be special; Σ11(1 1 3) θ=50.5° GB, Σ3(1 1 1) θ=109.5° GB and Σ9(2 2 1) θ=141.1° GB, which were composed entirely of the C, D, and E structural units respectively. These units were considered to be the preferred structural unit models to represent the GBs, while other boundaries consisted of two

or more different types of the preferred structural units. For example, the Σ9(1 1 4) GB in Fig.5.3(a) contains two C and one D structural units for each boundary period and the Σ11(3 3 2) GB in Fig.5.4(b) contains one E and one D structural units per boundary period. Note that three boundaries in Fig.5.3(d)-(f) exhibited a dissociated GB structure that was caused by the asymmetric dissociation of secondary GB dislocations with Burgers vector of the Shockley partial type[180]. This structure lowered the energy of the atomic arrangement in the boundary plane but it also created an extra stacking fault area inside the grain. To accommodate the intrinsic stacking fault facets, the C units were tilted downwards relative to the positive X-axis, while the D unit lies at the termination of an intrinsic stacking fault that extends from the bicrystal interface.

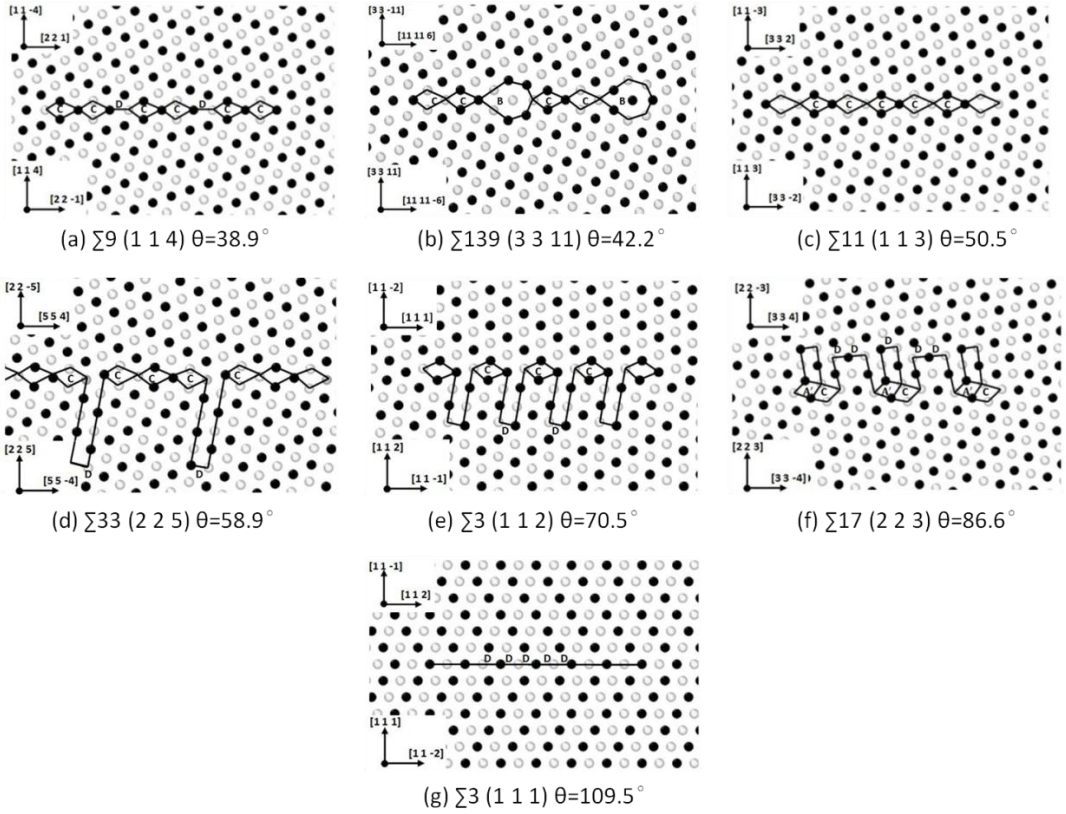

Figure 5.3 The equilibrium structures of the Cu <1 1 0> tilt GB structures with misorientation angles θ<109.5 °obtained by the energy minimization procedure and subsequent MD relaxation at 10 K. The structures are viewed along the [1 $\bar{1}$ 0] tilt axis. Atoms on consecutive (0 0 2) planes are shown as black and white. The GB normal and period vectors are given for grain-A and grain-B on the left hand side of each structure. The structural units at each boundary plane are outlined by the solid line.

Fig.5.4 shows six GB structures within a misorientation range of θ>109.5 °, all of which contain the E structural units. Specifically, the GBs with θ<141.1 ° contain a combination of E and D units, while the GBs with θ>141.1 ° contain a combination of E and A units. Notice that the A′ and E′ units marked in Fig.5.4(f) contain topologically identical atoms as A and E units, but they differ in their direction. The <1 1 0> tilt GB structures presented here agree with the structures reported in the published work[180,109]. Some of the GB structures observed in this study are comparable with the HRTEM observations of FCC metals (Al[184,185], Ni[186,187] and Au[188]).

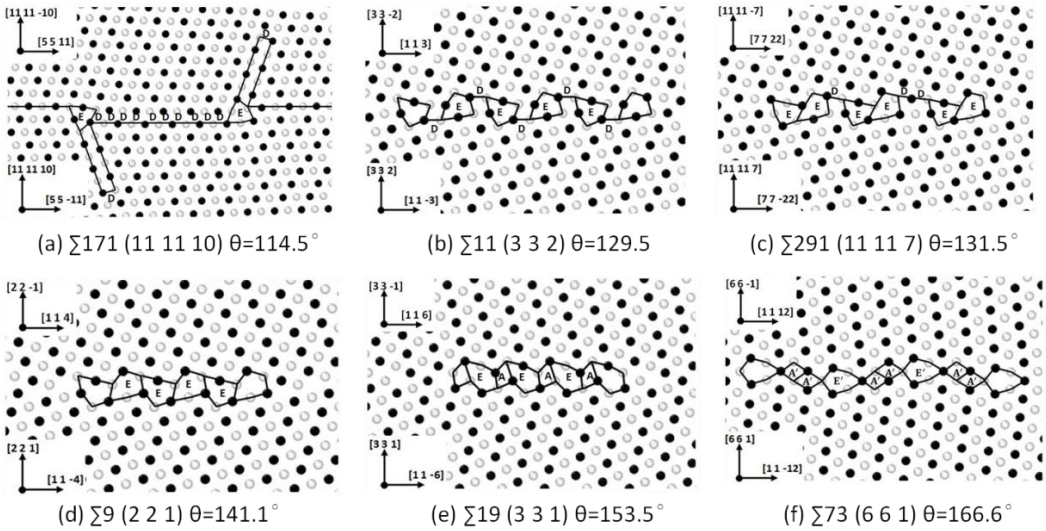

Figure 5.4 The equilibrium structures of the Cu <1 1 0> tilt GB structures with misorientation angles θ>109.5 °obtained by the energy minimization procedure and subsequent MD relaxation at 10 K.

The GB energy as a function of the GB misorientation angle is plotted in Fig.5.5, and it shows that this curve contains local minimums and cusps corresponding to the misorientation angles of 50.5 °and 109.5. At misorientation angles of 0 °and 180 °, the atoms are in perfect lattice configuration, giving a GB energy of zero. At misorientation angles of 50.5 °and 109.5 °, the GBs are the special Σ11(1 1 3) GB and Σ3(1 1 1) GB, and consist entirely of the preferred structural units. Therefore, low GB energies were observed at these misorientation angles. The misorientation angle of

109.5 °corresponded to the coherent twin boundary.

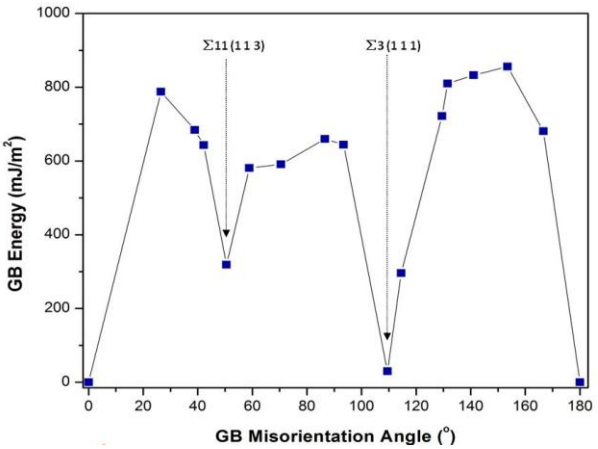

Figure 5.5 The energy of Cu <1 1 0> tilt GBs shown as a function of the misorientation angle at 0 K after energy minimization procedure.

5.3.2 Tensile response

After the GB equilibrium structures were achieved, the simulation models were deformed under a uniaxial tensile loading at 10 K. The stress-strain curves are shown in Fig.5.6. Figs.5.6(a) and 5.6(b) correspond to the GB structures with misorientation angles of θ<109.5 ° and θ>109.5 °, respectively. Here, the elastic stiffness of the bicrystal models increased as the misorientation angle increased within θ<109.5 °, whereas the trend was opposite for θ>109.5 °.

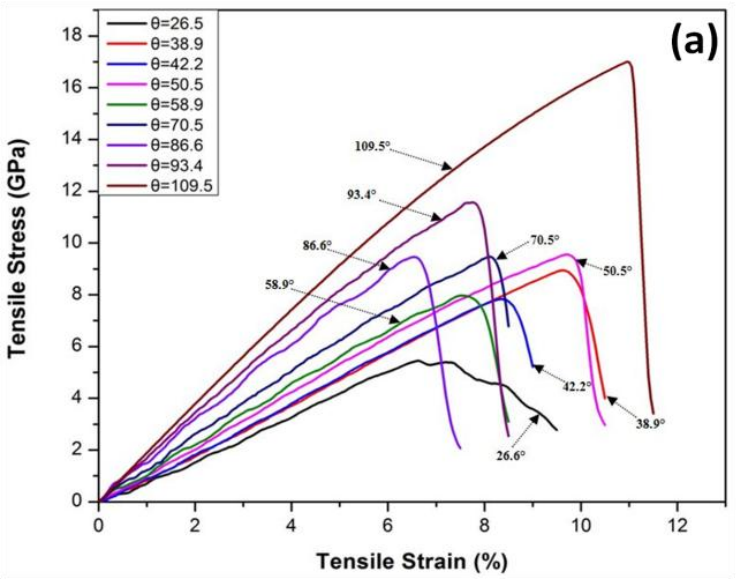

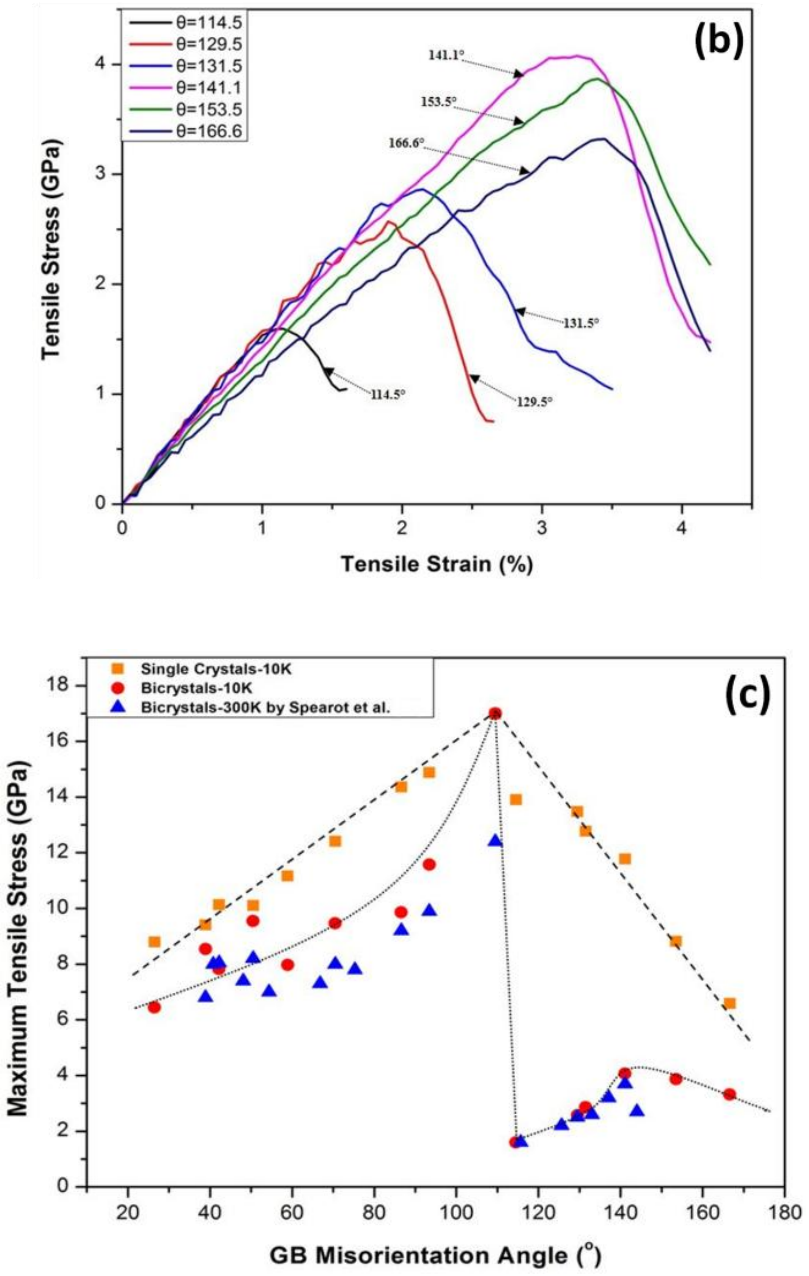

Figure 5.6 Stress-strain curves of Cu <1 1 0> tilt GBs with misorientation angles (a) θ<109.5 °and (b) θ>109.5 °at 10 K. (c) Maximum tensile stress as a function of misorientation angle. The values of single crystals were calculated and plotted for comparison. The simulation results from Spearot et al.[42] are also listed for comparison.

The maximum tensile stresses were collected from the curves in Fig. 5.6(a) and 5.6(b) and are listed in Table 5.1. Fig. 5.6(c) plots the maximum tensile stress as a function of the GB misorientation angle. In order to analyse the role of lattice orientation on the maximum tensile stress, the results of single crystals were also plotted in the figure for comparison. Here, the maximum stress of the Cu <1 1 0>

single crystals generally increased as the misorientation angle increased up to 109.5 °, and then it gradually decreased with the misorientation angle as the misorientation angle exceeded 109.5 °. For the Cu bicrystals, the general trend of their maximum stress was in accordance with Cu single crystals for θ<109.5 °although the values of the former were lower than the latter. This lower stress of the Cu bicrystal was due to the existence of GBs where the atoms have a higher energy than the lattice atoms and the dislocation was easier to nucleate. It was interesting to find that the maximum stress of the bicrystals dropped abruptly when the misorientation angle exceeded 109.5 °. The trend of maximum stress for the bicrystals within the range of θ>109.5 °was different to the single crystals. This unique mechanical behaviour of Cu bicrystals for θ>109.5 ° can be attributed to their intrinsic GB structures with the E structural units[105,109,110]. The effect of the E units on the deformation mechanism will be discussed in the following context. Fig. 5.6(c) shows that the Σ3(1 1 1) GB had a relatively higher stress which resulted from its simple boundary structure and lowest boundary energy.

5.3.3 Dislocation nucleation from GB with θ<109.5°

During the early stage of loading, the system responded elastically and the lattices were stretched without any dislocations forming, but as the strain increased a visual inspection of the MD simulation results indicated that the maximum tensile stress of the Cu bicrystal corresponded to the nucleation of dislocations from the GB. Figs.5.7(a)-(d) show snapshots of four GBs with θ<109.5 ° at the beginning of dislocation nucleation from the boundary plane at 10 K. These images are coloured according to the common neighbour analysis (CNA) values[63]. Only those atoms in defective arrangements are shown in the figure, while those atoms with perfect FCC lattice structure are not shown. The yellow atoms indicate the GB plane and the dislocation core and the blue atoms represent the stacking fault.

For Σ9(1 1 4) GB, as shown in Fig. 5.7(a), partial dislocations were nucleated almost simultaneously on the primary and secondary slip systems from the GB plane.

Some atoms on the GB plane became chaotic before the simulation system reached its maximum tensile stress, but eventually the collective motion of the disordered atoms nucleated partial dislocation loops along the active slip planes within grain-B at ε=9.7%. The nucleated dislocation loops had a V-shaped structure where the exterior of the dislocation loop was the partial dislocation core that bound an intrinsic stacking fault. An examination of the V-shaped dislocation loops indicated that they were nucleated on the $(1\ \bar{1}\ 1)$ and $(\bar{1}\ 1\ 1)$ slip plane, which are the secondary slip systems with a Schmid factor $SF_{(1\ \bar{1}\ 1)} = SF_{(\bar{1}\ 1\ 1)} = 0.419$ (see Table-5.2 for the calculations of the Schmid factor). The two intrinsic stacking faults were bounded by leading $a/6[1\ \bar{1}\ \bar{2}]$ and $a/6[1\ \bar{1}\ 2]$ Shockley partial dislocations, and they intersected at a $a/6[1\ \bar{1}\ 0]$ stair-rod dislocation. Meanwhile, a set of extrinsic partial dislocations were nucleated from the boundary plane into both grain-A and grain-B after the maximum stress. This slip occurred on the $(1\ 1\ \bar{1})$ and $(1\ 1\ 1)$ planes respectively, and they are the primary slip planes according to Schmid factor analysis with $SF^{max}_{(1\ 1\ \bar{1})} = SF^{max}_{(1\ 1\ 1)} = 0.471$. The nucleation of extrinsic partial dislocations resulted from the deformation of the C structural units. This process will be illustrated in the introduction to the Σ11(1 1 3) GB, which consists entirely of C structural units. A further increase in the tensile strain caused dislocation interactions as the dislocation loops propagated throughout the crystal. As with Σ9(1 1 4) GB, a number of the V-shaped structural dislocations nucleated from the Σ139(3 3 11) GB and began to propagate onto the $(1\ \bar{1}\ 1)$ and $(\bar{1}\ 1\ 1)$ slip planes once the maximum tensile stress at ε=8.3% had been reached. Moreover, the embryos of partial dislocations were evidenced on the $(1\ 1\ \bar{1})$ and $(1\ 1\ 1)$ planes, as shown in Fig.5.7(b).

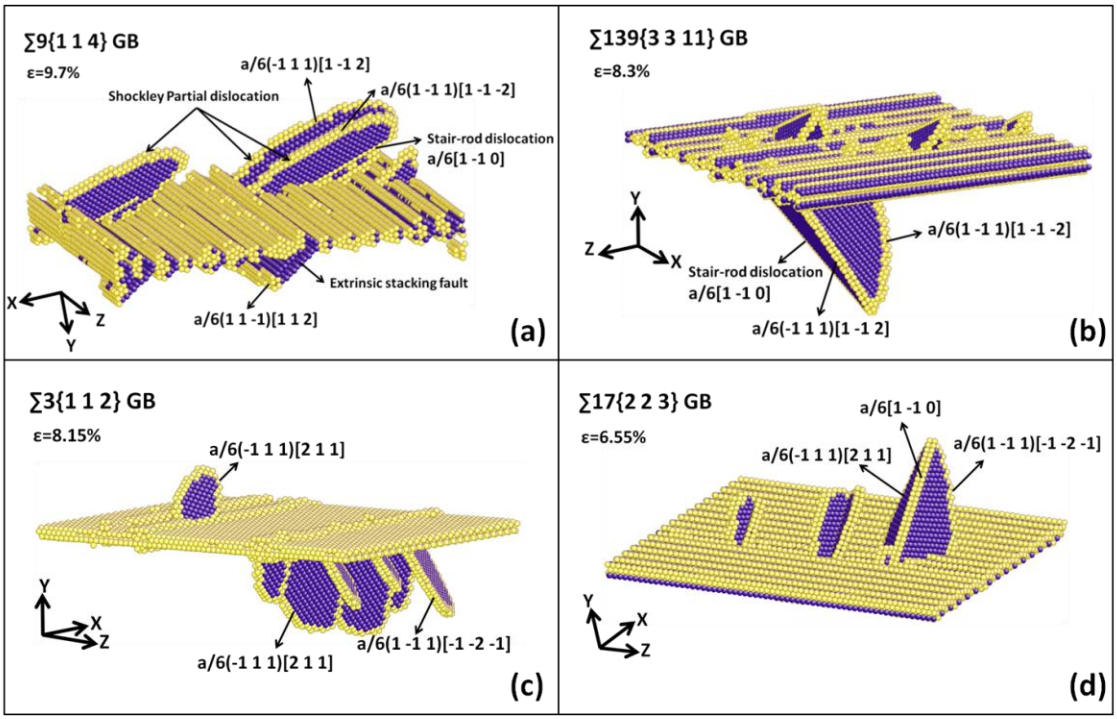

Figure 5.7 Dislocation nucleation from Cu bicrystal with (a) Σ9(1 1 4) θ=38.9 °GB (b) Σ139(3 3 11) θ=42.2 °GB (c) Σ3(1 1 2) θ=70.5 °GB and (d) Σ17(2 2 3) θ=86.6 °GB under uniaxial tension at 10 K. Atoms with perfect fcc structures were removed to facilitate viewing the defective structures. The yellow atoms organized the GB plane and the dislocation core, and the blue atoms represented the stacking fault.

The dislocation nucleation process on the Σ11(1 1 3) GB is shown in Fig.5.8. Recall that the Σ11(1 1 3) GB had a simple boundary structure consisting entirely of C structural units, while the boundary energy was local minimum (the first cusp in Fig.5.5). This special boundary structure resulted in a different nucleation mechanism. In Fig.5.8(a) at ε=9.85%, dislocations nucleated on the (1 1 $\bar{1}$) and (1 1 1) planes from the GB when the maximum tensile stress was reached, and then they propagated symmetrically in grain-A and grain-B. They are the primary slip systems with $SF^{max}_{(1\,1\,\bar{1})}$=$SF^{max}_{(1\,1\,1)}$=0.429. Subsequently, the V-shaped partial dislocation loops began to nucleate in perfect lattice and slipped along the (1 $\bar{1}$ 1) and ($\bar{1}$ 1 1) planes at ε=10%, as shown in Fig.5.8(b). The atoms forming the Σ11(1 1 3) GB were stable due to their comparatively low boundary energies, so it was not as easy as the other cases to nucleate the V-shaped partial dislocation loops from the Σ11(1 1 3) GB by shuffling local atoms. However, the intrinsic free volume of the C structural unit

provided another path for the dislocations nucleating from the boundary along the secondary slip systems. This was seen at the sites of ‘a’ and ‘b’ in Fig.5.8(a), where an extrinsic stacking fault and a twin fault were generated after the dislocations nucleation. More specifically, the distance of the twinning fault can become broad as the tensile strain increased, as shown at ‘b’ in Fig.5.8(b).

The nucleation process of an extrinsic stacking fault or a twin fault from the Σ11(1 1 3) GB is illustrated in Fig.5.8(c). The uniaxial tensile strain elongated the bicrystal in the Y direction and shortened the bicrystal in the X and Z directions. A careful examination of the images indicated that the bicrystal diminished in size in the X direction as a number of C structural units shrunk during the dislocation nucleation. The first C unit shrank as a result of atom 1 translating in the negative X direction, which caused the atoms on plane ‘a’ to slip towards the GB and the atoms on plane ‘b’ to slip out of the GB. This resulted in the first partial dislocation nucleation with an intrinsic stacking fault behind. Similarly, the translation of atom 2 caused the second partial dislocation nucleation by a relative shifting of atoms on plane ‘b’ and plane ‘c’. Notice that the slip direction caused by atom 2 on plane ‘b’ was opposite to that caused by atom 1, which drove the atoms on plane ‘b’ to turn back to the perfect fcc position and generated an extrinsic stacking fault, as shown in Figs.5.8(c)-(i). This extrinsic stacking fault nucleation mechanism was also evidenced in Fig.5.7(a) for the Σ9(1 1 4) GB. However, unlike the Σ9(1 1 4) GB, the consecutive shrinkage of the C units along the Σ11(1 1 3) GB provided continuous nucleation sources for the consequent partial dislocations, and led to a broadening of the twinning region. As shown in Figs.5.8(c)-(ii) and (iii), the translation of atom 3 and atom 4 in the negative X direction resulted in the twin-boundary broadening to four and five (1 1 1) lattice spacings.

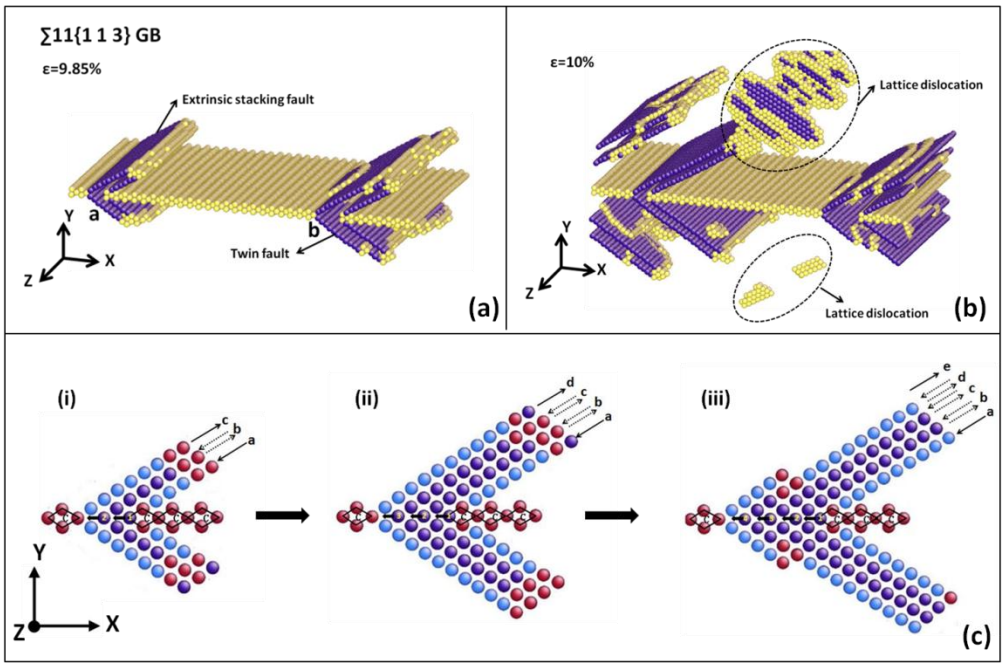

Figure 5.8 Dislocation nucleation from Cu bicrystal with Σ11(1 1 3) θ=50.5 °GB under uniaxial tension at 10 K. In Fig.5.8(a) and (b), atoms with perfect fcc structures are removed and atoms of different colours represent the same as described in Fig.5.7. In Fig.5.8(c), the dark blue atoms have the perfect fcc structure, atoms coloured with red organize the GB plane and the dislocation core, the light blue atoms represent the twin fault.

The GBs with a dissociated facet structures in the misorientation angle range of 50.5 °<θ<109.5 ° evolved before the dislocation nucleation event. Figs.5.7(c) and (d) show the Σ3(1 1 2) GB and Σ17(2 2 3) GB cases respectively. The length of the dissociated intrinsic stacking fault decreased as the tensile deformation increased, until it was accommodated entirely by the boundary plane. Subsequently, the V-shaped dislocation loops nucleated on the (1 $\bar{1}$ 1) and ($\bar{1}$ 1 1) slip planes, as did the cases of θ<50.5 °. Notice that, according to the Schmid factor analysis and the dislocation extraction algorithm (DXA)[145,183], the (1 $\bar{1}$ 1) and ($\bar{1}$ 1 1) slip plane are now the primary slip systems, and the Burgers vector of the two leading Shockley partial dislocations are $a/6[\bar{1}\,\bar{2}\,\bar{1}]$ and $a/6[2\,1\,1]$ respectively. Spearot et al.[106] previously investigated three Cu [1 $\bar{1}$ 0] tilt GBs with dissociated facet structures (θ=53.1 °, 53.1 ° and 59 °). By comparing their findings with the present simulation results, it can be concluded that as the misorientation angle of the GB increased from

50.5 ° to 109.5 °, the spacing between the intrinsic stacking fault facets gradually decreased and caused the nucleation mechanism to change from one dominated by dislocation nucleation on the secondary slip systems (*i.e.* slip on (1 1 $\bar{1}$) and (1 1 1) planes) to one dominated by a mixture of dislocation nucleation on both primary and secondary slip systems, and then to one dominated by dislocation nucleation on the primary slip systems (*i.e.* slip on (1 $\bar{1}$ 1) and ($\bar{1}$ 1 1) planes).

5.3.4 Dislocation nucleation from θ=109.5° and θ=114.5 °GBs

The maximum tensile stress of Σ3(1 1 1) GB was calculated as 17 GPa, which is the same as the maximum tensile stress of the corresponding single crystal with an orientation angle θ=109.5°. Recall that the Σ3(1 1 1) coherent twin boundary had a very simple boundary structure and the lowest boundary energy of all the <1 1 0> tilt GBs. This simple boundary structure has no excess free volume for local atoms to rearrange themselves at the boundary plane, and therefore it is hard to serve as a source of dislocation when the maximum tensile stress has been reached. Lattice dislocations nucleated homogeneously and their propagation intra-grains are visible in the bicrystal model, as shown in Fig.5.9(a). This is the same deformation mechanism as a single crystal, so the calculated tensile strength was identical. In Fig.5.9(b), the dislocation loops were nucleated on three active slip planes (1 1 $\bar{1}$), (1 $\bar{1}$ 1) and ($\bar{1}$ 1 1) at a very similar strain, both of which were the favoured slip systems with the maximum Schmid factor $SF^{max}_{(1\,1\,\bar{1})}$= $SF^{max}_{(1\,\bar{1}\,1)}$=$SF^{max}_{(1\,\bar{1}\,\bar{1})}$=0.314. No dislocation appeared to nucleate from the boundary plane during the process of tension deformation. Actually, the Σ3(1 1 1) GB was the only case in our study of the <1 1 0> tilt GBs that did not emit dislocations.

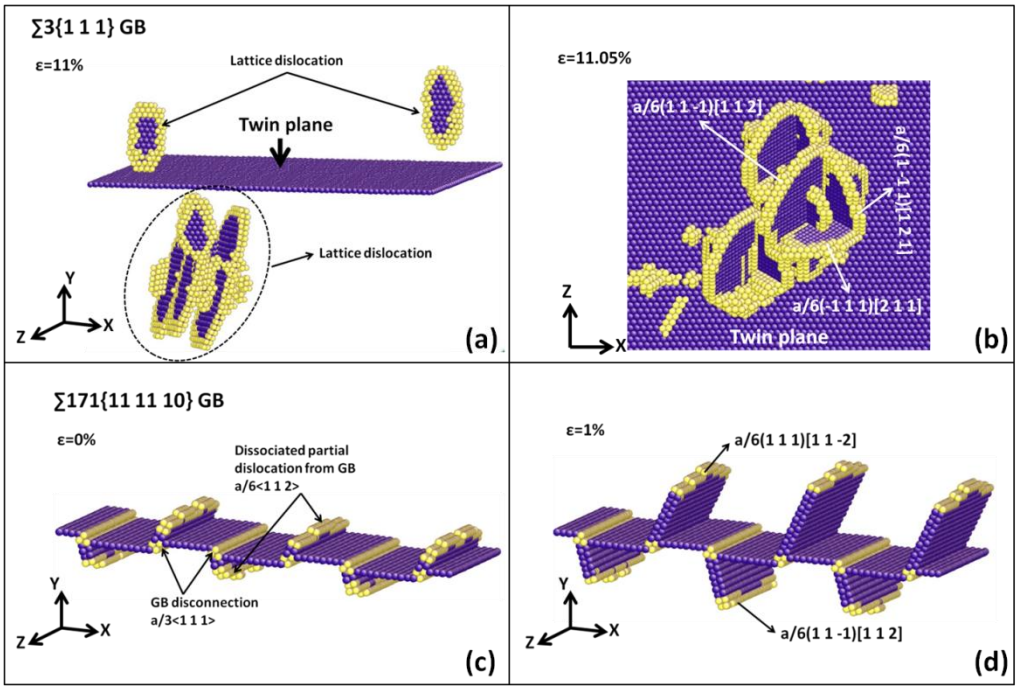

Figure 5.9 (a)-(b) Dislocation nucleation from Cu bicrystal with Σ3(1 1 1) θ=109.5 °GB under uniaxial tension at 10 K. (c)-(d) Dislocation nucleation from Cu bicrystal with Σ171(11 11 10) θ=114.5° GB under uniaxial tension at 10 K.

Compared to the Σ3(1 1 1) coherent twin boundary, there was only a small deviation in lattice misorientation across the Σ171(11 11 10) θ=114.5° GB. This kind of GB structure can be defined as a vicinal twin boundary[189] where a 5 °misorientation is accommodated by a number of distorted E structural units and dissociated D structural units to provide a symmetrical structure. Following the work of Rittner and Merkle[180], the distorted E units can be described as cores of alternating a/3<1 1 1> twin dislocations, or disconnections, while the dissociated D units can be represented as a/6 <1 1 2> Shockley partial dislocations. The a/3 <1 1 1> disconnections were observed in previous experimental work by HRTEM in some fcc metals[188,190,191]. The Σ171(11 11 10) GB disconnection and its dissociated partial dislocations are indicated by the arrows in Fig.5.9(c), and a detailed view can be seen in Fig.5.4(a). It is worth noting that unlike the structure of GBs with 50.5 °<θ<109.5 °, the dissociated facet in Σ171(11 11 10) GB was along the primary slip plane in grain-A and Grain-B, and therefore when subjected to the uniaxial tensile deformation, the pre-nucleated Shockley partial dislocations can propagate rapidly with an increasing length of

intrinsic stacking fault behind at ε=1.4%, as shown in Fig.5.9(d). Since the partial dislocations have already nucleated in the equilibrium boundary structure, only a low stress can drive it to emit, which can explain the sharp decrease in the peak stress from the Σ3(1 1 1) coherent twin boundary to the Σ171(11 11 10) vicinal twin boundary.

5.3.5 Dislocation nucleation from GB with θ>114.5°

As described previously, all the GBs with θ>109.5 °contained the E structural units. Sansoz and Molinari[65,192] correlated the E structural unit with the incidence of atomic shuffling during shear deformation and proposed that the free volume inherent to this structural feature triggered the atomic shuffling event, while Spearot et al.[109,193] correlated the mechanical behaviour of the Cu <1 1 0> GBs with the intrinsic large free volume of the E structural unit and its evolution during the dislocation nucleation. How the E units act as the source of dislocation nucleation in different <1 1 0> GBs with θ>114.5 °is investigated in this section.

A visual inspection of the MD simulation results indicated that the maximum tensile stress corresponded to the nucleation of partial dislocations from the GBs with θ>109.5 °. Fig.5.10 shows the dislocation nucleation from the Σ11(3 3 2) GB, Σ9(2 2 1) GB, Σ19(3 3 1) GB, and Σ73(6 6 1) GB at an early stage after the maximum tensile stresses have been reached. Fig.5.10 shows that the Shockley partial dislocations have nucleated and propagated on the (1 1 1) and (1 1 $\bar{1}$) plane, after originating from the collapsed E units that were connected to the boundary by a stacking fault. According to the Schmid analysis they are the primary slip systems. Notice here that the nucleation of Shockley partial dislocations were not nucleated collectively in all the E units from the boundary plane and only certain nucleated dislocations propagated away from the plane. Interestingly, the collapsed E units evolved into the C structural units shown in Figs.5.10(a), (b) and (d), In Fig.5.10(c), the collapsed E units did not evolve into the C units, which indicated there was a different deformation mechanism.

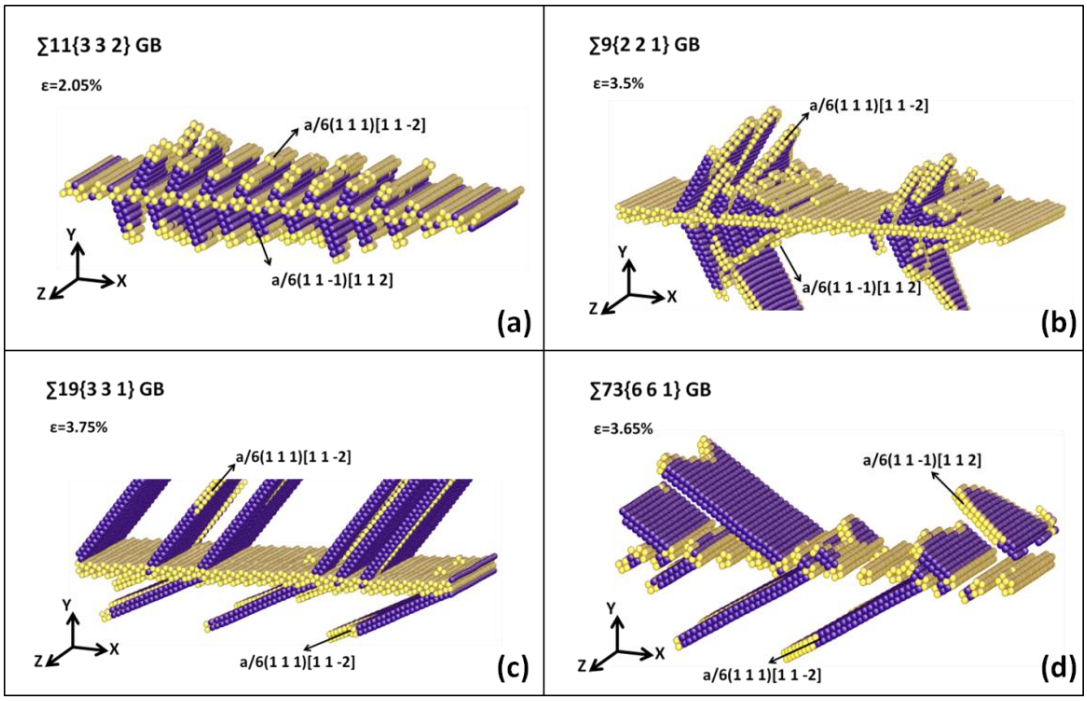

Figure 5.10 Dislocation nucleation and propagation from (a) Σ11(3 3 2) GB, (b) Σ9(2 2 1) GB, (c) Σ19(3 3 1) GB and (d) Σ73(6 6 1) GB under a uniaxial tension at 10 K.

Fig.5.11 shows a detailed view of the transformation of the E structural units in the Σ11(3 3 2) GB, Σ9(2 2 1) GB, Σ19(3 3 1) GB, and Σ73(6 6 1) GB during the dislocation nucleation process. One structural period of each GB was extracted for analysis in Fig.5.11. In Fig.5.11(a)-i, the Σ11(3 3 2) GB before the dislocation nucleation consisted of the undeformed E units connected by the D units. The left hand side E unit is tilted downwards and the atoms involved are marked from 1 to 6, while the atoms involved in the right E unit, which is tilted upwards, are indexed $1'$ to $6'$. When the maximum tensile stress was reached, partial dislocation began to nucleate from the downwards E unit into the upper grain by the relative shift of opposing (1 1 1) slip plane, that is, Atom 4 slipped out of the E unit along the (1 1 1) slip plane while Atom 5 slipped into the E unit. Meanwhile, partial dislocation nucleated from the upwards E unit into the lower grain, while Atoms $5'$ and $6'$ slipped on the opposing $(1\ 1\ \bar{1})$ plane. This rearrangement of Atoms 4 and 5, and Atoms $5'$ and $6'$ resulted in a subsequent reduction of the free volume at each E unit during the dislocation nucleation process, but eventually both of the E units evolved into C units that consisted of Atoms 1, 2, 3, 5, and Atoms $1'$, $2'$, $3'$, $5'$, as shown in

Fig.5.11(a)-ii. With Σ9(2 2 1) GB, the period boundary structure consisted of overlapped E structural units, i.e. every two E units shared two atoms, which were indexed 5 and 6 in the downwards E unit, and $1^{'}$ and $3^{'}$ in the upwards E unit. As with the dislocation nucleation process for Σ11(3 3 2) GB, the relative slip of Atoms 4 and 5 along the (1 1 1) plane in the downwards E unit, and Atoms $5^{'}$ and $6^{'}$ along the (1 1 $\bar{1}$) plane in the upwards E unit caused the E units to transform into C units, as shown in Fig.5.11(b).

For the Σ19(3 3 1) GB, all the E units at the boundary plane were tilted upwards. Unlike the Σ11(3 3 2) GB and Σ9(2 2 1) GB, where the dislocations only nucleated and were emitted into the upper grain from the downward E units and into the lower grain from the upward E units, and the deformation of upward E units in Σ19(3 3 1) GB can facilitate the emission of partial dislocations into the upper and lower grains. This process is shown in Fig.5.11(c). First, Atom 2 slipped out of the E unit along the (1 1 1) plane while Atom 4 slipped in the opposite direction, so the relative shift of the opposing (1 1 1) slip plane resulted in a partial dislocation that nucleated from the E unit and propagated into the upper grain. Notice that when the first dislocation was nucleated by the movement of Atoms 2 and 4, other atoms involved in the E unit that were numbered 1, 3, 5, and 6 remained at their equilibrium position, as shown in Fig.5.11(c)-ii. Second, as the applied tensile strain increased, the first nucleated partial dislocation was emitted further away from the boundary plane, and then the second partial dislocation began to nucleate into the lower grain by the relative shift of Atoms 3 and 6 along the (1 1 1) slip plane. Like the previous cases, the free volume of the E unit diminished after the dislocation nucleation, but due to the arrangement of different atoms during the deformation of the E unit, the transformation of the 'E - C' structural unit observed in the Σ11(3 3 2) GB and Σ9(2 2 1) GB cases was not seen in the Σ19(3 3 1) GB case.

Fig.5.11(d) shows that the structural period of the Σ73(6 6 1) GB contained a higher E unit and a lower E unit, both of which were almost symmetrical along the X axis.

Like the Σ19 (3 3 1) GB, each E structural unit can act as the source of dislocation for the upper and lower grains because the nucleation process was similar to the Σ11(1 1 3) GB case. Dislocation nucleation was realised by when Atom 5 was translated in the positive X direction, which triggered the relative slip of Atoms 4 and 5 along the (1 1 $\bar{1}$) slip plane in the upper grain, and the relative slip of Atoms 5 and 6 along the (1 1 1) slip plane in the lower grain. Eventually, the E unit evolved into a feature that was characteristic of the C unit, and the total free volume was reduced.

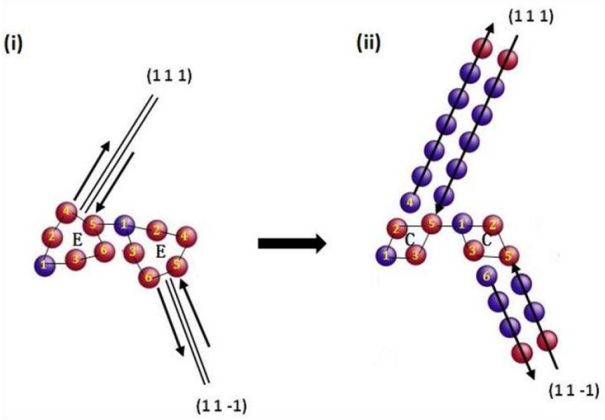

(a) ∑11 (3 3 2) θ=129.5°

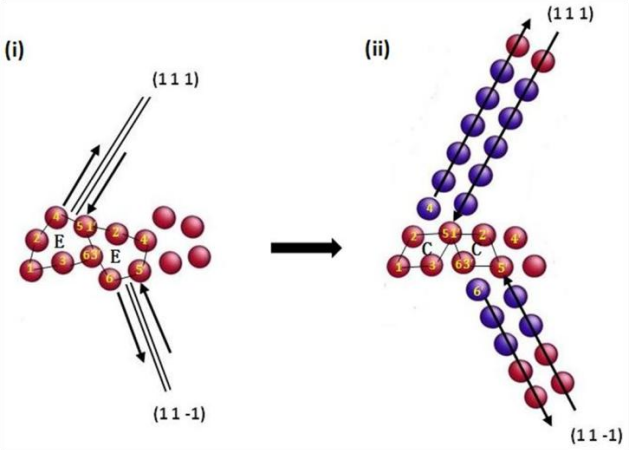

(b) ∑9 (2 2 1) θ=141.1°

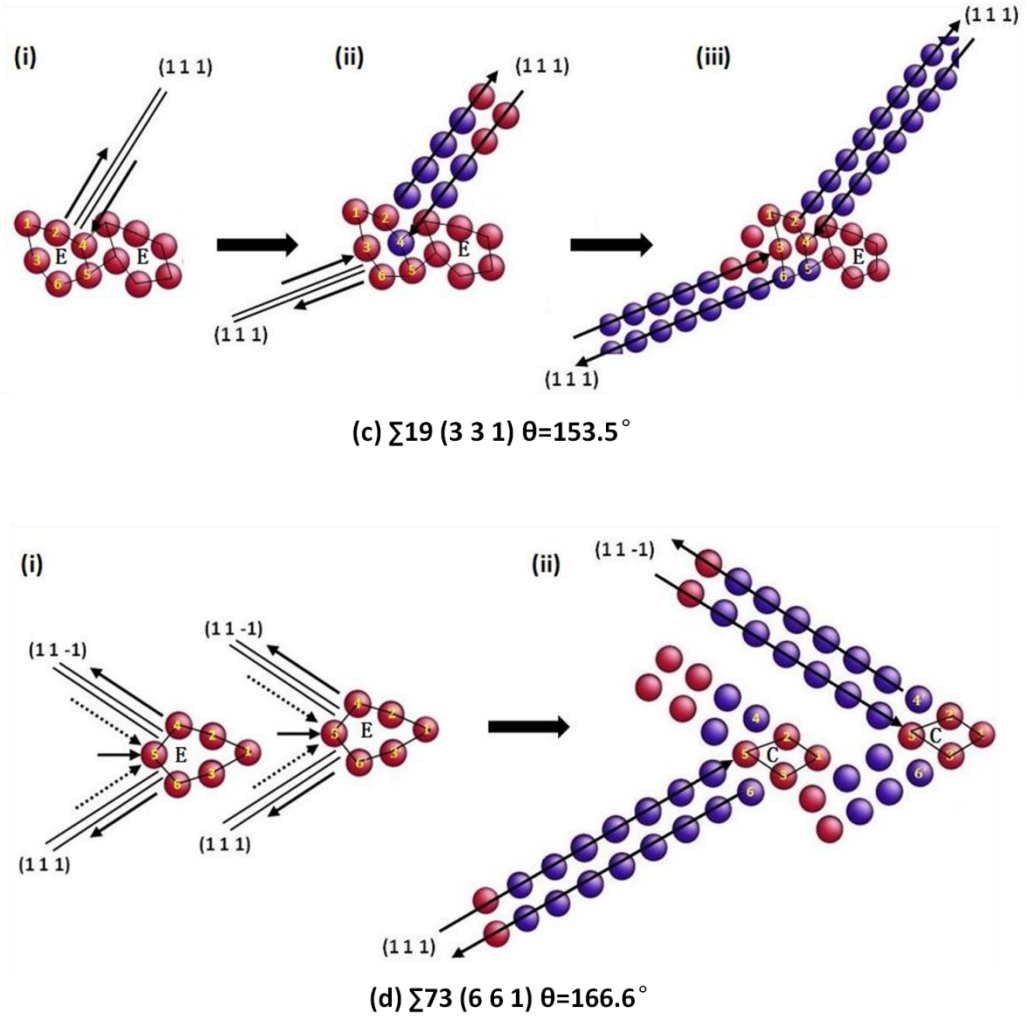

Figure 5.11 Enlarged view of dislocation nucleation from (a) Σ11(3 3 2) GB, (b) Σ9(2 2 1) GB, (c) Σ19(3 3 1) GB and (d) Σ73(6 6 1) GB. One structural period of each GB is extracted for analysis.

5.4 Discussion

In all the cases in this study, the maximum tensile stress of the bicrystal corresponded to the heterogeneous nucleation of partial dislocations from the GB, except for the Σ3(1 1 1) θ=109.5 °coherent twin boundary. Within the misorientation angle range of θ<109.5 °, the maximum stress-misorientation angle relationship of the bicrystals had a similar trend to single crystals, implying that the crystallographic orientation played an important role in the GB mechanical behaviour. The incipient plastic deformation of the bicrystal models was evidenced by a number of V-shaped partial dislocation loops nucleated from the GB plane, as well as the nucleation of extrinsic stacking fault or twin fault. The maximum tensile stress of the GBs with θ>109.5 °was much lower

than the single crystals and showed a different relationship with the misorientation angle. The simulation results indicated that an intrinsic GB structure, instead of a lattice orientation, became the predominant factor that determined the mechanical behaviour of GBs in this range of misorientation angles.

The maximum tensile stress of each GB was plotted in Fig.5.12 as a function of GB energy. The energy barrier of dislocation nucleation from different GBs against their maximum tensile stress is plotted in Fig.5.13. Since the Σ3(1 1 1) GB (coherent twin boundary) has a very simple structure and a stable configuration, the dislocations were nucleated in the matrix lattice without any dislocation nucleation from the GB plane during the simulation. Therefore, there is no energy barrier for the value of Σ3(1 1 1) GB in Fig.5.13. The maximum stress generally decreased with the GB energy, while the energy barrier associated with the dislocation nucleation from the GB increased with the maximum stress. These results indicated that the lower energy GBs with more stable boundary structures required higher tensile stress to nucleate dislocations during the onset of plastic deformation, and therefore the nucleation barrier was correspondingly higher. This was the case for GBs with $\theta \leq 109.5°$. In reverse, for the less stable GBs ($\theta > 109.5°$) with a higher boundary energy, a lower tensile stress can overcome the energy barrier to activate the dislocation nucleation from the GB, but the GB energy alone cannot determine the GB tensile strength and the dislocation nucleation energy barrier. For example, the energy of the Σ11(1 1 3) $\theta = 50.5°$ GB corresponded to the local energy cusp in Fig.5.5, but its tensile strength (9.55 GPa) and the nucleation energy barrier (4.85 mJ/m^3) were not the local maximum. Moreover, there appears to be no explicit relationship between the GB energy and maximum tensile stress in the two circled areas shown in Fig.5.12.

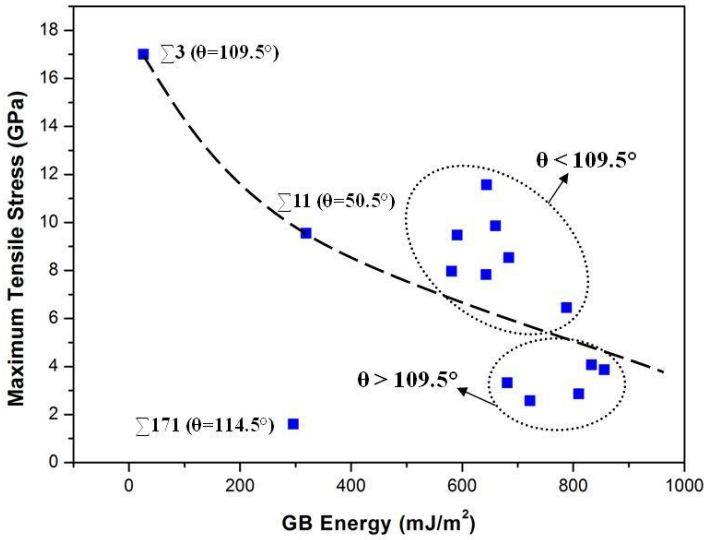

Figure 5.12 Maximum tensile stress of GBs plotted as a function of GB energy.

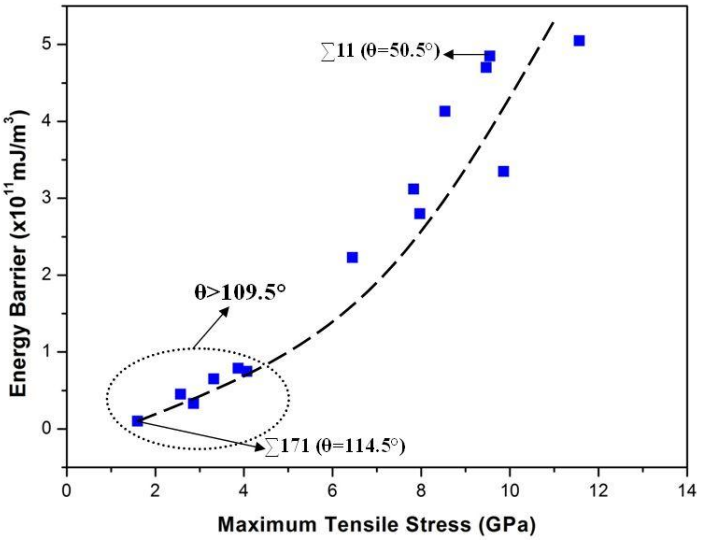

Figure 5.13 Energy barrier of dislocation nucleation from GB plotted as a function of maximum tensile stress.

Based on the results of this study, the orientation of the applied loading plays an important role in the process of dislocation nucleation in the range of θ<109.5 °, while the GB structure plays a dominant role for θ>109.5 °. The intrinsic large free volume (E structural units) involved in the boundary plane of the GBs with θ>109.5 °resulted in a high boundary energy and provided enough space for the GB atoms to be rearranged during tension deformation to facilitate the dislocation nucleation and accommodate the local stress. Moreover, the impact of the GB structure on dislocation nucleation was also evidenced by the GBs with the C structural units. For

example, the consecutive shrinkage of the C units along the Σ11(3 3 2) GB provided a nucleation source for an extrinsic stacking fault and a twin fault. Moreover, a very special case was found for the Σ171(11 11 10) GB (vicinal twin boundary) because it had the second lowest boundary energy (296 mJ/m^2) of all the GBs investigated in this study, but its tensile strength (1.6 GPa) and nucleation barrier (0.1mJ/m^3) was the lowest. This contradicted the general trend shown in Fig.5.12, where the lower boundary energy caused higher nucleation stress. As mentioned previously, this was mainly due to the dissociated dislocation from the boundary plane in the equilibrium structure of the Σ171(11 11 10) GB which facilitates the nucleation process. This result further emphasizes the important effect that the GB structures have on the mechanical property of materials.

5.5 Summary

Molecular dynamics simulations were conducted on Cu bicrystals with different <1 1 0> tilt GBs to investigate the GB structures, energy, mechanical property, and the dislocation nucleation mechanisms under tensile loading. In this chapter, the GB properties were quantified, including the GB energy, GB tensile strength, and the dislocation nucleation energy barrier. The atomistic mechanisms of the dislocation nucleation from various GBs were illustrated and their correlation with the GB properties was investigated.

Table 5.2 Schmid factor of resolved shear stress on the {1 1 1}<1 1 2> slip system for the $[1\ \bar{1}\ 0]$ tilt grain boundaries.

Slip plane	Slip direction	Grain boundary plane [h k l] and misorientation angle (θ)							
		[1 1 6] θ=26.5°	[1 1 4] θ=38.9°	[3 3 11] θ=42.2°	[1 1 3] θ=50.5°	[2 2 5] θ=58.9°	[1 1 2] θ=70.5 °	[2 2 3] θ=86.6°	[3 3 4] θ=93.4 °
(1 1 1)	[1 1 $\bar{2}$]	0.496	0.471	0.461	0.429	0.386	0.314	0.194	0.138
	[1 $\bar{2}$ 1]	0.248	0.236	0.231	0.215	0.193	0.157	0.097	0.069
	[$\bar{2}$ 1 1]	0.248	0.236	0.231	0.215	0.193	0.157	0.097	0.069
(1 1 $\bar{1}$)	[1 1 2]	0.347	0.262	0.237	0.172	0.100	0	0.139	0.194
	[$\bar{1}$ 2 1]	0.174	0.131	0.119	0.086	0.05	0	0.069	0.097
	[2 $\bar{1}$ 1]	0.174	0.131	0.119	0.086	0.05	0	0.069	0.097
(1 $\bar{1}$ 1)	[$\bar{1}$ 1 2]	0.447	0.419	0.410	0.386	0.357	0.314	0.250	0.222
	[1 2 1]	0.335	0.366	0.373	0.386	0.393	0.393	0.374	0.360
	[2 1 $\bar{1}$]	0.112	0.052	0.037	0	0.036	0.079	0.125	0.138
($\bar{1}$ 1 1)	[1 $\bar{1}$ 2]	0.447	0.419	0.410	0.386	0.357	0.314	0.250	0.222
	[1 2 $\bar{1}$]	0.112	0.052	0.037	0	0.036	0.079	0.125	0.138
	[2 1 1]	0.335	0.366	0.373	0.386	0.393	0.393	0.374	0.360
Slip plane	**Slip direction**	**Grain boundary plane [h k l] and misorientation angle (θ)**							
		[1 1 1] θ=109.5 °	[11 11 10] θ=114.5 °	[3 3 2] θ=129.5 °	[11 11 7] θ=131.5 °	[2 2 1] θ=141.1 °	[3 3 1] θ=153.5 °	[6 6 1] θ=166.6 °	
(1 1 1)	[1 1 $\bar{2}$]	0	0.044	0.172	0.188	0.262	0.347	0.420	
	[1 $\bar{2}$ 1]	0	0.022	0.086	0.094	0.131	0.174	0.210	
	[$\bar{2}$ 1 1]	0	0.022	0.086	0.094	0.131	0.174	0.210	
(1 1 $\bar{1}$)	[1 1 2]	0.314	0.347	0.429	0.437	0.471	0.496	0.497	
	[$\bar{1}$ 2 1]	0.157	0.174	0.215	0.219	0.236	0.248	0.249	
	[2 $\bar{1}$ 1]	0.157	0.174	0.215	0.219	0.236	0.248	0.249	
(1 $\bar{1}$ 1)	[$\bar{1}$ 1 2]	0.157	0.138	0.086	0.079	0.052	0.025	0.006	
	[1 2 1]	0.314	0.296	0.236	0.227	0.183	0.124	0.061	
	[2 1 $\bar{1}$]	0.157	0.158	0.150	0.147	0.131	0.099	0.055	
($\bar{1}$ 1 1)	[1 $\bar{1}$ 2]	0.157	0.138	0.086	0.079	0.052	0.025	0.006	
	[1 2 $\bar{1}$]	0.157	0.158	0.150	0.147	0.131	0.099	0.055	
	[2 1 1]	0.314	0.296	0.236	0.227	0.183	0.124	0.061	

* The maximum value of Schmid factor for each grain boundary are shaded

** SF[1 $\bar{2}$ 1]= SF[$\bar{2}$ 1 1], SF[$\bar{1}$ 2 1]= SF[2 $\bar{1}$ 1], SF[$\bar{1}$ 1 2]=SF[1 $\bar{1}$ 2], SF[1 2 1]=SF[2 1 1], SF[2 1 $\bar{1}$]=SF[1 2 $\bar{1}$]

CHAPTER 6

Tensile Deformation Behaviour of ∑5 Tilt Grain Boundaries in Copper Bicrystal

In this chapter, MD simulations were used to investigate the structures and mechanical behaviour of symmetric and asymmetric Σ5[0 0 1] tilt GBs of copper bicrystal. The influence of the stress state on the mechanical behaviour is discussed. The work of this chapter has been published previously in *Scientific Reports* **4**, 5919.

6.1 Introduction

It has long been recognised that grain boundaries (GBs) are important microstructural features that can significantly affect the properties of polycrystalline materials[194]. When the grain size is reduced to ultrafine or nano scale, the effect of GBs on the material properties becomes more significant because the traditional deformation mechanisms based on nucleation and propagation of lattice dislocation are gradually replaced by GB mediated processes such as GB sliding[195], grain rotation[13,196], diffusional creep[197], dislocation nucleation or absorption at GB[1,11,102,198,199] etc. A great deal of experimental work and many atomistic simulations has been carried out to examine various GBs energy, structure, and properties, but this research work focused primarily on symmetric GBs with mirror symmetry of crystallographic planes; very few atomistic simulations have been carried out on the structure and related properties of asymmetric GBs, even though experimental observations have shown that most GBs in real polycrystalline materials are actually asymmetric[200-202] and they can affect the material properties more significantly[203,204].

Recently, both experimental observations[48,205-209] and atomistic simulations[45,108,210-213] of asymmetric tilt GBs have been attempted, and they have

given us a better understanding of the structures and energy on these boundaries as well as providing an insight into the related GB properties, e.g., the structural transformations, dissociations, faceting transitions etc. Most of these works concentrated on the Σ3 family because the most common Σ3 GB is the coherent twin boundary with very low boundary energy and they were observed more frequently in polycrystals[201,202,214-216]. Tschopp and McDowell[45] took advantage of atomistic simulation on symmetric and asymmetric Σ3<1 1 0> tilt GBs and found that the structure and energy of asymmetric GBs were closely related to the corresponding symmetrical ones. Their investigation[108] on dislocation nucleation from different Σ3 asymmetric boundaries under uniaxial tension revealed that the properties of GB depended not only upon the misorientation between grains, but also upon the inclination of the GB plane. Lin[210] and Luo[211] performed simulations on the asymmetric Σ3<1 1 0>(1 1 0)/(1 1 4) GB in copper bicrystals under shock loading to examine the influence of GB on the mechanical behaviour of a bicrystal system. Compared to the productive research findings on Σ3 asymmetric boundaries, very few experiments or simulations have focused on other low index coincident site lattice (CSL) systems. Tschopp and coworkers[46] investigated the structure and energy of several low CSL bicrystal systems, i.e. Σ5, Σ13 GBs around the [0 0 1] misorientation axis and Σ9, Σ11 GBs around the [1 1 0] misorientation axis. However, they did not study the correlation between the asymmetric GB structures and the mechanical behaviour. Zhang et al. performed a series of simulations to examine the influence of GB inclination on the mobility[213], diffusivity[217] and migration[212,218] of Σ5 tilt asymmetric GBs, but no further research was carried out to analyse the mechanical response in relation to the deformation mechanism at atomic scale.

In this chapter, MD simulations were carried out to investigate the mechanical behaviour and related deformation mechanisms in Cu bicrystals with two symmetric and four asymmetric Σ5 GBs under tensile deformation. Although the primary aim

of this work was to study the effect of GB inclination on tensile response, the influence of the transverse stress on the mechanical behaviour was also examined. In these simulations, tensile deformation was applied under both 'free' and 'constrained' boundary conditions.

Table 6.1 Details of Σ5 grain boundary and dimensions of bicrystal models.

Boundary type	**Inclination angle Φ (°)**	**Boundary plane (h k l)A/B**	**Model dimensions X×Y×Z (Å)**	**Number of atoms**
Symmetric	0	(-3 1 0)/(3 1 0)	144.4×218.4×108.3	285,000
Asymmetric	11.31	(-8 1 0)/(7 4 0)	146.2×216.6×108.3	288,330
Asymmetric	18.43	(1 0 0)/(4 3 0)	142.6×216.6×108.3	279,960
Asymmetric	26.57	(7 1 0)/(1 1 0)	145.1×218.4×108.3	289,140
Asymmetric	30.96	(9 2 0)/(6 7 0)	146.2×215.9×108.3	287,400
Symmetric	45	(2 1 0)/(1 2 0)	146.2×216.6×108.3	287,280

6.2 Simulation Method

6.2.1 Model construction

In this study a bicrystal model with a fixed orientation of the GB plane (θ=36.9° for Σ5 GBs) and a fixed tilt axis ([0 0 1] axis) was used because it enabled a more controlled investigation of specific GB properties. Fig.6.1 shows a schematic of the computational cell used in the simulations. A bicrystal model was created by constructing two separate crystal lattices (Grain A and Grain B in Fig.6.1) with different crystallographic orientations and joining them together along the Y axis. Misorientation is defined as the angle θ between the [1 0 0] direction of the two single crystal grains, and the inclination is defined as the angle Φ between the bisector of the misorientation and the boundary plane. The values of Φ considered in this study and the Miller indices of the boundary plane are presented in Table 6.1. Due to the fourfold symmetry of the fcc lattice, the inclination angles from 0 ° to 45 ° cover all distinct boundary structures.

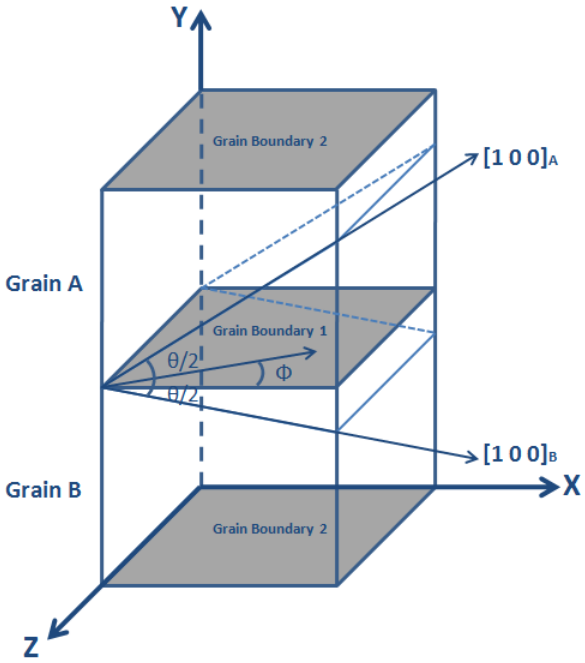

Figure 6.1 Schematic of Cu bicrystal with a Σ5 [0 0 1] asymmetric tilt grain boundary. The misorientation is defined as angle θ between the [1 0 0] direction of the two single crystal grains and the inclination is defined as angle Φ between the boundary plane and the bisector of misorientation θ.

Periodic boundary conditions were used in all directions (X, Y and Z). Specifically, periodic boundary conditions were applied to the X and Z directions to simulate an infinite boundary plane between the two grains that can eliminate the effect of a free surface. The periodic boundary condition in the Y direction introduced a second boundary plane into the model. For each initial configuration, it was important to adjust the size of the model to construct identical atomic structures of the two boundary planes to ensure they had the same equilibrium structures and energies after energy minimisation. Otherwise the different equilibrium structures of the two boundary planes could result in a higher energy metastable plane at grain boundary 1 and a stable plane at grain boundary 2, a result that could significantly affect further simulation results. A number of initial "starting positions" of grain A and grain B were tested to find the possible GB structures[180-182]. Molecular statics calculations which used a standard conjugate gradient algorithm were conducted on all the tested GB structures to determine their minimum energy configurations.

6.2.2 GB energy calculation

After minimising the energy, the energy of each equilibrium GB structure was then calculated and compared to find the possible global minimum energy configuration. In this study the GB structure with the lowest energy was regarded as the stable structure, while other GB structures with higher GB energy were reckoned to be metastable and therefore were not considered. Since the periodic boundary condition in the Y direction generated a pair of boundary planes in the bicrystal model, the energy associated with the grain boundary was calculated by equation:

$$\gamma_{GB} = \frac{E_{system} - N \cdot E_{atom}}{2A} \tag{6-1}$$

where E_{system} is the system energy of the equilibrium bicrystal model, E_{atom} is the potential energy of a single atom in the perfect Cu lattice (-3.54eV), N is the total number of atoms contained in the model and A is the area of the GB plane.

6.2.3 Molecular dynamics simulation

All the simulations in this study were performed with the parallel molecular dynamics code LAMMPS[139]. The embedded-atom method (EAM) potential developed by Mishin et al. for copper[137] was used because it can fit a large set of experimental and first-principles data. After the minimum energy configuration was attained, the simulation model was equilibrated using MD in the isobaric-isothermal (NPT) ensemble at a pressure of 0 bar and a temperature of 10 K for 20 ps. A constant rate of $2\times10^{8}s^{-1}$ was applied perpendicular to the boundary plane (along the Y direction) at a temperature of 10 K. Tensile deformation was performed under either ‘free’ or ‘constrained’ boundary conditions. These boundary conditions were very similar to those used by Kitamura et al.[219] and Spearot et al.[220] to study the effect of boundary condition on the tensile deformation of nickel single crystal and copper bicrystal respectively. Under free tension boundary conditions, the boundaries in the lateral directions were allowed to expand or contract during the deformation process and the transverse stresses were kept free ($\sigma_{xx} = \sigma_{zz} = 0$).

Under constraint tension boundary condition, computational models were strained at a constant rate along the Y axis while keeping the model dimensions along the X and Z axis fixed ($\varepsilon_{xx} = \varepsilon_{zz} = 0$). This boundary condition considered the transverse stress along the X and Z axis during the tensile deformation process. A schematic of the tension simulation is shown in Fig.6.2.

In order to further validate the Mishin et al. EAM potentials and the molecular dynamics code, simulations are designed to calculate the elastic stiffness (C_{11} and C_{12}) of Cu single crystal model. As introduced above, the displacement (or strain) in X and Z directions is equal to zero under constrained tension boundary condition. Thus, the set of elastic equations to describe the response of a homogeneous cubic crystal,

$$\begin{bmatrix}\sigma_1\\ \sigma_2\\ \sigma_3\\ \sigma_4\\ \sigma_5\\ \sigma_6\end{bmatrix} = \begin{bmatrix}C_{11} & C_{12} & C_{12} & & & \\ C_{12} & C_{11} & C_{12} & & & \\ C_{12} & C_{12} & C_{11} & & & \\ & & & C_{44} & & \\ & & & & C_{44} & \\ & & & & & C_{44}\end{bmatrix}\begin{bmatrix}\varepsilon_1\\ \varepsilon_2\\ \varepsilon_3\\ \varepsilon_4\\ \varepsilon_5\\ \varepsilon_6\end{bmatrix} \tag{6-2}$$

reduces to ,

$$\sigma_1 = C_{12}\varepsilon_2 = \sigma_3$$

$$\sigma_2 = C_{11}\varepsilon_2 \tag{6-3}$$

Thus, the elastic constants C_{11} and C_{12} can be determined by measuring the slope of the appropriate stress-strain relation. For the mechanical properties, the system stress is attained by calculating the pressure of the entire system of atoms. The pressure is computed by the formula

$$P_{ij} = \frac{1}{V}\left[\sum_k^N m_k v_{k_i} v_{k_j} + \sum_k^N r_{k_i} f_{k_j}\right], (i, j = x, y, z) \tag{6-4}$$

where the first term uses components of the kinetic energy tensor and the second term uses components of the virial tensor. N is the total number of atoms in the simulation model, V is the simulation model volume. r and f is the force vector and the distance

vector respectively. System strain is derived from the positions of the periodic boundaries. The elastic constants calculated from the initial slope of the MD simulations are 173.2GPa and 124.8GPa, which are all within acceptable accuracy of the experimental values of 168.4GPa and 121.4 GPa.

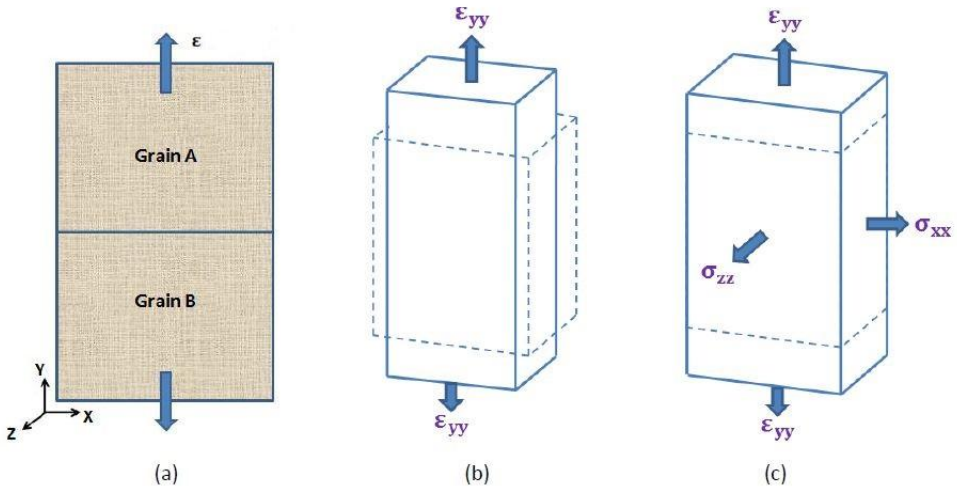

Figure 6.2 (a) Schematic of tension simulation model under (b) free tension boundary condition and (c) constrained tension boundary condition. The dotted lines in (b) and (c) represent the initial shape of the model, while the solid lines represent the deformed shape.

The visualisation tools Atomeye[140] and Ovito[141] were used to illustrate the bicrystal models. The common neighbour analysis (CNA) technique[63] was used to identify the defect structure and its evolution during the simulations, and the dislocation extraction algorithm (DXA)[145,183] was used to convert identified dislocations into continuous lines and compute their Burgers vectors.

6.3 Results

6.3.1 GB structure and energy

Fig.6.3 shows the equilibrium structures of the two symmetric and four asymmetric Σ5 GBs of Cu at 0K. The black and white balls correspond to the two adjacent atom layers along the [0 0 1] tilt axis. Structural units defined by Rittner[180] were used to illustrate the boundary structures. The six member kite-shaped unit was referred to as the "E" unit that forms the symmetric Σ5(3 1 0)(Φ = 0°) boundary, as outlined in Fig.6.3(a). The symmetric Σ5(2 1 0)(Φ = 45°) consists of the topologically identical

structure unit "E′", which differs only in direction and arrangement along the boundary plane, as shown in Fig.6.3(f). An investigation of the four asymmetric GBs showed they all consisted of the E and E′ units that are the preferred structural units for symmetric Σ5(3 1 0) and Σ5(2 1 0) boundaries respectively. In other words, the asymmetric GBs can be decomposed into their corresponding symmetrical boundaries. For example, the period vector for the asymmetric Σ5(9 2 0)/(6 7 0)(Φ = 30.96°) is $a_0[7\ \bar{6}\ 0]$ or $a_0[2\ \bar{9}\ 0]$ and this GB can be separated into one period of the Σ5 (3 1 0)(Φ = 0°) symmetric GB and three period of the Σ5 (2 1 0) (Φ = 45°) symmetric GBs. This reaction can be described by:

$$a_0[7\ \bar{6}\ 0] = a_0[1\ \bar{3}\ 0] + 3a_0[2\ \bar{1}\ 0]$$

or

$$a_0[2\ \bar{9}\ 0] = a_0[\bar{1}\ \bar{3}\ 0] + 3a_0[1\ \bar{2}\ 0]$$

It should be noted that the ratio of the E unit to the E′ unit decreased with the inclination angle Φ and an equal ratio was found in the Σ5 (1 0 0)/(4 3 0) (Φ = 18.43°) boundary, as shown in Fig.6.3(c). This finding that asymmetric GBs can be faceted into their corresponding symmetric ones was consistent with the observation for the Σ3[1 1 0] grain boundary family[45].

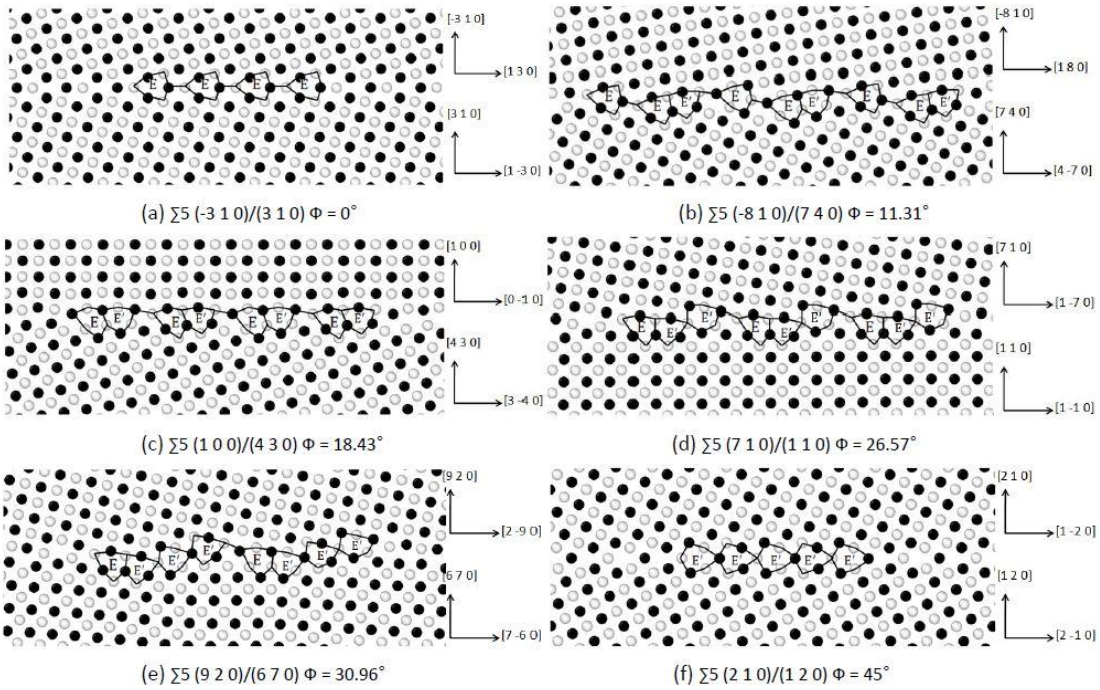

Figure 6.3 Σ5 GB structures of Cu for various inclination angles Φ at 0K. The structures are viewed along the [0 0 1] tilt axis, atoms on consecutive (0 0 2) plane are shown as black and white. The boundary normal vector of grain A and grain B are marked on the right-hand side for each GB. The structure unit at each boundary plane are outlined by the solid line as marked by E and E′. (a) and (f) are the two symmetric GBs, (b)-(e) are the four asymmetric GBs.

Since the structures of asymmetric GBs are closely related to their corresponding symmetric boundary structures, a faceting model was proposed to predict the energy of asymmetric GBs with idea faceting structures, i.e. the energy of the faceted asymmetric boundaries can be predicted by simply using a weighted fraction of the relative contribution of facet lengths times the respective symmetric boundary energy[46]. This relationship can be expressed by the equation,

$$\gamma_A = \gamma_{S1} \cdot \left[\cos\Phi - \sin\Phi\left(\frac{\cos\alpha}{\sin\alpha}\right)\right] + \gamma_{S2} \cdot \left[\frac{\sin\Phi}{\sin\alpha}\right] \quad (6\text{-}5)$$

where γ_A is the predicted energy of the asymmetric GB with different inclination angles Φ, γ_{S1} and γ_{S2} are the calculated energy of the two corresponding symmetric GBs, α is the interval angle separating the two symmetric GBs which depends on the crystal symmetry around the tilt axis (α=30° for [1 1 1] axis, α=45° for [0 0 1] axis and α=90° for [1 1 0] axis). Here, the calculated energies of the two Σ5 symmetric GBs are 948mJ/m^2 and 997mJ/m^2 respectively. The predicted

energy value by Equation (6-5) and the calculated energy value from MD simulations of the four asymmetric GBs are compared in Fig.6.4. The consistent trend and small deviation between the predicted and calculated energy values indicated that the faceting of asymmetric GBs into the structure units of the corresponding symmetric GBs was favourable from the point of view of energy.

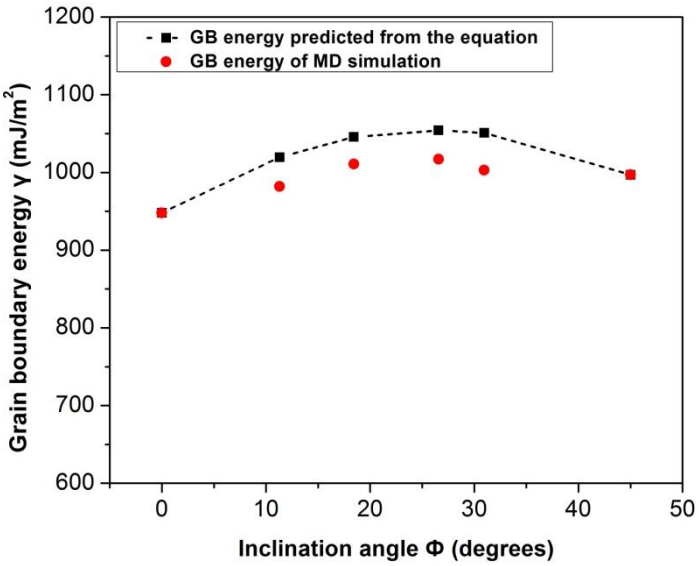

Figure 6.4 Grain boundary energy as a function of inclination angle of six Σ5 GBs. The solid square is the predict GB energy from equation (6-5), the dotted line is fitted by the predicted results which represents the trend of energy for Σ5 asymmetric GBs. The solid dot is the GB energy of MD simulation.

6.3.2 Mechanical response

Tensile simulations were conducted under both free tension boundary conditions and constrained tension boundary conditions in the present study. Figs.6.5(a) and (b) show the tensile stress-strain response of bicrystal models with different Σ5 GBs at 10 K. The tensile stress of the mechanical properties was attained by calculating the average stress along the Y direction of all the atoms of the simulation system, while the strain was derived from the positions of the periodic boundaries. Here, the maximum tensile stresses of the two symmetric GBs ($\Phi = 0°$ and $\Phi = 45°$) were higher than the four asymmetric GBs. The mechanical behaviour of different Σ5 GBs can be associated with their energy, as seen in Fig.6.4. Σ5 GBs with $\Phi = 0°$ and $\Phi = 45°$ show the comparative lower energy, and they have a more stable structure

and their tensile stresses are higher. Note that the maximum tensile stress of each case under constrained boundary conditions was much higher than with free boundary conditions, this was due to the stress that developed transverse to the loading direction during the deformation process.

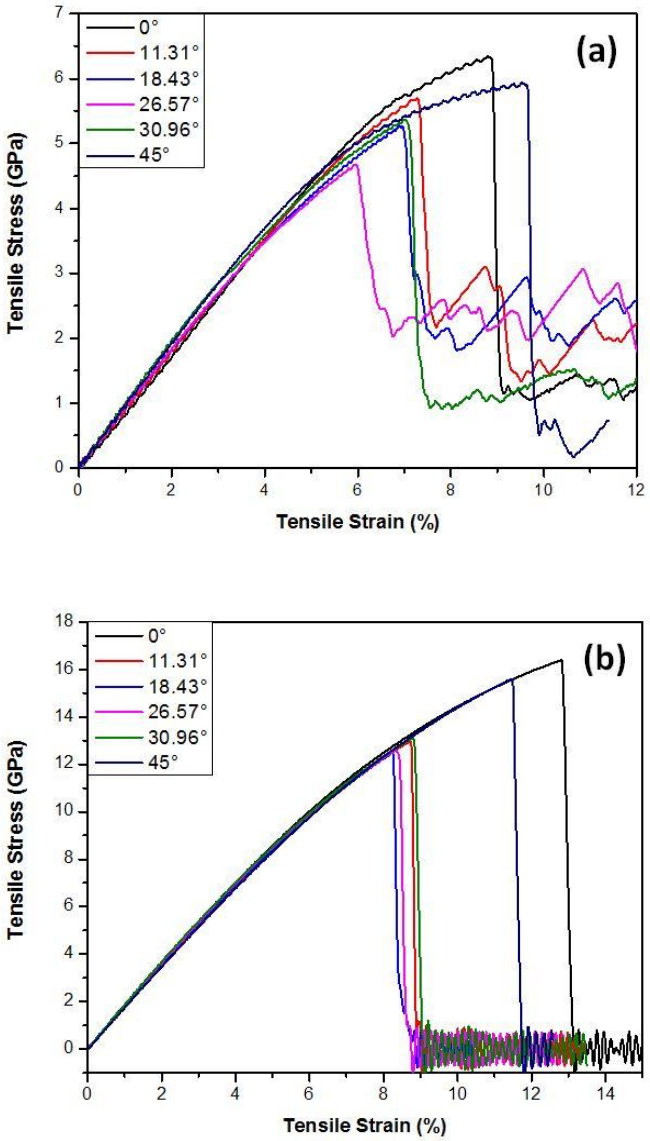

Figure 6.5 Mechanical response of Σ5 GBs with different inclination angles Φ at 10 K under (a) free tension boundary condition and (b) constrained tension boundary condition.

6.3.3 Deformation mechanism

A visual inspection of the MD simulation results indicated that the maximum tensile stress corresponded to the nucleation of partial dislocations, in agreement with the results for uniaxial tensile of Cu bicrystal studied by Spearot et al.[106,108]. Fig.6.6

shows a snapshot of atoms in Cu bicrystal with Σ5 (Φ = 0°) GB at different stages of deformation under free tension boundary conditions. The images are coloured according to their CNA value. Atoms with a perfect fcc structure were removed to facilitate viewing the defective structures. Atoms coloured yellow represent the GB plane and the dislocation core, while the blue atoms represent the stacking fault. The GB region coarsened when the tensile deformation was increasing until it reached its maximum tensile stress. In Fig.6.6(b), at the beginning of the stress drop (ε=8.9%), the image shows that partial dislocation loops with both edge and screw character were simultaneously nucleated from the bicrystal interface into the upper and lower grain. A DXA analysis indicated that Shockley partial dislocation with Burger's vectors **b**=(1/6)[1 1 2] and **b**=(1/6)[1 1 $\bar{2}$] nucleated from the bicrystal interface and slipped on the (1 1 1) and (1 1 $\bar{1}$) plane. According to the Schmid factor analysis they are the most favourable slip systems. The tensile stress required to nucleate the first partial dislocation from the Σ5 (Φ = 0°) GB at 10 K was 6.28 GPa, which corresponded to a critical resolved shear stress of approximately 3.08 GPa for the given lattice orientation. This result was comparable to the maximum resolved shear stress under the uniaxial tensile deformation of bicrystal Cu at 300 K obtained by Spearot[106]. With this increase in tensile strain the dislocations nucleated continuously from the GB plane and slipped in each grain, as seen in Fig.6.6(c).

Fig.6.7 shows the atomic details of Cu bicrystal with Σ5(Φ = 11.31°) GB at different stages of deformation under a free boundary condition. The GB region expands as deformation proceeds. Partial dislocations with Burger's vectors **b**=(1/6)[1 1 2] and **b**=(1/6)[1 1 $\bar{2}$] were nucleated in the lower grain region, as shown in Fig.6.7(b) at ε=7.3%, but unlike the case of Σ5 (Φ = 0°) GB, the dislocation only propagated into one crystal lattice when the maximum tensile stress was reached. This phenomenon can be attributed to the asymmetric GB with different orientation angles in the two grains. Partial dislocations were continuously nucleated and emitted into the lower grain until the tensile strain reached ε=7.6%, as

shown in Fig.6.7(c). The slip system was now activated in the upper grain, as shown by a partial dislocation with Burger's vectors **b**=(1/6)[1 1 2] nucleated from the interface and slipped along the $(1\,1\,\bar{1})$ plane. After that, the dislocation slipped collectively in both grain regions to accommodate plastic deformation during the tensile process. This same phenomenon has been observed in other cases of Cu bicrystals with asymmetric GBs, as shown in Fig.6.11.

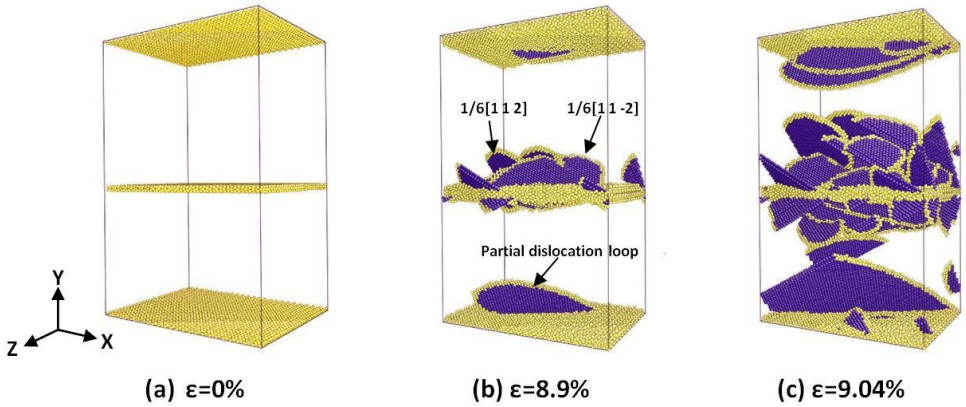

Figure 6.6 Snapshots of Cu bicrystal with Σ5 (Φ=0°) GB at different deformation stage under free tension boundary condition. Images are coloured according to the CNA parameter. Atoms with perfect fcc structures are removed to facilitate viewing of the defective structures. Atoms coloured with yellow organize the GB plane and the dislocation core, while the blue atoms represent the stacking fault.

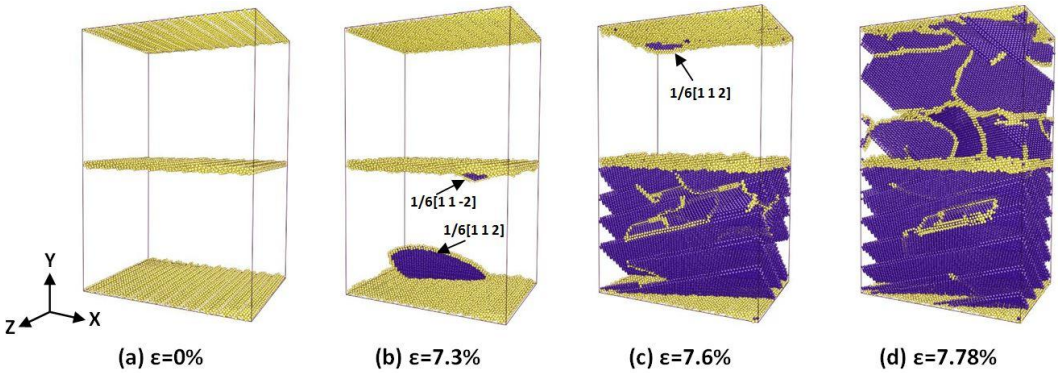

Figure 6.7 Snapshots of Cu bicrystal with Σ5 (Φ=11.31°) GB at different deformation stage under free tension boundary condition. Images are coloured according to the CNA parameter. Atoms with perfect fcc structures are removed to facilitate viewing of the defective structures. Atoms coloured with yellow organize the GB plane and the dislocation core, while the blue atoms represent the stacking fault.

Fig.6.8 shows the different stages of deformation of Cu bicrystal with Σ5 (Φ = 18.43°) GB when subjected to tensile deformation under constrained boundary

conditions. Figs.6.8(a)-(c) show a projected view of the atomic snapshots. Atoms with a perfect fcc structure are rendered as dark blue and atoms at the GB area and dislocation core are yellow. The light blue atoms indicate the stacking fault. Dislocations were extracted and are shown by continuous lines in Figs.6.8(d)-(f). In the elastic deformation stage, all the boundary atoms were well organised and the GB maintained its equilibrium configuration until it reached its maximum tensile stress. Fig.6.8(a) corresponds to the initial stage of plastic deformation when a crack was simultaneously initiated on 'grain boundary 1' and 'grain boundary 2' (the periodic boundary condition applied in the Y direction introduced a second boundary plane). Atoms are beginning to shuffle at the crack tips where a partial dislocation had nucleated, as seen in the enlarged area in Fig.6.8(a). Again, DXA analysis indicates the slip of partial dislocations occurred on both activated (1 1 1) and (1 1 $\bar{1}$) planes in the lower grain region, which agrees with the Schmid factor analysis. As the tensile strain increased the fast drop in tensile stress was associated with the progressive separation of the GBs and the partial dislocation nucleation from the crack tips, as seen in Figs.6.8(b) and (e). The high density of the dislocation network at ε=8.44% only remained for a short period and then gradually decreased as the GB plane cleaved and the two grains separated, as seen in Figs.6.8(c) and (f). Interestingly, this dislocation was not emitted into the upper grain region during the tension process. Unlike the massive dislocations and slipping in the bicrystal models under free tension boundary conditions, only limited dislocations occurred in the cases studied under constrained boundary conditions. The crack began and extended along the GB plane in a cleavage manner, and eventually resulted in the model fracturing, as shown in Fig.6.12.

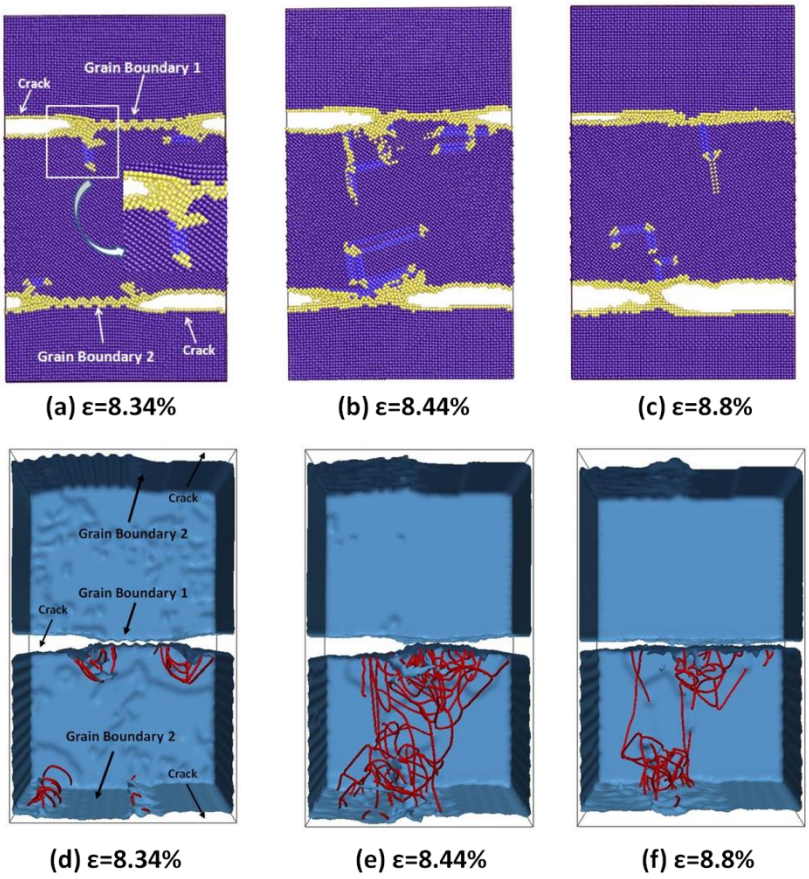

Figure 6.8 Snapshots of Cu bicrystal with Σ5 (Φ=18.43°) GB at different deformation stage under constrained tension boundary condition. Images (a)-(c) are coloured according to the CNA parameter, atoms with perfect fcc structure are rendered as dark blue, atoms at GB area and the dislocation core are rendered as yellow, the light blue atoms indicate the stacking fault. Dislocation segments are extracted in (d)-(f).

6.4 Discussion

Unlike the symmetrical GBs which possessed a mirror symmetry of crystallographic planes, the asymmetric GBs were relative complex with a multiplicity of atomic structures resulting from boundary dissociation, nano-faceting, and other fundamentally interesting structural effects. Simulations[45,46] revealed that asymmetric GBs tended to break into nano-scale facets that consist of their corresponding symmetric boundaries. Sutton and Balluffi[51] proved that geometrically, an asymmetric GB could facet into a symmetric GB. This was also confirmed in the simulation of e Σ5 GBs where all the asymmetric boundaries were organised by a combination of different ratios of E and E′ structure units that correspond to the Φ =

0° and Φ = 45° symmetric boundary respectively. However, a recent study of Σ11 [1 1 0] tilt GBs[47] with different angles of inclination revealed that it is not necessary for the asymmetric boundaries to dissociate into symmetric ones because the faceted boundary may not even belong to any particular CSL. It was reported that the asymmetric Σ11 [1 1 0] GBs dissociated into a low-angle GB formed by Shockley partial dislocations and a high-angle non-Σ11 boundary. This kind of faceting into non-symmetric boundary structures and incorporating facets of non-Σ boundary do not exist in our simulation of Σ5 GBs, primarily because of the differences in boundary energy. Gokon et al.[49,50] experimentally determined the boundary energies of Σ11 [1 1 0] and Σ9 [1 1 0] tilt GBs in Cu for various angles of inclination and found the facet planes often corresponded to a nearby symmetric or asymmetric boundary with low energy. According to the simulation of Σ5 GB energy in the present study, as seen in Fig.6.4, the energies of asymmetric GBs are comparable to the Φ = 45° symmetric boundary and higher than the Φ=0° symmetric boundary. From the point of view of energy, this may explain why Σ5 asymmetric GBs were faceted into the symmetric Φ = 0° and Φ = 45° planes.

The simulations revealed that dislocations can be emitted into both grains of the symmetric GBs once they reached their maximum tensile stress. However, in the simulation with an asymmetric GB the dislocation emission only occurred at the lower grain region at the beginning, and then the slip systems in the upper grain can be activated, as shown in Fig.6.11. Grains on each side of an asymmetric GB are oriented differently relative to the tensile stress direction, and result in different Schmid factors. Therefore, the slip systems can easily be activated in the grain which associates with the higher Schmid factor because the slip systems in this grain have a higher resolved shear stress. Fig.6.9 shows the maximum Schmid factor for both grains of the bicrystal models as a function of the inclination angle. Fig.6.9 shows that the maximum Schmid factor was higher in the lower grain for all the cases with asymmetric GBs, which might explain why the partial dislocations

nucleated first into the lower grain. For the asymmetric GBs, the nucleation of dislocations in the upper grain only occurred at higher strains when excessive dislocation emission severely altered the initial orientation of the lower grain.

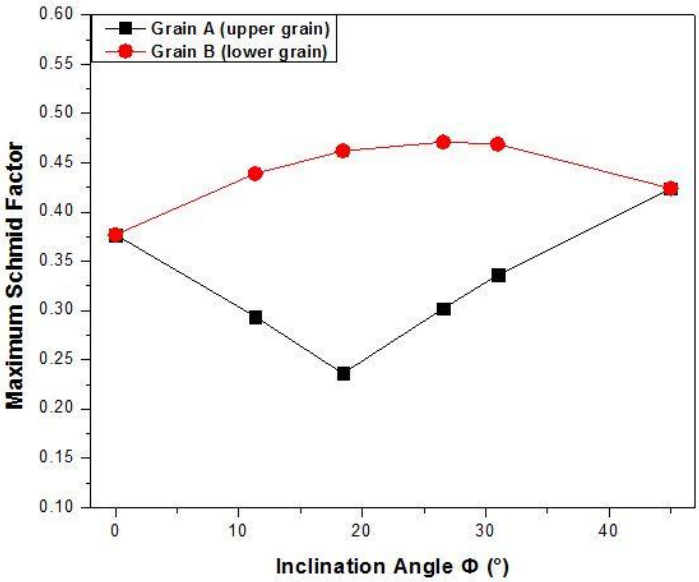

Figure 6.9 The maximum Schmid factor as a function of GB inclination angle for grain A and grain B of the bicrystal models. Grain A and Grain B are defined in the bicrystal model in Fig.6.1.

It has been found in this study that the stress state played an important role in the deformation mechanisms of nanocrystalline materials. The well established von Mises yield criterion can be used to explain the MD results. In this study, only principle stress was applied, so the von Mises yield criterion can be described as following,

$$\sigma_v = \sqrt{\frac{1}{2}[(\sigma_1 - \sigma_2)^2 + (\sigma_1 - \sigma_3)^2 + (\sigma_2 - \sigma_3)^2} \quad (6\text{-}6)$$

In the case of free tension boundary condition ($\sigma_1 = \sigma_3 = 0$), the von Mises criterion simply reduces to,

$$\sigma_v = \sigma_2 \quad (6\text{-}7)$$

which means the material starts to yield when σ_2 reaches the yield strength of the material σ_v, and is in agreement with the definition of tensile yield strength. On the other hand, in the case of constrained tension boundary condition ($\sigma_2 > \sigma_1 = \sigma_3 \neq 0$),

the von Mises criterion can expressed as,

$$\sigma_v=\sigma_2-\sigma_1=\sigma_2-\sigma_3 \quad (6\text{-}8)$$

From equation (6-7) and (6-8), it is deduced that the simulation model starts to yield at a higher tensile stress (σ_2) under constrained boundary condition than the value under free boundary condition. This deduction was confirmed by the MD simulations.

The dislocation nucleation from the GB and its propagation was the dominant deformation mechanism during tensile deformation under free tension boundary conditions, as shown in Fig.6.11. However, due to the transverse stress applied perpendicular to the tensile stress under constrained tension boundary condition, the nucleation of dislocation and its propagation was restrained. Meanwhile, cracks are prone to begin and can extend rapidly along the GB plane, and then crack propagation dominates in the following deformation and leads to a brittle failure, as shown in Fig.6.12. It was seen that only partial dislocation loops were nucleated from the Cu bicrystal interfaces during the tensile process under free tension boundary condition, but it is interesting to find that full dislocation loops can also nucleate from boundary plane under a constrained tension boundary condition, as shown in Fig.6.10 for the case of Σ5 ($\Phi = 0°$) GB. In Fig.6.10(a), the leading partial dislocations have nucleated and moved away from the boundary plane, leaving behind an intrinsic stacking fault. As this deformation proceeded the trailing partial dislocation began to emit, resulting in a full dislocation loop. The latter then passed through the periodic boundaries, as shown in Fig.6.10(b) and (c). In the published studies[33,104,157], the trailing partial dislocation mainly nucleated in the fcc metals with high stacking fault energy (*e.g.* Al 146 mJ/m^2 [221]), while the nucleation of full dislocation in the fcc metals with low stacking fault energy (*e.g.* Cu 44.4 mJ/m^2 [137]) was thought to be difficult. To the best understanding of the author, few of the previous simulation studies have reported the full dislocations nucleation from the Cu sample. The observation of the full dislocations of Cu bicrystals under constrained tension boundary condition in this study emphasised the important influence of the

stress state on the deformation mechanism of nanocrystalline materials.

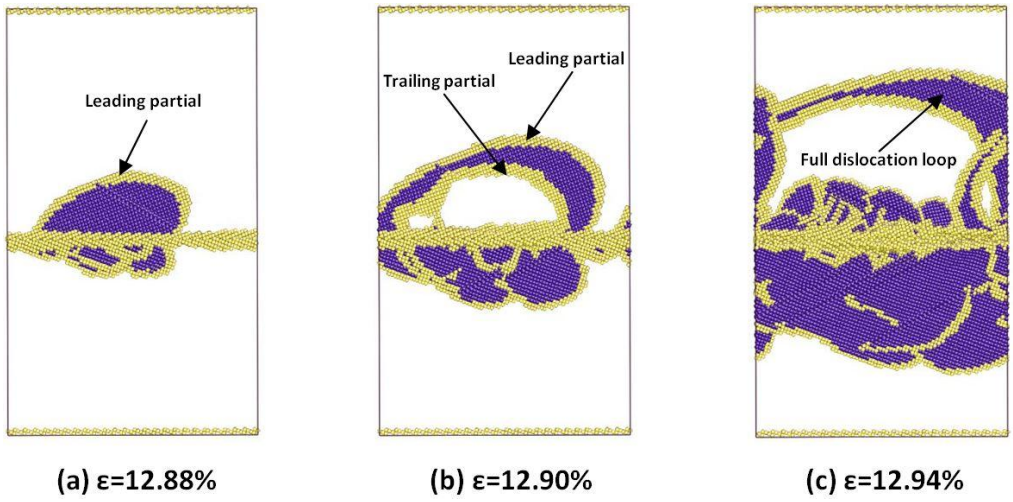

Figure 6.10 Snapshots of Cu bicrystal with Σ5 (Φ=0°) GB at different deformation stage under constrained tension boundary condition. Images are coloured according to the CNA parameter. Atoms with perfect fcc structures are removed to facilitate viewing of the defective structures. Atoms coloured with yellow organize the GB plane and the dislocation core, while the blue atoms represent the stacking fault.

6.5 Summary

Molecular dynamics simulations were conducted to study the structures and mechanical behaviour of Σ5[0 0 1] tilt GBs in copper bicrystal. First, equilibrium GB structures were generated by molecular statics simulation at 0K. It was found that the Σ5 asymmetric GBs with different inclination angles (Φ) consisted of only two structural units that corresponded to the two Σ5 symmetric GBs. Molecular dynamics simulations were then conducted to investigate the mechanical response and underlying deformation mechanism in the bicrystals with different Σ5 GBs under tension. Tensile deformation was applied under both 'free' and 'constrained' boundary conditions. The simulation results revealed different mechanical properties of the symmetric and asymmetric GBs and indicated that the stress state plays an important role in the deformation mechanism of nanocrystalline materials.

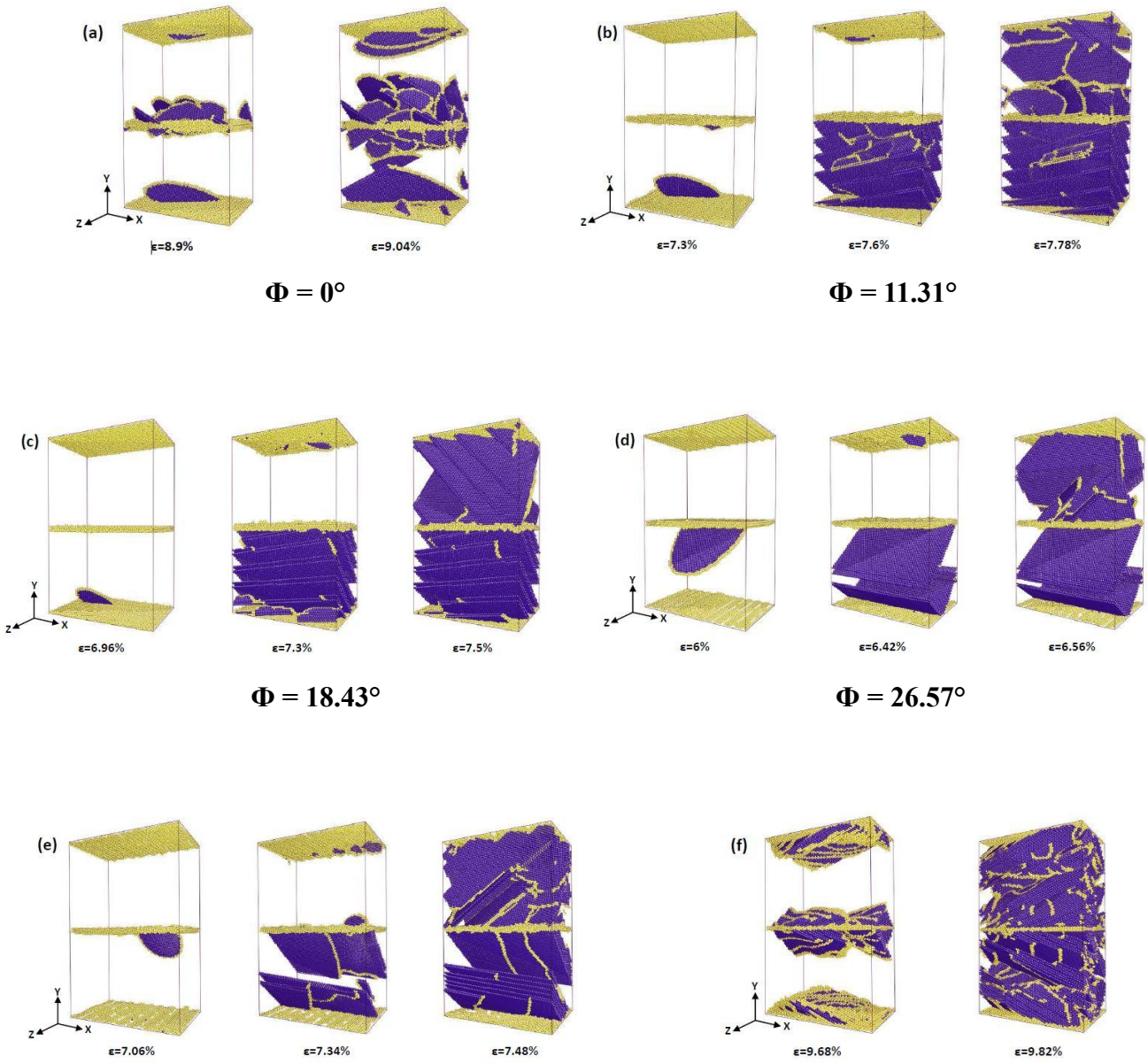

Figure 6.11 Dislocation nucleation and propagation in Cu bicrystal under free tension boundary condition at 10 K with (a) Σ5 (Φ = 0°) GB, (b) Σ5 (Φ = 11.31°) GB, (c) Σ5 (Φ = 18.43°) GB, (d) Σ5 (Φ = 26.57°) GB, (e) Σ5 (Φ = 30.96°) GB and (f) Σ5 (Φ = 45°) GB.

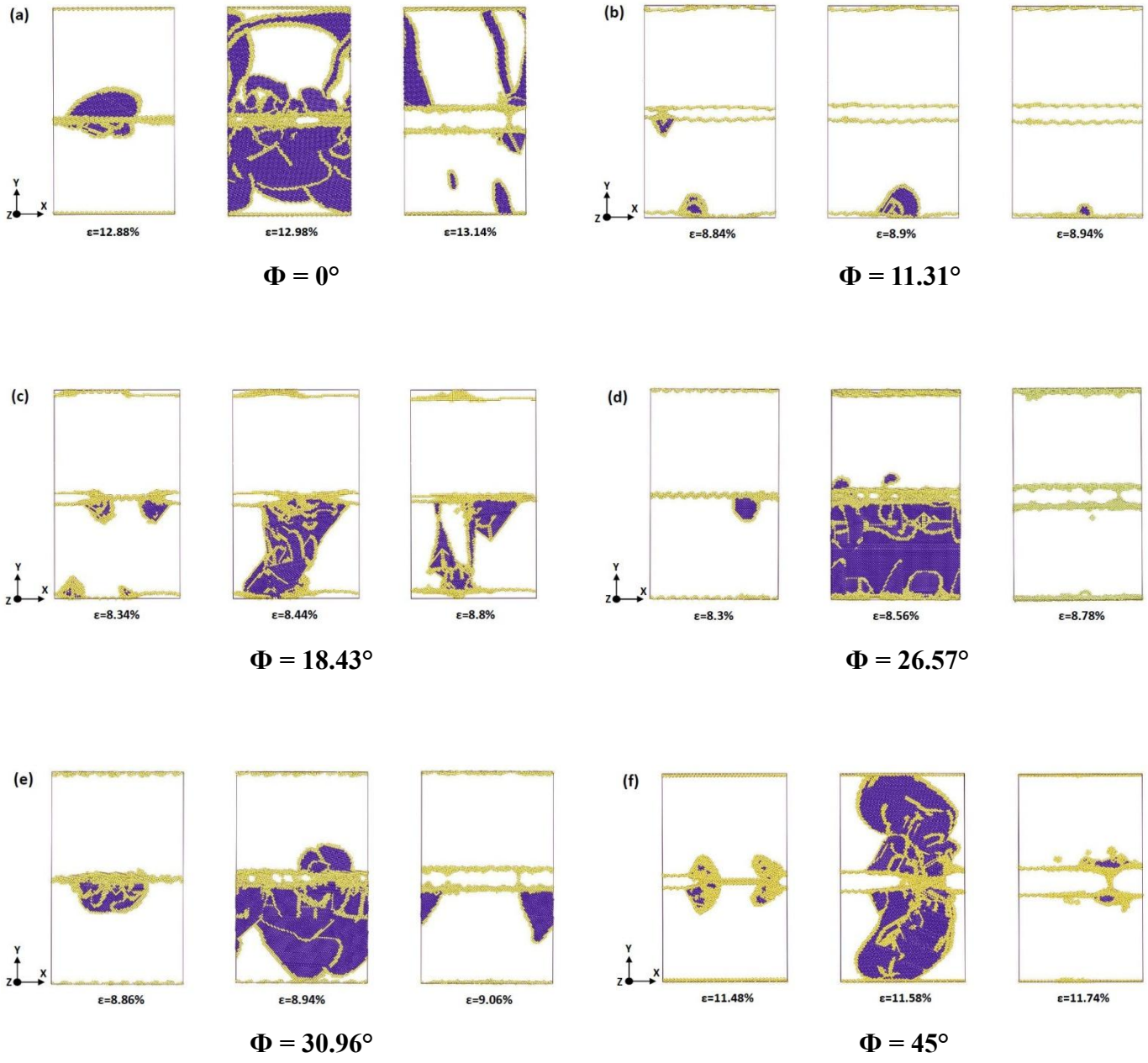

Figure 6.12 Dislocation nucleation and propagation in Cu bicrystal under constrained tension boundary condition at 10 K with (a) Σ5 (Φ = 0°) GB, (b) Σ5 (Φ = 11.31°) GB, (c) Σ5 (Φ = 18.43°) GB, (d) Σ5 (Φ = 26.57°) GB, (e) Σ5 (Φ = 30.96°) GB and (f) Σ5 (Φ = 45°) GB.

CHAPTER 7

Shear Response of Copper Bicrystals with Σ11 Tilt Grain Boundaries

In this chapter molecular dynamics simulations were carried out to investigate the shear response and deformation mechanisms of symmetric and asymmetric Σ11<1 1 0> tilt GBs in copper bicrystal. Different deformation mechanisms were reported, depending on the GB inclination angles and equilibrium GB structures, including GB migration coupled to shear deformation, GB sliding caused by local atomic shuffling, and dislocation nucleation from GB. The work of this chapter has been published previously in *Nanoscale* **7**, 7224-7233.

7.1 Introduction

Many recent experimental and simulation works indicated that the dislocation activities in the interior grains decrease when the average grain size is less than 100 nm, whereas mechanisms mediated by the grain boundary (GB) become dominant[3,56]. A strong interplay between inter-granular and intra-granular deformation processes was found in nanocrystalline metals, so understanding how the nanoscale grain boundary networks affect deformation is critical. The grain boundary in nanocrystalline structures can restrict dislocation propagation and also act as a source for new dislocations which affect the detailed dynamics of dislocation-mediated plasticity[222]. In particular, grain boundary accommodation mechanisms such as GB sliding, GB migration, and grain rotation has long been recognised as important mechanisms of deformation for very small grain sizes[223]. Unlike experimental observations which are difficult at the nanoscale level, and very time consuming, atomistic simulation has a lot of advantages. For example, molecular dynamics (MD) simulation helps in the study of plasticity because the

deformation conditions can be controlled and a detailed investigation of the underlying atomic scale processes that results in extremely detailed atomistic information can be carried out. Moreover, the visualisation tools[140,141] and sophisticated automated dislocation detection techniques[144,145,183] have improved greatly in recent years, so we can now gather more information at the atomic scale.

Bicrystal atomic configuration geometry is often used to systematically study the correlation of grain boundary structures and material properties, and that makes it ideal for studying high-angle coincident site lattices (CSL). Bicrystal models have been used in many previous research works with fruitful results. For instance, Sansos and Molinari[43,65] correlated individual failure mechanisms to the presence of certain structural units along the interface plane using the quasi-continuum method, and reported different failure mechanisms of bicrystal Cu and Al, depending on when their grain boundary structures are subjected to tensile and shear deformation, including GB sliding by atoms shuffling, nucleation of partial dislocations from GB, and GB migration. Using MD simulations, Cahn and Mishin et al.[71], and Wan et al.[224] showed that some symmetric tilt GBs can migrate when a shear deformation is applied parallel to the GB plane, and they also provided a correlation between the shear stress, the structure of grain boundaries (in terms of structural units) and their normal motion. Koning et al.[225,226] and Jin et al.[95,96] used bicrystal models to investigate the barrier effect of different GBs and twin boundaries with respect to dislocations, and then proposed the conditions under which dislocation transmission can occur across a grain boundary. Spearot and McDowell et al.[104-106] used MD simulations to examine the dislocation nucleation from different GB planes in bicrystal Cu and Al, by focusing on the evolution of the grain boundary structures during dislocation nucleation and the resulting structure of the grain boundary after dislocation emission. Because bicrystal systems enable a more controlled investigation of specific GB properties, the present study will take full advantage of the bicrystal model to investigate the mechanical properties and deformation

mechanisms of certain grain boundaries.

Most of the experiments and simulations conducted so far focused primarily on symmetric tilt GBs, whereas the less studied cases of asymmetric tilt GBs are more complex but pose new and interesting questions. For example, Bachurin et al.[227] carried out an atomistic simulation to study the interaction of dislocations with some GBs in Ni bicrystal, and showed that symmetric GBs and asymmetric GBs can play a different role in blocking the incoming dislocations. Tschopp et al.[108] and Zhang et al.[164] used an MD simulation to investigate dislocation nucleation from both symmetric and asymmetric Σ3<1 1 0> tilt GBs and Σ5<0 0 1> tilt GBs under uniaxial tension and found that the mechanical properties of GB depended upon GB misorientation and the inclination of the GB plane. The simulation results from Trautt and Mishin et al.[78], Hao et al.[212], and Fensin et al.[79] indicated that stress-driven GB migration not only occurs in symmetric GBs but also in some asymmetric GBs. Although this previous work on asymmetric GBs has increased our understanding of the structures and energy on these boundaries, and provided an insight into related GB properties, our understanding of the deformation mechanisms of asymmetric GBs at the atomic scale is still limited. In this study molecular dynamics simulations were carried out to investigate the shear response of Cu bicrystal with symmetric and asymmetric Σ11<1 1 0> tilt GBs, and reported that different mechanical properties and deformation mechanisms exist, depending on the GB inclination angles and local GB structures.

7.2 Simulation Methodology

In this study MD simulations were carried out using the parallel molecular dynamics code LAMMPS[139] with the embedded-atom method (EAM) potentials for Cu developed by Mishin et al.[137]. A bicrystal model was created by constructing two separate crystal lattices (grain-A and grain-B in Fig.7.1) with different crystallographic orientation and joining them together along the Y axis. A periodic boundary condition was applied in the X and Z directions while a non-periodic

boundary condition was applied in the Y direction. Details of the grain boundary and the dimensions of the bicrystal models are presented in Table 7.1.

Table 7.1 Details of Σ11 grain boundary and dimensions of bicrystal models.

Boundary type	Inclination angle Φ (°)	Boundary plane (h k l)A/B	Boundary energy γ (mJ/m^2)	Structural unit period	Model dimensions X×Y×Z (Å)
Symmetric	0	(1 1 -3)/(1 1 3)	307	|…C.C.C.C.C…|	144.4×216.6×36.1
Asymmetric	54.74	(2 2 5)/(4 4 1)	662	|…DCE.DCE…|	146.9×218.4×36.1
Asymmetric	70.53-A	(5 5 7)/(7 7 -1)	706	|…DDE.DDE…|	152.7×216.6×36.1
Asymmetric	70.53-B	(5 5 7)/(7 7 -1)	702	|…DED.DED…|	152.7×216.6×36.1
Symmetric	90	(3 3 2)/(3 3 -2)	722	|…ED.ED.ED…|	144.4×216.6×36.1

The equilibrium GB structure was prepared using a combination of molecular statics and MD simulations. A molecular statics calculation using an energy minimisation procedure with a standard conjugate-gradient algorithm was carried out to determine the minimum energy configuration of each grain boundary. A number of initial "starting positions" of grain-A and grain-B were tested to find the most favoured GB structures from the point of view of energy[45,181,182,228]. While changing the positions of the two grains before the energy minimisation procedure, an overlap between the grains may result in an unphysically short distance between two atoms. If the pairs of atoms whose distance of separation was within the cut off distance then one atom was arbitrarily deleted in grain-B. In the simulation, the cut off distance was specified as $0.5a_0$, where a_0 is the lattice constant. This insures that the first nearest neighbour atoms ($\sqrt{2}/2a_0$) are not within the cut off distance for the crystal structure. After energy minimisation, the energy of each GB structure was then calculated and compared to find the possible global minimum energy configuration. After the minimum energy structure was attained, the simulation model was equilibrated using MD in the isobaric-isothermal (NPT) ensemble at a pressure of 0 bar and a temperature of 10 K for 20 ps. The primary goal of this present study was to investigate the shear response of different GBs and its

connection with the structure evolution, so the simulation temperature was set at 10 K throughout the simulations to avoid thermal disturbance of atoms at high temperatures.

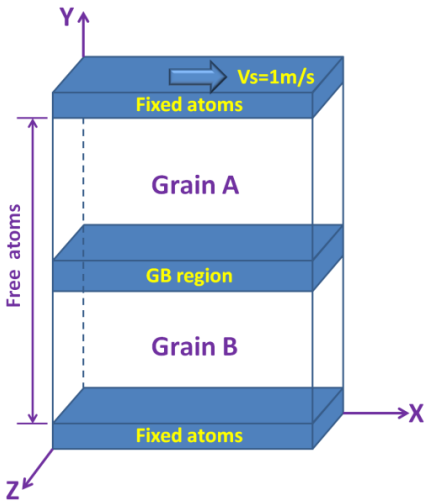

Figure 7.1 Schematic of shear deformation applied onto the bicrystal model. Atoms on the top of grain-A and atoms at the bottom of grain-B are fixed, all the other atoms in the model were set free. A constant shear velocity V_s=1m/s parallel to the boundary plane was applied on the fixed area of grain A along the X direction.

Once the equilibrium state of GB was reached, a shear deformation was applied to the bicrystal model. Atoms on the top of grain-A and atoms at the bottom of grain-B were fixed, the thickness of each fixed slab was approximately twice the cut off radius of atomic interactions[71], while all the other atoms in the model were set free. Fig.7.1 shows a schematic of the computational cell in the simulations. A constant shear velocity V_s=1m/s (about 4.6×10^7/s shear strain in this study) parallel to the boundary plane was applied onto the fixed area of grain-A in the X direction. The fixed atoms in grain-A did not participate in the MD simulations and only moved at 1m/s as a rigid body, while the fixed atoms in grain-B remained stationary. Stress and temperature calculations were performed on the dynamic atoms between the two fixed slabs, while the stress tensor was calculated by the standard virial expression. Throughout the MD simulation, the NPT method was used and the time increment of simulations was fixed at 1 fs.

7.3 Results and Discussion

7.3.1 Grain boundary structure

Two symmetric (Φ=0°, Φ=90°) and two asymmetric (Φ=54.74°, Φ=70.53°) Σ11<1 1 0> (θ=50.5°) tilt grain boundaries were investigated in this study, where θ is the misorientation angle of the two grains constructed in the bicrystal model, and Φ is the inclination angle of the GB plane which is defined as the angle between the boundary plane and the bisector of the misorientation angle θ. The structures of the two selected asymmetric GBs can represent the typical structure of Σ11<1 1 0> asymmetric GBs in a wide range of inclination angles (0°<Φ<90°)[46,229]. Fig.7.2 shows the equilibrium GB structures that resulted from the energy minimisation procedure and subsequent MD relaxation at 10 K with a zero stress state for the Cu bicrystal. The GB structure area was identified using the common neighbour analysis (CNA) technique[63]. Note that for the asymmetric Σ11(5 5 7)/(7 7 $\bar{1}$) Φ=70.53° GB, two different equilibrium structures with a similar GB energy (706 mJ/m^2 and 702 mJ/m^2) were found after constructing the model. Since the GB energy of the two structures are very close and were much lower than the value of other structures, they were both considered in this study. For convenience, the two different GB structures will be known as Φ=70.53°-A and Φ=70.53°-B (see Fig.7.2). Structural units as defined by Rittner and Seidman[180] were used to illustrate the boundary structures, while the symmetric Σ11(1 1 3) Φ=0° GB and Σ11(3 3 2) Φ=90° GB consisted entirely of C and E structural units respectively. For the asymmetric Σ11(2 2 5) Φ=54.74° GB, the boundary area was a combination of C and E units at the boundary plane and a D unit at the termination of an intrinsic stacking fault that extended from the boundary plane. Similarly, a dissociated GB structure was also observed in the two structures of Σ11(5 5 7) Φ=70.53° GB, where the periodic units can be described as "DDE" and "DED" respectively.

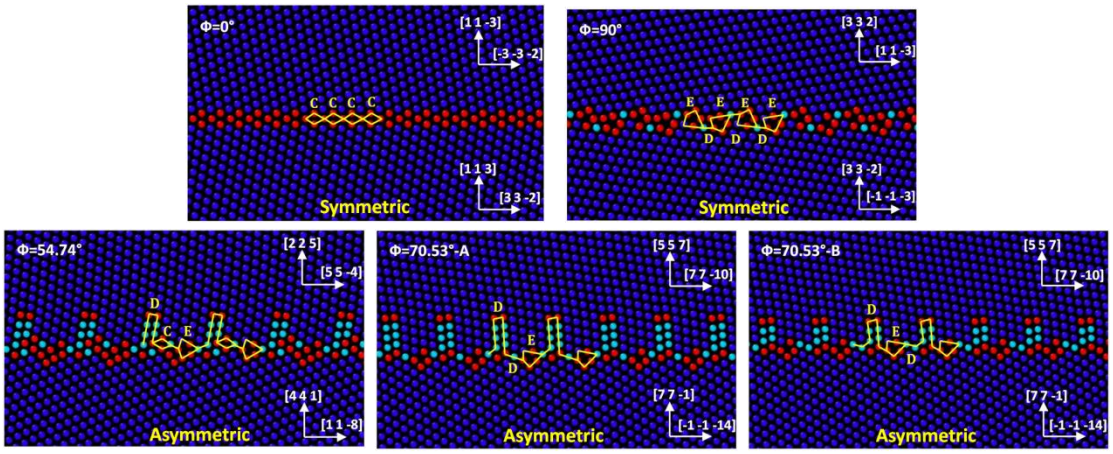

Figure 7.2 The equilibrium structures of the Σ11 symmetric and asymmetric GBs obtained by the energy minimization procedure and subsequent MD relaxation at 10 K. The images are viewed along the [1 $\bar{1}$ 0] tilt axis and are coloured according to the CNA parameter. Atoms with perfect fcc structures are blue, the red atoms organize the GB plane and the dislocation core, and the continuous light blue atoms represent the stacking fault. The boundary normal vector of the two grains are marked on the right hand side for each GB. The structural units at each boundary plane are outlined by the solid line and marked by C, D, and E.

7.3.2 The shear response of Σ11(1 1 3) Φ=0 °GB

The shear stress of the bicrystal model with Σ11(1 1 3) GB as a function of simulation time is plotted in Fig.7.3(a). After reaching its critical shear stress (3.61 GPa) the Σ11(1 1 3) GB showed a sliding-migration coupling motion with a further increase of shear deformation where the upper grain slide was relative to the lower grain while the GB migrated from the centre of the bicrystal to the upper grain. The four abrupt drops in the stress curve corresponded to the four intensive GB migrations. The movement of high-angle GBs in the coupled manner under stress can be regarded as the motion of perfect GB dislocation[230] where in this case the GB plane remained almost flat during the coupling motion. This result suggested that the sliding of Σ11(1 1 3) GB resulted from the motion of GB dislocations with Burgers vector parallel to the GB plane. Of the different GB dislocations formed by the crystal lattice dislocations, perfect GB dislocations with Burgers vector **b**=(1/22)<3 3 2> satisfy this condition. This theoretical speculation was identified by Fukutomi and Kamijio in their experimental observation on bicrystal aluminium[231] as well as in the present MD simulation.

The detailed process of GB coupling motion is shown in Fig.7.3. Figs.7.3(b) and (c) are two consecutive snapshots from the MD results that indicated the first GB migration event. Fig.7.3(d) shows the dislocation extracted from the corresponding MD results by the Crystal Analysis Tool[144,145]. All the C structural units were in the same plane until t=1.584 ns, when a step at the GB plane appeared, as shown in Fig.7.3(b). The left part of GB_1 had migrated upwards to GB_2 (marked by the dashed line) by a distance (H1) of two atomic layer heights along the [1 1 3] direction. The GB step, or GB disconnection was caused by the GB dislocation **b**=(1/22)[3 3 2], as marked with 'GB dislocation 1' in Fig.7.3(b). It is indicated by the extracted red line in Fig.7.3(d) at t=1.584 ns. This was consistent with the previous experiment result[231], but unlike the experimental observation, the simulation showed that (1/22)<3 3 2> was not the only type of GB dislocation existing in the process of GB migration. With a further increase of shear deformation, while the former step between GB_1 and GB_2 still existed, another two steps appeared at the boundary area which introduced two new GB planes indexed as GB_3 and GB_4 (see Fig.7.3(c) at t=1.586ns). Notice that the two steps are only one atom layer height (H2) along the [1 1 3] direction, indicating that another type of dislocation may exist in the boundary plane. This is confirmed in Fig.7.3(d) when the dislocations were detected at this time. It is easy to find that the red line with **b**=(1/22)[3 3 2] represents the former step, while the two blue lines with **b**=(1/22)[7 4 $\bar{1}$] indicate the two evolutive steps. The new type of GB dislocation is marked with 'GB dislocation 2' in Fig.7.3(c).

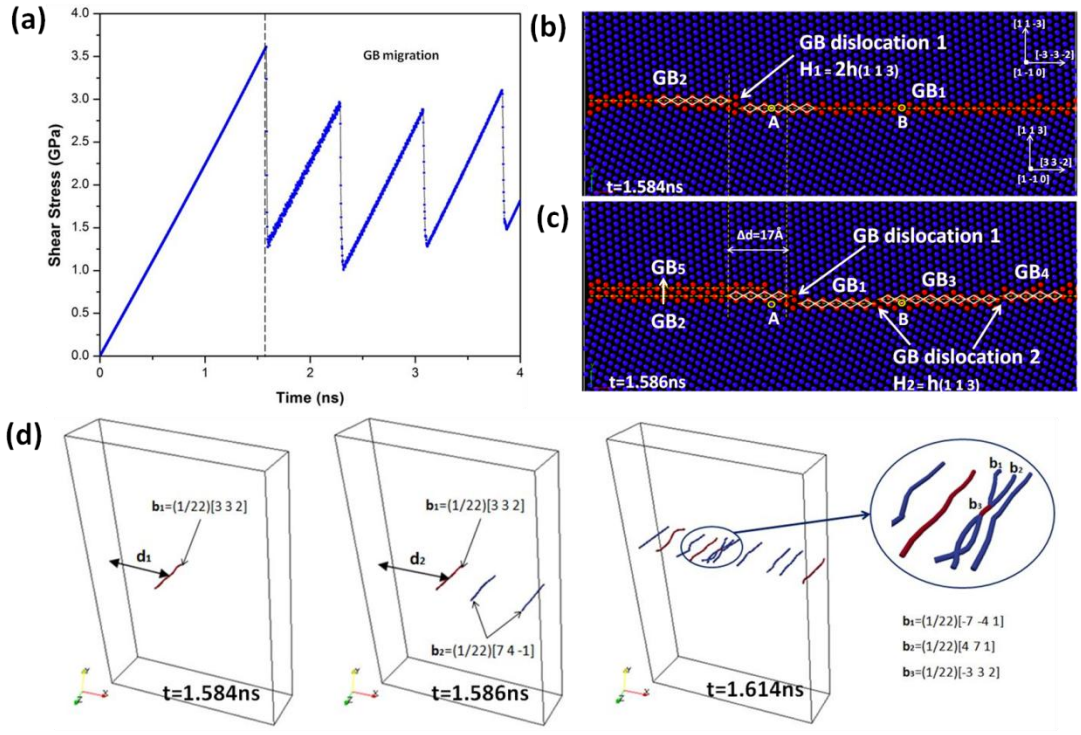

Figure 7.3 Shear response of Σ11(1 1 3) Φ=0° GB. (a) Shear stress as a function of simulation time. (b) and (c) Snapshots of the enlarged GB area at t=1.584 ns and t=1.586 ns. Atoms with perfect fcc structures are blue, and the red atoms organize the GB plane. (d) Dislocation extracted from the corresponding MD results.

From Figs.7.3(b) to (c), the step has moved along the grain boundary a distance (Δd=d2-d1) of about 17Å. Meanwhile, more of GB_1 has migrated to GB_2 which implies that the sliding of GB dislocation was closely connected to GB migration. Specifically, after the GB dislocation had passed, atoms such as A and B, which were a coincidence site before the migration of GB_1 in Fig.7.3(b), were no longer a coincidence site in Fig.7.3(c). If all the GB atoms were uniquely arranged around the coincidence site, the GB was considered to migrate. Moreover, the migrating GB plane was not completed one layer after another, as shown in Fig.7.3(c), when the migration of GB_1 to GB_2 was still in progress due to the propagation of GB dislocation, the trailing part of GB_2 was already prepared for another migration to GB_5. An inconsonant movement of the GB plane can result in a series of steps or disconnections at the boundary plane, indeed Fig.7.3(d) at t=1.614 ns shows that a number of GB dislocations (1/22)<3 3 2> (red lines) and (1/22)<7 4 1> (blue lines)

coexist. As the experiment[231] and geometric analysis indicated, the coupling motion of Σ11(1 1 3) GB was attributed to a GB dislocation (1/22)<3 3 2> sliding along the GB plane. So how does GB dislocation (1/22)<7 4 1> work? Fig.7.3(c) shows that GB_4 was at the same height as GB_2, in other words the two steps caused by the GB dislocation (1/22)<7 4 1> had the same effect on GB migration as the step result from the GB dislocation (1/22)<3 3 2>. It was naturally assumed there should be some correlation between the two types of GB dislocations where this assumption is identified in the enlarged area in Fig.7.3(d) at t=1.614 ns. The two blue lines with Burger's vectors $\mathbf{b_1}$ and $\mathbf{b_2}$ have merged into the red line with Burger's vector $\mathbf{b_3}$, which implies the (1/22)<7 4 1> dislocation can transform to (1/22)<3 3 2> dislocation through a GB dislocation reaction. This reaction can be described as,

$$(1/22)[\bar{7}\ \bar{4}\ 1] + (1/22)[4\ 7\ 1] \rightarrow (1/22)[\bar{3}\ 3\ 2]$$

In this study the Burger vectors of boundary dislocations in all the equations of dislocation reaction were defined based on the upper lattice frame (grain-A).

7.3.3 The shear response of Σ11(2 2 5)/(4 4 1) Φ=54.74° GB

The shear stress of the bicrystal model with Σ11(2 2 5)/(4 4 1) GB as a function of simulation time is plotted in Fig.7.4(a). It was found that the bicrystal model deformed in four stages: elastic, plastic, strain-hardening, and strain-softening. These stages are divided by the dashed line in Fig.7.4(a) and the corresponding deformation configurations are presented in Fig.7.4(b).

In the elastic stage, the GB structure kept its initial equilibrium configuration until it reached the yield stress (σ_y=0.54 GPa). According to the Crystal Analysis results in Fig.7.4(c), the equilibrium boundary structure can be regarded as consisting of an array of GB dislocations with Burgers vector **b**=(1/6)[$\bar{1}\ \bar{1}\ \bar{4}$] and **b**=(1/3)[1 1 $\bar{1}$]. The onset of plasticity corresponded to the collective movement of the dissociated 1/6[1 1 $\bar{2}$] Shockley partial dislocations from the GB plane and the extension of the intrinsic stacking fault behind (see Fig.7.4(b) at t=0.6 ns).

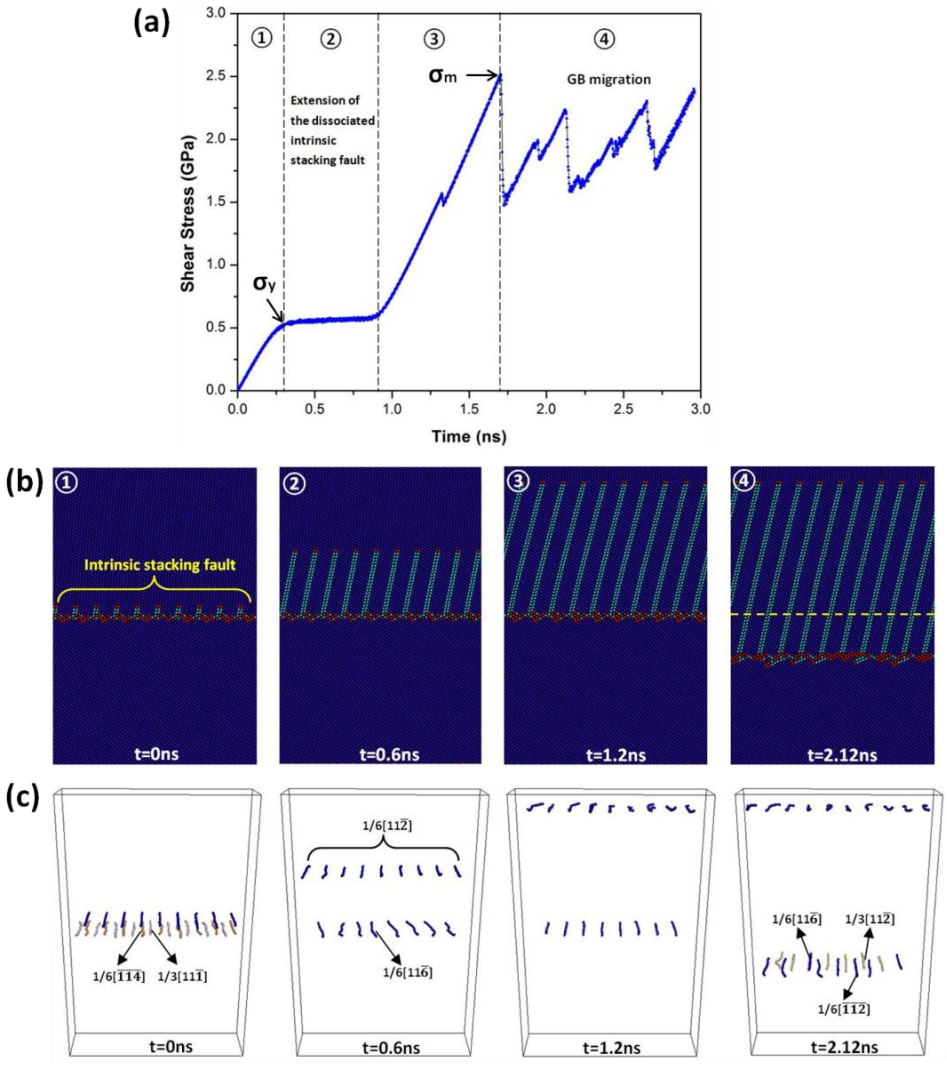

Figure 7.4 Shear response of Σ11(2 2 5)/(4 4 1) Φ=54.74° GB. (a) Shear stress as a function of simulation time. (b) Snapshots of the deformation stage corresponding to the four dominant regimes in (a). Atoms with perfect fcc structures are blue, the red atoms organize the GB plane and the dislocation core, and the continuous light blue atoms represent the stacking fault. (c) Snapshots of the extracted dislocations during the shear process.

Note that the stress curve reached a plateau in the plastic stage, which indicated that the dislocations emitted from the GB played a small role in accommodating the system stress, unlike the previous finding where the stress curve started to drop once the dislocation became active[43,104,105,164]. This was mainly due to the intrinsic structure of the GB with the embryo dislocations where only a low stress can drive them to emit. Here, this process is described as dislocation "emission" instead of "nucleation" because the yield stress corresponded to the release of the dissociated

partial dislocations rather than nucleating new dislocations from the GB plane into the bulk crystal lattice. During the emission process in stage-2, the boundary rearranged itself by adjusting the positions of local atoms. This rearrangement can be regarded as a combination of GB dislocations that can be described by:

$$(1/6)[\bar{1}\ \bar{1}\ \bar{4}] + (1/3)[1\ 1\ \bar{1}] \rightarrow (1/6)[1\ 1\ \bar{6}]$$

Note that the propagation of dislocations was blocked when they reached the fixed area of the simulation model. After that, the stress curve reached the strain-hardening stage with a continuous increase in stress without any new deformation mechanisms to release the system stress (see Fig.7.4(b) at t=1.2 ns). From a physical perspective, the fixed area in the model can be regarded as another grain boundary which blocks the dislocation slipping. This always happens in polycrystalline materials where the grain boundaries hinder the transmission of dislocations and create a dislocation pile-up at the boundary and thereby make the materials hard to deform[130,177]. The strain-hardening effect stops, i.e. the maximum shear stress (σ_y=2.51 GPa) has been reached when the grain boundary begins to migrate, leading to the strain-softening stage. The migration of GB downwards to the lower grain caused the upper grain to grow and the lower grain to shrink, while once again increasing the length of the intrinsic stacking fault. Fig.7.4(b) (at t=2.12 ns) shows a snapshot of bicrystal configuration after two jumps of GB migration. The original GB position is indicated by the dashed line for comparison. Note that, based on the classic theory proposed by Read and Shockley[76], the non-uniform structure of asymmetric GBs consist of more than two types of dislocations that can block each other when gliding on the intersection planes and prevent a coupled motion. Therefore, the migration of asymmetric GBs was thought to be impossible, but recent observations of coupled GB motion in bicrystal experiments[232,233] has suggested that this may not be true. The migration of Σ11(Φ=54.74°) asymmetric GB in the present simulation study also confirmed this view. The Crystal Analysis results indicated that the GB migrating process was accompanied by the GB

dislocation decomposition with some embryonic Shockley partial dislocations. This process can be described as:

$$(1/6)[1\ \ 1\ \ \bar{6}] \rightarrow (1/3)[1\ \ 1\ \ \bar{2}] + (1/6)[\bar{1}\ \ \bar{1}\ \ \bar{2}]$$

Overall, the propagation of dissociated partial dislocations from the GB plane and GB migration coupling with the shear deformation were the deformation mechanisms of the Σ11(2 2 5)/(4 4 1) GB under shear. To the best of the author's knowledge the dual accommodation mechanisms of the same GB at different levels of stress has never been reported.

7.3.4 The shear response of Σ11(5 5 7)/(7 7 $\bar{1}$) Φ=70.53° GB

As mentioned above, two equilibrium structures with similar GB energy were attained for Σ11(5 5 7)/(7 7 $\bar{1}$) GB. They were indexed as Φ=70.53°-A GB and Φ=70.53°-B GB (see Fig.7.2). Fig.7.5 shows the shear stress-time curve and the corresponding stages of deformation for the Φ=70.53°-A GB. As with the asymmetric Σ11(2 2 5)/(4 4 1) GB, the shear response of the bicrystal model can be divided into four dominant regimes where the onset of yielding (σ_y=0.36 GPa) was also associated with the emission of dissociated dislocations from the grain boundary plane and an increased stacking fault behind; the stress curve remained almost flat during the stacking fault extension. A key result is that after the slipping dislocations were blocked and the critical shear stress (σ_m=1.31 GPa) was reached, the GB plane did not migrate, the strain-softening resulting from the second group of dislocations nucleated from the grain boundary (see Fig.7.5(b) at t=1.76 ns). Fig.7.5(c) shows snapshots of the extracted dislocations during the shear process. According to the analysis, the original periodic GB structure was organised by an array of repeated GB dislocations with Burgers vector **b**=(1/3)[0 0 $\bar{1}$] and **b**=(1/3)[1 1 $\bar{1}$] along with the dissociated Shockley partial dislocations **b**=(1/6)[1 1 $\bar{2}$], as shown in Fig.7.5(c).

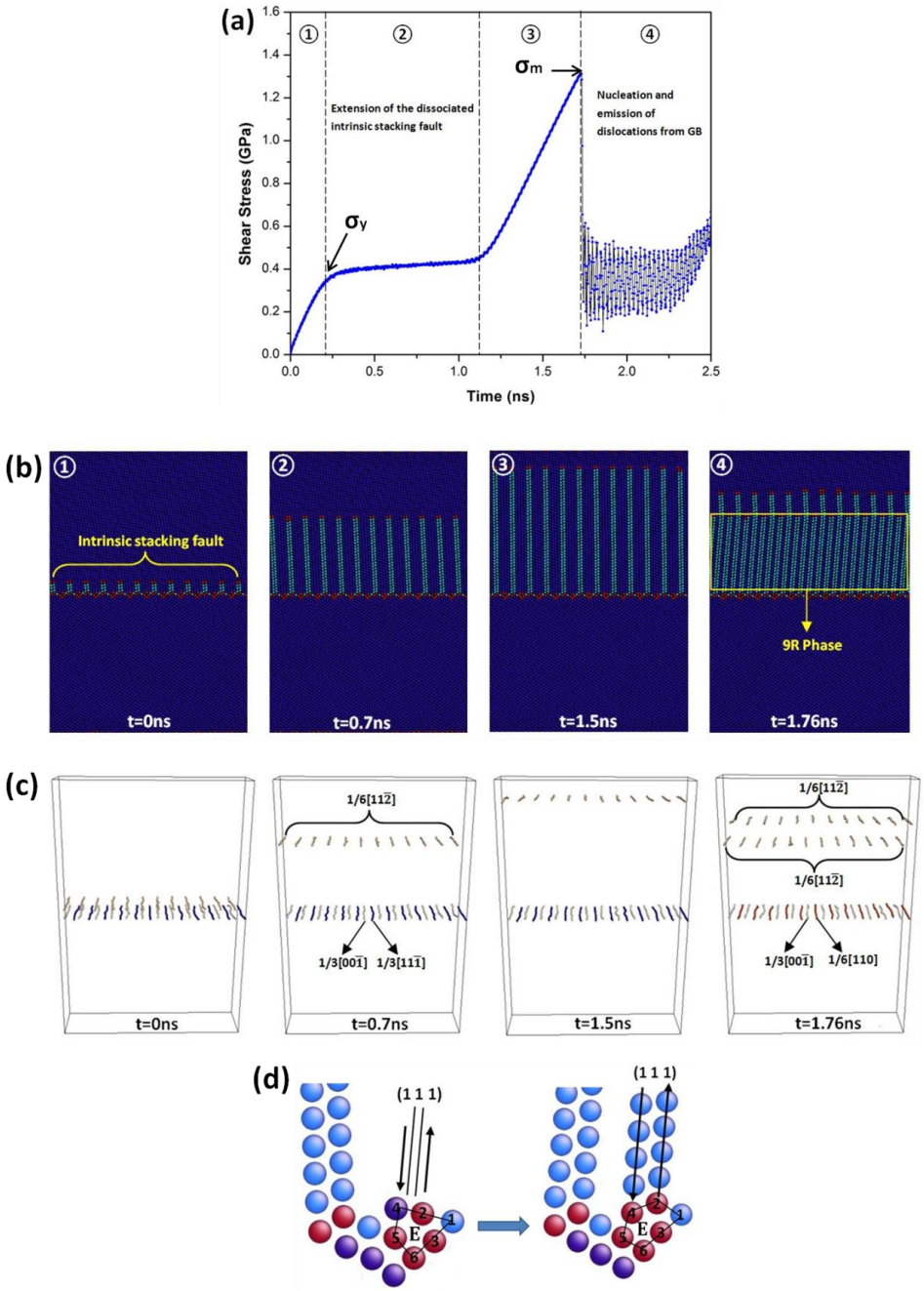

Figure 7.5 Shear response of Σ11(5 5 7)/(7 7 $\bar{1}$) Φ=70.53°-A GB. (a) Shear stress as a function of simulation time. (b) Snapshots of the deformation stage corresponding to the four dominant regimes in (a). Atoms of different colours represent the same as described in Fig.4. (c) Snapshots of the extracted dislocations during the shear process. (d) Enlarged view of one periodic structural unit to illustrate the deformation of E unit after dislocation nucleation.

During the stages of elastic, plastic, and strain-hardening, the GB retained its initial configuration until the onset of strain-softening, when another group of Shockley partial dislocations nucleated from the GB plane. The nucleation process

can be described by the dislocation decomposition as:

$$(1/3)[1\ \ 1\ \ \bar{1}] \rightarrow (1/6)[1\ \ 1\ \ 0] + (1/6)[1\ \ 1\ \ \bar{2}]$$

After examining the atomic configuration, one structural period of GB was extracted for analysis (see Fig.7.5(d)). It was found that the nucleation of the second group of dislocations was closely correlated to the deformation of the E structural unit. The E unit is a kite-shaped structure with six atoms involved before nucleation, and these atoms are numbered 1 to 6. After the critical shear stress, Atom 2 slipped out of the E unit along the (1 1 1) slip plane while Atom 4 slipped into the E unit. This relative shift of atoms onto the opposing (1 1 1) slip plane eventually resulted in a partial dislocation nucleation, whereas the propagation of the second group of dislocations created a 9R phase in the upper grain region (i.e. the repeat intrinsic stacking fault on every third plane). The GB structure containing the 9R phase agreed with the experimental HRTEM images of low stacking fault energy materials[234,235].

Fig.7.6 shows the shear stress-time curve and the corresponding stages of deformation for the Φ=70.53°-B GB. The stress curve shows a similar trend to Φ=70.53°-A GB with the same deformation mechanisms occurring in the elastic, plastic, and strain-hardening stages (see Fig.7.6(b)). When the critical shear stress (σ_m=1.68 GPa) was reached the GB plane did not migrate and the onset of the strain-softening stage resulted from the nucleation of a second group of dislocations from the GB plane. One structural period of GB was extracted to present the nucleation process more clearly, as shown in Fig.7.6(d), but unlike the Φ=70.53°-A GB case, a group of extrinsic stacking faults were created after the dislocation nucleation event. First, the E unit was shaped like a kite at the elastic and plastic stages, and after the first group of dislocation had been stopped from slipping the increased shear stress in the GB area rearranged the local atoms. Specifically, the free volume of the E unit was gradually shrunk by the translation of Atom 4 while another E unit was under construction. The newly formed E unit is shown as E′

with the six atoms involved numbered with $1'$ to $6'$. Notice that the E unit and E′ unit shared two common atoms, i.e. Atoms 5 & 6 in the E unit and Atoms $4'$ & $5'$ in the E′ unit. According to the dislocation reaction analysis (see Fig.7.6(c)), this rearrangement of local atoms can be regarded as a combination of GB dislocations that can be described by:

$$(1/3)[0\ 0\ \bar{1}] + (1/3)[1\ 1\ \bar{1}] \rightarrow (1/3)[1\ 1\ \bar{2}]$$

Once the critical shear stress was reached the relative shift of Atoms $2'$ & $4'$ on the opposing (1 1 1) slip plane resulted in a second partial dislocation nucleation, but the slip direction caused by Atom $2'$ in the second dislocation was opposite to that caused by the first (dissociated) dislocation. This action turned the atoms back onto the overlapped plane (in the middle) to the perfect fcc position and generated an extrinsic stacking fault. This nucleation process can be described as dislocation decomposition where:

$$(1/3)[1\ 1\ \bar{2}] \rightarrow (1/6)[1\ 1\ \bar{2}] + (1/6)[1\ 1\ \bar{2}]$$

In summary, the deformation mechanism of the $\Sigma 11(5\ 5\ 7)/(7\ 7\ \bar{1})$ GB under shear was the emission of dissociated partial dislocations and the nucleation and propagation of partial dislocations from the GB plane through to deformation of the E structural unit. For different equilibrium boundary structures the nucleation of the second group of partial dislocations created a 9R phase and extrinsic stacking fault in the bicrystal model with Φ=70.53°-A GB and Φ=70.53°-B GB respectively. This partial dislocation is prone to being nucleated from a collapsed E structural unit, which is consistent with the previous finding[105,110]. Having the E unit as a source of dislocation can be attributed to an intrinsically large free volume involved in it that provides space for the arrangement of atoms to accommodate the concentration of local stress.

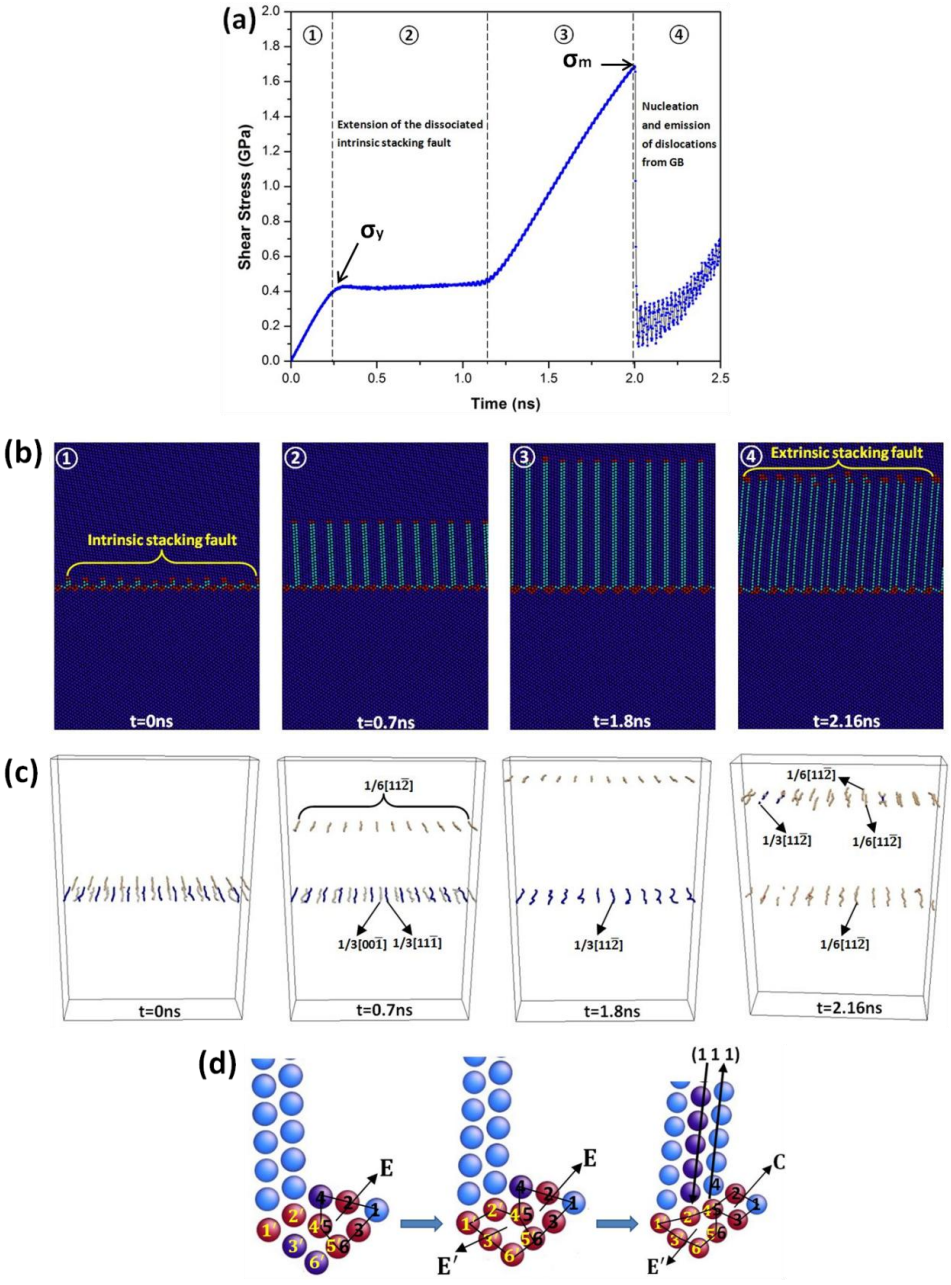

Figure 7.6 Shear response of Σ11(5 5 7)/(7 7 $\bar{1}$) Φ=70.53°-B GB. (a) Shear stress as a function of simulation time. (b) Snapshots of the deformation stage corresponding to the four dominant regimes in (a). Atoms of different colours represent the same as described in Fig.4. (c) Snapshots of the extracted dislocations during the shear process. (d) Enlarged view of one periodic structural unit to illustrate the deformation of E unit after dislocation nucleation.

7.3.5 The shear response of Σ11(3 3 2) Φ=90° GB

Fig.7.7 shows the results of the bicrystal model with the Σ11(3 3 2) symmetric GB. Snapshots of the atomic configurations of bicrystal were captured at a certain number of time steps during the straining simulations. Fig. 7.7(a) shows that as a

shear strain was applied the bicrystal model deformed elastically (stage-1), and when the simulation cell reached a maximum stress (σ_m =2.08 GPa), the curve dropped abruptly from σ_m to σ_d (0.55 GPa). This relaxation in stress was associated with the grain boundary sliding. The shear stress then increased again with a smaller slope (stage-2), and when the shear stress reached another threshold value (1.81 GPa), the curve dropped again to σ_d. This behaviour agreed with the so-called "stick-slip" phenomenon of GB sliding[236,237]. While the "stick" stages corresponded to the elastic straining processes, the "slip" events should be related to some kind of structural transformation processes occurring within the bicrystal model. Fig.7.7(b) shows the GB configurations after the first and second sliding events at t=0.92 ns and t=1.6 ns respectively, where local atomic shuffling activities were accompanied by GB sliding during the straining process. Notice that some dislocations were nucleated in the GB area after GB sliding, but there was no dislocation slipping or GB migration. However, the third decline in the stress curve was associated with the partial and full dislocations from the GB plane. As shown in Fig.7.7(b), at t=1.93 ns, two partial dislocations with Burgers vector **b**=(1/6) [$\bar{1}$ 1 $\bar{2}$] propagated from the boundary plane with an increasing stacking fault behind while a full dislocation with a leading partial **b**=(1/6) [$\bar{2}$ $\bar{1}$ 1] and a trailing partial **b**=(1/6) [$\bar{1}$ 1 2] was slipping in the lower grain area. The interaction between full and partial dislocation resulted in the shear stress fluctuating in stage-4.

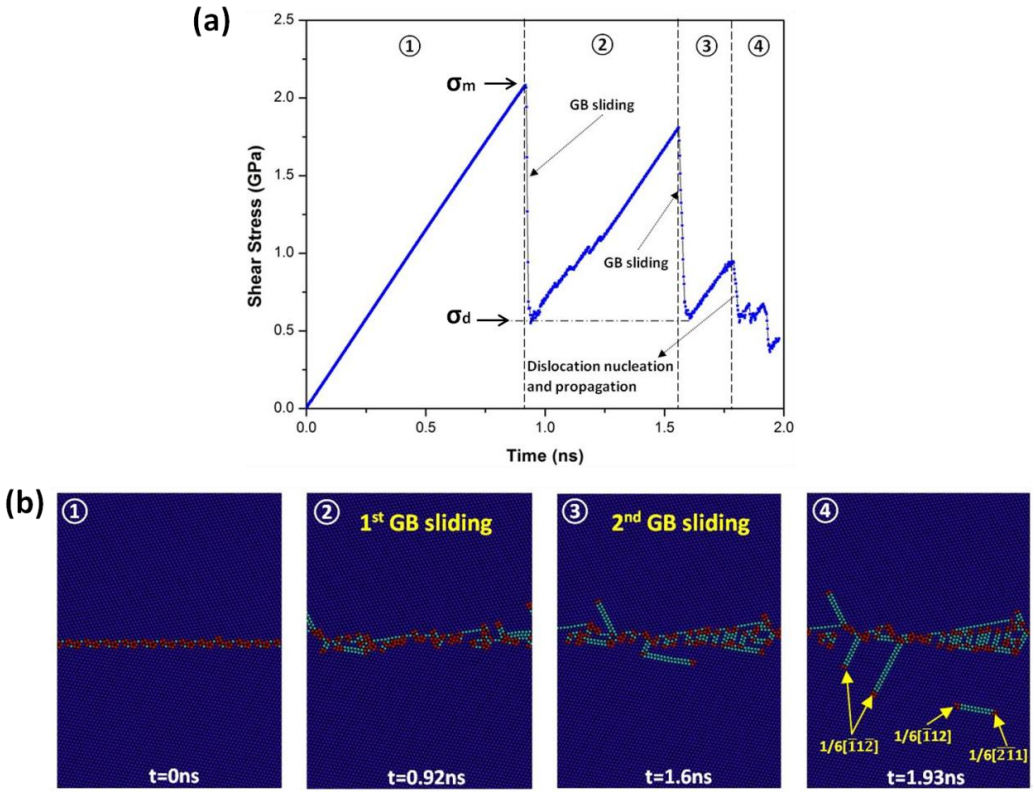

Figure 7.7 Shear response of Σ11(3 3 2) Φ=90° GB. (a) Shear stress as a function of simulation time. (b) Snapshots of the deformation stage corresponding to the four dominant regimes in (a). Atoms of different colours represent the same as described in Fig.7.4.

7.3.6 Evolution of the dissociated stacking fault

The length of the stacking faults for the asymmetric GBs at different stages of deformation were plotted in Fig.7.8 as a function of the simulation time. The length of the stacking fault was defined in the boundary normal direction based on the atomic coordinates of the Shockley partial dislocations in the upper grain. For the Cu bicrystal with Σ11 asymmetric GBs, a low shear stress could drive the dissociated dislocations to propagate and extend the stacking fault, and this would cause the simulated models to yield and the rapid growth in the length of the stacking fault, as seen in Fig.7.8. Moreover, the simulation results indicated that these dissociated Shockley partial dislocations were pure edges so they therefore have Burgers vectors with large y-components and small x-components. Consequently, the region swept by this array in grain-A underwent a tilt rotation and suffered a misfit strain. These distortions altered the local stress distributions quite

significantly and caused the stress to become very non-uniform in its distribution. Once this had occurred the stress-time curve in stage-2 of Fig.7.4, Fig.7.5, and Fig.7.6 essentially has no physical significance in depicting the stresses within the models, and therefore the dislocation movement did not reduce the stress value, the stress curve actually plateaued in the plastic stage. This indicated that the dissociated GB structure can increase ductility and retain the high strength of the simulated cells under shear.

Moreover, strain-hardening for asymmetric GBs occurred once the dissociated dislocations stopped. This action corresponded to the flat stage after a rapid growth in the length of the dissociated stacking fault, as shown in Fig.7.8, after which the stacking fault for the Φ=54.74° GB increased in length again because the GB migrated downwards to the lower grain. However, this did not occur for the Φ=70.53° GBs. The enlarged area in Fig.7.8(b) and (c) shows that the length of the first group of stacking faults decreased as the blocked dislocations began to move back, while the length of the second group of stacking faults began to increase after the dislocations nucleated from the boundary plane. This decrease in the length of the dissociated stacking faults can be attributed to the elastic interaction between the two defects, but once the length of the nucleated (2^{nd} group) stacking faults arrived at the same level as the length of the dissociated(1^{st} group) stacking faults, they increased together as the shear strain increased. As illustrated above, the nucleation of dislocations from different local GB structures resulted in the '9R phase' and 'extrinsic stacking faults' for the Φ=70.53°-A GB and Φ=70.53°-B GB respectively.

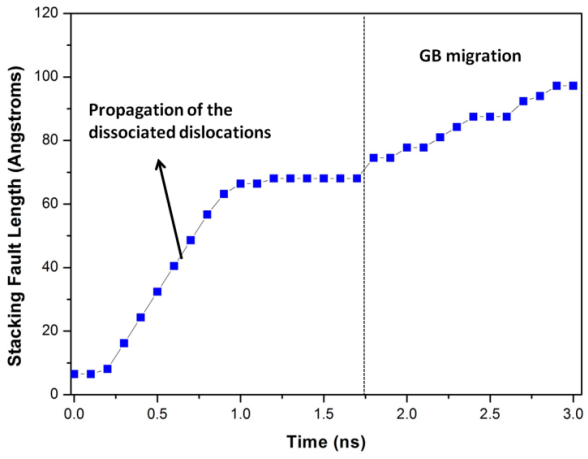

(a) Φ=54.74°

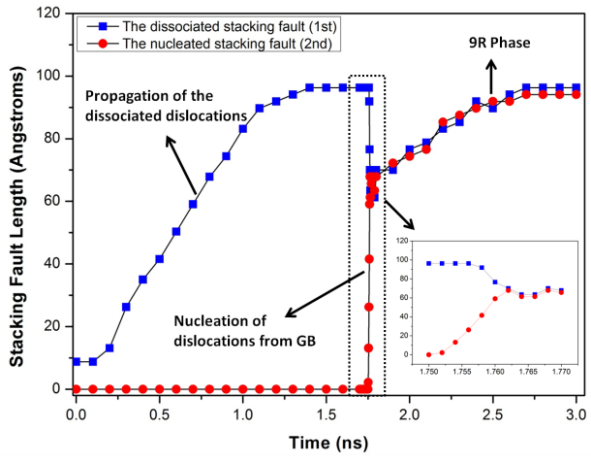

(b) Φ=70.53°-A

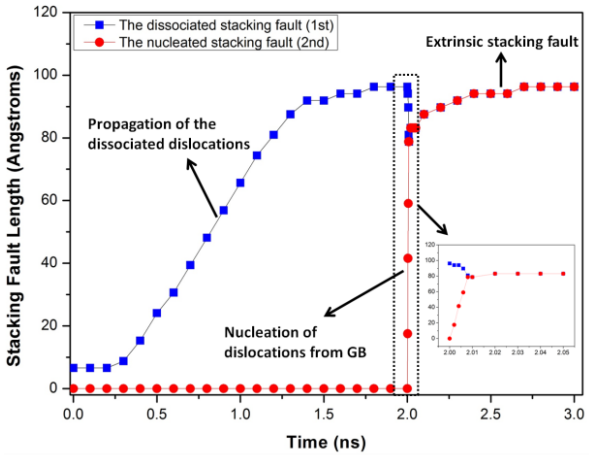

(c) Φ=70.53°-B

Figure 7.8 The length of stacking fault as a function of simulation time for different Σ11 asymmetric GBs. The blue squares represent the dissociated stacking fault within the equilibrium GB structures, and the red points indicate the nucleated stacking fault from the GB plane.

7.4 Summary

Molecular dynamics simulations were carried out in this chapter to investigate the shear response of symmetric and asymmetric Σ11<1 1 0> tilt GBs in copper bicrystal. Different deformation mechanisms were reported due the grain boundary structures. The simulations showed that migrating Σ11(1 1 3) GB under shear can be regarded as the GB dislocations sliding and their combination along the boundary plane. A non-planar structure with dissociated intrinsic stacking fault was prevalent in Σ11 asymmetric GBs of Cu, and this type of structure can significantly increase the ductility of bicrystal models under shear deformation. The grain boundary can be a source of dislocation and also migrate at different levels of stress. The intrinsic free volume involved in the grain boundary area was correlated to dislocation nucleation and GB sliding, while the dislocation nucleation mechanism can differ from a grain boundary due to its different equilibrium structures.

CHAPTER 8

Atomic Mechanisms of Stacking Fault Tetrahedron Induced Plasticity in Copper Single Crystal

Stacking fault tetrahedron (SFT) is the most common type of vacancy clustered defect in fcc metals and alloys, and can play an important role in the mechanical properties of metallic materials. Molecular dynamics simulations were carried out in this chapter to investigate the incipience of plasticity and the underlying atomic mechanisms in copper single crystal with SFT. Different deformation mechanisms of SFT were reported due to the crystal orientations and the loading directions.

8.1 Introduction

The propagation and interaction of lattice dislocations within the grains is fundamentally important for the plastic deformation of conventional coarsened metallic materials, but dislocations for nanocrystalline metallic materials are less likely to be present because at very small grain sizes it is less likely that the dislocation loops will be stable[1,2]. In a small enough volume (at nanometer-scale) of a material with limited pre-existing dislocations, the deformation mechanisms of the incipience of plasticity can be dominated by dislocation nucleation rather than dislocation propagation, or multiplication and interactions[56,177,223]. Generally, a dislocation can nucleate homogeneously in small volumes from s perfect lattice, or heterogeneously from structural defects. For a sample free from defects, dislocation nucleation occurs spontaneously throughout the volume[238,239] but this deformation mechanism needs very large stresses, whereas heterogeneous dislocation nucleation occurs with crystal defects such as point defects[16], voids[17,18], free surfaces[240,241] and grain boundaries[106,108,164,242-244]. These defects act as stress concentrators that emit dislocations at stresses less than that required for homogeneous dislocation

nucleation.

Among the different point defects (e.g. single or di-vacancies, interstitial or impurity atoms), stacking fault tetrahedra (SFTs) are the common ones that form in fcc crystals under various circumstances. This special shape of vacancy cluster was first observed in samples of quenched gold by Silcox and Hirsch[21]. They suggested that the tetrahedra were formed as the quenched-in vacancies clustered to produce a faulted loop and then evolved to form a closed defect with stair rod dislocations along the edges of the tetrahedra and stacking faults on four {111} planes. SFTs were subsequently observed in many pure metals and alloys that had been deformed at room and higher temperatures[245]. Later, SFTs were observed in situ in electron-irradiated metals[246] using high voltage electron microscopy, while only recently, SFTs have been observed in the Ni-based superalloy R104 after low cycle fatigue at high temperatures and under strain-controlled conditions[247]. In addition to experimental observation, this type of vacancy defect has also been modelled in a number of papers using molecular dynamics (MD) simulations[248-252]. Based on these experimental and simulation results, Loretto et al.[253] concluded there were three basically distinct mechanisms for producing SFT; (i) the clustering of vacancies based on the Silcox-Hirsch mechanism; (ii) various mechanisms involving dislocation glide and cross slip, and (iii) the merging of glide elements followed by growth. In their experiment, Matsukawa and Zinkle[254] observed nanometer-sized clusters of vacancies with one dimensional fast migration, so they proposed that 1D migration may be a key physical mechanism for the self- organisation of nanometer sized SFT arrays.

Besides those studies on the formation mechanisms of SFT, many recent research interests now focus on the interaction of SFT with other structural defects, mainly dislocations[29,111-117] and twin boundary[121,255]. For example, previous MD studies revealed that SFT can provide a strong obstacle for glide dislocations that ultimately increase the yield strength and decrease ductility[25,26]. Robach et al.[29] investigated the

interaction of an edge dislocation with an SFT in copper and gold with an in situ transmission electron microscope (TEM) and MD simulations and found that this interaction can result in the tetrahedra being sheared into two defects, be converted to another type of defect, or be annihilated. Lee and Wirth[114] used MD simulations to study the interaction between a mixed dislocation and SFT in copper and noted that depending on the interaction geometry, it can result in shearing, partial absorption, destabilisation, or a simple bypass of the SFT. By using MD simulations Niewczas and Hoagland[121] studied the interaction of moving twin boundaries with SFT and found that this interaction generally damaged the parent SFT and the formation of new defects in the twin lattice. Yu et al.[255] observed the radiation induced migration of coherent and incoherent twin boundaries and found that the migrating twin boundaries played a remarkable role during the removal of radiation-induced SFTs.

While previous literatures are mostly limited to the formation of SFT or their interaction with other structural defects, very few studies focused on the effect of SFT on the mechanical response of materials with very small grain size where dislocations are unlikely to be present, even though SFT affects the mechanical response of materials with incipient plasticity. For example, the atomistic simulations of nanoindentation tests showed that SFT reduced the pressure needed to nucleate a dislocation by almost half that of a perfect crystal[30]; this means the governing deformation mechanisms must be explored in the presence of this defect. Salehinia and Bahr[27] performed MD simulations in a nanoindentation test of copper single crystal to investigate how the orientation of SFT affects the load needed to initiate plastic deformation; their results indicated that a downward SFT affected the mechanical behaviour of a copper single crystal much more than an upward orientated SFT. Salehinia and Bahr recently studied the effect of crystal orientation on the mechanical response and dislocation nucleation of copper single crystal with SFT under uniaxial tension and compression[28] and found that SFT lowered the stress needed for plastic deformation, and this reduction in yield stress was more in

compression than in tension for almost all orientations; in fact this simulation indicated that the compression/tension (C/T) asymmetry decreased or even reversed due to the presence of SFT. Although in their studies some atomic configurations were present at the onset of plasticity, there was no concise atomic picture of the dislocation mechanisms that actually induced the incipience of plasticity, which means that some remaining issues need further discussion. For example, what is the deformation mechanism that caused the different reduction in yield stress under tension and compression? Why can the C/T asymmetry decrease or reverse in the presence of SFT? How does the structural transformation of SFT occur during the applied loading? To the best of the authors' knowledge, the underlying deformation mechanisms related to these behaviours has not been reported, so our objective was to obtain an atomic insight into the underlying dislocation mechanisms of stacking fault tetrahedron needed to understand the incipience of plasticity in small volume crystal induced by SFT.

In this chapter, molecular dynamics simulations were performed on copper single crystal with SFT under uniaxial tension and compression, and with a variety of crystal orientations. Copper single crystals with a perfect structural model were also investigated in the same simulation conditions for a comparison. A detailed analysis of three crystal orientations ([1 0 0], [1 1 0] and [1 1 1]) are presented in this chapter, and the results of the selected cases can represent most of the typical deformation mechanisms of SFT (see Fig.8.14).

8.2 Simulation method

In order to investigate the influence of SFT on the incipience of plasticity of a single crystal, perfect single crystals with various crystal orientations were constructed and then an SFT was placed at the centre of each crystal. Periodic boundary conditions were applied to the simulation model in all directions. The simulation box was approximately $20\times20\times20$ nm^3, and contained approximately 6.7×10^5 atoms. It was thought that a 16^3 nm^3 cell would be large enough to avoid any significant effects

from periodic boundaries on the 3D dislocation nucleation dynamics[238]. This meant that the stress required for the incipient of crystal plasticity was essentially unaffected by any further increases in the size of the simulation cell. In this study the SFT defect was generated based on the Silcox-Hirsch mechanism[21], which indicated that a platelet of vacancies can collapse to form a loop of Frank partial dislocations and then evolve into an SFT. By referencing the previous method[27], a triangular Frank loop platelet of vacancies was removed in the (1 1 1) plane. The triangular platelet contained 55 vacancies, 10 on each edge, that corresponded to an SFT with a 2.3 nm long edge that was similar to the size of SFTs in copper observed in the experiments[256]. The density of SFT in this modelling was approximately 10^{24} m^{-3}, and that was close to the 10^{23} m^{-3} reported for copper single crystal[257].

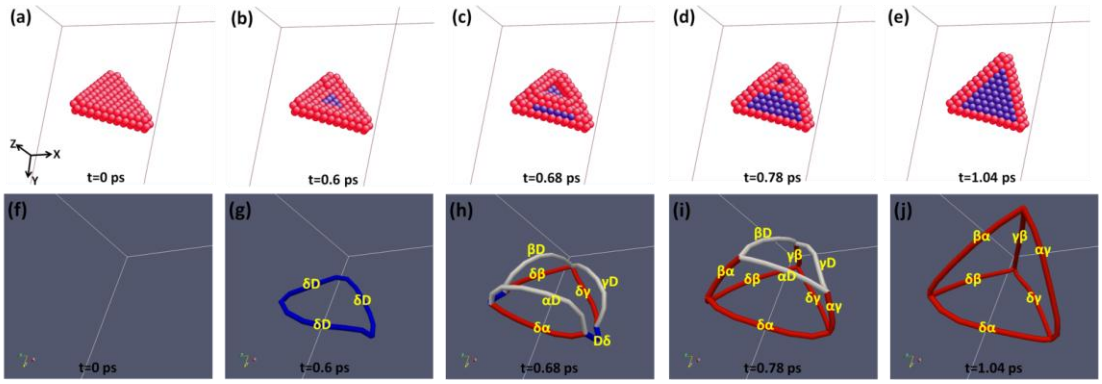

Figure 8.1 Snapshots to illustrate the process of an SFT generated from a vacancy triangular platelet based on the Silcox-Hirsch mechanism. (a)-(e) show the results from MD simulation; (f)-(j) show the extracted dislocation segment by using the dislocation extraction algorithm.

The simulation system was initially relaxed for 20 ps using the isobaric-isothermal (NPT) ensemble at a temperature of 10 K and a pressure of 0 bar. Fig.8.1 shows five snapshots from the MD simulation (a)-(e) and the results of the dislocation extraction (f)-(j) to illustrate how an SFT was transformed from a vacancy triangular platelet. Here, the atoms with a perfect fcc structure were removed to make the defects easier to see. The times denote the time that elapsed from when the vacancies were first introduced. In the first 0.6 ps, a closed dislocation loop of a Frank partial dislocation was produced after a platelet of vacancies collapsed, as shown in Fig.8.1(g). From an

atomistic perspective, this process can be regarded as the collective displacement of atoms within the tetrahedra as they gradually dropped into the hole left by the original vacancy platelet[248] (see Fig.8.1(b)). By convention this is called a negative Frank dislocation, whereas a positive Frank dislocation may be formed by the precipitation of a closely packed platelet of interstitial atoms[258]. Positive and negative Frank loops contain stacking faults, while a stacking fault will be stable if the fault energy is low enough, but this was not the case for copper in this study (about 44.4 mJ/m^2 [221]). The Frank partial soon dissociated into a low energy stair-rod dislocation and a Shockley partial dislocation on an intersecting slip plane, as shown in Fig.8.1(c) and (h). This process is according to a reaction of the type:

$$\delta\ D \rightarrow \delta\ \alpha + \alpha\ D \qquad (1/3)[1\ 1\ 1] \rightarrow (1/6)[1\ 0\ 1] + (1/6)[1\ 2\ 1]$$

$$\delta\ D \rightarrow \delta\ \gamma + \gamma\ D \qquad (1/3)[1\ 1\ 1] \rightarrow (1/6)[0\ 1\ 1] + (1/6)[2\ 1\ 1]$$

$$\delta\ D \rightarrow \delta\ \beta + \beta\ D \qquad (1/3)[1\ 1\ 1] \rightarrow (1/6)[1\ 1\ 0] + (1/6)[1\ 1\ 2]$$

The dislocations and slip planes are described using Thompson tetrahedra[21] notation and the definition given by Hirth and Lothe[259]. Fig.8.1(d) and (i) shows that when the propagated Shockley partial dislocations met each other they soon reacted to form another set of stair-rod dislocations. This process can be described by the reaction where:

$$\alpha\ D + D\ \gamma \rightarrow \alpha\ \gamma \qquad (1/6)[1\ 2\ 1] + (1/6)[\bar{2}\ \bar{1}\ \bar{1}] \rightarrow (1/6)[\bar{1}\ 1\ 0]$$

$$\gamma\ D + D\ \beta \rightarrow \gamma\ \beta \qquad (1/6)[2\ 1\ 1] + (1/6)[\bar{1}\ \bar{1}\ \bar{2}] \rightarrow (1/6)[1\ 0\ \bar{1}]$$

$$\beta\ D + D\ \alpha \rightarrow \beta\ \alpha \qquad (1/6)[1\ 1\ 2] + (1/6)[\bar{1}\ \bar{2}\ \bar{1}] \rightarrow (1/6)[0\ \bar{1}\ 1]$$

The Shockley partials glided towards the apex of the tetrahedra and finally constructed a tetrahedron of intrinsic stacking faults on {111} planes with 1/6<110> type stair-rod dislocations along the edges of the tetrahedra, as shown in Fig.8.1(e) and (j). It was noted that the entire process of SFT formation takes about 1 ps.

After obtaining an equilibrium structure of SFT and the initial relaxation of the simulation system, either uniaxial tensile or compressive loading with a constant

strain rate of 1×10^8 s^{-1} was applied along the Y axial on the simulated sample, while pressure in the lateral directions was kept at zero. An integration time step of 1 fs was used throughout the MD simulations. For the mechanical response, the system stress was attained by calculating the pressure of the entire system of atoms, while system strain was derived from the positions of the periodic boundaries. By considering the influence of temperature, simulations were carried out at 10K, 100K, 300K, 500K, and 800K respectively; higher temperatures close to the pre-melting temperature of copper were not considered.

8.3 Results

8.3.1 Compressive and tensile stress response

The yield stress of perfect crystals and crystals with SFT at different temperatures for [1 0 0], [1 1 0] and [1 1 1] orientations are listed in Table.1. Note that the yield stress in this study was defined as the maximum tensile or compressive stress and it corresponded to the incipient of plasticity. The yield stress in both tension and compression generally decreased as the temperature increased because the thermal activation definitely assisted the nucleation of dislocations, and also reduced the stress needed for the incipient plasticity.

The mechanical response of copper single crystal with SFT defects for [1 0 0], [1 1 0] and [1 1 1] orientations under uniaxial loading at 10 K are shown in Fig.8.2. The results of the simulation for other crystal orientations at 10 K are presented in Fig.8.14. The stress-strain curves of perfect crystals were also plotted for comparison. The stress response showed an obvious anisotropy due to the crystal orientations. In the elastic stage, either elastic hardening or softening occurred in different loading conditions. The elastic hardening and elastic softening defined here were used to describe the non-linear stress-strain curves at higher stress and strain, where the non-linear elastic behaviour either exceeded or was lower than the expected value, assuming pure linear elastic conditions. For example, compressive loading produced an obvious elastic hardening and tensile loading exhibited an obvious elastic

softening for the orientations of [1 1 0], [8 7 1] and [4 3 1] etc.; elastic hardening and softening also occurred in the cases of [1 1 1], [4 1 1], [4 3 3], and [8 7 6] etc. but is less obvious. The non-Schmid normal factor (NF, resolved loading stress normal to the slip plane) played a significant role in the non-linear elastic behaviour[161]. The orientations near [1 1 0] axis had higher NF values than the other orientations and therefore the orientations in this area showed a more significant non-linear elastic behaviour. From a physical point of view, the tensile (compressive) normal stress acts to increase (decrease) the inter-planar spacing between the slip planes, which may effectively decrease (increase) the inter-atomic 'friction' to slip along these planes and eventually result in the elastic softening (hardening) in the elastic stage. While the NF can explain the non-linear behaviour of most crystal orientations, it does not describe the behaviour observed for all orientations. For example, the [1 0 0] orientation showed an opposite performance where elastic hardening occurred in tension and elastic softening occurred in compression, indicating that additional factors may have contributed to this behaviour. Salehinia and Bahr[28] recently proposed that the NF and Schmid ratio ($SF_{compression}/SF_{tension}$, the ratio of Schmid factor in compression to the value in tension) are required to explain the asymmetry between elastic behaviour in compression and tension loading conditions in perfect crystals. The MD simulations in their study showed the largest Schmid ratio in the [1 0 0] orientation, which may have caused its abnormal stress response compared to other orientations.

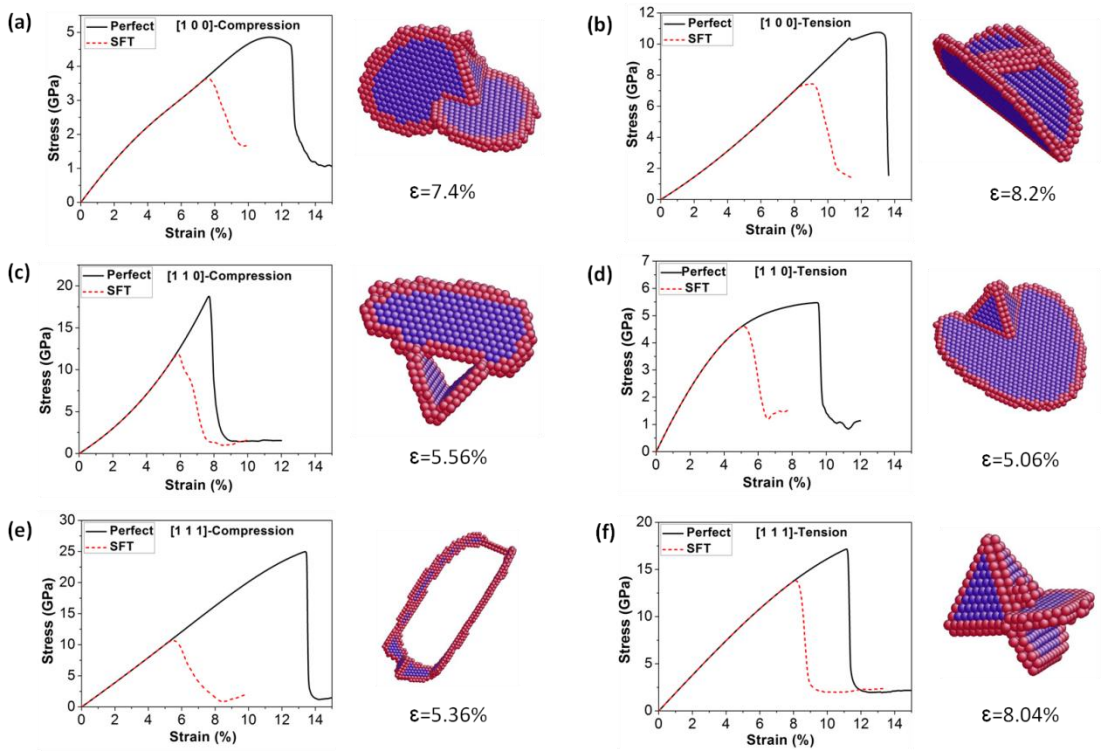

Figure 8.2 Stress-strain curves of perfect crystals and crystals with SFT under uniaxial compression and tension for [1 0 0], [1 1 0] and [1 1 1] directions. The inserted snapshots show the atomistic configurations of SFT at the incipient of plasticity.

In the early stage of plastic deformation there was a big difference in yield stress for different crystal orientations in the simulations of perfect crystals and crystals with an SFT. A previous study revealed that the compressive strength in perfect copper single crystals was higher than the tensile strength for most crystal orientations[161]. This was also the case in this study, except that the [1 0 0] orientation had a higher yield stress in tension than in compression. The maximum compressive and tensile stresses were all evidenced in the [1 1 1] orientation at 24.97 GPa and 17.17 GPa respectively. As could be expected, crystals with SFT generally responded to stress the same as perfect crystals, i.e. the higher compressive (tensile) strength in the perfect crystals resulted in a higher compressive (tensile) strength in the crystals with SFT because the resolved shear stresses on the closely packed plane were the same, although the yield stresses were smaller in the presence of defects. Indeed, the maximum tensile stress of crystal with SFT was also evidenced in [1 1 1] orientation (13.85 GPa). However, the maximum compressive stress of crystal with SFT occurred in the [8 7 1] orientation

that was calculated as 13.97 GPa. Meanwhile, there was a sharp decrease in this value in the [1 1 1] direction compared to its perfect counterpart. These results indicated that in the presence of SFT, both of the crystal orientation and the deformation mechanisms of SFT are needed to explain the anisotropy of stress response and the incipience of plasticity for the simulated samples. The simulations revealed that when the maximum compressive or tensile stress had been reached, plasticity commenced due to the activated dislocation movement from the SFT (see the snapshots inserted in Fig.8.2). The detailed deformation mechanisms of SFT for different crystal orientations and loading directions are specified in the next few subsections. Another remarkable feature of the stress-strain curves was the compression/tension asymmetry (different yield stress between compression and tension); this part will be discussed in Section 8.4 based on the deformation mechanisms of SFT.

Table 8.1 Yield stress of perfect crystals and crystals with SFT at different temperatures.

Orientation	**Loading type**	**Yield stress (GPa)**				
		T=10K	T=100K	T=300K	T=500K	T=800K
[1 0 0]	compression-perfect	4.86	4.43	3.76	3.05	2.23
	compression-SFT	3.56	3.44	3.09	2.71	2.18
	tension-perfect	10.75	10.13	8.75	7.60	5.52
	tension-SFT	7.44	7.21	6.46	6.03	5.05
[1 1 0]	compression-perfect	18.76	17.77	15.92	13.92	10.56
	compression-SFT	11.79	11.21	10.26	8.79	7.03
	tension-perfect	5.47	5.15	4.50	3.90	2.98
	tension-SFT	4.61	4.35	3.88	3.36	2.67
[1 1 1]	compression-perfect	24.97	23.02	19.73	16.84	12.83
	compression-SFT	10.67	10.20	8.94	8.02	6.56
	tension-perfect	17.17	14.70	11.46	9.89	7.36
	tension-SFT	13.85	12.71	9.90	8.57	6.63

8.3.2 Deformation mechanism of SFT for [1 0 0] orientation

The simulation showed that the higher temperature used in this study did not affect the

formation of SFT, and similar deformation mechanisms occurred at the onset of crystal plasticity at different temperatures, so only the simulation results at 10K are presented here. A low temperature can avoid any thermal disturbance of atoms and provide a clearer view of the transformed SFT structure and dislocation activities.

The results of simulating copper single crystal with SFT under uniaxial compression is presented in Fig.8.3. Fig.8.3(a)-(d) shows the result obtained from the MD computer simulation, while the four selected snapshots show the SFT configurations near the yield point. The atoms were coloured by the CNA parameter and then removed with the fcc structures to facilitate any defective structures; the red atoms represent the dislocation core and the blue atoms represent the stacking fault. Fig.8.3(e)-(h) shows the dislocations extracted from the MD results, while their Burgers vectors were computed using the dislocation extraction algorithm (DXA). A visual inspection of the MD simulation results indicated that the onset of yielding corresponded to the nucleation of partial dislocations from the SFT. The tetrahedra retained its original structure until a compressive strain equal to ε=6.8% was applied, and then a Shockley partial dislocation (δA) with Burger's vectors **b**=(1/6)[$\bar{1}$ 2 $\bar{1}$] nucleated from the SFT on (1 1 1) slip plane, as shown in Fig.8.3(b) and (f). There were three other potentially active slip planes, i.e. (1 1 $\bar{1}$), (1 $\bar{1}$ 1), and ($\bar{1}$ 1 1). This is shown in Fig.8.3(c) and (g) at ε=7.2%, where the embryo dislocation loops can be seen on the four {1 1 1} planes. According to the Schmid factor analysis, they are the favoured slip systems with the maximum Schmid factor $SF^{max}_{(1\,1\,1)} = SF^{max}_{(1\,1\,\bar{1})} = SF^{max}_{(1\,\bar{1}\,1)} = SF^{max}_{(1\,\bar{1}\,\bar{1})}$ =0.471. In Fig.8.3(d) and (h), the nucleated Shockley partial dislocation δA and Bγ propagated quickly when the compressive strain reached ε=7.4%, and this finally resulted in the incipience of crystal plasticity. The nucleation process can be described by the dislocation reaction:

$$\delta\,\gamma \rightarrow \delta\,A + A\,\gamma \qquad (1/6)[0\,1\,1] \rightarrow (1/6)[\bar{1}\,2\,\bar{1}] + (1/6)[1\,\bar{1}\,2]$$

$$\delta\,\beta \rightarrow \delta\,A + A\,\beta \qquad (1/6)[1\,1\,0] \rightarrow (1/6)[\bar{1}\,2\,\bar{1}] + (1/6)[2\,\bar{1}\,1]$$

and

$$\delta\,\gamma \rightarrow \delta\,B + B\,\gamma \qquad (1/6)[0\ 1\ 1] \rightarrow (1/6)[\bar{1}\ \bar{1}\ 2] + (1/6)[1\ 2\ \bar{1}]$$

$$\alpha\,\gamma \rightarrow \alpha\,B + B\,\gamma \qquad (1/6)[\bar{1}\ 1\ 0] \rightarrow (1/6)[\bar{2}\ \bar{1}\ 1] + (1/6)[1\ 2\ \bar{1}]$$

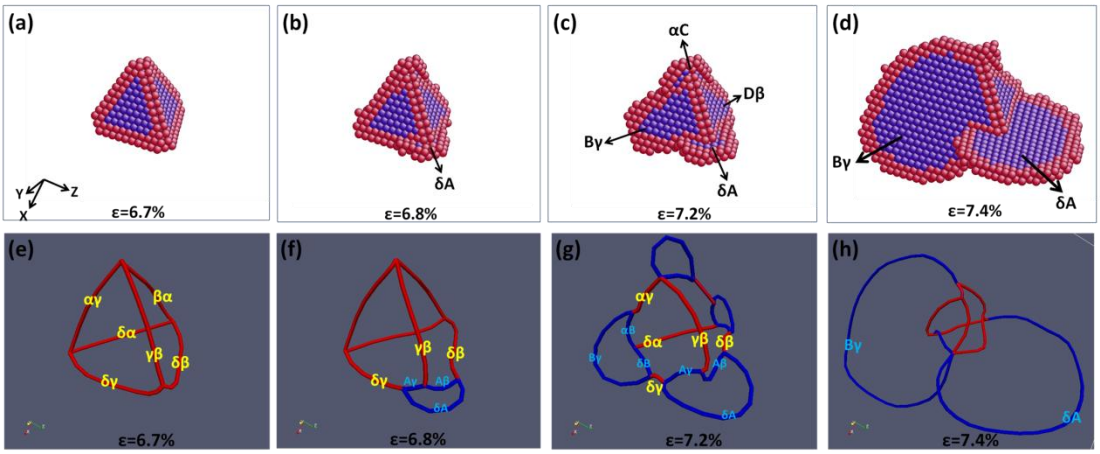

Figure 8.3 Snapshots of SFT configuration in crystal with [1 0 0] orientation at different stages of deformation during uniaxial compression. (a)-(d) shows the results from MD simulation; (e)-(h) shows the extracted dislocation segment by using the dislocation extraction algorithm. The red line represents the stair-rod dislocation and the blue line indicates the Shockley partial dislocation.

Fig.8.4 shows the evolution of the SFT configuration in crystal with [1 0 0] orientation during tensile loading. When the applied tensile strain equalled ε=5.5%, the SFT can still retain its original structure. It is interesting to find that the SFT structure in equilibrium had changed to another configuration with two unfaulted planes in Fig.8.4(c) at ε=6.2%. The stress-strain curve in this case was checked and revealed that this structural transformation had no effect on the elastic trend and did not contribute to the incipience of plasticity. Moreover, the new structure could now retain its configuration until the tensile loading increased to about ε=8.2%. In this study we tentatively called this metastable structure as "semi-faulted SFT". The process of transforming the structure from an SFT to a semi-faulted SFT is shown in Fig.8.4(e)-(k) based on the dislocation reaction analysis. For a clearer illustration, we indexed the four vertices of SFT as 1, 2, 3 and 4. Initially, four of the SFT stair-rod dislocations (δβ, αβ, δγ and αγ) tended to dissociate to Shockley partial dislocations from the vertices, as shown in Fig.8.4(b) and (f) at ε=5.8%: for example, the dissociation at vertex 2 and vertex 3 can be described as:

$$\delta\,\beta \rightarrow \delta\,C + C\,\beta \qquad (1/6)[1\ 1\ 0] \rightarrow (1/6)[2\ \bar{1}\ \bar{1}] + (1/6)[\bar{1}\ 2\ 1]$$

$$\alpha\,\beta \rightarrow \alpha\,C + C\,\beta \qquad (1/6)[0\ 1\ \bar{1}] \rightarrow (1/6)[1\ \bar{1}\ \bar{2}] + (1/6)[\bar{1}\ 2\ 1]$$

and

$$\delta\,\gamma \rightarrow \delta\,B + B\,\gamma \qquad (1/6)[0\ 1\ 1] \rightarrow (1/6)[\bar{1}\ \bar{1}\ 2] + (1/6)[1\ 2\ \bar{1}]$$

$$\alpha\,\gamma \rightarrow \alpha\,B + B\,\gamma \qquad (1/6)[\bar{1}\ 1\ 0] \rightarrow (1/6)[\bar{2}\ \bar{1}\ 1] + (1/6)[1\ 2\ \bar{1}]$$

As the tensile deformation increased the partial dislocation Cβ which was dissociated from δβ and αβ, glided on the $(1\ 1\ \bar{1})$ plane, while the partial dislocation Bγ which was dissociated from δγ and αγ glided on the $(\bar{1}\ 1\ 1)$ plane. However, the movement of partial dislocations at vertex 1 and vertex 4 were either restrained or even recovered to the initial stair-rod dislocations, as shown in Fig.8.4(g) and (h) at ε=6.065% and ε=6.07%, Fig.8.4(i) indicates that when the glissile Shockley dislocation Cβ moved forwards and reached the edge of SFT, it will react with the non-dissociated stair-rod dislocation γB to form a sessile Frank dislocation γC by the reaction:

$$\gamma\,\beta + \beta\,C \rightarrow \gamma\,C \qquad (1/6)[1\ 0\ \bar{1}] + (1/6)[1\ \bar{2}\ \bar{1}] \rightarrow (1/3)[1\ \bar{1}\ \bar{1}]$$

Soon after, the Shockley dislocation Bγ from vertex 3 reacted with γC to form a perfect dislocation BC, as shown in Fig.8.4(j) at ε=6.1%. This reaction can be described as:

$$B\,\gamma + \gamma\,C \rightarrow B\,C \qquad (1/6)[1\ 2\ \bar{1}] + (1/3)[1\ \bar{1}\ \bar{1}] \rightarrow (1/2)[1\ 0\ \bar{1}]$$

The process of structural transformation was completed at about ε=6.2%, so the semi-faulted SFT now consisted of four Shockley partial dislocations (δC, αC, δB and αB) connected by a stair-rod dislocation (δα) and a perfect dislocation (BC). The MD simulation indicated that the onset of yielding began because four Shockley partial dislocations propagated from the semi-faulted SFT.

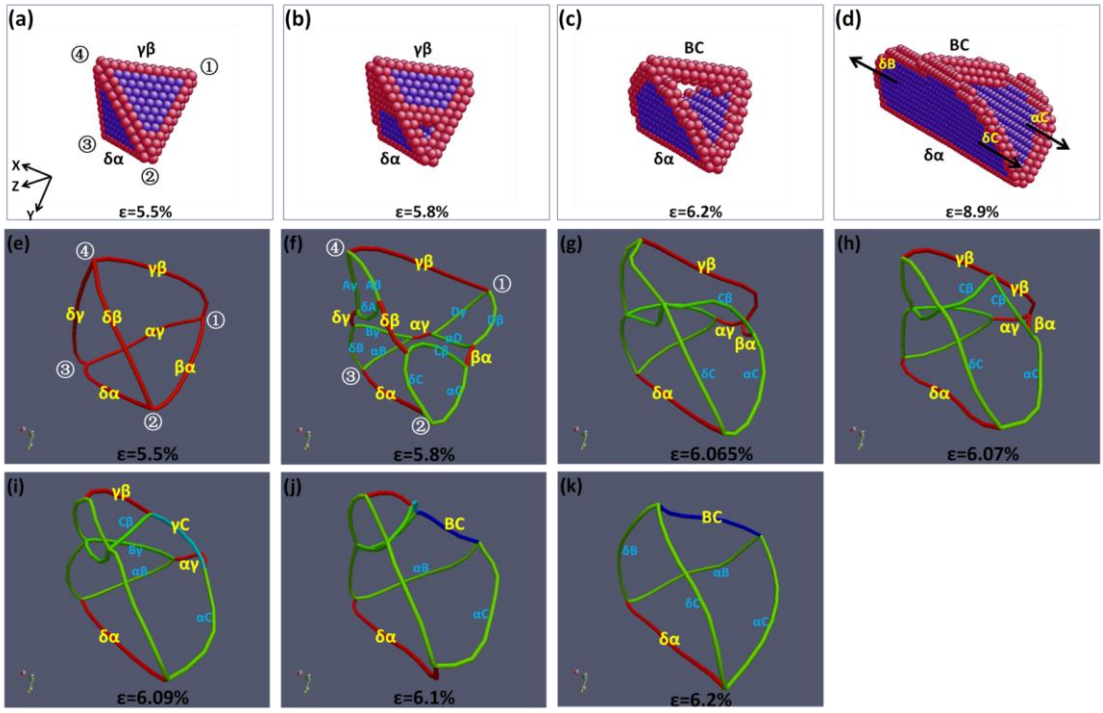

Figure 8.4 Snapshots of SFT configuration in crystal with [1 0 0] orientation at different stages of deformation during uniaxial tension. (a)-(d) shows the results from MD simulation; (e)-(k) shows the extracted dislocation segment by using the dislocation extraction algorithm. The red line represents the stair-rod dislocation, the green line represents the Shockley partial dislocation, the light blue line indicates the Frank partial dislocation, and the dark blue line indicates the perfect dislocation.

8.3.3 Deformation mechanism of SFT for [1 1 0] orientation

Fig.8.5 shows the SFT configuration in crystal with [1 1 0] orientation at different stages of deformation during uniaxial compression. As was the case with [1 0 0] orientation in tension, the equilibrium SFT structure evolved into a metastable structure, i.e. the semi-faulted SFT shown in Fig.8.5 (b) and (f) at ε=4%. However, the Shockley partial dislocations (αB, γB, αD and γD) involved in the semi-faulted SFT did not propagate with the increased compressive stress, unlike the case of [1 0 0] orientation in tension. Fig.8.5 (c) and (g) indicates that the onset of yielding resulted from the nucleation of a Shockley partial dislocation δB from the perfect dislocation DB in the semi-faulted SFT by the reaction:

$$D\,B \rightarrow D\,\delta + \delta\,B \qquad (1/2)[1\,1\,0] \rightarrow (1/3)[1\,1\,1] + (1/6)[1\,1\,\bar{2}]$$

Subsequently, the partial dislocation δB propagated on the (1 1 1) plane and resulted

in the crystal plastic deformation shown in Fig.8.5(d) and (h). This result is consistent with the Schmid factor analysis as $SF_{(1\,\bar{1}\,1)}=SF_{(\bar{1}\,1\,1)}=0$ and $SF^{max}_{(1\,1\,1)}=0.471$, which indicates that the gliding of Shockley partial dislocations (αB, γB, αD and γD) on $(1\,\bar{1}\,1)$ and $(\bar{1}\,1\,1)$ planes cannot be activated, while δB slips on (1 1 1) plane is the favoured slip system.

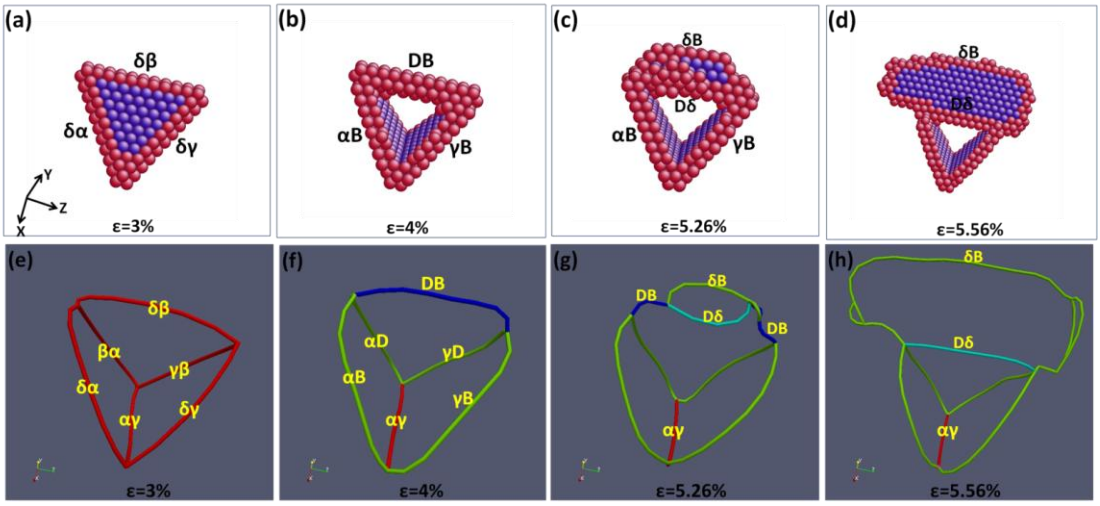

Figure 8.5 Snapshots of SFT configuration in crystal with [1 1 0] orientation at different stages of deformation during uniaxial compression. (a)-(d) shows the results from MD simulation; (e)-(h) shows the extracted dislocation segment by using the dislocation extraction algorithm. The red line represents the stair-rod dislocation, the green line represents the Shockley partial dislocation, the light blue line indicates the Frank partial dislocation, and the dark blue line indicates the perfect dislocation.

The snapshots presented in Fig.8.6 shows the atomistic view of SFT at the onset of yielding (a)-(c) and the corresponding dislocation mechanism (d)-(h). When the maximum tensile stress reached about ε=4.98%, two stair-rod dislocations (βα and γβ) on the $(1\,1\,\bar{1})$ plane began to be simultaneously dissociated into Shockley partial dislocations (see Fig.8.6(e)) by the reaction:

$$\alpha\,\beta \rightarrow \alpha\,D + D\,\beta \qquad (1/6)[0\,1\,\bar{1}] \rightarrow (1/6)[1\,2\,1] + (1/6)[\bar{1}\,\bar{1}\,\bar{2}]$$

$$\gamma\,\beta \rightarrow \gamma\,D + D\,\beta \qquad (1/6)[1\,0\,\bar{1}] \rightarrow (1/6)[2\,1\,1] + (1/6)[\bar{1}\,\bar{1}\,\bar{2}]$$

The dissociated Shockley partial Dβ from βα and γβ merged together and propagated as further tensile strain was applied. This process was similar to the case of [1 0 0]

orientation in compression. However, Fig.8.6(e) indicates that the residual Shockley partial dislocations (αD and γD) neither propagated or remained stable, instead, they split into a stair-rod dislocation and another Shockley partial dislocation βD by the reaction:

$$\alpha\, D \rightarrow \alpha\, \beta + \beta\, D \qquad (1/6)[1\ 2\ 1] \rightarrow (1/6)[0\ 1\ \bar{1}\ ] + (1/6)[1\ 1\ 2]$$

$$\gamma\, D \rightarrow \gamma\, \beta + \beta\, D \qquad (1/6)[2\ 1\ 1] \rightarrow (1/6)[1\ 0\ \bar{1}] + (1/6)[1\ 1\ 2]$$

This step can be regarded as a reverse process of the last step because the original stair-rod dislocation (βα and γβ) reverted and the partial dislocation βD had the same Burger vector as Dβ but it differed in the slip direction. Subsequently, βD propagated on $(1\ 1\ \bar{1})$ plane inside the SFT and then reacted with the stair-rod dislocation δβ to form a Frank partial δD and then slipped across δβ. This process can be described by the reaction:

$$\delta\, \beta + \beta\, D \longleftrightarrow \delta\, D \qquad (1/6)[1\ 1\ 0] + (1/6)[1\ 1\ 2] \longleftrightarrow (1/3)[1\ 1\ 1]$$

Note that the SFT on $(1\ 1\ \bar{1})$ plane became unfaulted as βD slipped, although this is not shown in the pictures, and as βD traversed it introduced an extrinsic ledge near the edge of the SFT which caused βD to slip on the $(1\ 1\ \bar{1})$ plane one layer of atoms higher than Dβ. Since the Shockley partial dislocations Dβ and βD propagated on the two consecutive $(1\ 1\ \bar{1})$ planes, an extrinsic stacking fault was generated inside the partial loop, as shown in Fig.8.6(c).

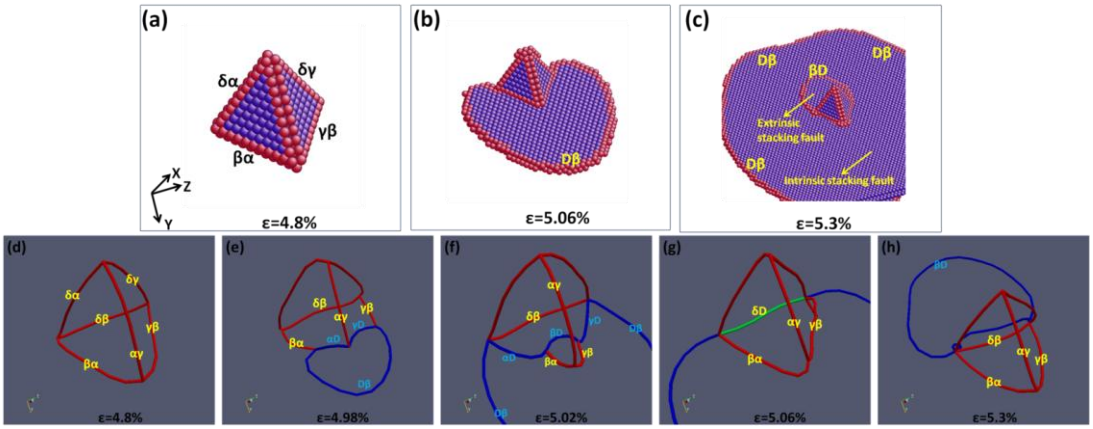

Figure 8.6 Snapshots of SFT configuration in crystal with [1 1 0] orientation at different stages of

deformation during uniaxial tension. (a)-(c) shows the results from MD simulation; (d)-(h) shows the extracted dislocation segment by using the dislocation extraction algorithm. The red line represents the stair-rod dislocation, the blue line represents the Shockley partial dislocation, and the green line indicates the Frank partial dislocation.

8.3.4 Deformation mechanism of SFT for [1 1 1] orientation

The sequence of snapshots presented in Fig.8.7 shows the SFT configuration at various stages in crystal with [1 1 1] orientation under uniaxial compression where the loading direction was perpendicular to the (1 1 1) plane of the tetrahedra. It was interesting to find that the perfect SFT structure gradually collapsed as the compressive deformation increased, and the unzipping of SFT from a single vertex corresponded to the inverse of the Silcox-Hirsch mechanism; this resulted in a perfect SFT being transformed into a triangular Frank loop, as shown in Fig.8.7(a) and (e).This was consistent with the experiment result[260] where the compressive stress acting on a {1 1 1} plane can promote the formation of faulted loops from vacancy clusters on this plane. By checking the stress-strain curve, the process of structural transformation did not alter the elastic stage. A visual inspection of the MD simulation results indicated that the onset of yielding corresponded to the propagation of a perfect dislocation loop, which poses the key question; how did a sessile Frank partial dislocation loop convert into a perfect glissile dislocation loop? This process is shown in Fig.8.7(e)-(k). Firstly, as shown in Fig.8.7(f), one edge of the Frank loop tended to dissociate to a Shockley partial dislocation Cβ and a dislocation with Burgers vector **b**=1/6[3 0 1]. This was the same for another edge where the Frank dislocation tended to dissociate to Cα and a dislocation with **b**=1/6[3 1 0], although it is not shown in Fig.8.7(f). This process can be expressed by:

$$\delta\ D \rightarrow C\ \beta + (1/6)[3\ 0\ 1] \qquad (1/3)[1\ 1\ 1] \rightarrow (1/6)[\bar{1}\ 2\ 1] + (1/6)[3\ 0\ 1]$$

$$\delta\ D \rightarrow C\ \alpha + (1/6)[3\ 1\ 0] \qquad (1/3)[1\ 1\ 1] \rightarrow (1/6)[\bar{1}\ 1\ 2] + (1/6)[3\ 1\ 0]$$

Fig.8.7(g) shows that when the dissociated segments Cβ and Cα met, they formed a stair-rod dislocation βα by the reaction:

$$\beta\ C + C\ \alpha \rightarrow \beta\ \alpha \qquad (1/6)[1\ \bar{2}\ \bar{1}] + (1/6)[\bar{1}\ 1\ 2] \rightarrow (1/6)[0\ \bar{1}\ 1]$$

On the other hand the dislocations with **b**=1/6[3 0 1] and **b**=1/6[3 1 0] were quite unstable and soon split into two Shockley partial dislocations respectively, as described by:

$$(1/6)[3\ 0\ 1] \rightarrow \delta\ C + \beta\ D \qquad (1/6)[3\ 0\ 1] \rightarrow (1/6)[2\ \bar{1}\ \bar{1}] + (1/6)[1\ 1\ 2]$$

$$(1/6)[3\ 1\ 0] \rightarrow \delta\ C + \alpha\ D \qquad (1/6)[3\ 1\ 0] \rightarrow (1/6)[2\ \bar{1}\ \bar{1}] + (1/6)[1\ 2\ 1]$$

Overall, according to the above reactions we can regard the dissociation process as a Frank partial dislocation that split into three Shockley partial dislocations by the reactions:

$$\delta\ D \rightarrow \delta\ C + C\ \beta + \beta\ D \qquad (1/3)[1\ 1\ 1] \rightarrow (1/6)[2\ \bar{1}\ \bar{1}] + (1/6)[\bar{1}\ 2\ 1] + (1/6)[1\ 1\ 2]$$

$$\delta\ D \rightarrow \delta\ C + C\ \alpha + \alpha\ D \qquad (1/3)[1\ 1\ 1] \rightarrow (1/6)[2\ \bar{1}\ \bar{1}] + (1/6)[\bar{1}\ 1\ 2] + (1/6)[1\ 2\ 1]$$

These simulation results indicated that a partial dislocation δC formed inside the loop and then spread across the loop and removed the stacking fault, as shown in Fig.8.7(b) and (h) at ε=5.13%. When δC slipped to the edge of the Frank loop it reacted with the stair-rod dislocation δD to form a perfect dislocation CD, while at the outside the two remaining dissociated Shockley partials (Cβ and βD, Cα and αD) reacted with each other to produce a perfect dislocation CD, as shown in Fig.8.7 (i) and (j). Thus, the perfect dislocation loop CD can be generated by the dislocation reactions as:

$$C\ \beta + \beta\ D \rightarrow C\ D \qquad (1/6)[\bar{1}\ 2\ 1] + (1/6)[1\ 1\ 2] \rightarrow (1/2)[0\ 1\ 1]$$

$$C\ \alpha + \alpha\ D \rightarrow C\ D \qquad (1/6)[\bar{1}\ 1\ 2] + (1/6)[1\ 2\ 1] \rightarrow (1/2)[0\ 1\ 1]$$

$$C\ \delta + \delta\ D \rightarrow C\ D \qquad (1/6)[\bar{2}\ 1\ 1] + (1/3)[1\ 1\ 1] \rightarrow (1/2)[0\ 1\ 1]$$

The dislocation loop expanded rapidly as the compressive stress increased due to the CD slipping until it eventually induced the incipience of a plastic stage. Note that the original Frank loop was on the (1 1 1) plane, while the converted perfect loop was on the (1 1 $\bar{1}$) plane. According to the Schmid factor analysis, the perfect dislocation CD where **b**= (1/2)[0 1 1] slips on (1 1 $\bar{1}$) plane is the favoured slip system with

$SF^{max}_{(1\,\bar{1}\,\bar{1})}$=0.408. While the CD was slipping it tended to dissociate back to the initial Shockley partials (Cβ and βD, Cα and αD) due to the comparatively low staking fault energy of copper (44.4mJ/m^{-2}), as shown in Fig.8.7(d) and (k). However, the simulation indicated that this was only an oscillating process because the Shockley partial dislocations cannot slip very far away, and the slipping of a perfect dislocation loop still plays a dominant role during plastic deformation.

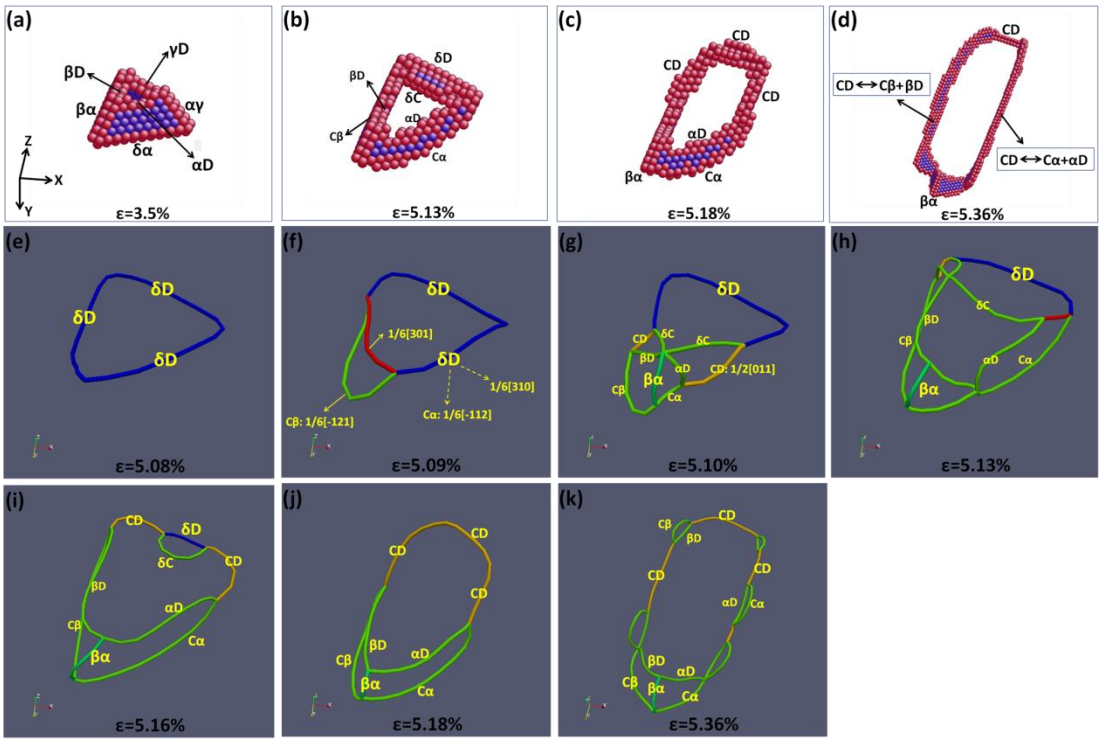

Figure 8.7 Snapshots of SFT configuration in crystal with [1 1 1] orientation at different stages of deformation during uniaxial compression. (a)-(d) shows the results from MD simulation; (e)-(h) shows the extracted dislocation segment by using the dislocation extraction algorithm. The blue line represents the Frank partial dislocation, the green line represents the Shockley partial dislocation, the yellow line indicates the perfect dislocation, and the red line is the undefined dislocation.

The series of snapshots presented in Fig.8.8 shows the SFT configuration near the yield point in crystal with [1 1 1] orientation during uniaxial tension. When the maximum tensile stress was reached, Fig.8.8 (b) and (f) shows that a Shockley partial dislocation was dissociated from one edge (βα) of the SFT and its reaction was:

$$\beta\,\alpha \rightarrow \beta\,D + D\,\alpha \qquad (1/6)[0\,\bar{1}\,1] \rightarrow (1/6)[1\,1\,2] + (1/6)[\bar{1}\,\bar{2}\,\bar{1}]$$

This was different from the cases in [1 0 0] orientation in compression and [1 1 0] orientation in tension, where the partial dislocation was nucleated from the vertex of the tetrahedra with two edges of SFT involved. The dissociation of βα was completed at ε=8%, as shown in Fig.8.8(c) and (g). Subsequently, the partial dislocation βD and Dα slipped on (1 1 $\bar{1}$) plane and (1 $\bar{1}$ 1) plane respectively, and resulted in yielding. The Schmid factor analysis showed they were the favoured slip systems, with $SF_{(1\,1\,\bar{1})}=SF_{(1\,\bar{1}\,1)}=0.314$.

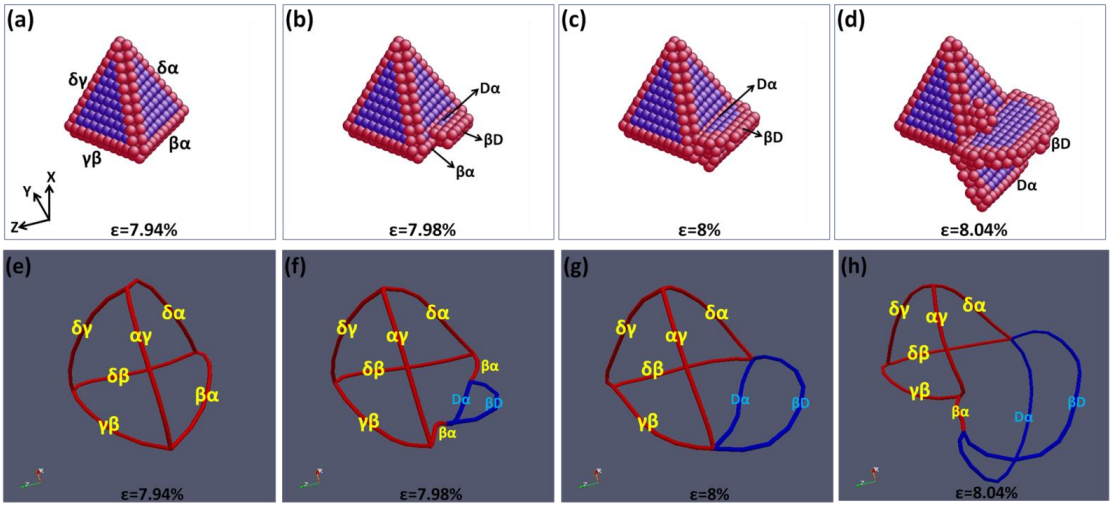

Figure 8.8 Snapshots of SFT configuration in crystal with [1 1 1] orientation at different stages of deformation during uniaxial tension. (a)-(c) shows the results from MD simulation; (d)-(h) shows the extracted dislocation segment by using the dislocation extraction algorithm. The red line represents the stair-rod dislocation, the blue line represents the Shockley partial dislocation, and the green line indicates the Frank partial dislocation.

8.4 Discussion

8.4.1 Different reduction in yield stress

The simulation indicated that the stress in compression and tension needed for plastic deformation was reduced for crystals with SFT in all orientations (see Table 8.2). This is reasonable because more stress was needed for a homogeneous dislocation from a perfect crystal structure than the heterogeneous dislocation nucleation from an existing structural defect (e.g. SFT in this study). It is worth noting that the reduced yield stress caused by the SFT depended almost entirely on the crystal orientation and loading

direction. For example, at a temperature of 10 K, the reduced yield stress in compression was less than in tension for the [1 0 0] orientation, at 24.9% and 30.8% respectively. However, this reduction seemed to be much higher in compression (37.1% and 57.3%) than in tension (15.8% and 19.3%) for [1 1 0] and [1 1 1] orientation.

Since copper has a high degree of elastic anisotropy as a function of the loading axis orientation; for example the calculated elastic modulus in the [1 1 1] orientation ($E_{[111]}$ = 189 GPa) was almost three times greater than in the [1 0 0] orientation ($E_{[100]}$ = 65 GPa), it is instructive to examine the influence of elastic modulus on the simulation results. Fig.8.9 plots the yield stress of perfect single crystals and crystals with SFT as a function of the elastic modulus. In compression the yield stress generally increased with the increased elastic modulus for perfect single crystals, whereas in the presence of SFT, the overall yield stress also increased as a function of increasing elastic modulus, but the influence of elastic modulus on the yield stress was less obvious than for the perfect crystal. For example, in this study the maximum yield stress (13.97 GPa) in compression was observed in the [8 7 1] orientation, which only had a moderate elastic modulus ($E_{[871]}$ = 152 GPa). In tension, the elastic modulus had less influence on the yield stress when the value was less than 120 GPa, while there was an obvious increase in the yield stress at a higher elastic modulus. Fig.8.10 shows the reduction in the yield stresses due to the presence of SFT as a function of elastic modulus for different crystal orientations. Obviously, the elastic modulus can play an important role in the different reduction of yield stresses because the reduction is more significant for stiffer orientations in compression while the opposite is the case in tension. However, the scattered points (e.g. [8 2 1] and [4 2 1] orientation) indicated that the elastic modulus is insufficient to explain the different reduction in yield stress between compression and tension.

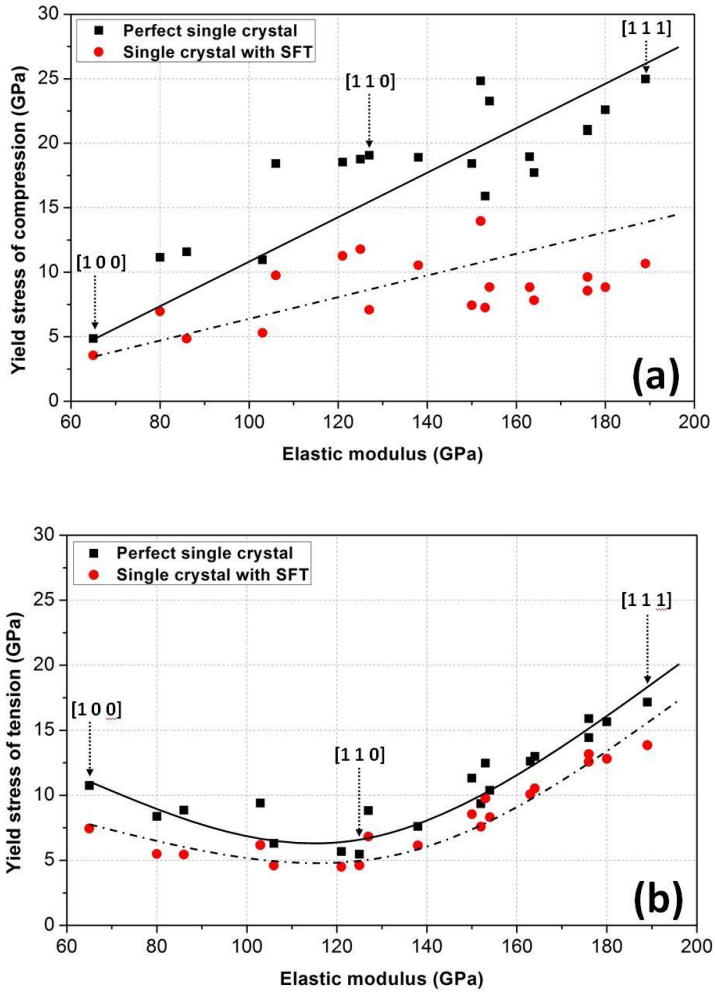

Figure 8.9 Yield stresses of perfect single crystals and crystals with SFT as a function of elastic modulus for various of crystal orientations under (a) uniaxial compression and (b) uniaxial tension. The solid line and the dash-dot line are draw to guide the eye.

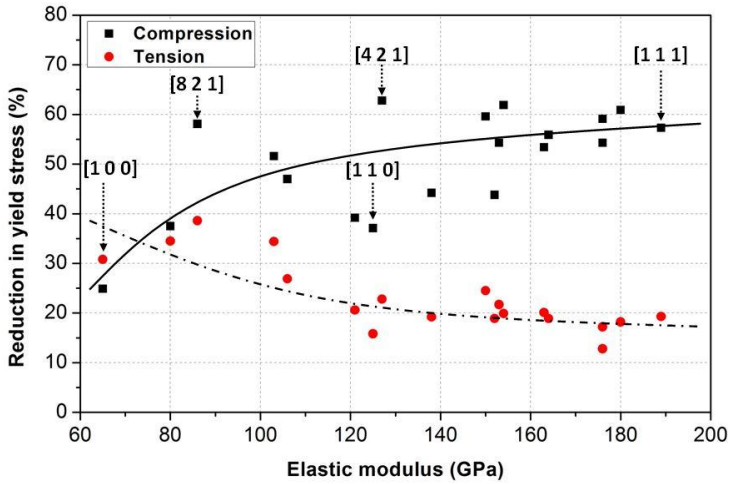

Figure 8.10 The reduction in yield stresses under uniaxial compression and tension as a function of elastic modulus for various of crystal orientations. The solid line and the dash-dot line are draw to guide the eye.

A visual inspection of the MD simulation revealed that this difference can be attributed to the different deformation mechanisms between compression and tension at the incipience of plastic deformation. For example, for [1 0 0] orientation in compression and [1 1 0], [1 1 1] orientations in tension, the onset of yielding resulted from the dislocations nucleation from the stair-rod dislocations on the edge of the SFT, as shown in Fig.8.2 (a), (d) and (f). This detailed nucleation process is shown in Fig.8.3, Fig.8.6, and Fig.8.8 respectively. However, for the [1 0 0] orientation in tension and the [1 1 0] and [1 1 1] orientations in compression, an obvious structural transformation occurred before dislocation propagation, although this process was still in the elastic stage and had almost no effect on the stress-strain curve. This transformation from a perfect SFT led to the formation of a metastable semi-faulted SFT in the cases of [1 0 0] and [1 1 0] orientation (see Fig.8.4 and Fig.8.5), while for the [1 1 1] orientation, the perfect 3D SFT collapsed to a 2D Frank loop (see Fig.8.7). This structural transformation was a stress assisted process where the transformed structures had higher energy than the original perfect SFT. From the perspective of energy, the structures with higher energy can facilitate the dislocation nucleation, which makes the incipient plastic deformation easier than the original perfect SFT, and therefore the relative change of stress required to trigger plastic deformation is greater in crystals with transformed SFT. Thus, the reduced yield strength was more obvious in those cases where structural transformation occurred during loading, as shown in Fig.8.14.

Note that the collapse of an SFT during compressive loading was not always carried out simultaneously on the three stacking fault planes from a single vertex. The unzipping of an SFT can be completed in one or two stacking fault planes depending on the different crystal orientations, resulting in the nucleation of a single or double perfect dislocation loops (e.g. the [4 3 1] and [4 1 1] orientations). The partial unzipping of the SFT can be attributed to the different resolved shear stress on the staking fault planes, and therefore different slip systems are activated.

Fig.8.11 shows that an increased temperature had no significant role in the result even though the reduction in the yield stress was less as the temperature increased; this weakening seemed to be more obvious for the [1 0 0] orientation. Recall that the [1 0 0] orientation showed the most compliant elastic property ($E_{[100]}$ = 65 GPa), which makes it more sensitive to an increased temperature and this effect was more obvious when the temperature was close to the pre-melting value.

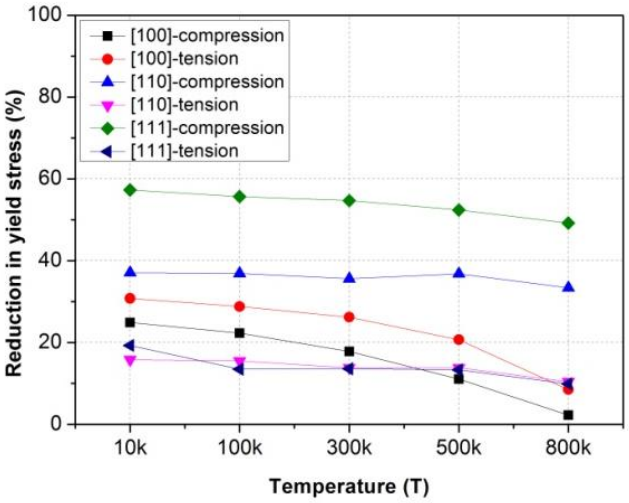

Figure 8.11 The reduction in yield stresses under uniaxial compression and tension for [1 0 0], [1 1 0] and [1 1 1] orientations at different simulation temperatures.

8.4.2 Compression/tension asymmetry

The simulation revealed an obvious C/T asymmetry for perfect crystals and crystals with SFT, i.e. there was a difference in the yield stress between compression and tension. The C/T asymmetry ratio was plotted as a function of elastic modulus in Fig.8.12. For the perfect single crystals, elastic-hardening in compression can result in a higher yield stress than in tension, which usually exhibits an elastic-softening (see Fig.8.14), therefore most of the asymmetry values for the perfect single crystals were larger than unity and represented a higher yield stress in compression than in tension. The [1 1 0] orientation shows the highest C/T ratio (3.42) due to its largest non-Schmid normal factor. The [1 0 0] orientation was a special case with a C/T ratio of less than unity (0.45), indicating a higher tensile stress than the compressive stress. As introduced previously, not only the non-Schmid factor, but also the Schmid factor ratio

($SF_{compression}/SF_{tension}$) is needed to explain the asymmetry of mechanical response for the perfect single crystals.

Compared to the perfect crystals, the C/T asymmetry can be decreased or even reversed in the presence of SFT. For example, the C/T asymmetry ratio decreased from 3.42 to 2.56 for the [1 1 0] orientation at a temperature of 10 K, indicating a decreased C/T asymmetry. Moreover, this ratio decreased from 1.45 to 0.77 for the [1 1 1] orientation, indicating that the C/T asymmetry had reversed due to the presence of SFT. Actually, almost half of the crystals with SFT in this study showed a C/T ratio very close to or less than unity, as shown in Fig.8.12. Recall that the reduction in yield stress was more in compression than in tension for almost all orientations, and this deviation seemed more obvious with the increased elastic modulus, which eventually resulted in an overall decreased C/T ratio. Moreover, the MD simulation indicated that the generation of a perfect dislocation loop during loading can be an important reason why the C/T asymmetry reversed. In the cases of [1 0 0] orientation in tension and [1 1 0] orientation in compression, the transformed semi-faulted SFT was a metastable structure that can steadily exist in the crystal during an applied load, and more stress was needed to drive the dislocation nucleation away from it and induce yielding, as shown in Fig.8.4 and Fig.8.5. However, with the [1 1 1] orientation during compression, the Frank loop that transformed from a collapsed SFT was quite unstable and soon converted to a perfect dislocation loop. Compared to a sessile Frank loop, a perfect glissile loop is easy to propagate because a small increase in stress can make it move and induce the onset of plastic deformation. Since the stress needed for dislocation propagation is much less than that needed for dislocation nucleation, the reduction in the yield stress was much higher for [1 1 1] orientation (57.3%) than the dislocation nucleation from the semi-faulted SFT in the cases of [1 0 0] and [1 1 0] orientation (30.8% and 37.1% respectively). This sharp decline in compressive stress due to the propagation of a perfect dislocation loop caused the C/T asymmetry to reverse in the [1 1 1] orientation crystal. By checking the results in Table 8.2 and Fig.8.14, the perfect

dislocation loop that generated from a full unzipped or partial unzipped SFT can always result in a much higher reduction in the compressive stress. The C/T asymmetry ratios for [1 0 0], [1 1 0] and [1 1 1] orientations at different simulation temperatures are plotted in Fig.8.13. An increased temperature appeared to play a small role on the C/T asymmetry.

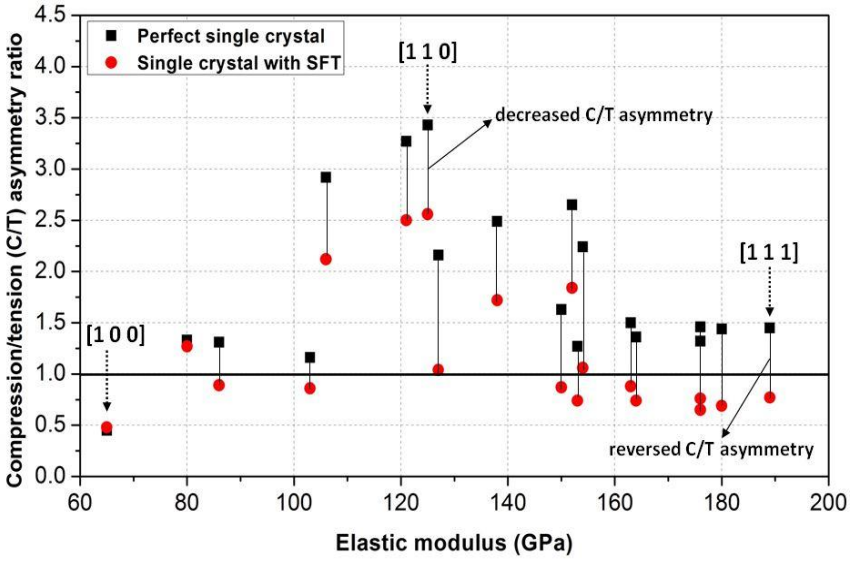

Figure 8.12 C/T asymmetry ratio of perfect crystal and crystal with SFT as a function of elastic modulus for different crystal orientations.

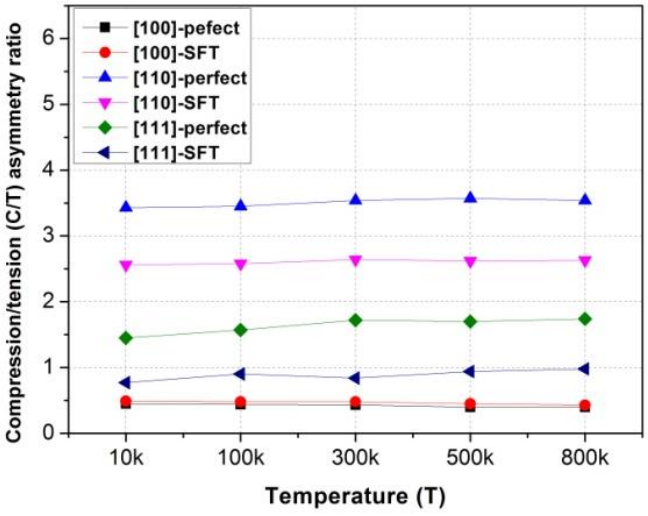

Figure 8.13 C/T asymmetry ratio for [1 0 0], [1 1 0] and [1 1 1] orientations at different simulation temperatures.

8.4.3 Unfaulting of the Frank loop

A similar case of structural conversion from a Frank loop to a perfect loop was

reported in previous experiments[29,261,262]. For example, Westmacott et al.[261] observed a large number of Frank dislocation loops in an aluminium 3.5% magnesium alloy quenched from 550℃ into oil at -20℃. After being heated slightly, some of the Frank loops were unfaulted and converted to perfect dislocation loops. Note that the conversion of a Frank partial loop to a perfect dislocation loop was probably a spontaneous process in their experiment because conversion occurred in a stress free condition and the only inducement was the slightly increased temperature. However, conversion in this study was determined as a stress assisted process. In the case of [1 1 1] crystal orientation, a 5% compressive strain, according to 10 GPa compressive stress, was needed to achieve this conversion. Recall that in this study, after a Frank loop was generated from a vacancy cluster it spontaneously dissociated to an SFT through the Silcox-Hirsch mechanism (see Fig.1) instead of converting to a perfect dislocation loop. Therefore, the critical questions are: what are the conditions in which an unfaulting Frank loop tends to occur, and in what conditions is an SFT unlikely to be produced from a vacancy cluster?

As Fig.7 shows, the unfaulting process was caused by the dissociation of Shockley partial dislocations from the stair-rod dislocation on the edge of the Frank loop and the subsequent glide of one Shockley partial dislocation across the fault. The essential problem is whether or not the prevailing conditions in the Frank loop would result in the nucleation of a Shockley partial dislocation and its spread across the stacking fault. A necessary condition is that the energy of the Frank loop with its associated stacking fault is greater than the energy of the perfect dislocation loop, i.e. there was a reduction in energy when the stacking fault was removed from the loop. According to the elasticity theory of dislocation[258,259], the total strain energy per unit length of dislocation is:

$$E_{el(screw)} = \frac{Gb^2}{4\pi} \tag{8-1}$$

$$E_{el(edge)} = \frac{Gb^2}{4\pi(1-\nu)} \ln\left(\frac{R}{r_0}\right) \tag{8-2}$$

where G is the shear modulus, b is the magnitude of the Burgers vector, ν is Poisson's ratio, R is outer radius, and r_o is the radius of the dislocation core. To a good approximation, by noting that the line length of a dislocation loop is 2πr, the elastic energy of a circular edge loop in an isotropic solid with Burgers vector $\mathbf{b_e}$ perpendicular to the loop plane is:

$$E = \frac{Gb_e^2 r}{2(1-\nu)} \ln\left(\frac{2r}{r_0}\right) \tag{8-3}$$

and for a circular shear loop with Burgers vector $\mathbf{b_s}$ lying in the loop plane, the elastic energy is:

$$E = \frac{Gb_s^2 r}{2(1-\nu)} \left(1 - \frac{\nu}{2}\right) \ln\left(\frac{2r}{r_0}\right) \tag{8-4}$$

The shear loop is a mixture of dislocation of edge and screw character. The stress fields of dislocation segments on opposite sides of a loop will tend to cancel at distances ≈2r from the loop, so that the outer cut-off parameter R is ≈2r. For the Frank loop with **b** =1/3[1 1 1], $b_e^2 = a^2/3$ and $b_s^2 = 0$, and for the perfect loop with **b** =1/2[1 1 0], $b_e^2 = a^2/3$ and $b_s^2 = a^2/6$. Thus, the difference in energy between the Frank loop containing the stacking fault and the perfect, unfaulted loop is:

$$\Delta E = \pi r^2 \gamma - \frac{Ga^2 r}{24} \left(\frac{2-\nu}{1-\nu}\right) \ln\left(\frac{2r}{r_0}\right) \tag{8-5}$$

Therefore, the unfaulting reaction will be energetically favourable if:

$$\gamma > \frac{Ga^2}{24\pi r} \left(\frac{2-\nu}{1-\nu}\right) \ln\left(\frac{2r}{r_0}\right) \tag{8-6}$$

Equation (8-6) indicates that the removal of a fault in a Frank partial loop depends on the size of the loop (r) and the stacking fault energy (γ). For a certain size Frank loop, Equation (8-6) gives a lower limit to the value of γ for the removal of a fault. In the experiment with aluminum alloy by Westmacott et al.[261], taking a=0.405 nm (lattice constant of aluminum), r=10 nm (which is close to the minimum size for resolving loops in the electron microscope), G=30 GN m^{-2}, r_o=0.5 nm, and ν=0.33, the critical

stacking fault energy was calculated to be almost 60 mJ m^{-2}, which was much less than the stacking fault energy of aluminum (about 146 mJ m^{-2} [221]). So that the Frank loops tended to convert to perfect loops in their experiment is reasonable, but in this study, by taking a=0.361 nm (lattice constant of copper), r=2 nm (considering the size of the introduced vacancy cluster and converted perfect loop), G=45 GN m^{-2}, r_o=0.5 nm, and ν=0.33, the critical stacking fault energy was calculated to be almost 202 mJ m^{-2}. This was much higher than the stacking fault energy of copper (about 44.4 mJ m^{-2} [221]), and therefore the Frank loop tended to be dissociated to an SFT with a lower energy instead of converting to a perfect loop. However, an MD simulation for the [1 1 1] orientation in compression implied that a concentration of local stress can promote this conversion.

8.5 Summary

Molecular dynamics (MD) simulations were carried out in this chapter to investigate the incipience of plasticity and the underlying atomic mechanisms in copper single crystals with SFT. Different deformation mechanisms of SFT were reported due to the crystal orientations and loading directions (compression and tension). The results showed that the incipience of plasticity in crystals with SFT resulted from the heterogeneous dislocation nucleation from SFT, so the stress required for plastic deformation was less than that needed for perfect single crystals. Three crystal orientations ([1 0 0], [1 1 0] and [1 1 1]) were specified in this study because they can represent most of the typical deformation mechanisms of SFT. MD simulations revealed that the structural transformation of SFT was prevalent under the applied loading. A metastable SFT structure and the unzipping of SFT were usually observed. The structural transformation resulted in a different reduction of yield stress in compression and tension, and also caused a decreased or reversed compression/tension asymmetry. Compressive stress can result in the unfaulting of Frank loop in some crystal orientations. According to the elastic theory of

dislocation, the process of unfaulting was closely related to the size of the dislocation loop and the stacking fault energy.

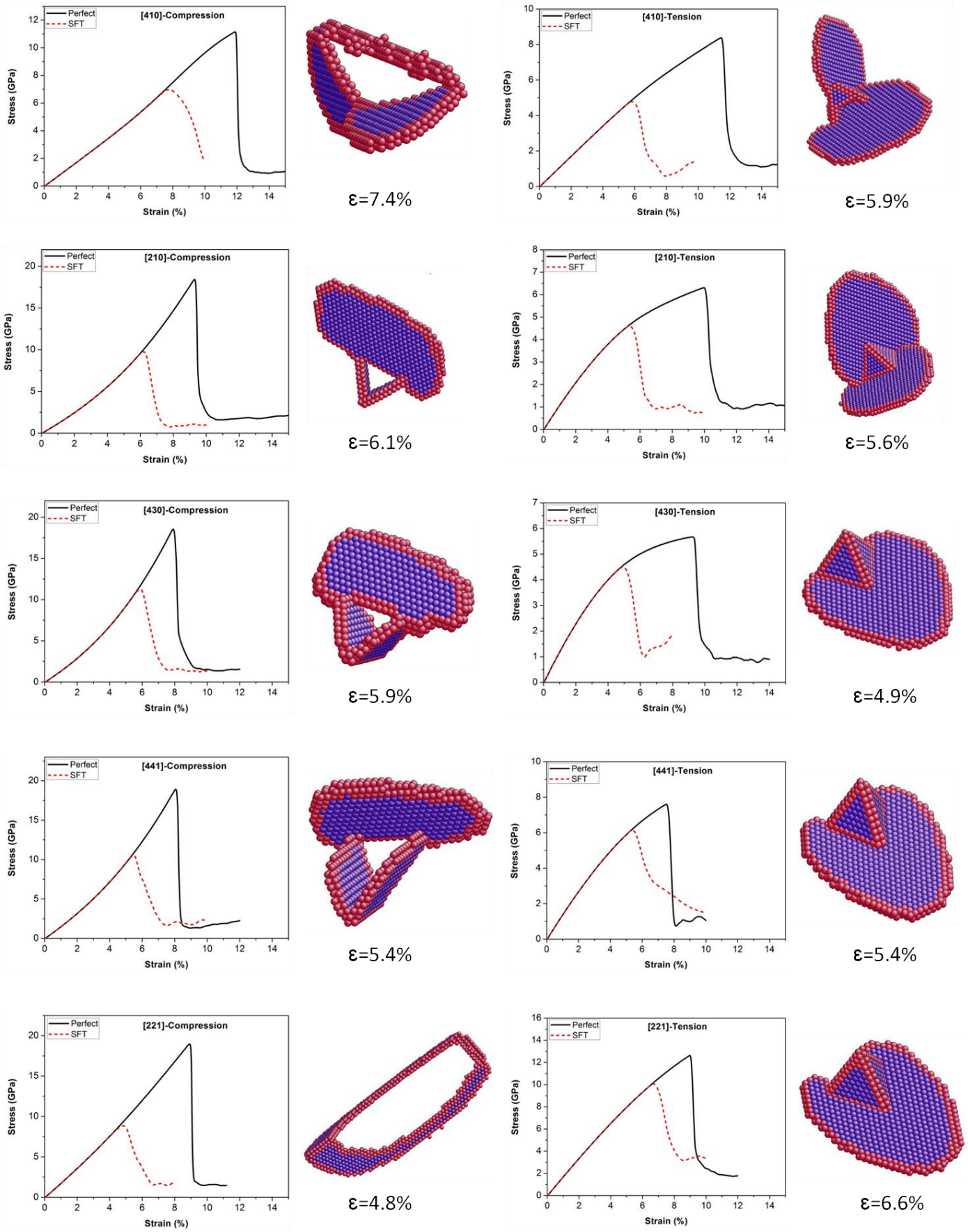

Figure 8.14 Stress-strain curves of perfect crystals and crystals with SFT under uniaxial compression and tension along different crystal orientations. The inserted snapshots show the atomistic configurations of SFT at the incipient of plasticity.

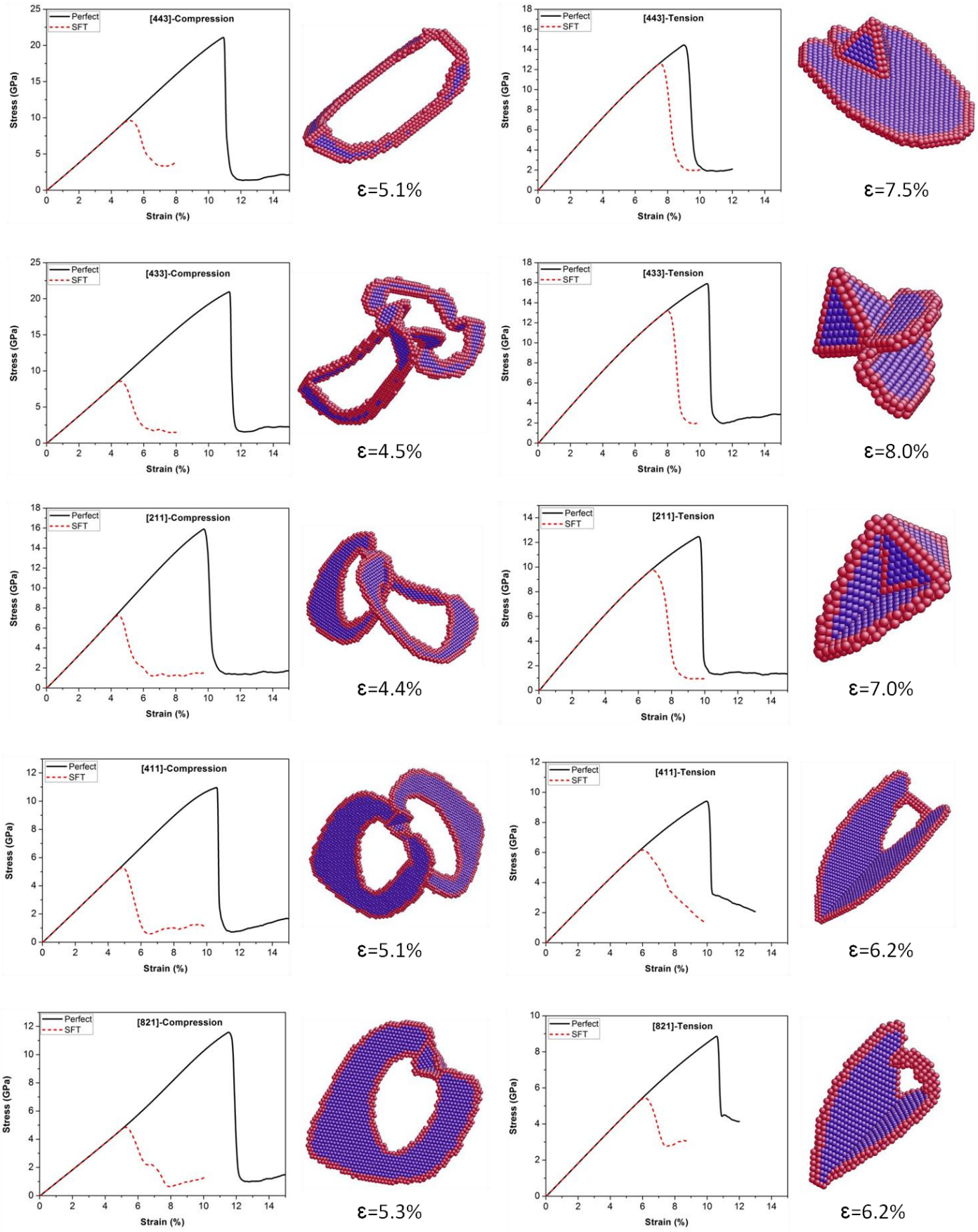

Figure 8.14 (continued)

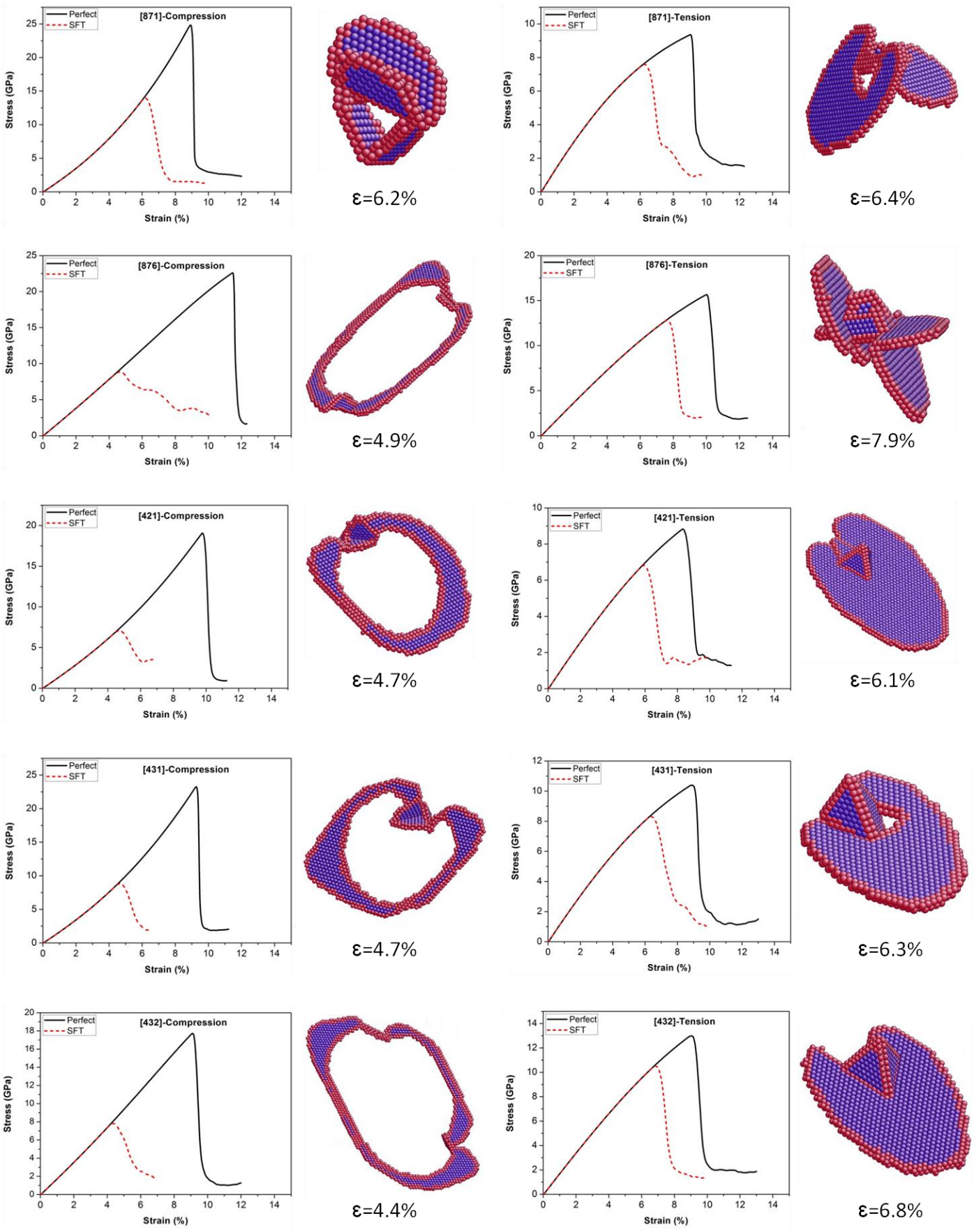

Figure 8.14 (continued)

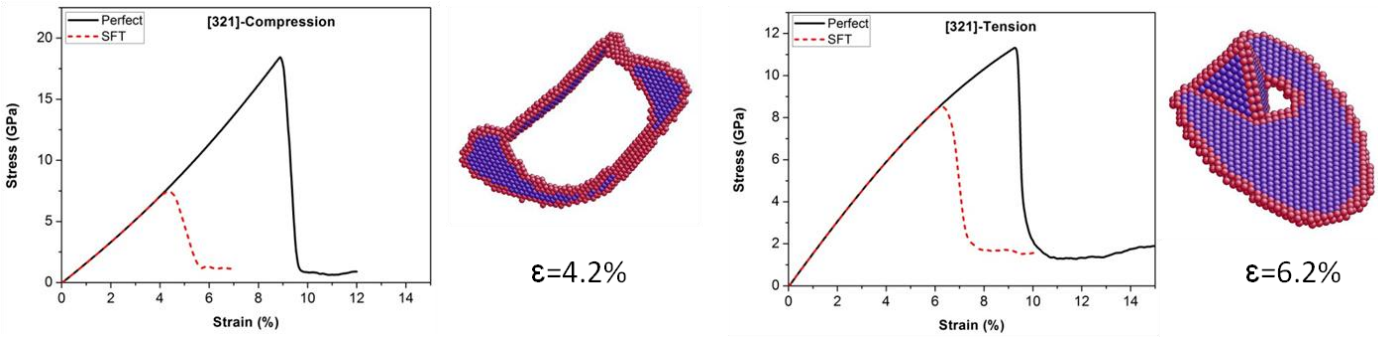

Figure 8.14 (continued)

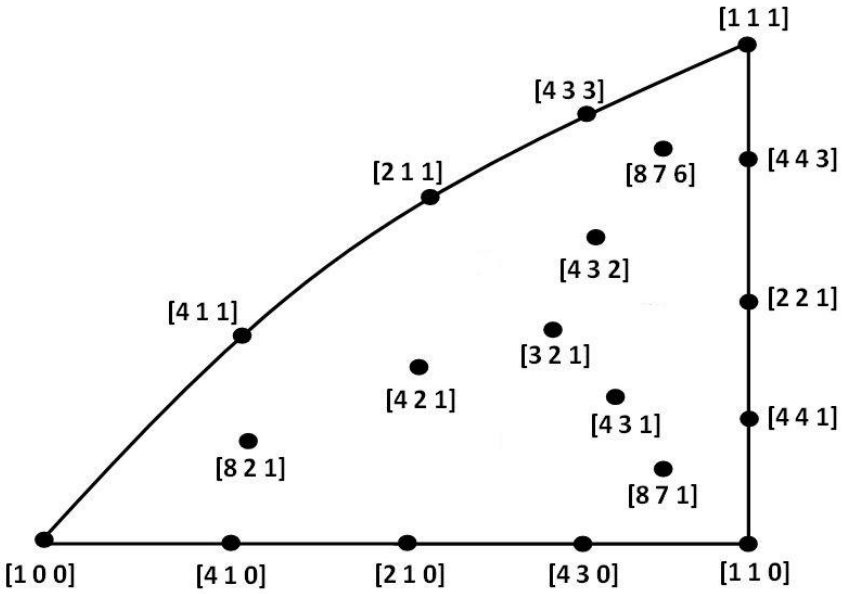

Figure 8.15 Stereographic triangle showing the crystallographic orientations investigated in this chapter. Each orientation denotes the uniaxial compression or tension direction axis for the deformation simulation.

Table 8.2 Simulation results of perfect crystals and crystals with an SFT under uniaxial compression (C) and tension (T) at 10 K.

Orientation	Elastic modulus (GPa)	Yield stress C-perfect (GPa)	Yield stress T-perfect (GPa)	Yield stress C-SFT (GPa)	Yield stress T-SFT (GPa)	Reduction of yield stress-C (%)	Reduction of yield stress-T (%)	C/T asymmetry ratio-perfect	C/T asymmetry ratio-SFT
[100]	65	4.86	10.75	3.56	7.44	24.9	30.8	0.45	0.48
[410]	80	11.15	8.38	6.97	5.49	37.5	34.5	1.33	1.27
[210]	106	18.42	6.3	9.76	4.6	47	26.9	2.92	2.12
[430]	121	18.54	5.67	11.27	4.5	39.2	20.6	3.27	2.5
[110]	125	18.76	5.47	11.79	4.61	37.1	15.8	3.43	2.56
[441]	138	18.9	7.6	10.54	6.14	44.2	19.2	2.49	1.72
[221]	163	18.95	12.62	8.84	10.08	53.4	20.1	1.5	0.88
[443]	176	21.08	14.43	9.63	12.58	54.3	12.8	1.46	0.76
[111]	189	24.97	17.17	10.67	13.85	57.3	19.3	1.45	0.77
[411]	103	10.96	9.41	5.3	6.17	51.6	34.4	1.16	0.86
[211]	153	15.9	12.47	7.26	9.76	54.3	21.7	1.27	0.74
[433]	176	20.96	15.9	8.57	13.17	59.1	17.2	1.32	0.65
[821]	86	11.58	8.86	4.85	5.44	58.1	38.6	1.31	0.89
[871]	152	24.84	9.36	13.97	7.59	43.8	18.9	2.65	1.84
[876]	180	22.59	15.66	8.84	12.81	60.9	18.2	1.44	0.69
[421]	127	19.06	8.83	7.09	6.82	62.8	22.8	2.16	1.04
[431]	154	23.26	10.39	8.85	8.32	61.9	19.9	2.24	1.06
[432]	164	17.72	12.98	7.82	10.53	55.9	18.9	1.36	0.74
[321]	150	18.43	11.32	7.44	8.54	59.6	24.5	1.63	0.87

CHAPTER 9

Conclusions and Recommendations

9.1 Overview

This thesis focused on understanding the role of grain boundary and stacking fault tetrahedron induced plasticity in nanocrystalline metals. Molecular dynamics simulations were conducted throughout the work. This is an important subject given the interest in the atomic deformation mechanisms of nanocrystalline metals with FCC structures. The three main parts of this thesis are: (1) dislocation nucleation from a series of <1 1 0> symmetric tilt GBs which cover a wide range of misorientation angles; (2) the tensile and shear response of both symmetric and asymmetric Σ5 and Σ11 GBs; (3) deformation mechanisms of SFT induced plasticity in single crystal Cu with different crystal orientations. A number of independent studies were carried out to gain a better understanding of the plastic deformation mechanisms of nanocrystalline metals at the atomic scale, including:

- Simulation of the generalised stacking fault energy in FCC metals
- Grain boundary dislocation source in copper bicrystal with <1 1 0> symmetrical tilt grain boundary
- Tension deformation behaviour of Σ5 grain boundaries in copper bicrystal
- Shear response of copper bicrystals with Σ11 grain boundaries
- Stacking fault tetrahedra induced plasticity in copper single crystals

The significant contributions of this work are summarised in the following sections, which were organised by chapters.

9.2 Study on the Generalised Stacking Fault Energy of FCC Metals

In chapter 4, MD simulations were used to investigate the influences of tensile and compressive stress on (1 1 1)[1 1 -2] GSF energy curves in the [1 1 1], [1 1 -2], and [1 -1 0] directions for three different fcc metals. The widely used EAM potentials developed by Mishin for Cu, Al, and Ni were tested in this study. The results showed that the GSF curves of the three elements can be influenced by the preloading stress. The values of γ_{usf}, γ_{sf} and γ_{utf} increased or decreased when preloading tensile or compressive stress was applied in a certain direction. The effects of stress on the ratios of γ_{sf}/γ_{usf} and $\gamma_{utf}/\gamma_{usf}$, which were closely related to the deformation mechanisms in nanocrystalline materials, were also investigated in this study. The results quantitatively demonstrated that not only the resolved stress along the slip plane (traditional Schmid factor), but also the resolved stress normal to the slip plane and the resolved stress perpendicular to the slip direction can play important roles in dislocation nucleation and twinning formation. The change in the GSF energy curve with applied stress indicated that the stress state was another important factor that can influence the deformation mechanism of nanocrystalline material.

9.3 Dislocation Nucleation in Cu Bicrystal with <1 1 0> Symmetric Tilt GBs

In chapter 5, MD simulations were conducted on Cu bicrystals with different <1 1 0> tilt GBs to study their structures, energy, mechanical property, and the dislocation nucleation mechanisms under uniaxial tension. In this study some of the GB properties such as GB energy, GB tensile strength, and the dislocation nucleation barrier on GB were quantified. We also presented the atomistic mechanisms of the dislocation nucleation from various GBs and investigated their correlation with GB properties. The results of this study are summarised as follows:

1. In every case the maximum tensile stress of the bicrystal models corresponded to the heterogeneous nucleation of partial dislocations from GBs, except for the ∑3(1 1 1) θ=109.5 ℃oherent twin boundary due to its simple and stable boundary

structure and extremely low boundary energy.

2. Within the misorientation range of $\theta<109.5°$, the tensile strength of bicrystals showed a consistent trend with the value of single crystals, which implied that lattice crystallographic geometry played a dominant role in the mechanical behaviour of GB. The incipient plastic deformation of bicrystal models was evidenced by a number of V-shaped partial dislocation loops with Burgers vector $\mathbf{b}=a/6[\bar{1}\,\bar{2}\,1]$ and $\mathbf{b}=a/6[2\,1\,\bar{1}]$ and their propagation on the $(1\ \bar{1}\ \bar{1})$ and $(1\ \bar{1}$ 1) planes.
3. The maximum tensile stress of GBs with $\theta>109.5°$ was much lower than the value of single crystals and showed a different trend. The simulation results indicated that the intrinsic GB structure, instead of having a lattice orientation, became the predominant factor that determined the mechanical behaviour of GBs. Dislocation nucleation was realised by the E structural unit transforming on the boundary plane. Some typical deformation mechanisms of E unit were illustrated in this study.
4. There was a strong interplay between GB properties, but higher boundary energy generally resulted in a lower boundary tensile strength and a lower dislocation nucleation barrier. However, the GB structure found another factor that can significantly influence its properties and nucleation mechanisms. For example, the consecutive shrinkage of C structural units along the $\sum11(3\ 3\ 2)$ GB provided a nucleation source for an extrinsic stacking fault and a twin fault, while the lowest tensile strength occurred for the low energy $\sum171(11\ 11\ 10)$ vicinal twin boundary with the dissociated boundary structure.

9.4 Tension Deformation Behaviour of Σ5 GBs in Cu Bicrystal

In chapter 6, MD simulations were carried out on two symmetric and four asymmetric $\sum5[001]$ tilt GBs of Cu with EAM potential to investigate the mechanical properties and the relevant deformation mechanisms under uniaxial tension. The main conclusions of this chapter are summarised as follows:

1. The equilibrium 0K GB structures were generated by molecular statics simulation. The simulation showed that the four ∑5 asymmetric GBs with different inclination angles (Φ=11.31 °, 18.43 °, 26.57 °, 30.96 °) consisted of only two structural units which corresponded to the two ∑5 symmetric tilt GBs (Φ=0 ° and Φ=45 °). GB energies were calculated according to the simulation results and they are agreed with the predicted energy values as a function of inclination angel based on faceting into the two symmetric boundaries.
2. Tensile deformations were performed on the bicrystal models under either 'free' or 'constrained' boundary conditions. The symmetric GBs showed a higher tensile strength under both tension boundary conditions than the asymmetric ones, which suggested that the symmetric GBs may have more stable boundary structures. This can be attributed to the comparatively lower boundary energy of the symmetric GBs.
3. Stress state can play an important role in the deformation mechanisms of nanocrystalline materials. The maximum tensile stress required for dislocation emission from the bicrystal models under constrained boundary condition was much higher than that required under free boundary conditions due to their different deformation mechanisms. A visual inspection of the MD simulation results indicated that massive dislocation nucleation and propagation was the dominant mechanism during tensile deformation under free tension boundary conditions, while under constrained boundary conditions, the nucleation of dislocation and its movement was severely restrained and the propagation of cracks became dominant due to the transverse stress.

9.5 Shear Response of Cu Bicrystals with Σ11 GBs

In chapter 7, MD simulations were carried out to study the mechanical response and deformation mechanisms of Σ11 tilt GBs in Cu bicrystal. Both symmetric and asymmetric GBs were tested under simple shear, and deformation modes were found to operate by GB migration coupled to shear deformation, with GB sliding caused

by local atomic shuffling, or nucleation of dislocations and stacking faults from the GB. The results of this chapter can be concluded as follow:

1. The non-planar GB structure, i.e. a GB plane with a dissociated stacking fault, was observed in the Σ11 asymmetric GBs in Cu. The dissociated structure observed in this study was mainly due to the comparatively low stacking fault energy of Cu. This indicated that the stacking fault energy had a significant effect on the grain boundary structure.
2. The stress driven motion of symmetric tilt GBs was regarded as occurring by the glide of identical dislocations along parallel slip planes. This mechanism was illustrated in our simulation of the Σ11(1 1 3) symmetric GB. The coupling motion of the Σ11(1 1 3) GB caused by shear deformation can be regarded as a combination of GB dislocation (1/22)<7 4 1> and GB dislocation (1/22)<3 3 2> sliding along the GB plane.
3. For the asymmetric Σ11 (Φ=54.74°) GB, shear deformation was accommodated by dislocation emissions from the GB plane, whereas GB can migrate itself at different levels of stress. Moreover, the dislocation nucleation mechanism can be different for the asymmetric Σ11 (Φ=70.53°) GB due to its different equilibrium structures.
4. The dissociated stacking fault from the GB plane can significantly affect the mechanical response of nanocrystalline material; for instance, it can increase ductility while retaining the high strength of the simulated cells under shear. This kind of structure can help to improve and optimise the mechanical properties by engineering the microstructure on the nanoscale in high-quality nanocrystalline metals.

9.6 Stacking Fault Tetrahedron Induced Plasticity in Cu Single Crystal

In chapter 8, MD simulations were carried out to investigate the effect of stacking fault tetrahedra on the incipience of plasticity in copper single crystal with different orientations under uniaxial compression and tension. Cases with three crystal

orientations ([1 0 0], [1 1 0]. and [1 1 1]) were specified. The results of this study can help us better understand the underlying deformation mechanisms of SFT induced plasticity in small volume crystals and provide a theoretical basis to design nanocrystalline materials that may be applied in some extreme environments. The main conclusions can be summarised as follows:

1. The incipience of plasticity in crystals with an SFT resulted from the heterogeneous dislocation nucleation from SFT, while homogeneous dislocation nucleation accounted for the onset of plasticity in the perfect crystals. Therefore, the stress needed for plastic deformation in the crystals with an SFT was less than that needed for the perfect crystals in all cases. This result implies that a stricter test standard should be carried out when testing materials that will be used in some extreme conditions, e.g. materials exposed in a radiation environment where a large amount of SFT exists.
2. The structural transformation of SFT was prevalent under applied loading. For example, a metastable structure called semi-faulted SFT, was found in the cases of [1 0 0] orientation in tension and [1 1 0] orientation in compression. For the [1 1 1] orientation, the SFT tended to collapse to a Frank loop and finally converted to a perfect dislocation loop under compression. The stress required for dislocation nucleation from a transformed SFT structure was much less than from an original SFT structure, which resulted in a different reduction in yield stress for different crystal orientations and loading directions.
3. The reduction in yield stress due to the presence of SFT was higher in compression than in tension for almost all orientations, and this deviation seemed more obvious with the increased elastic modulus. This reduction in yield stress can lead to a decreased or even reversed compression/tension asymmetry. This result suggested that tension and compression tests are both needed to test the mechanical property of materials where SFT are easy to form, and a compression test is more reliable because it can usually induce a higher

reduction in the yield stress.

4. The removal of SFT is very challenging and typically requires annealing at very high temperature, and the incorporation of interstitials or interaction with mobile dislocations. In this study the simulation results indicated that compressive loading can usually result in the collapse of SFT and facilitate its conversion to a perfect dislocation loop that can effectively improve the defect-free channel formation in irradiated materials. According to the elastic theory of dislocation, the size of a dislocation loop and the stacking fault energy play a significant role on the formation of SFT and the unfaulting of Frank loop to form a perfect dislocation loop.

9.7 Recommendations for Future Work

Atomistic simulations in this thesis provide a wealth of information regarding the mechanisms associated with crystal defects (grain boundary and stacking fault tetrahedra) induced plasticity in nanocrystal metal, which can help us to better understand the deformation mechanisms of crystal plasticity at the atomic scale. While this thesis has revealed some possible answers to the research questions posed in Chapter 1, further research questions also arise from this work. Some potential research areas are as follows:

1. **Low-angle grain boundary.** While high-angle GBs ($\theta>15°$) can be described using simple structural units, low-angle GBs ($\theta<15°$) are considered as consisting of an array of dislocations. The structure and mechanical property of high-angle GBs has been widely reported in previous research work due to their comparatively stable boundary structures. In this thesis the simulations were also limited to high-angle GBs; for example, high-angle <1 1 0> tilt GBs with misorientation angle ranged from $26.5°$ to $166.6°$ were studied in Chapter 5. With low-angle GBs it is difficult to attain the equilibrium boundary structures, i.e. for a given misorientation angle, various boundary structures (dislocation

arrays) with similar boundary energy were generated when constructing the simulation model. It was necessary to compare the simulated structures of low-angle GB with the experimental observations. The different mechanical response and underlying deformation mechanism between low-angle and high-angle GBs should also be investigated.

2. **Grain boundary with point defects.** In actual nanocrystalline materials, point defects (e.g. impurity atoms or vacancy) can affect the yield and fracture strengths of a material. For example, Millett et al.[263] showed that the inclusion of impurity atoms can dramatically change the structure of the local interface and potentially activate different dislocation nucleation mechanisms during the deformation process. The dislocation nucleation simulations in this thesis provided an upper bound for the nucleation stress in nanocrystalline materials. Research in this area can improve our understanding of the role of impurities and vacancies on GB induced crystal plasticity.

3. **Migration of asymmetric grain boundary.** Based on the classic theory by Read and Shockley[76], the non-uniform structure of asymmetric GBs consists of more than two types of dislocations which can block each other when gliding on the intersection planes, and prevent a coupled motion. Therefore, the migration of asymmetric GBs was thought to be impossible, but recent observations of coupled GB motion in bicrystal experiments[232,233] has suggested that this may not be true. The migration of $\Sigma 11(\Phi=54.74°)$ asymmetric GB in our simulation study also confirmed this view. While the atomic mechanisms for the migration of some symmetric GBs can be illustrated quite well, the mechanisms which caused the migration of asymmetric GB is still unclear. Trautt et al.[49] proposed two possible mechanisms by which the dislocations could avoid blocking each other and eventually result in the migration of asymmetric GB, i.e. dislocation reactions and dislocation avoidance (see Fig.2.16 and Fig.2.17). Further atomistic simulations are expected to give more information on this topic.

4. **Other types of GBs and material systems.** There is a significant fraction of GBs with tilt character[261], therefore this thesis concentrated on the tilt GBs for both symmetric and asymmetric GBs. However, the GB character of polycrystalline materials will often contain a twist component to the misorientation between grains. The structures and properties of twist GBs is of interest in any future study. Moreover, in most of the previous work, as well as in this thesis, simulations were used to investigate the structure and properties of GBs in FCC metals. However, with the appropriate potentials, the same methodology can be applied to BCC and HCP metals to understand how boundary structure is influenced in these systems.

5. **Imperfect stacking fault tetrahedra.** In Chapter 8, a comprehensive study on the formation of perfect SFT and its application to crystal plasticity were conducted using atomistic simulations, but a recent transmission electron microscopy investigation of high-energy proton irradiated copper[119] has shown that almost 50% of the visible SFT population are not perfect SFTs, but rather consist of truncated SFT and overlapping SFT.

REFERENCES

1. Kumar KS, Van Swygenhoven H, Suresh S. Mechanical behavior of nanocrystalline metals and alloys. *Acta Materialia* **51**, 5743-5774 (2003).

2. Meyers MA, Mishra A, Benson DJ. Mechanical properties of nanocrystalline materials. *Progress in Materials Science* **51**, 427-556 (2006).

3. Dao M, Lu L, Asaro RJ, De Hosson JTM, Ma E. Toward a quantitative understanding of mechanical behavior of nanocrystalline metals. *Acta Materialia* **55**, 4041-4065 (2007).

4. Zhu T, Li J. Ultra-strength materials. *Progress in Materials Science* **55**, 710-757 (2010).

5. Mishin Y, Asta M, Li J. Atomistic modeling of interfaces and their impact on microstructure and properties. *Acta Materialia* **58**, 1117-1151 (2010).

6. Farkas D. Atomistic simulations of metallic microstructures. *Current Opinion in Solid State and Materials Science* **17**, 284-297 (2013).

7. Khan AS, Suh YS, Chen X, Takacs L, Zhang H. Nanocrystalline aluminum and iron: Mechanical behavior at quasi-static and high strain rates, and constitutive modeling. *International Journal of Plasticity* **22**, 195-209 (2006).

8. Chen J, Lu L, Lu K. Hardness and strain rate sensitivity of nanocrystalline Cu. *Scripta Materialia* **54**, 1913-1918 (2006).

9. Chokshi AH, Rosen A, Karch J, Gleiter H. On the validity of the hall-petch relationship in nanocrystalline materials. *Scripta Metallurgica* **23**, 1679-1683 (1989).

10. Sanders PG, Eastman JA, Weertman JR. Elastic and tensile behavior of nanocrystalline copper and palladium. *Acta Materialia* **45**, 4019-4025 (1997).

11. Liao XZ, *et al.* Deformation mechanism in nanocrystalline Al: Partial dislocation slip. *Applied Physics Letters* **83**, 632-634 (2003).

12. Liao XZ, *et al.* Formation mechanism of wide stacking faults in nanocrystalline Al. *Applied Physics Letters* **84**, 3564-3566 (2004).

13. Shan Z, Stach EA, Wiezorek JMK, Knapp JA, Follstaedt DM, Mao SX. Grain Boundary-Mediated Plasticity in Nanocrystalline Nickel. *Science* **305**, 654-657 (2004).

14. Van Swygenhoven H, Caro A, Farkas D. Grain boundary structure and its influence on plastic deformation of polycrystalline FCC metals at the nanoscale: A molecular dynamics study. *Scripta Materialia* **44**, 1513-1516 (2001).

15. Schiøtz J, Jacobsen KW. A maximum in the strength of nanocrystalline copper. *Science* **301**, 1357-1359 (2003).

16. T an TY. Atomic Modelling of Homogeneouse Nucleation of Dislocations from Condensation of Point Defects in Silicon. *Philosophical Magazine A* **44**, 101-125 (1981).

17. Lubarda VA, Schneider MS, Kalantar DH, Remington BA, Meyers MA. Void growth by dislocation emission. *Acta Materialia* **52**, 1397-1408 (2004).

18. Pohjonen AS, Djurabekova F, Nordlund K, Kuronen A, Fitzgerald SP. Dislocation nucleation from near surface void under static tensile stress in Cu. *Journal of Applied Physics* **110** (2011).

19. Kiritani M. Story of stacking fault tetrahedra. *Materials Chemistry and Physics* **50**, 133-138 (1997).

20. Schibli R, Schäublin R. On the formation of stacking fault tetrahedra in irradiated austenitic stainless steels - A literature review. *Journal of Nuclear Materials* **442**, 761-767 (2013).

21. Silcox J, Hirsch PB. Direct observations of defects in quenched gold. *Philosophical Magazine* **4**, 72-89 (1959).

22. Wirth BD, Bulatov V, Diaz de la Rubia T. Atomistic simulation of stacking fault tetrahedra formation in Cu. *Journal of Nuclear Materials* **283–287, Part 2**, 773-777 (2000).

23. Czjzek G, Seeger A, Mader S. Die Stabilität von Stapelfehlertetraedern in abgeschreckten kubisch-flächenzentrierten Metallen und Legierungen. *physica status solidi (b)* **2**, 558-565 (1962).

24. Uberuaga BP, Hoagland RG, Voter AF, Valone SM. Direct Transformation of Vacancy Voids to Stacking Fault Tetrahedra. *Physical Review Letters* **99**, 135501 (2007).

25. Martinez E, Marian J, Arsenlis A, Victoria M, Perlado JM. A dislocation dynamics study of the strength of stacking fault tetrahedra. Part I: interactions with screw dislocations. *Philosophical Magazine* **88**, 809-840 (2008).

26. Martinez E, Marian J, Perlado JM. A dislocation dynamics study of the strength of stacking fault tetrahedra. Part II: interactions with mixed and edge dislocations. *Philosophical Magazine* **88**, 841-863 (2008).

27. Salehinia I, Lawrence SK, Bahr DF. The effect of crystal orientation on the stochastic behavior of dislocation nucleation and multiplication during nanoindentation. *Acta Materialia* **61**, 1421-1431 (2013).

28. Salehinia I, Bahr DF. Crystal orientation effect on dislocation nucleation and

multiplication in FCC single crystal under uniaxial loading. *International Journal of Plasticity* **52**, 133-146 (2014).

29. Robach JS, Robertson IM, Lee HJ, Wirth BD. Dynamic observations and atomistic simulations of dislocation–defect interactions in rapidly quenched copper and gold. *Acta Materialia* **54**, 1679-1690 (2006).

30. Salehinia I, Bahr DF. The impact of a variety of point defects on the incipience of plastic deformation in dislocation-free metals. *Scripta Materialia* **66**, 339-342 (2012).

31. Kumar KS, Suresh S, Chisholm MF, Horton JA, Wang P. Deformation of electrodeposited nanocrystalline nickel. *Acta Materialia* **51**, 387-405 (2003).

32. Stern EA, Siegel RW, Newville M, Sanders PG, Haskel D. Are nanophase grain boundaries anomalous? *Physical Review Letters* **75**, 3874-3877 (1995).

33. Van Swygenhoven H, Derlet PM, Frøseth AG. Stacking fault energies and slip in nanocrystalline metals. *Nature Materials* **3**, 399-403 (2004).

34. Cahn JW, Mishin Y, Suzuki A. Duality of dislocation content of grain boundaries. *Philosophical Magazine* **86**, 3965-3980 (2006).

35. Mori T, Miura H, Tokita T, Haji J, Kato M. Determination of the energies of [001] twist boundaries in Cu with the shape of boundary SiO2 particles. *Philosophical Magazine Letters* **58**, 11-15 (1988).

36. Mori T, Ishii T, Kajihara M, Kato M. Determination of the energies of [001] symmetric tilt boundaries in Cu from the shape of boundary SiO2 particles. *Philosophical Magazine Letters* **75**, 367-370 (1997).

37. Sangid MD, Sehitoglu H, Maier HJ, Niendorf T. Grain boundary characterization and energetics of superalloys. *Materials Science and Engineering: A* **527**, 7115-7125 (2010).

38. Merkle KL, Wolf D. Low-energy configurations of symmetric and asymmetric tilt grain boundaries. *Philosophical Magazine A* **65**, 513-530 (1992).

39. Hofmann D, Finnis MW. Theoretical and experimental analysis of near Σ3 (211) boundaries in silver. *Acta Metallurgica Et Materialia* **42**, 3555-3567 (1994).

40. Schmidt C, Ernst F, Finnis MW, Vitek V. Prediction and Observation of the bcc Structure in Pure Copper at a Σ3 Grain Boundary. *Physical Review Letters* **75**, 2160-2163 (1995).

41. Ernst F, *et al.* Theoretical prediction and direct observation of the 9R structure in Ag. *Physical Review Letters* **69**, 620-623 (1992).

42. Schmidt C, Finnis MW, Ernst F, Vitek V. Theoretical and experimental

investigations of structures and energies of Σ = 3[112] tilt grain boundaries in copper. *Philosophical Magazine A* **77**, 1161-1184 (1998).

43. Sansoz F, Molinari JF. Mechanical behavior of Σ tilt grain boundaries in nanoscale Cu and Al: A quasicontinuum study. *Acta Materialia* **53**, 1931-1944 (2005).

44. Zhang H, Srolovitz DJ. Simulation and analysis of the migration mechanism of Σ5 tilt grain boundaries in an fcc metal. *Acta Materialia* **54**, 623-633 (2006).

45. Tschopp MA, McDowell DL. Structures and energies of Σ3 asymmetric tilt grain boundaries in copper and aluminium. *Philosophical Magazine* **87**, 3147-3173 (2007).

46. Tschopp MA, McDowell DL. Asymmetric tilt grain boundary structure and energy in copper and aluminium. *Philosophical Magazine* **87**, 3871-3892 (2007).

47. Brown JA, Mishin Y. Dissociation and faceting of asymmetrical tilt grain boundaries: Molecular dynamics simulations of copper. *Physical Review B* **76**, 134118 (2007).

48. Lee SB, Sigle W, Kurtz W, Rühle M. Temperature dependence of faceting in Σ5(310)[001] grain boundary of SrTiO3. *Acta Materialia* **51**, 975-981 (2003).

49. Goukon N, Yamada T, Kajihara M. Boundary energies of Σ11[110] asymmetric tilt boundaries in Cu determined from the shape of boundary silica particles. *Acta Materialia* **48**, 2837-2842 (2000).

50. Gokon N, Kajihara M. Experimental determination of boundary energies of Σ9 [110] asymmetric tilt boundaries in Cu. *Materials Science and Engineering: A* **477**, 121-128 (2008).

51. Sutton AP, Balluffi RW. Overview no. 61 On geometric criteria for low interfacial energy. *Acta Metallurgica* **35**, 2177-2201 (1987).

52. Langdon TG. A unified approach to grain boundary sliding in creep and superplasticity. *Acta Metallurgica Et Materialia* **42**, 2437-2443 (1994).

53. T. G. Nieh JW, Sherby OD. *Mechanisms of high-temperature deformation and phenomenological relations for fine-structure superplasticity Superplasticity in Metals and Ceramics*. Cambridge University Press (1997).

54. Barnes AJ. Superplastic aluminum forming - expanding its techno-economie niche. *Materials Science Forum* **304-306**, 785-796 (1999).

55. Schroth JG. General motors' quick plastic forming process. *Advaces in Superplasticity and Superplastic Forming* (2004).

56. Wolf D, Yamakov V, Phillpot SR, Mukherjee A, Gleiter H. Deformation of

nanocrystalline materials by molecular-dynamics simulation: Relationship to experiments? *Acta Materialia* **53**, 1-40 (2005).

57. Agarwal S, Briant CL, Krajewski PE, Bower AF, Taleff EM. Experimental validation of two-dimensional finite element method for simulating constitutive response of polycrystals during high temperature plastic deformation. *Journal of Materials Engineering and Performance* **16**, 170-178 (2007).

58. Bower AF, Wininger E. A two-dimensional finite element method for simulating the constitutive response and microstructure of polycrystals during high temperature plastic deformation. *Journal of the Mechanics and Physics of Solids* **52**, 1289-1317 (2004).

59. Qi Y, Krajewski PE. Molecular dynamics simulations of grain boundary sliding: The effect of stress and boundary misorientation. *Acta Materialia* **55**, 1555-1563 (2007).

60. Du N, Qi Y, Krajewski PE, Bower AF. Aluminum Σ3 grain boundary sliding enhanced by vacancy diffusion. *Acta Materialia* **58**, 4245-4252 (2010).

61. Chandra N, Dang P. Atomistic simulation of grain boundary sliding and migration. *Journal of Materials Science* **34**, 655-666 (1999).

62. Namilae S, Chandra N, Nieh TG. Atomistic simulation of grain boundary sliding in pure and magnesium doped aluminum bicrystals. *Scripta Materialia* **46**, 49-54 (2002).

63. Schiøtz J, Di Tolla FD, Jacobsen KW. Softening of nanocrystalline metals at very small grain sizes. *Nature* **391**, 561-563 (1998).

64. Schiøtz J, Vegge T, Di Tolla FD, Jacobsen KW. Atomic-scale simulations of the mechanical deformation of nanocrystalline metals. *Physical Review B* **60**, 11971-11983 (1999).

65. Sansoz F, Molinari JF. Incidence of atom shuffling on the shear and decohesion behavior of a symmetric tilt grain boundary in copper. *Scripta Materialia* **50**, 1283-1288 (2004).

66. Kurtz RJ, Hoagland RG, Hirth JP. Effect of extrinsic grain-boundary defects on grain-boundary sliding resistance. *Philosophical Magazine A* **79**, 665-681 (1999).

67. Kurtz RJ, Hoagland RG, Hirth JP. Computer simulation of extrinsic grain-boundary defects in the ∑11<101>{131}symmetric tilt boundary. *Philosophical Magazine A* **79**, 683-703 (1999).

68. Hoagland RG, Kurtz RJ. The relation between grain-boundary structure and sliding resistance. *Philosophical Magazine A* **82**, 1073-1092 (2002).

69. Cahn JW, Taylor JE. A unified approach to motion of grain boundaries, relative tangential translation along grain boundaries, and grain rotation. *Acta Materialia* **52**, 4887-4898 (2004).

70. Taylor JE, Cahn JW. Shape accommodation of a rotating embedded crystal via a new variational formulation. *Interfaces and Free Boundaries* **9**, 493-512 (2007).

71. Cahn JW, Mishin Y, Suzuki A. Coupling grain boundary motion to shear deformation. *Acta Materialia* **54**, 4953-4975 (2006).

72. Ivanov VA, Mishin Y. Dynamics of grain boundary motion coupled to shear deformation: An analytical model and its verification by molecular dynamics. *Physical Review B* **78**, 064106 (2008).

73. Molodov DA, Ivanov VA, Gottstein G. Low angle tilt boundary migration coupled to shear deformation. *Acta Materialia* **55**, 1843-1848 (2007).

74. Molodov DA, Gorkaya T, Gottstein G. Mechanically driven migration of <100> tilt grain boundaries in Al-Bicrystals. *Materials Science Forum* **558-559**, 927-932 (2007).

75. Winning M. In-situ observations of coupled grain boundary motion. *Philosophical Magazine* **87**, 5017-5031 (2007).

76. Read WT, Shockley W. Dislocation Models of Crystal Grain Boundaries. *Physical Review* **78**, 275-289 (1950).

77. Zhang H, Du D, Srolovitz DJ. Effects of boundary inclination and boundary type on shear-driven grain boundary migration. *Philosophical Magazine* **88**, 243-256 (2008).

78. Trautt ZT, Adland A, Karma A, Mishin Y. Coupled motion of asymmetrical tilt grain boundaries: Molecular dynamics and phase field crystal simulations. *Acta Materialia* **60**, 6528-6546 (2012).

79. Fensin SJ, Asta M, Hoagland RG. Temperature dependence of the structure and shear response of a Σ11 asymmetric tilt grain boundary in copper from molecular-dynamics. *Philosophical Magazine* **92**, 4320-4333 (2012).

80. Dewald MP, Curtin WA. Multiscale modelling of dislocation/grain boundary interactions. II. Screw dislocations impinging on tilt boundaries in Al. *Philosophical Magazine* **87**, 4615-4641 (2007).

81. Dewald MP, Curtin WA. Multiscale modelling of dislocation/grain-boundary interactions: I. Edge dislocations impinging on Σ11 (1 1 3) tilt boundary in Al. *Modelling and Simulation in Materials Science and Engineering* **15**, S193-S215 (2007).

82. Jang H, Farkas D. Interaction of lattice dislocations with a grain boundary during

nanoindentation simulation. *Materials Letters* **61**, 868-871 (2007).

83. Shenoy VB, Miller R, Tadmor EB, Phillips R, Ortiz M. Quasicontinuum models of interfacial structure and deformation. *Physical Review Letters* **80**, 742-745 (1998).

84. Priester L. "Dislocation-interface" Interaction - Stress accommodation processes at interfaces. *Materials Science and Engineering A* **309-310**, 430-439 (2001).

85. De Koning M, *et al.* Modeling of dislocation-grain boundary interactions in FCC metals. *Journal of Nuclear Materials* **323**, 281-289 (2003).

86. Dewald MP, Curtin WA. Multiscale modeling of dislocation/grain-boundary interactions: III. 60° dislocations impinging on Σ3, Σ9 and Σ11 tilt boundaries in Al. *Modelling and Simulation in Material Science and Engineering* **19**, 055002 (2011).

87. Bachurin DV, Weygand D, Gumbsch P. Dislocation-grain boundary interaction in <111> textured thin metal films. *Acta Materialia* **58**, 5232-5241 (2010).

88. Cheng Y, Mrovec M, Gumbsch P. Atomistic simulations of interactions between the 1/2 <1 1 1> edge dislocation and symmetric tilt grain boundaries in tungsten. *Philosophical Magazine* **88**, 547-560 (2008).

89. Sangid MD, Ezaz T, Sehitoglu H, Robertson IM. Energy of slip transmission and nucleation at grain boundaries. *Acta Materialia* **59**, 283-296 (2011).

90. Shen Z, Wagoner RH, Clark WAT. Dislocation pile-up and grain boundary interactions in 304 stainless steel. *Scripta Metallurgica* **20**, 921-926 (1986).

91. Shen Z, Wagoner RH, Clark WAT. Dislocation and grain boundary interactions in metals. *Acta Metallurgica* **36**, 3231-3242 (1988).

92. Lee TC, Robertson IM, Birnbaum HK. Prediction of slip transfer mechanisms across grain boundaries. *Scripta Metallurgica* **23**, 799-803 (1989).

93. Koning MD, Miller R, Bulatov VV, Abraham FF. Modelling grain-boundary resistance in intergranular dislocation slip transmission. *Philosophical Magazine A* **82**, 2511-2527 (2002).

94. de Koning M, *et al.* Modeling of dislocation–grain boundary interactions in FCC metals. *Journal of Nuclear Materials* **323**, 281-289 (2003).

95. Jin ZH, *et al.* Interactions between non-screw lattice dislocations and coherent twin boundaries in face-centered cubic metals. *Acta Materialia* **56**, 1126-1135 (2008).

96. Jin ZH, *et al.* The interaction mechanism of screw dislocations with coherent twin boundaries in different face-centred cubic metals. *Scripta Materialia* **54**,

1163-1168 (2006).

97. Shimokawa T, Kinari T, Shintaku S. Interaction mechanism between edge dislocations and asymmetrical tilt grain boundaries investigated via quasicontinuum simulations. *Physical Review B* **75** (2007).

98. Lee TC, Robertson IM, Birnbaum HK. An In Situ transmission electron microscope deformation study of the slip transfer mechanisms in metals. *Metallurgical Transactions A* **21**, 2437-2447 (1990).

99. Lee TC, Robertson IM, Birnbaum HK. TEM in situ deformation study of the interaction of lattice dislocations with grain boundaries in metals. *Philosophical Magazine A* **62**, 131-153 (1990).

100. Dewald M, Curtin WA. Multiscale modeling of dislocation/grain-boundary interactions: III. 60° dislocations impinging on Σ3, Σ9 and Σ11 tilt boundaries in Al. *Modelling and Simulation in Materials Science and Engineering* **19**, 055002 (2011).

101. Yu W, Wang Z. Interactions between edge lattice dislocations and Σ11 symmetrical tilt grain boundaries in copper: A quasi-continuum method study. *Acta Materialia* **60**, 5010-5021 (2012).

102. Van Swygenhoven H, Derlet PM, Frøseth AG. Nucleation and propagation of dislocations in nanocrystalline fcc metals. *Acta Materialia* **54**, 1975-1983 (2006).

103. Van Swygenhoven H, Derlet PM, Hasnaoui A. Atomic mechanism for dislocation emission from nanosized grain boundaries. *Physical Review B* **66**, 241011-241018 (2002).

104. Spearot DE, Jacob KI, McDowell DL. Nucleation of dislocations from [0 0 1] bicrystal interfaces in aluminum. *Acta Materialia* **53**, 3579-3589 (2005).

105. Spearot DE, Tschopp MA, Jacob KI, McDowell DL. Tensile strength of <1 0 0> and <1 1 0> tilt bicrystal copper interfaces. *Acta Materialia* **55**, 705-714 (2007).

106. Spearot DE, Jacob KI, McDowell DL. Dislocation nucleation from bicrystal interfaces with dissociated structure. *International Journal of Plasticity* **23**, 143-160 (2007).

107. Tschopp MA, McDowell DL. Grain boundary dislocation sources in nanocrystalline copper. *Scripta Materialia* **58**, 299-302 (2008).

108. Tschopp MA, McDowell DL. Dislocation nucleation in Σ3 asymmetric tilt grain boundaries. *International Journal of Plasticity* **24**, 191-217 (2008).

109. Tschopp MA, Tucker GJ, McDowell DL. Structure and free volume of <1 1 0> symmetric tilt grain boundaries with the E structural unit. *Acta Materialia* **55**, 3959-3969 (2007).

110. Tucker GJ, Tschopp MA, McDowell DL. Evolution of structure and free volume in symmetric tilt grain boundaries during dislocation nucleation. *Acta Materialia* **58**, 6464-6473 (2010).

111. Wirth BD, Bulatov VV, De La Diaz Rubia T. Dislocation-stacking fault tetrahedron interactions in Cu. *Journal of Engineering Materials and Technology, Transactions of the ASME* **124**, 329-334 (2002).

112. Osetsky YN, Stoller RE, Rodney D, Bacon DJ. Atomic-scale details of dislocation-stacking fault tetrahedra interaction. *Materials Science and Engineering A* **400-401**, 370-373 (2005).

113. Saintoyant L, Lee H-J, Wirth BD. Molecular dynamics study of the interactions between dislocation and imperfect stacking fault tetrahedron in Cu. *Journal of Nuclear Materials* **361**, 206-217 (2007).

114. Lee HJ, Wirth BD. Molecular dynamics simulation of the interaction between a mixed dislocation and a stacking fault tetrahedron. *Philosophical Magazine* **89**, 821-841 (2009).

115. Niewczas M, Hoagland RG. Molecular dynamics studies of the interaction of a/6 h112i Shockley dislocations with stacking fault tetrahedra in copper. Part I: Intersection of SFT by an isolated Shockley. *Philosophical Magazine* **89**, 623-640 (2009).

116. Kiener D, Hosemann P, Maloy SA, Minor AM. In situ nanocompression testing of irradiated copper. *Nature Materials* **10**, 608-613 (2011).

117. Wei Wang J, Narayanan S, Yu Huang J, Zhang Z, Zhu T, Mao SX. Atomic-scale dynamic process of deformation-induced stacking fault tetrahedra in gold nanocrystals. *Nature Communications* **4**, 2340 (2013).

118. Fan H, Wang Q. A complete absorption mechanism of stacking fault tetrahedron by screw dislocation in copper. *Journal of Nuclear Materials* **441**, 211-215 (2013).

119. Schäublin R, Yao Z, Baluc N, Victoria M. Irradiation-induced stacking fault tetrahedra in fcc metals. *Philosophical Magazine* **85**, 769-777 (2005).

120. Bailat C, Gröschel F, Victoria M. Deformation modes of proton and neutron irradiated stainless steels. *Journal of Nuclear Materials* **276**, 283-288 (2000).

121. Niewczas M, Hoagland RG. Molecular dynamic studies of the interaction of a/6112 Shockley dislocations with stacking fault tetrahedra in copper. Part II: Intersection of stacking fault tetrahedra by moving twin boundaries. *Philosophical Magazine* **89**, 727-746 (2009).

122. Yu KY, *et al.* Removal of stacking-fault tetrahedra by twin boundaries in

nanotwinned metals. *Nature Communications* **4** (2013).

123. Swope WC, Andersen HC, Berens PH, Wilson KR. A computer simulation method for the calculation of equilibrium constants for the formation of physical clusters of molecules: Application to small water clusters. *The Journal of Chemical Physics* **76**, 637-649 (1982).

124. Martyna GJ, Tuckerman ME, Tobias DJ, Klein ML. Explicit reversible integrators for extended systems dynamics. *Molecular Physics* **87**, 1117-1157 (1996).

125. Andersen HC. Molecular dynamics simulations at constant pressure and/or temperature. *The Journal of Chemical Physics* **72**, 2384-2393 (1980).

126. Melchionna S, Ciccotti G, Lee Holian B. Hoover NPT dynamics for systems varying in shape and size. *Molecular Physics* **78**, 533-544 (1993).

127. Nos éS. A molecular dynamics method for simulations in the canonical ensemble. *Molecular Physics* **52**, 255-268 (1984).

128. Hoover WG. Canonical dynamics: Equilibrium phase-space distributions. *Physical Review A* **31**, 1695-1697 (1985).

129. Yamakov V, Wolf D, Salazar M, Phillpot SR, Gleiter H. Length-scale effects in the nucleation of extended dislocations in nanocrystalline Al by molecular-dynamics simulation. *Acta Materialia* **49**, 2713-2722 (2001).

130. Yamakov V, Wolf D, Phillpot SR, Mukherjee AK, Gleiter H. Dislocation processes in the deformation of nanocrystalline aluminium by molecular-dynamics simulation. *Nature Materials* **1**, 45-48 (2002).

131. Chen M, Ma E, Hemker KJ, Sheng H, Wang Y, Cheng X. Deformation twinning in nanocrystalline aluminum. *Science* **300**, 1275-1277 (2003).

132. Yamakov V, Wolf D, Phillpot SR, Mukherjee AK, Gleiter H. Deformation mechanism crossover and mechanical behaviour in nanocrystalline materials. *Philosophical Magazine Letters* **83**, 385-393 (2003).

133. Hasnaoui A, Van Swygenhoven H, Derlet PM. Cooperative processes during plastic deformation in nanocrystalline fcc metals: A molecular dynamics simulation. *Physical Review B* **66**, 1841121-1841128 (2002).

134. Hasnaoui A, Van Swygenhoven H, Derlet PM. Dimples on nanocrystalline fracture surfaces as evidence for shear plane formation. *Science* **300**, 1550-1552 (2003).

135. Daw MS, Baskes MI. Semiempirical, quantum mechanical calculation of hydrogen embrittlement in metals. *Physical Review Letters* **50**, 1285-1288 (1983).

136. Daw MS, Baskes MI. Embedded-atom method: Derivation and application to impurities, surfaces, and other defects in metals. *Physical Review B* **29**, 6443-6453 (1984).

137. Mishin Y, Mehl MJ, Papaconstantopoulos DA, Voter AF, Kress JD. Structural stability and lattice defects in copper: Ab initio, tight-binding, and embedded-atom calculations. *Physical Review B* **63**, 2241061-22410616 (2001).

138. Zope RR, Mishin Y. Interatomic potentials for atomistic simulations of the Ti-Al system. *Physical Review B* **68**, 0241021-02410214 (2003).

139. Plimpton S. Fast Parallel Algorithms for Short-Range Molecular Dynamics. *Journal of Computational Physics* **117**, 1-19 (1995).

140. Li J. AtomEye: an efficient atomistic configuration viewer. *Modelling and Simulation in Materials Science and Engineering* **11**, 173-177 (2003).

141. Stukowski A. Visualization and analysis of atomistic simulation data with OVITO–the Open Visualization Tool. *Modelling and Simulation in Materials Science and Engineering* **18**, 015012-015012 (015017) (2010).

142. Stukowski A, Albe K. Dislocation detection algorithm for atomistic simulations. *Modelling and Simulation in Materials Science and Engineering* **18**, (2010).

143. Stukowski A, Albe K. Extracting dislocations and non-dislocation crystal defects from atomistic simulation data. *Modelling and Simulation in Materials Science and Engineering* **18**, (2010).

144. Stukowski A, Bulatov VV, Arsenlis A. Automated identification and indexing of dislocations in crystal interfaces. *Modelling and Simulation in Materials Science and Engineering* **20**, (2012).

145. Stukowski A. Structure identification methods for atomistic simulations of crystalline materials. *Modelling and Simulation in Materials Science and Engineering* **20**, (2012).

146. Champion Y, Langlois C, Guérin-Mailly S, Langlois P, Bonnentien J-L, Hÿtch MJ. Near-Perfect Elastoplasticity in Pure Nanocrystalline Copper. *Science* **300**, 310-311 (2003).

147. Lu L, Shen Y, Chen X, Qian L, Lu K. Ultrahigh Strength and High Electrical Conductivity in Copper. *Science* **304**, 422-426 (2004).

148. Ma E. Nanocrystalline materials: Controlling plastic instability. *Nature Materials* **2**, 7-8 (2003).

149. Schiøtz J, Jacobsen KW. A Maximum in the Strength of Nanocrystalline Copper. *Science* **301**, 1357-1359 (2003).

150. Zhou Y, Erb U, Aust KT, Palumbo G. The effects of triple junctions and grain boundaries on hardness and Young's modulus in nanostructured Ni-P. *Scripta Materialia* **48**, 825-830 (2003).

151. Wang YM, Hamza AV, Ma E. Activation volume and density of mobile dislocations in plastically deforming nanocrystalline Ni. *Applied Physics Letters* **86** (2005).

152. Wang YM, Hamza AV, Ma E. Temperature-dependent strain rate sensitivity and activation volume of nanocrystalline Ni. *Acta Materialia* **54**, 2715-2726 (2006).

153. Schiøtz J. Atomic-scale modeling of plastic deformation of nanocrystalline copper. *Scripta Materialia* **51**, 837-841 (2004).

154. Asaro RJ, Krysl P, Kad B. Deformation mechanism transitions in nanoscale fee metals. *Philosophical Magazine Letters* **83**, 733-743 (2003).

155. Koch CC. Optimization of strength and ductility in nanocrystalline and ultrafine grained metals. *Scripta Materialia* **49**, 657-662 (2003).

156. Van Swygenhoven H. Grain boundaries and dislocations. *Science* **296**, 66-67 (2002).

157. Yamakov V, Wolf D, Phillpot SR, Mukherjee AK, Gleiter H. Deformation-mechanism map for nanocrystalline metals by molecular-dynamics simulation. *Nature materials* **3**, 43-47 (2004).

158. Vítek V. Thermally activated motion of screw dislocations in B.C.C. metals. *physica status solidi (b)* **18**, 687-701 (1966).

159. Vítek V. Intrinsic stacking faults in body-centred cubic crystals. *Philosophical Magazine* **18**, 773-786 (1968).

160. Zimmerman JA, Gao H, Abraham FF. Generalized stacking fault energies for embedded atom FCC metals. *Modelling and Simulation in Materials Science and Engineering* **8**, 103 (2000).

161. Tschopp MA, McDowell DL. Influence of single crystal orientation on homogeneous dislocation nucleation under uniaxial loading. *Journal of the Mechanics and Physics of Solids* **56**, 1806-1830 (2008).

162. Ogata S, Li J, Yip S. Ideal pure shear strength of aluminum and copper. *Science* **298**, 807-811 (2002).

163. Tschopp MA, Tucker GJ, McDowell DL. Atomistic simulations of tension–compression asymmetry in dislocation nucleation for copper grain boundaries. *Computational Materials Science* **44**, 351-362 (2008).

164. Zhang L, Lu C, Tieu K. Atomistic Simulation of Tensile Deformation Behavior

of ∑5 Tilt Grain Boundaries in Copper Bicrystal. *Scientific Reports* **4**, (2014).

165. Zhang L, Lu C, Tieu K, Pei L-Q, Zhao X. Effect of stress state on deformation and fracture of nanocrystalline copper：Molecular dynamics simulation. *Chinese Physics B* **23**, 98102-098102 (2014).

166. Rice JR. Dislocation nucleation from a crack tip: An analysis based on the Peierls concept. *Journal of the Mechanics and Physics of Solids* **40**, 239-271 (1992).

167. Hai S, Tadmor EB. Deformation twinning at aluminum crack tips. *Acta Materialia* **51**, 117-131 (2003).

168. Tadmor EB, Hai S. A Peierls criterion for the onset of deformation twinning at a crack tip. *Journal of the Mechanics and Physics of Solids* **51**, 765-793 (2003).

169. Mishin Y, Farkas D, Mehl MJ, Papaconstantopoulos DA. Interatomic potentials for monoatomic metals from experimental data and *ab initio* calculations. *Physical Review B* **59**, 3393-3407 (1999).

170. Ebrahim A, Mohsen Asle Z, Amitava M, Mark AT. Effect of vacancy defects on generalized stacking fault energy of fcc metals. *Journal of Physics: Condensed Matter* **26**, 115404 (2014).

171. Lu K, Lu L, Chen X, Huang X. Revealing the Maximum Strength in Nanotwinned Copper. *Science* **323**, 607-610 (2009).

172. Liao XZ, Zhou F, Lavernia EJ, He DW, Zhu YT. Deformation twins in nanocrystalline Al. *Applied Physics Letters* **75**, 5062-5064 (2003).

173. Fougere GE, Weertman JR, Siegel RW, Kim S. Grain-size dependent hardening and softening of nanocrystalline Cu and Pd. *Scripta Metallurgica et Materiala* **26**, 1879-1883 (1992).

174. Scattergood RO, Koch CC. A modified model for hall-petch behavior in nanocrystalline materials. *Scripta Metallurgica et Materiala* **27**, 1195-1200 (1992).

175. Champion Y, Langlois C, Guérin-Mailly S, Langlois P, Bonnentien JL, Hÿtch MJ. Near-perfect elastoplasticity in pure nanocrystalline copper. *Science* **300**, 310-311 (2003).

176. Yamakov V, Wolf D, Phillpot SR, Gleiter H. Dislocation-dislocation and dislocation-twin reactions in nanocrystalline Al by molecular dynamics simulation. *Acta Materialia* **51**, 4135-4147 (2003).

177. Van Swygenhoven H, Weertman JR. Deformation in nanocrystalline metals. *Materials Today* **9**, 24-31 (2006).

178. Tucker GJ, McDowell DL. Non-equilibrium grain boundary structure and

inelastic deformation using atomistic simulations. *International Journal of Plasticity* **27**, 841-857 (2011).

179. Randle V. The role of the grain boundary plane in cubic polycrystals. *Acta Materialia* **46**, 1459-1480 (1998).

180. Rittner JDSDN. <110> symmetric tilt grain-boundary structures in fcc metals with low stacking-fault energies. *Physical ReviewB* **54**, 6999-7015 (1996).

181. Olmsted DL, Foiles SM, Holm EA. Survey of computed grain boundary properties in face-centered cubic metals: I. Grain boundary energy. *Acta Materialia* **57**, 3694-3703 (2009).

182. Zhang L, Lu C, Michal G, Tieu K, Cheng K. Molecular dynamics study on the atomic mechanisms of coupling motion of [0 0 1] symmetric tilt grain boundaries in copper bicrystal. *Materials Research Express* **1**, 015019 (2014).

183. Stukowski A, Albe K. Extracting dislocations and non-dislocation crystal defects from atomistic simulation data. *Modelling and Simulation in Materials Science and Engineering* **18**, 085001 (2010).

184. Medlin DL, Mills MJ, Stobbs WM, Daw MS, Cosandey F. HRTEM observations of a Σ=3 {112} bicrystal boundary in aluminum. Materials Research Society Symposium Proceedings **295**,91-96 (1993).

185. Mills MJ, Daw MS, Thomas GJ, Cosandey F. High-resolution transmission electron microscopy of grain boundaries in aluminum and correlation with atomistic calculations. Uitramicroscopy **40**, 247-257.

186. Hardouin Duparc O, Poulat S, Larere A, Thibault J, Priester L. High-resolution transmission electron microscopy observations and atomic simulations of the structures of exact and near Σ=11{332} tilt grain boundaries in nickel. *Philosophical Magazine A* **80**, 853-870 (2000).

187. Poulat S, Thibault J, Priester L. HRTEM studies of the structures and the defects of exact and near Σ=11{332} tilt grain boundaries in Ni. *Interface Science* **8**, 5-15 (2000).

188. Marquis EA, Medlin DL. Structural duality of 1/3⟨111⟩ twin-boundary disconnections. *Philosophical Magazine Letters* **85**, 387-394 (2005).

189. Frøseth AG, Derlet PM, Van Swygenhoven H. Vicinal twin boundaries providing dislocation sources in nanocrystalline Al. *Scripta Materialia* **54**, 477-481 (2006).

190. Medlin DL, Carter CB, Angelo JE, Mills MJ. Climb and glide of a/3<111> dislocations in an aluminium Σ = 3 boundary. *Philosophical Magazine A* **75**, 733-747 (1997).

191. Foiles SM, Medlin DL. Structure and climb of 1/3⟨111⟩ twin dislocations in

aluminum. *Materials Science & Engineering A* **319**, 102-106 (2001).

192. Sansoz F, Molinari JF. Mechanical behavior of Sigma tilt grain boundaries in nanoscale Cu and Al: A quasicontinuum study. *Acta Materialia* **53**, 1931-1944 (2005).

193. Spearot DE. Evolution of the E structural unit during uniaxial and constrained tensile deformation. *Mechanics Research Communications* **35**, 81-88 (2008).

194. Sutton AP, Balluffi RW. *Interfaces in crystalline materials*. Clarendon (1995).

195. Van Swygenhoven H, Derlet PM. Grain-boundary sliding in nanocrystalline fcc metals. *Physical Review B* **64**, 224105 (2001).

196. Ma E. Watching the Nanograins Roll. *Science* **305**, 623-624 (2004).

197. Yamakov V, Wolf D, Phillpot SR, Gleiter H. Grain-boundary diffusion creep in nanocrystalline palladium by molecular-dynamics simulation. *Acta Materialia* **50**, 61-73 (2002).

198. Van Swygenhoven H, Derlet PM, Hasnaoui A. Atomic mechanism for dislocation emission from nanosized grain boundaries. *Physical Review B* **66**, 024101 (2002).

199. Budrovic Z, Van Swygenhoven H, Derlet PM, Van Petegem S, Schmitt B. Plastic Deformation with Reversible Peak Broadening in Nanocrystalline Nickel. *Science* **304**, 273-276 (2004).

200. Rohrer GS, Saylor DM, El Dasher B, Adams BL, Rollett AD, Wynblatt P. The distribution of internal interfaces in polycrystals.*Materials Research and Advanced Techniques* **95**, 197-214 (2004).

201. Saylor DM, El Dasher BS, Rollett AD, Rohrer GS. Distribution of grain boundaries in aluminum as a function of five macroscopic parameters. *Acta Materialia* **52**, 3649-3655 (2004).

202. Kim C-S, Rollett AD, Rohrer GS. Grain boundary planes: New dimensions in the grain boundary character distribution. *Scripta Materialia* **54**, 1005-1009 (2006).

203. Minkwitz C, Herzig C, Rabkin E, Gust W. The inclination dependence of gold tracer diffusion along a Σ3 twin grain boundary in copper. *Acta Materialia* **47**, 1231-1239 (1999).

204. Miyamoto H, Ikeuchi K, Mimaki T. The role of grain boundary plane orientation on intergranular corrosion of symmetric and asymmetric [1 1 0] tilt grain boundaries in directionally solidified pure copper. *Scripta Materialia* **50**, 1417-1421 (2004).

205. Gemming T, Nufer S, Kurtz W, Rühle M. Structure and Chemistry of

Symmetrical Tilt Grain Boundaries in α-Al2O3: I, Bicrystals with "Clean" Interface. *Journal of the American Ceramic Society* **86**, 581-589 (2003).

206. Lee SB, Sigle W, Rühle M. Faceting behavior of an asymmetric SrTiO3 Σ5 [001] tilt grain boundary close to its defaceting transition. *Acta Materialia* **51**, 4583-4588 (2003).

207. Lee SB, Kim Y-M. Kinetic roughening of a Σ5 tilt grain boundary in SrTiO3. *Acta Materialia* **57**, 5264-5269 (2009).

208. Bourret A, Rouviere JL, Penisson JM. Structure Determination of Planar Defects in Crystals of Germanium and Molybdenum by HREM. *Acta Crystallogr A* **A44**, 838-847 (1988).

209. Lee HS, Mizoguchi T, Yamamoto T, Kang SJL, Ikuhara Y. Characterization and atomic modeling of an asymmetric grain boundary. *Physical Review B* **84**, (2011).

210. Lin EQ, Shi HJ, Niu LS, Jin EZ. Shock response of copper bicrystals with a Σ3 asymmetric tilt grain boundary. *Computational Materials Science* **59**, 94 (2012).

211. Sheng-Nian L, Germann TC, Tonks DL, Qi A. Shock wave loading and spallation of copper bicrystals with asymmetricΣ3<110> tilt grain boundaries. *Journal of Applied Physics* **108**, 093526 (2010).

212. Zhang H, Duy D, Srolovitz DJ. Effects of boundary inclination and boundary type on shear-driven grain boundary migration. *Philosophical Magazine* **88**, 243-256 (2008).

213. Zhang H, Mendelev MI, Srolovitz DJ. Mobility of Sigma 5 tilt grain boundaries: Inclination dependence. *Scripta Materialia* **52**, 1193-1198 (2005).

214. Saylor DM, Morawiec A, Rohrer GS. Distribution of grain boundaries in magnesia as a function of five macroscopic parameters. *Acta Materialia* **51**, 3663-3674 (2003).

215. Rohrer GS, Randle V, Kim C-S, Hu Y. Changes in the five-parameter grain boundary character distribution in α-brass brought about by iterative thermomechanical processing. *Acta Materialia* **54**, 4489-4502 (2006).

216. Liu L, Wang J, Gong SK, Mao SX. Atomistic observation of a crack tip approaching coherent twin boundaries. *Scientific Reports* **4** (2014).

217. Mendelev MI, Zhang H, Srolovitz DJ. Grain boundary self-diffusion in Ni: Effect of boundary inclination. *Journal of Materials Research* **20**, 1146-1153 (2005).

218. Zhang H, Srolovitz DJ, Douglas JF, Warren JA. Characterization of atomic motion governing grain boundary migration. *Physical Review B* **74** (2006).

219. Kitamura T, Yashiro K, Ohtani R. Atomic simulation on deformation and fracture of nano-single crystal of nickel in tension. *JSME Internatinal Journal Series A-Solid Mechanics and Meterials Engineering* **40**, 430-435 (1997).

220. Spearot DE. Evolution of the E structural unit during uniaxial and constrained tensile deformation. *Mechanics Research Communications* **35**, 81-88 (2008).

221. Mishin Y, Farkas D, Mehl MJ, Papaconstantopoulos DA. Interatomic potentials for monoatomic metals from experimental data and ab initio calculations. *Physical Review B* **59**, 3393-3407 (1999).

222. Derlet PM, *et al.* Atomistic Simulations of Dislocations in Confined Volumes. *MRS Bulletin* **34**, 184-189 (2009).

223. Farkas D. Atomistic simulations of metallic microstructures. *Current Opionion in Solid State and Materials Science* **17**, 284-297 (2013).

224. Wan L, Wang S. Shear response of the Σ9<110>{221} symmetric tilt grain boundary in fcc metals studied by atomistic simulation methods. *Physical Review B* **82** (2010).

225. de Koning M, *et al.* Modeling of dislocation–grain boundary interactions in FCC metals. *Journal of Nuclear Materials* **323**, 281-289 (2003).

226. de Koning M, Miller R, Bulatov VV, Abraham FF. Modelling grain-boundary resistance in intergranular dislocation slip transmission. *Philosophical Magazine A* **82**, 2511-2527 (2002).

227. Bachurin DV, Weygand D, Gumbsch P. Dislocation–grain boundary interaction in <1 1 1> textured thin metal films. *Acta Materialia* **58**, 5232-5241 (2010).

228. Rittner JD, Seidman DN. <1 1 0> symmetric tilt grain-boundary structures in fee metals with low stacking-fault energies. *Physical Review B* **54**, 6999-7015 (1996).

229. Cui CB, Beom HG. Molecular statics simulations of intergranular fracture along ∑11 tilt grain boundaries in copper bicrystals. *Journal of Materials Science* **49**, 8355-8364 (2014).

230. Rae CMF, Smith DA. On the mechanisms of grain boundary migration. *Philosophical Magazine A* **41**, 477-492 (1980).

231. Fukutomi H, Kamijo T. Grain Boundary Sliding-Migration of Aluminum <110>Σ11{113} Symmetric Tilt Coincidence Grain Boundary and Its Interpretation Based on the Motion of Perfect DSC Dislocations. *Scripta Materialia* **19**, 195-197 (1985).

232. Molodov DA, Gorkaya T, Gottstein G. Dynamics of grain boundaries under applied mechanical stress. *Journal of Materials Science* **46**, 4318-4326 (2011).

233. Syed B, Catoor D, Mishra R, Kumar KS. Coupled motion of [1010] tilt boundaries in magnesium bicrystals. *Philosophical Magazine* **92**, 1499-1522 (2012).

234. Ernst F, *et al*. Theoretical Prediction and Direct Observation of the 9R Structue in Ag. *Physical Review Letters* **69**, 620-623 (1992).

235. Wolf U, Ernst F, Muschik T, Finnis MW, Fischmeister HF. The Influence of Grain Boundary Inclination on the Structure and Energy of Σ3 Grain Boundaries in Copper. *Philosophical Magazine A* **66**, 991-1016 (1992).

236. Mishin Y, Suzuki A, Uberuaga BP, Voter AF. Stick-slip behavior of grain boundaries studied by accelerated molecular dynamics. *Physical Review B* **75**, 224101 (2007).

237. Hu Q, Li L, Ghoniem NM. Stick–slip dynamics of coherent twin boundaries in copper. *Acta Materialia* **57**, 4866-4873 (2009).

238. Tschopp MA, Spearot DE, McDowell DL. Atomistic simulations of homogeneous dislocation nucleation in single crystal copper. *Modelling and Simulation in Materials Science and Engineering* **15**, 693-709 (2007).

239. Norman GE, Yanilkin AV. Homogeneous nucleation of dislocations. *Physics of the Solid State* **53**, 1614-1619 (2011).

240. Brochard S, Junqua N, Grilhé J. Nucleation of partial dislocations from a free surface: Theoretical study. *Philosophical Magazine A* **77**, 911-922 (1998).

241. Roos B, Kapelle B, Richter G, Volkert CA. Surface dislocation nucleation controlled deformation of Au nanowires. *Applied Physics Letters* **105**, 201908 (2014).

242. Tschopp MA, Spearot DE, McDowell DL. Chapter 82 Influence of Grain Boundary Structure on Dislocation Nucleation in FCC Metals. In: *Dislocations in Solids* (2008).

243. Zhang L, Lu C, Tieu K, Pei L, Zhao X, Cheng K. Molecular dynamics study on the grain boundary dislocation source in nanocrystalline copper under tensile loading. *Materials Research Express* **2**, 035009 (2015).

244. Zhang L, Lu C, Tieu K, Zhao X, Pei L. Shear Response of Copper Bicrystal with Σ11 Symmetric and Asymmetric Tilt Grain Boundaries by Molecular Dynamics Simulation. *Nanoscale* **7**, 7224-7233 (2015).

245. Loretto MH, Clarebrough LM, Segall RL. Stacking-fault tetrahedra in deformed face-centred cubic metals. *Philosophical Magazine* **11**, 459-465 (1965).

246. Kiritani M, Takamura Ji, Doyama M. *Point defects and defect interactions in metals*. University of Tokyo Press (1982).

247. Phillips PJ, Mills MJ. Fine-scale structure of dislocations and debris in deformed Ni-based superalloy R104. *Philosophical Magazine* **93**, 82-95 (2013).

248. Wirth BD, Bulatov V, Diaz de la Rubia T. Atomistic simulation of stacking fault tetrahedra formation in Cu. *Journal of Nuclear Materials* **283**, 773-777 (2000).

249. Osetsky YN, Bacon DJ, Singh BN, Wirth B. Atomistic study of the generation, interaction, accumulation and annihilation of cascade-induced defect clusters. *Journal of Nuclear Materials* **307**, 852-861 (2002).

250. Wang H, Xu DS, Yang R, Veyssière P. The formation of stacking fault tetrahedra in Al and Cu. *Acta Materialia* **59**, 1-9 (2011).

251. Wang H, Xu DS, Yang R, Veyssière P. The formation of stacking fault tetrahedra in Al and Cu. *Acta Materialia* **59**, 10-18 (2011).

252. Wang H, Xu DS, Yang R, Veyssière P. The formation of stacking fault tetrahedra in Al and Cu. *Acta Materialia* **59**, 19-29 (2011).

253. Loretto MH, Phillips PJ, Mills MJ. Stacking fault tetrahedra in metals. *Scripta Materialia* **94**, 1-4 (2015).

254. Matsukawa Y, Zinkle SJ. One-Dimensional Fast Migration of Vacancy Clusters in Metals. *Science* **318**, 959-962 (2007).

255. Yu KY, *et al.* Removal of stacking-fault tetrahedra by twin boundaries in nanotwinned metals. *Nature Communications* **4**, 1377 (2013).

256. Dai Y, Victoria M. Defect structures in deformed f.c.c. metals. *Acta Materialia* **45**, 3495-3501 (1997).

257. Dai Y, Victoria M. Defect cluster structure and tensile properties of copper single crystals irradiated with 600 MeV protons. In: *Materials Research Society Symposium Proceedings* (1997).

258. Hull D, Bacon D. *Introduction to Dislocations.* (Fifth Edition) (2011).

259. Hirth JP. *Theory of Dislocations*. (Second Edition) (1982).

260. Sato A, Sugisaki Y, Mori T. Effect of external stress on formation of vacancy loops in quenched aluminum. *Acta Metallurgica* **31**, 805-811 (1983).

261. Westmacott. Vacancy trapping in quenched aluminum alloys. *Philosophical magazine* **6**, 929-935 (1961).

262. Yoshida S. Dislocation loops with stacking fault in quenched aluminum. *Journal of the Physical Society of Japan* **18**, 175-183 (1963).

263. Millett PC, Selvam RP, Bansal S, Saxena A. Atomistic simulation of grain boundary energetics - Effects of dopants. *Acta Materialia* **53**, 3671-3678 (2005).